

# **Studies of the Solar Wind with Interplanetary Scintillation**

**Stuart A. Hardwick, MPhys (Hons)**

Solar System Physics Group  
Departments of Mathematics and Physics  
Penglais Campus  
Aberystwyth University  
SY23 3BZ

Dr. H. Morgan – Supervisor

Dr. M. M. Bisi – Supervisor

November 2015

This thesis is submitted in fulfillment of the requirements for the degree of  
Doctor of Philosophy of Aberystwyth University

## Declaration

This thesis has not previously been accepted in substance for any degree and is not being concurrently submitted in candidature for any degree.

Signed .....  ..... (candidate)  
Date ..... 27/11/2015 .....

## Statement 1

This thesis is the result of my own investigations, except where otherwise stated. Other sources are acknowledged by footnotes giving explicit references. A bibliography is appended.

Signed .....  ..... (candidate)  
Date ..... 27/11/2015 .....

## Statement 2

I hereby give consent for my thesis, if accepted, to be made available for photocopying and for inter-library loan, and for the title and summary to be made available to outside organisations.

Signed .....  ..... (candidate)  
Date ..... 27/11/2015 .....

# Acknowledgements

I would like to thank all of my supervisors (past and present) for all their support throughout the entirety of my Ph.D. I thank Dr. Andy Breen (R.I.P) for providing me with inspiration for solar physics as an undergraduate and giving me the opportunity to do my Ph.D. at Aberystwyth in the field. I thank my supervisors Dr. Huw Morgan, Dr. Jackie Davies, Professor Richard Harrison MBE and especially Dr. Mario Bisi who stepped in to become my supervisor and has continually given me the support I needed. I thank Dr. Richard Fallows and Dr. Jackie Davies for their time and patients as they taught me all the programming and analysis techniques which have made this thesis possible.

I would especially like to thank my best friends and team mates from the Aberystwyth Motorsports team; Hannah Mottershead, Alex Harrison, Artem Drobysh, Joseph Cauchi (Joe 2), Sophie Winter, Jon Aldridge, Joe Matheson (Joe 1), Verivaldo Teles (Veri), Daniel Headlam (Fresher), Joseph Sergeant (Joe 4), among many others for providing me with the joy of motorsports and giving me their constant support which has kept me sane over the years. I would also like to thank Ffion Roberts and Kane's Bar for continually supporting me and providing me and my friends with a place to relax and socialize and Cardigan Bay Karting Wales for always giving us a place to race karts.

My thanks go out to all my other friends at Aberystwyth in particular; Tine Funderud, Adele Teras, Meelika Leholá, Laura Anushka, Jason Murphy, Ryan Watson and James Evans who have given me some truly memorable times in Aberystwyth. I also thank my friends from Solihull; Daniel Dalton, Liam Glynn, Jennifer Geraghty (Jenni), Lisa Williams, Christine Kelby (Chrissie) and Lauren Jacobs who have always supported me even though I wasn't always around.

I would finally like to thank my brother Richard and my father Michael, whom have given me the encouragement and support (emotional and financial) that has made it possible for me to do my Ph.D.

# Summary

The Sun is at the centre of our solar system and it is constantly ejecting a flow of plasma outward into interplanetary space. This flow can take the form of two primary types; the fast solar wind; and the slow solar wind. The Sun may also eject plasma with more dynamic events which cause high density clouds of plasma to travel alongside the solar wind. In the modern world, a number of different techniques have been developed to study the solar wind from the Earth and also in interplanetary space. Interplanetary scintillation (IPS) is a technique that has been applied at Aberystwyth University to observe the continual density variations in the solar wind by observing a distant astronomical radio source and the scintillation of its radio waves as they pass through the solar wind. To perform this, a number of radio sites around the world have been used such as the European Incoherent SCATter radar (EISCAT) in northern Scandinavia, and the ever growing LOw Frequency ARray (LOFAR) based in the Netherlands. The IPS technique has also proved to be highly complementary with Heliospheric Imagers (HIs) onboard the Solar TERrestrial RELations Observatory (STEREO) spacecraft which detect the white light which has been scattered by the solar wind particles.

This thesis investigates the solar wind using a wide variety of techniques to observe the small- and large-scale structures which form in the solar wind. A study of IPS in 2007 and 2008 detected numerous events of rapid velocity variations which occurred in the slow solar wind. This showed evidence that the slow solar wind may have a 'blobular' nature formed of many small-scale transients as well as the large-scale transients which are already well known to us.

In November 2011 LOFAR observed its first coronal mass ejection (CME) while observing IPS. This event proved to become of interest as it was successfully detected by a number of different techniques and could modeled and tracked accurately as it propagated outward to Earth's orbit and even interacted with the Earth's magnetosphere.

A technique which could be applied to coronagraph observation separated the dynamic and quiescent solar wind structures from the images. The quiescent component became the basis for the development of a new solar wind model which could quickly and accurately map the background quiescent solar wind free from any of the complexities cause by CMEs.

# Contents

Declaration and Statements .....	i
Acknowledgments .....	ii
Summary .....	iii
Contents .....	iv
Chapter Zero .....	viii
<b>1 The Sun and Heliosphere .....</b>	<b>1</b>
1.1 The Solar Interior .....	3
1.1.1 The Core .....	4
1.1.2 Radiative Zone .....	4
1.1.3 Convection Zone .....	5
1.1.4 Photosphere.....	5
1.2 The Solar Atmosphere.....	6
1.2.1 Chromosphere .....	7
1.2.2 Corona.....	8
1.2.3 Solar Wind.....	10
1.2.4 The ‘Parker Spiral’ .....	15
1.2.5 Heliosphere.....	16
1.3 Solar Activity .....	17
1.3.1 Sunspots and the 11-(22-) Year Solar Cycle .....	17
1.3.2 Filaments (and Prominences) .....	19
1.3.3 Coronal Mass Ejections (CMEs).....	21
<b>2 Observations and Methods.....</b>	<b>25</b>
2.1 Radio Observations of the Sun.....	25

2.1.1 Interplanetary Scintillation (IPS) .....	25
2.1.1.1 The Beginnings of IPS .....	26
2.1.1.2 Scintillation Theory .....	27
2.1.1.3 Single-site Observations.....	30
2.1.1.4 Multi-site Observations .....	34
2.1.1.5 Dual-frequency IPS.....	37
2.2 White Light.....	38
2.2.1 Thomson Scattering .....	38
2.2.1.1 Coronagraphs and Heliospheric Imagers .....	41
2.3 Extreme Ultra-violet.....	43
<b>3 Sources of Experimental Data .....</b>	<b>45</b>
3.1 Ground-based Radio Telescopes for IPS .....	45
3.1.1 European Incoherent Scatter Radar (EISCAT) .....	45
3.1.2 Low Frequency Array (LOFAR) .....	47
3.2 Spacecraft.....	49
3.2.1 Solar and Heliospheric Observatory (SOHO) .....	49
3.2.1.1 Large Angle and Spectrometric Coronagraph (LASCO).....	52
3.2.2 Solar Terrestrial Relations Observatory (STEREO) .....	54
3.2.2.1 The Coronagraphs of STEREO .....	57
3.2.2.2 Heliospheric Imagers (HIs) .....	59
3.2.3 Solar Dynamics Observatory (SDO).....	61
3.2.4 Advanced Composition Explorer (ACE).....	64
3.2.5 Wind.....	67
<b>4 Analysis Methods .....</b>	<b>69</b>
4.1 IPS Analysis Package.....	69
4.2 Analysis Techniques of HI Observations .....	73
4.2.1 Difference Imaging.....	73
4.2.2 IPS P-point Mapping .....	74
4.2.3 Time-elongation Maps .....	78
4.2.3.1 Fixed Phi Model .....	79

4.2.3.2 Harmonic Mean Model .....	80
4.2.3.3 Self-similar Expansion .....	82
4.3 The Normalizing Radial Graded Filter (NRGF) .....	83
<b>5 Rapid Velocity Variation in the Slow Solar Wind .....</b>	<b>87</b>
5.1 Complementary Nature of IPS and the STEREO HIs .....	87
5.2 Observations .....	89
5.2.1 Survey of Observations .....	89
5.2.2 Case Study 1: 23 April 2007 .....	93
5.2.3 Case Study 2: 19 May 2007 (J0521+166) .....	98
5.2.4 Case Study 3: 19 May 2007 (J0431+206) .....	103
5.2.5 Case Study 4: 20 May 2007 .....	105
5.3 Conclusions .....	107
<b>6 Multi-technique Remote-sensing Observations and Modeling of a CME .....</b>	<b>110</b>
6.1 Preliminary Observation .....	110
6.2 Source Region – Extreme-ultraviolet (EUV) .....	111
6.3 Coronagraph Observations with LASCO and COR .....	117
6.3.1 Determining the CME Geometry Using a Flux Tub Wire Frame Model .....	120
6.4 Heliospheric Imager (HI) Observations .....	122
6.4.1 CME Fitting with J-maps .....	124
6.5 LOFAR Observations of IPS .....	127
6.5.1 IPS Projection on to HIs .....	129
6.6 Conclusions .....	131
<b>7 Ballistic Extrapolation Modeling of the Parker Spiral .....</b>	<b>135</b>
7.1 Parker Spiral Modeling .....	135
7.2 The Model .....	136
7.2.1 Tomographic Carrington Maps .....	137
7.2.2 Ballistic Propagation of the Parker Spiral .....	140
7.2.3 Propagation of Density .....	143

7.2.4 Projected Density Carrington Maps.....	143
7.3 Fully Automated Velocity Fitting.....	147
7.3.1 Velocity Profile Fitting and Remote-sensing Velocity Input .....	152
7.4 Conclusions .....	155
<b>8 Conclusions and Future Work.....</b>	<b>157</b>
8.1 Overall Summary.....	157
8.1.1 Rapid Velocity Variations in the Slow Solar Wind.....	158
8.1.2 Multi-technique Remote-sensing Observations and Modelling of a CME .....	159
8.1.3 Tomographic Ballistic Extrapolation Modelling of the Parker Spiral .....	160
8.2 Importance of Space Weather Research .....	161
<b>Bibliography.....</b>	<b>164</b>

# Chapter Zero

Within this thesis a number of techniques and analysis methods have been applied and built upon to produce the outcomes and results presented. This chapter aims to clarify the uniqueness of the work presented, and my personal contribution that has been made by myself for the development of the methods and tools used and also identify and acknowledge previously developed facilities that have been made available at Aberystwyth University and through other colleagues.

Interplanetary scintillation (IPS) has a long history at Aberystwyth University (previously University of Wales, Aberystwyth) with involvement with the EISCAT radar network for IPS beginning in the 1980s (Rishbeth and Williams, 1985). IPS was thus developed greatly from this point (discussed within chapter 3), and the current IPS analysis software package for use at Aberystwyth University was developed by Fallows (2001) and is detailed in chapter 4. This analysis package software allows the user to efficiently analyse raw dual-baseline antenna data to produce the cross-correlation between the antenna systems. Although designed to be fully automated, for best results the analysis requires manual control to remove noisy and erroneous data, and define limiting factors to filter radio signals from other sources so that only the solar wind is analyzed.

Chapter 5 of this thesis describes a survey of IPS results using a short, three minute, sliding window technique to analyze small temporal changes of velocity in the slow solar wind. A survey of this type had not previously been performed and thus it presented a new method to apply the IPS methodology to infer very small density variations in the slow solar wind. To provide a wider view of the solar wind during these observations, IPS P-Point (point of closest approach of the IPS ray path to the Sun) projection was performed onto the STEREO Heliospheric Imagers' field of view. The IPS P-Point technique developed by Dorrian (2009) was adopted for this purpose and is described in chapter 4.

Chapter 6 identifies and applies many observational techniques available for observing, tracking and predicting the evolution and path of a coronal mass ejection (CME) and validates the dual-antenna velocity estimations technique of IPS as a method for detecting CMEs and predicting their velocities. The projection of the IPS P-Point onto the STEREO HI's field of view provided new complexities for the period used, as the STEREO spacecraft were no longer near to the Earth (as they were in chapter 5) thus they no longer shared a near common line of sight. Instead the spacecraft were separated

near-perpendicular to the IPS antenna line of sight. This introduced a larger discrepancy between the IPS P-Point and the projected IPS P-Point (see chapter 4 for details). Thus the interpretation of this projection required additional scrutiny to determine an accurate position. To determine the velocity of the CME as viewed from STEREO HI, the fixed phi (Sheeley *et al.*, 2008; Rouillard *et al.*, 2008), harmonic mean (Lugaz, 2010; Möstl *et al.*, 2011), and self-similar expansion (Davies *et al.*, 2012; 2013) fitting models were used at all traceable angles of propagation. This chapter also introduced the application of the NRGF technique developed by Morgan *et al.* (2006; 2010; 2012) to enhance the visual prowess of the SOHO and STEREO coronagraph telescopes (LASCO and COR respectively) to observe CMEs and other dynamic events.

The NRGF technique of Morgan *et al.* (2006; 2010; 2012) also provides the quiescent solar wind component which was used as a base for the Ballistic Parker Spiral model developed in chapter 7. For the purpose of the model, the NRGF quiescent component required development to provide real densities inferred from the intensity of the solar wind streams of the image, and this was performed by Huw Morgan at Aberystwyth University to fit the requirements of the model being developed by myself. The Ballistic Parker Spiral model was thus developed, by myself, to extrapolate the quiescent solar wind from Carrington maps made using the NRGF technique produced by Huw Morgan.

# Chapter 1

## The Sun and Heliosphere

At the centre of our solar system is a large sphere of hot plasma, the Sun, our star. The Sun accounts for 99.86% of the total mass of our solar system. However special the Sun is within the solar system, the Sun remains a typical main sequence star in the Milky Way galaxy. The Earth orbits the Sun at an average distance of  $1.496 \times 10^8$  km, defined as an Astronomical Unit (AU), with a mean velocity of  $29.78 \text{ km s}^{-1}$ .

The Sun is primarily made up of Hydrogen (73.46% mass) and Helium (24.85% mass) (Kutner 1987). The remaining mass is trace amounts of heavier elements such as Oxygen and Carbon. The total mass of the Sun is ( $M$ ) of  $1.989 \times 10^{30}$  kg. This mass can easily be calculated using Kepler's third law, the law of periods:

$$M = \frac{r}{G} \left( \frac{2 \pi r}{T} \right)^2 \quad (1.1)$$

Where:

$r$  = Radius of Earth's orbit,

$G$  = Gravitational constant ( $6.672 \times 10^{-11} \text{ N m}^2 \text{ kg}^{-2}$ ),

$T$  = Time required for the Earth to make one complete orbit around the Sun ( $3.156 \times 10^7$  s or 365.256 days).

With a radius ( $R_S$ ) of  $6.9599 \times 10^8$  m the Sun is comfortably the largest body in the solar system and its average density ( $\rho$ ) calculated by equation 1.2 and results in an average density of  $1408 \text{ Kg m}^{-3}$ .

$$\rho = \frac{3M}{4\pi R_S^3} \quad (1.2)$$

Developing our understanding of the Sun allows a deeper understanding of other stars in the Milky Way galaxy and indeed the Universe. The Sun has constantly remained an area of particular interest

for physicists and astronomers alike. The Sun has been observed to produce many complex events of numerous differing scales throughout its structure, which may have dramatic effects on bodies within the solar system. These events and their modes of transport into the solar system, the solar wind, are introduced within this chapter.

<b>Solar Property</b>	<b>Accepted Measurement</b>
<b>Mass (kg)</b>	$1.989 \times 10^{30}$
<b>Volume (m<sup>3</sup>)</b>	$1.412 \times 10^{18}$
<b>Mean Density (kg m<sup>-3</sup>)</b>	1408
<b>Surface Gravity (m s<sup>-2</sup>)</b>	274.0
<b>Visual Magnitude</b>	- 26.74
<b>Absolute Magnitude</b>	+ 4.83
<b>Luminosity (J s<sup>-1</sup>)</b>	$3.846 \times 10^{26}$
<b>Spectral Type</b>	G2 V
<b>Sidereal Rotational Period (s)</b>	$2.1928 \times 10^6$

**Table 1.1** Summary of key properties of the Sun

Spacecraft have been launched with the primary objective of observing the Sun and measuring its extended solar atmosphere via *in-situ* and remote sensing methods. Ground-based instruments have also been developed to allow further remote-sensing observations of the Sun and the solar wind. Large radio antennas, telescopes or arrays are used to observe the light from the Sun and corona, as well as the scintillation of radio waves of astronomical radio sources due to the density structures which form in the heliosphere as a result of solar activity.

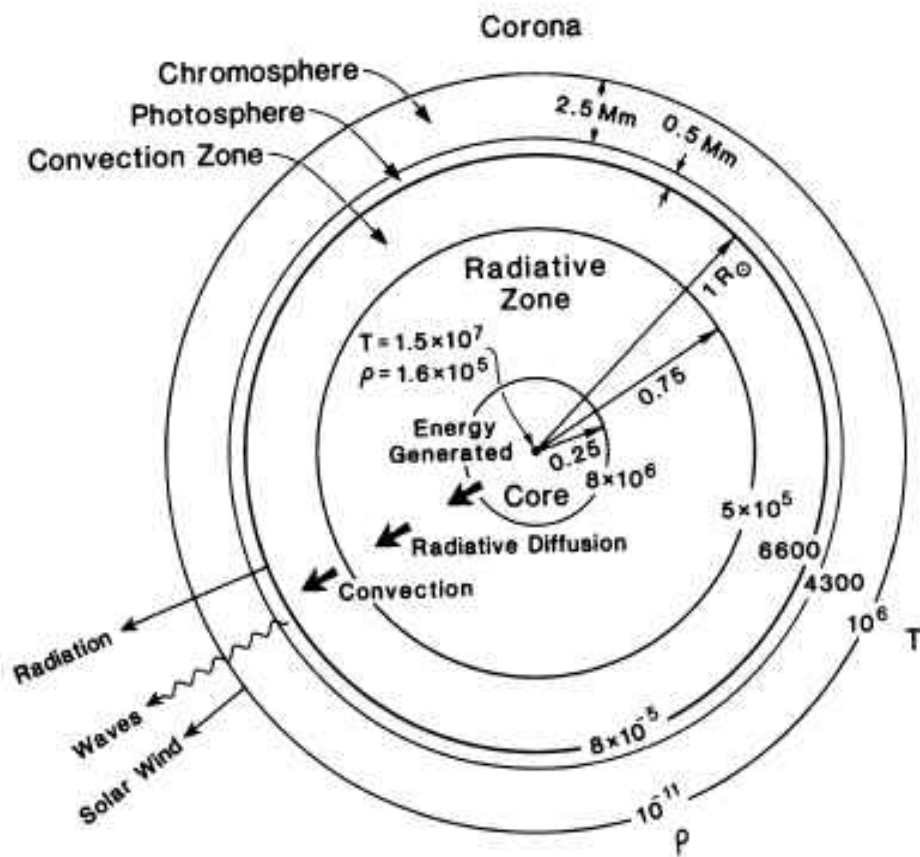


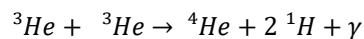
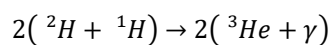
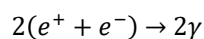
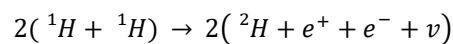
**Figure 1.1.** Internal structure of the solar interior and solar atmosphere, labelled with the different layers and their approximate densities ( $\text{kg m}^{-3}$ ), temperatures (Kelvin), and distances ( $R_{\odot}$ ) from Sun centre. (From Kivelson and Russell 1995)

### 1.1 The Solar Interior

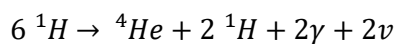
The Sun can be divided into different ‘layers’ as shown in figure 1.1. The solar interior is the name given to the region of the Sun extending from the core out towards the most visible layer in white light, the photosphere, and consists of four layers: the core, the radiative zone, the convection zone, and the photosphere. At the equator, the distance to the top of the photosphere (the external layer at which the solar interior is contained within) is  $6.9599 \times 10^8$  m, which is also known as a Solar Radius ( $R_{\odot}$ ), a unit of measurement frequently used for distance with regards to the Sun and within the heliosphere. 1 AU is approximately  $215.5 R_{\odot}$ .

### 1.1.1 The Core

The innermost region of the Sun is the Core, expanding out to 0.25 of a Solar Radius ( $R_s$ ). With a density estimated to be  $1.6 \times 10^5 \text{ kg m}^{-3}$  and temperature close to  $15 \times 10^6 \text{ K}$ , the Sun's core is the hottest and most-dense region of the Sun's interior. With these conditions, nuclear fusion of protons will occur allowing the solar core to produce the energy required to power the Sun. The fusion reaction that dominates in the core is known as the proton-proton (p-p) chain. During the p-p chain fusion two Hydrogen ( $^1\text{H}$ ) nuclei (protons) collide and combine to produce a Deuterium ( $^2\text{H}$ ) nucleus, a positron ( $e^+$ ), an electron ( $e^-$ ), and an electron neutrino ( $\nu_e$ ). The Deuterium nucleus can then combine with a further Hydrogen nucleus producing a Tralphium (Helium-3) nucleus ( $^3\text{He}$ ) and as a result releasing energy via gamma rays ( $\gamma$ -rays). The combination of two Tralphium nuclei allows the formation of a standard Helium nucleus ( $^4\text{He}$ ), two protons (Hydrogen nuclei), and the release of energy. To complete the p-p chain, the remaining electrons and positrons combine to produce further  $\gamma$ -rays. The reaction equations for the p-p chain are:



Overall:



(Kivelson and Russell 1995)

### 1.1.2 Radiative Zone

The energy produced by the fusion reaction is then transported outward from the core by radiative diffusion, giving the next region of the solar interior the name "the radiative zone". The energetic photons collide with protons and electrons within the radiative zone, in a 'random walk' process, each time losing some of their energy. Thus some of the radiative energy is converted into the kinetic energy (temperature) of the plasma. The Radiative zone extends out to  $0.75 R_s$ , and for this large region it can take high-energy photons  $10^5$  years to leave the radiative zone via the constant absorption and emission in a random walk process. With the decreased energy from absorption in this region the temperature also decreases, when compared to that of the core. Even though the

Radiative zone is one of the largest regions of the solar interior there is a shallow density gradient between the boundary regions, preventing convective methods of energy transfer occurring, meaning that most of the energy must be transported by radiative diffusion.

### 1.1.3 Convection Zone

At a height of  $0.75 R_s$  the temperature gradient begins to increase with height, allowing the possibility for energy to be primarily transported by convection. Within this convection zone the hot plasma becomes very turbulent, the matter forming convection cells to transport the hotter material higher, while forcing the cooler material to return to the base of the Convection Zone. In the convection cells the matter can rise at speeds of up to  $100 \text{ ms}^{-1}$ . When the material reaches the top of the convection cell, the material may emit photons out of the convection zone lowering the energy and temperature of the material so that it may sink to the base at a speed of  $200 \text{ ms}^{-1}$ . As in the radiative zone and core, the photons are still closely tied to the plasma and still experience the 'random walk' process of collision and emission, however the plasma itself is now moving upwards within the convection cells and carrying the radiation along with it.

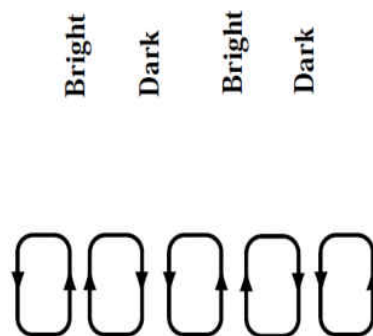


**Figure 1.2.** Illustration of the convection cells showing how the granulation pattern is produced as a result of the flow directions of each convection cell (From Kutner 1987).

### 1.1.4 Photosphere

The layer visible to the eye is found above the Convection Zone and is known as the Photosphere. The photosphere is one of the coolest layers of the Sun with a surface temperature of  $\sim 6600 \text{ K}$ . At this temperature much of the solar gas has cooled and no longer remains in its plasma state. When

we look at the Sun the photosphere appears as a surface layer of the Sun, however this is not the case and as a big ball of gas, has no finite layer. The visible appearance of the photosphere is due to the radiation of this layer being emitted in the white-light wavelengths which conveniently is electromagnetic radiation range that the human eye has become adept.

The convection cells, formed in the Convection Zone, produce a visible effect on the visible solar “surface”, known as granulation. The granulation pattern is produced when hot plasma is transported outward towards the solar surface in the convection cells producing a light region, and cooler plasma being transported downwards to replace the hot gas, producing the dark regions. A typical granulation cell has a diameter of 1,000km and has a lifetime of 5-10 minutes. The granulation pattern is illustrated in figure 1.2. Although the photosphere is not the most outer layer of the Sun, it is viewed as the solar surface and for which the solar radius is measured.

## **1.2 The Solar Atmosphere**

The Sun's atmosphere is very far reaching with its effects extending, by definition, across the entire solar system. The atmosphere is separated into regions, known as the Chromosphere, Corona and the largest extended region of the Sun, the heliosphere. Events which occur near the Sun often travel through the heliosphere into the interplanetary space and may affect planetary and magnetic fields and atmospheres. The temperatures observed in the solar atmosphere are very dynamic and between the chromosphere and corona, the temperature increases by several orders of magnitude. At the photosphere temperatures of the order of 6000 K are observed but as we enter the chromosphere this temperature falls to below 4500 K. Following the chromosphere, a thin transition region sees temperatures rise rapidly to over  $10^6$  K and this temperature is maintained in the corona. The temperature profile of the solar atmosphere is shown in figure 1.3.

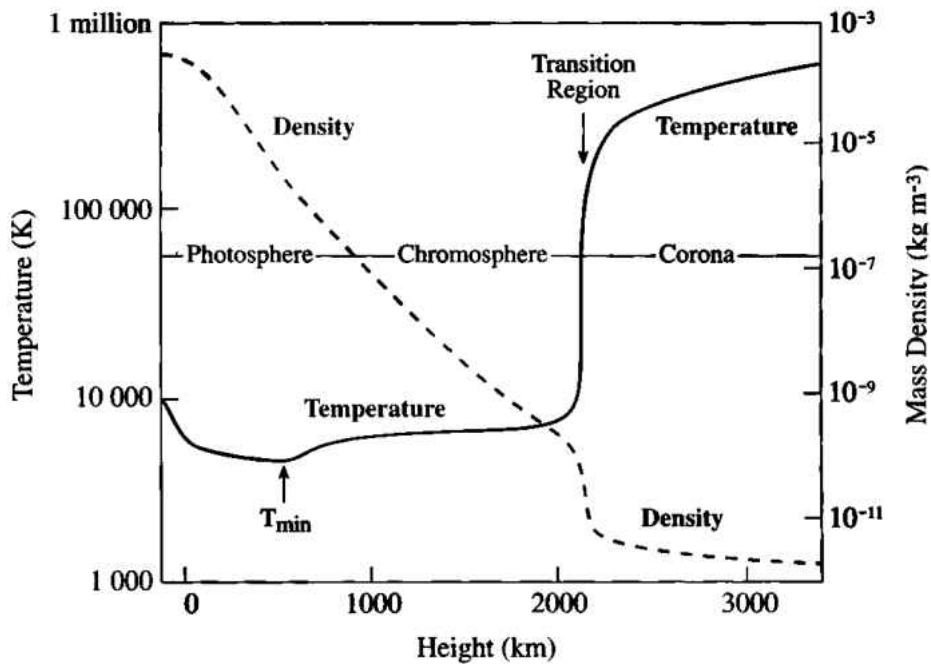


**Figure 1.3** Temperature and density profiles of the solar atmosphere against height (from Lang, 2001)

### 1.2.1 Chromosphere

Above the photosphere is the beginning of the solar atmosphere, the chromosphere. The chromosphere is not visible under normal conditions due to the overwhelming radiation from the photosphere below, however it can be viewed under solar-eclipse conditions when light from the much brighter photosphere is blocked from view (Kutner 1987). Under these conditions the chromosphere can be seen as a red glow from Hydrogen-alpha ( $H\alpha$ ) emission. When viewed using a  $H\alpha$  filter the chromosphere also shows granulation, similar to that found on the photosphere, however these granular cells are on a much larger scale, some reaching 30,000km in diameter. This supergranulation is formed as a result the Doppler shift of large convection cells with material moving upwards in the center of the cell and the material at the edge of the cell moving downwards (Kutner 1987).

Small-scale irregularities known as spicules also occur in the chromosphere. These spicules are dynamic jets of gas, observable in the  $H\alpha$  spectral lines, which erupt through the chromosphere into

the lower corona with a local upward mass flux 100 times that of the quiescent solar wind (Sterling, 2000). Figure 1.4 shows the chromospheric spicules as dark tube-like features as viewed in H $\alpha$ .

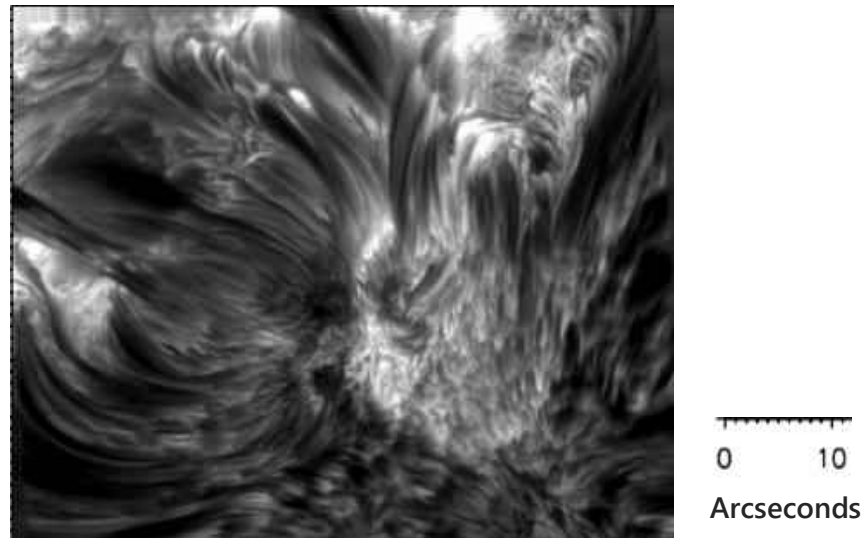


**Figure 1.4** H $\alpha$  Image of a small region of the Sun taken by Swedish Solar Telescope (SST) on 4 October 2005. The image shows an active region as well as the dark tube-like spicules which occur in the chromosphere (adapted from De Pontieu *et al.*, 2007).

### 1.2.2 Corona

Above the chromosphere, the corona extends far out into space to become the solar wind. This is a region of great interest for solar physicists, in particular the heating mechanism that can produce a very high temperature of  $\sim 1$  million Kelvin or higher in the very short transition region between the chromosphere and the corona (Kivelson and Russell 1995). Present models to solve the coronal heating problem include: small bursts of magnetic energy (nanoflares) and their associated magnetic reconnection (Parker 1988; Jain, Browning and Kusano 2005; Hood, Browning and van der Linden 2009), chromospheric spicules and Alfvén waves (Kudoh 2007; Dwivedi and Srivastava 2010). The corona can be viewed during solar eclipse when the much brighter light from the solar disk is blocked from the view of the telescope allowing the dimmer corona to be observed. Coronagraphs are telescopes which block out the solar disk simulating the effect of a solar eclipse, allowing routine observations of the corona (Brueckner, *et al.* 1995), an example of such is shown in figure 1.5. In coronagraphs, the higher density features appear as bright structures against the background (such as the bright extended features in figure 1.5 due to the high density slow solar wind – see the

following section) due to the Thomson scattering (see chapter 2) of the solar radiation by the coronal particles.

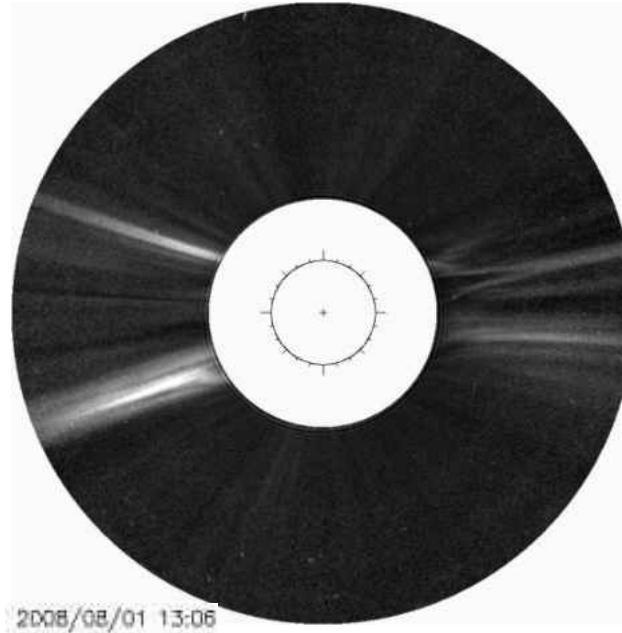


**Figure 1.5** NRGF LASCO C2 image (details are given in chapter 2 and 4) of the corona on 01 August 2008 13:06 UT.

The corona may also be observed in extreme ultra violet (EUV) by observing the solar disk directly. This is possible since the photosphere is not emitting at these wavelengths and all we see is the emission from the low corona. Within this wavelength range it is possible to distinguish regions of the corona by observing the spectral bands of different elements which can be associated with different temperature regimes. Observations by Newkirk Jr (1967) and Waldmeier (1975) revealed large regions of fainter corona (reduced emission) in X-ray and EUV emission lines and these dimming events are now known as coronal holes. These coronal holes are formed due to the temperature and density properties of the material being outside of the observing wavelength, thus reducing its luminosity to the surrounding corona in the observing wavelength. Coronal holes are the footprints of magnetic fields opening freely into the corona and are the source regions of the fast solar (Cranmer, 2009; Lowder *et al.*, 2014).

As the corona is heated the plasma is accelerated outwards into the heliosphere; this region is thus dubbed the acceleration region of the solar wind.

### 1.2.3 Solar Wind

Parker (1958) believed that the corona should act like an ideal gas and suggested that it could not maintain a static equilibrium while surrounded by the vacuum of space and thus proposed that the corona should expand isothermally as a steady state outward into interplanetary space, i.e. the temperature remains constant and the plasma properties do not change over time. Parker (1958) defined this continually expanding coronal material to become the solar wind. With the assumptions of a steady state, isothermal and spherically symmetric expansion Parker (1958) adapted the equation of continuity along with Euler's equation of motion to derive equation 1.3, a solution for the solar wind derived by Parker (1958).

$$\frac{1}{u} \frac{du}{dr} \left( u^2 - \frac{2 k_B T}{m_p} \right) = \frac{4 k_B T}{m_p r} - \frac{GM_S}{r^2} \quad (1.3)$$

Where:

$k_B$  = Boltzmann constant ( $1.3806 \times 10^{-23} \text{ m}^2 \text{ kg s}^{-2} \text{ K}^{-1}$ ),

$T$  = Plasma temperature,

$u$  = Radial expansion speed,

$m_p$  = Proton mass,

and  $r$  = Radius.

Equation 1.3 can be broken down to reveal four unique solutions. At the base of the corona at radius,  $R_C$ , the right-hand side of equation 1.3 will become zero at a coronal temperature,  $T_C$ . In reality this temperature is however, hotter than the actual coronal temperature. By introducing  $R_C$  and  $T_C$  into equation 1.3 and thus reducing the RHS of equation 1.3 to zero, equation 1.4 can be derived.

$$T_C \equiv \frac{G M_S m_p}{4 k_B R_C} \quad (1.4)$$

This solves  $T_C$  to be  $\sim 6 \times 10^6 \text{ K}$ , which is greater than the known temperature of the corona at the base of the corona. If  $T < T_C$  then the RHS of equation 1.3 will become negative at the base of the corona and at radius' greater than the coronal radius. For this to remain valid, the radius must also remains less than the radius at which the left-hand side (LHS) becomes negative (the critical radius),  $r_c$ , i.e.  $R_C < r < r_c$ , where:

$$\frac{r_C}{R_C} = \frac{T_C}{T} \quad (1.5)$$

Similarly the RHS of equation 1.3 is positive while  $r_C < r < \infty$ . From equation 1.5 it can be seen that equation 1.3 will become zero at  $r = r_C$ . For the LHS of equation 1.3 to be zero one either of equation 1.6 or equation 1.7 must be true.

$$\frac{du}{dr_C} = 0 \quad (1.6)$$

$$u^2 = \frac{2 k_B T}{m} \quad (1.7)$$

Equation 1.7 is equal to the coronal sound speed. These possibilities lead to the four solutions:

1. Flow remains subsonic and reaches a maximum velocity at  $r_C$ .
2. Initial flow is subsonic and accelerates to the sound speed at  $r_C$  becoming supersonic.
3. Initial flow is supersonic and decelerates, reaching the sound speed at  $r_C$ , and becoming subsonic.
4. Flow remains supersonic with a minimum velocity at  $r_C$ .

Figure 1.6 shows Parker's velocity solutions of an isothermally expanding corona against distance into the heliosphere. A coronal temperature between  $1 \times 10^6$  K and  $2 \times 10^6$  K gives realistic solar wind velocities at 1 AU between  $\sim 500 \text{ km s}^{-1}$  and  $\sim 750 \text{ km s}^{-1}$ .

In 1992 the NASA/ESA *Ulysses* mission entered a near polar orbit of the Sun so that it measured the properties of the high-latitude solar wind at a period of low solar activity (solar minimum) (*e.g.* McComas, *et al.* 2000). The completed polar pass of *Ulysses* confirmed latitudinal variations of solar wind velocities. At polar latitudes the solar wind was measured to be very fast with velocities exceeding  $700 \text{ km s}^{-1}$  (fast wind) compared to velocities of less than  $500 \text{ km s}^{-1}$  found at the solar equator (*e.g.* McComas, *et al.* 2000).

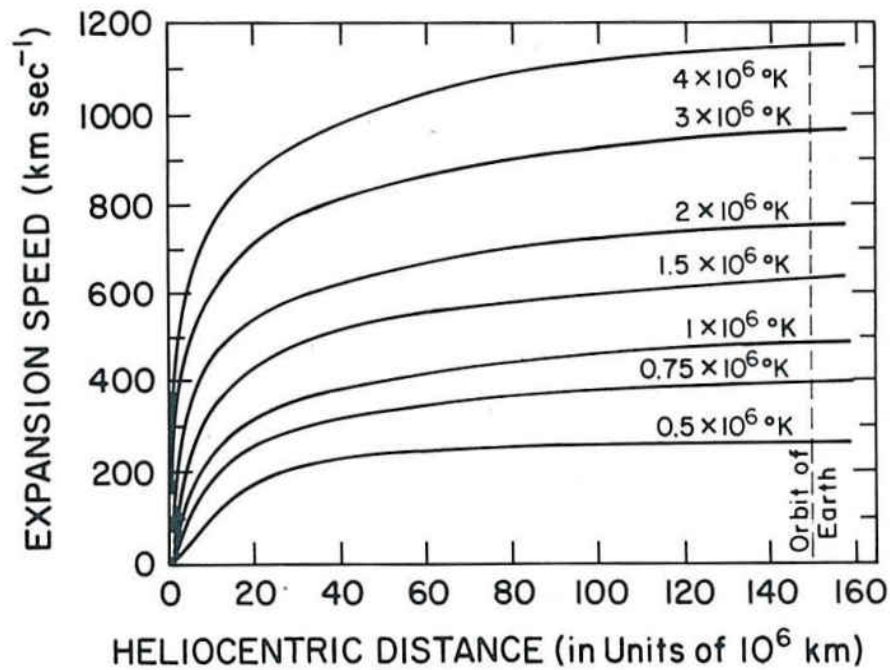


**Figure 1.6** Solutions of Parker's isothermal solar wind model for a range of temperatures (Parker, 1958).

Two further polar orbits have been completed by *Ulysses*, a second at solar maximum and a third at solar minimum. The final solar minimum orbit recorded velocity measurements which resulted in a similar trend to that of the first polar orbit, but with a reversed solar magnetic field and a general decrease in all measured parameters. During the third polar pass the solar wind was measured to be 3% slower, 17% less dense and 14% cooler than the first polar pass. McComas, *et al.* (2008) concluded that this was due to a weaker magnetic field during the third polar pass causing polar coronal holes to occur less frequently during the start of the minimum phase. The solar maximum orbit (*Ulysses*' second polar orbit) measured a much more random distribution of fast and slow solar winds (McComas, *et al.*, 2008) as expected from a less-structured solar-maximum interplanetary solar wind. The results of the *Ulysses* measurements of velocity during its orbits are shown in figure 1.7.

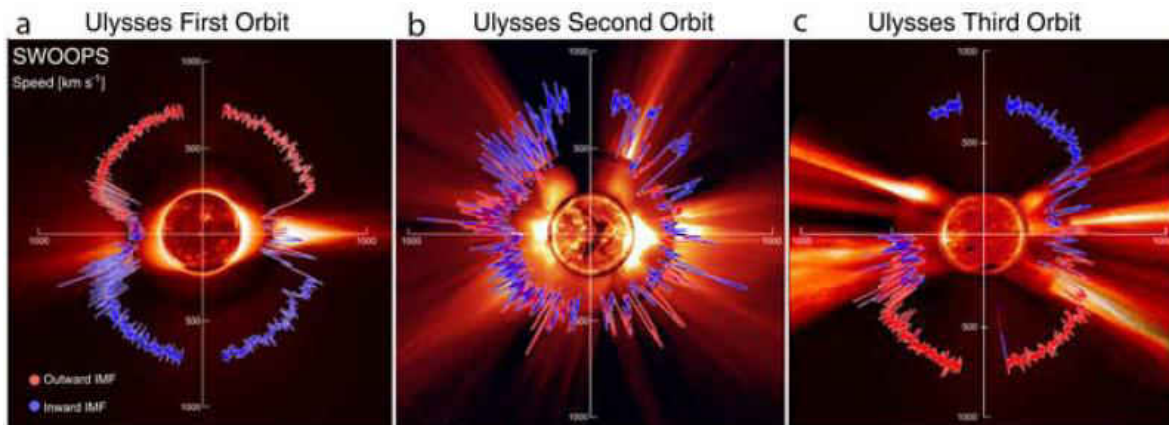


**Figure 1.7** *Ulysses'* polar plots for each of the polar orbits overlaid onto SOHO EIT Fe XII and LASCO C2 observations (From McComas, *et al.* 2008). During the quiescent phase of the Sun (a and c) the solar wind velocities are neatly defined into fast wind at the polar regions and slow wind in the equatorial regions, however at solar maximum the solar wind velocities are much more varied with no obvious dependency on latitude.

	Slow wind	Fast wind
<b>Flow speed</b>	250 – 400 km s <sup>-1</sup>	400 – 800 km s <sup>-1</sup>
<b>Proton density</b>	10.7 cm <sup>-3</sup>	3.0 cm <sup>-3</sup>
<b>Proton flux density</b>	3.7 x 10 <sup>8</sup> cm <sup>-2</sup> s <sup>-1</sup>	2.0 x 10 <sup>8</sup> cm <sup>-2</sup> s <sup>-1</sup>
<b>Proton temperature</b>	3.4 x 10 <sup>4</sup> K	2.3 x 10 <sup>5</sup> K
<b>Electron temperature</b>	1.3 x 10 <sup>5</sup> K	1 x 10 <sup>5</sup> K
<b>Momentum flux density</b>	2.12 x 10 <sup>8</sup> dyn cm <sup>-2</sup>	2.26 x 10 <sup>8</sup> dyn cm <sup>-2</sup>
<b>Total energy flux density</b>	1.55 erg cm <sup>-2</sup> s <sup>-1</sup>	1.43 erg cm <sup>-2</sup> s <sup>-1</sup>
<b>Helium content</b>	2.5% (variable)	3.6% (stationary)
<b>Source</b>	Streamer belt	Coronal holes

**Table 1.2** Properties of the slow and fast solar winds (Adapted from Schwenn 2006).

The *Ulysses* passes measured two unique forms of the solar wind, known as the fast and slow solar winds for which their primary locations are determined by the activity of the Sun. During a solar minimum the fast solar wind is primarily located towards the polar regions and the slower solar wind is located near to the solar equator. Typically the fast solar wind will have velocities of 400-800 km s<sup>-1</sup>, and the slow solar wind will have velocities up to 400 km s<sup>-1</sup> (Schwenn 2006). A concise table of each of the solar wind form properties is given in table 1.2.

Using data from the first polar pass of the *Ulysses* spacecraft, a bimodal fast solar wind was proposed by Woo and Habbal (1997) and Habbal and Woo (2001). A slower and denser mode of the fast solar wind emanates from the quiescent Sun and a faster and less dense wind mode emanates from the large polar coronal holes that dominate the higher latitude polar regions during solar minimum. A study of long baseline IPS data, during the solar minimum period of solar cycle 22, by Bisi *et al.* (2007) showed supporting evidence of a bimodal fast solar wind, by observing differing characteristics of fast streams at different latitudes. Bisi *et al.* (2007) suggests however, that the transition between the two modes is a gradual transition between the faster coronal hole and quiescent corona fast solar wind origins.

Although the source of the fast solar wind is known, the understanding of the origin of the slow solar wind is less well understood with a lack of observational evidence to support models. The current and most plausible model for the origin of the slow solar wind is the ejection of material which occurs from the helmet streamer belt (Gosling, 1997). The helmet streamer belt is a large loop of coronal magnetic fields which forms high above solar active regions and originating from the boundary regions of coronal holes. Radio observations of the solar corona during solar minimum by Kojima *et al.* (1999) and *in situ* measurements and modelling of the slow solar wind by Wang, Ko and Grappin (2009) were able to propose that the typical slow solar wind material is connected to small coronal holes located near active regions of the Sun. This material may then be transported along the magnetic field of the coronal streamer belt to become the solar wind

Until recently the coronal streamer belt was believed to be a steady flow of solar material however, observations have begun to see a more 'blobular' structure (Sheeley *et al.*, 1997). Sheeley *et al.* (1997) observed small concave-outward blob-like structures of enhanced density in the coronal streamers using the LASCO coronagraphs of SOHO (see chapter 2). These blobs displayed velocities similar to that of the slow solar wind and have been more recently tracked to beyond 1 AU using the STEREO HIs (see chapter 2) by Sheeley *et al.* (2008) and Rouillard *et al.* (2008; 2009). Sheeley *et al.* (2009) found evidence supporting the fact that they may contain a flux-rope topology. Further studies of these blobs have been performed by Kilpau *et al.* (2009) which observe a high frequency

of these blobs in the slow solar wind and suggest that they may form a component of the slow solar wind. These blobular features may have possibly been observed within chapter 5 of this thesis.

#### 1.2.4 The ‘Parker Spiral’

The Solar wind carries out the Sun’s magnetic field that is ‘frozen-in’ to the solar wind plasma itself. This magnetic field is known as the interplanetary magnetic field (IMF). The solar wind propagates approximately radially outward, and as such, when combined with the Sun’s rotation the wind streams form a spiral pattern within which the solar wind plasma and magnetic field are entrained. This is the Parker spiral, illustrated in figure 1.8. For the Parker spiral to form, a few assumptions of the magnetic field are required. A steady-state is assumed (Parker, 1958), solar wind acceleration and solar gravitation are neglected, and thus the radial flow of the solar wind is constant and its rotation is dictated by the rotational velocity of the Sun. To assume that the magnetic field is frozen-in to the solar wind plasma, the solar wind plasma is assumed to be a perfect conductor; with this assumption any particle interactions within the plasma are thus neglected.

Solar wind streams will have widely-varying velocities; however they are often divided into two different streams; the fast solar wind; and the slow solar wind. Hence the solar wind is bi-modal as discussed earlier. Due to these wide-ranging velocities it is inevitable that a leading slow wind stream will be followed by a faster wind stream which will encroach on the leading slow stream. The magnetic fields of the solar wind are described as ‘frozen-in’ to the solar wind plasma. ‘Frozen-in’ theory describes that in a perfectly conducting fluid the magnetic field moves along with the fluid i.e. frozen into the fluid, (Alfven, 1943). As the solar wind plasma is very electrically conductive, (Narita, 2012) Ohm’s law will reduce to equation 1.8, known as the perfect conductivity equation and the condition allowing for the ‘frozen-in’ theorem (Schnack, 2009).

$$\mathbf{E} + \mathbf{v} \times \mathbf{B} = 0 \quad (1.8)$$

In a ‘frozen-in’ solar wind the solar wind plasma may move freely along the magnetic field however, the plasma movement is limited so that it may only move in a direction perpendicular to the magnetic field such that a solar wind stream may not overtake another.

The wind streams will begin to form a compression region where the slower wind stream will be accelerated outward and deflected westward and the faster wind stream will be decelerated and deflected eastward (Gosling and Pizzo, 1999). This acceleration and deceleration of the slow and fast wind streams may often form an intermediate velocity (between 400 and 600 km s<sup>-1</sup>) enhanced

density structure which co-rotates along with the solar wind which is known as a stream interaction region (SIR) (Breen *et al.*, 1998; Bisi *et al.*, 2010a). Figure 1.8 displays an example of the formation of a SIR. When a SIR recurs over multiple solar rotations, then it may also be deemed a co-rotating interaction region (CIR).

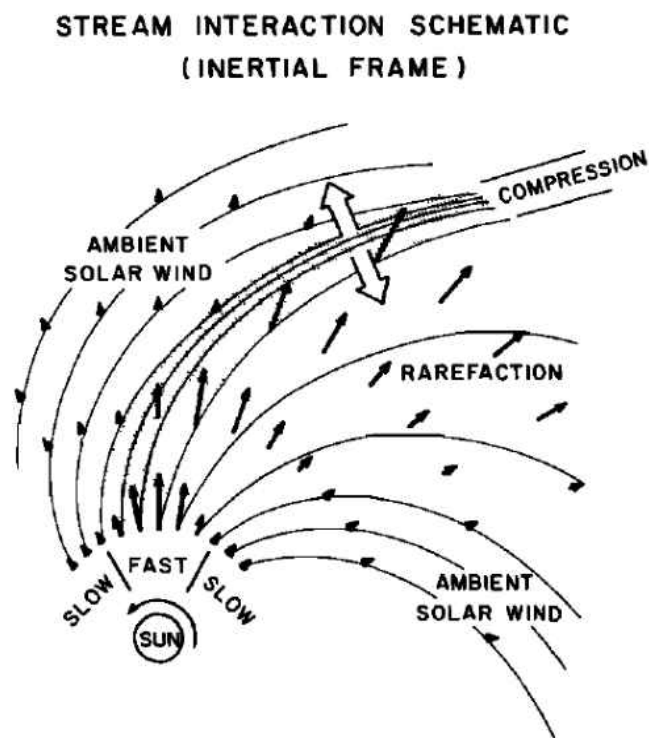


**Figure 1.8.** Illustration of the formation of a CIR/SIR in the equatorial plane of the Parker Spiral. (From Pizzo, 1978)

Similarly to the stream interactions which may form when a slow solar wind stream precedes a faster solar wind stream, when a slower solar wind stream follows a faster leading stream, a region of reduced density will form known as a rarefaction region (Pizzo, 1978).

### 1.2.5 Heliosphere

The heliosphere encompasses the Sun, corona, and the solar system - all the way out to where the solar wind meets the interstellar medium (ISM) and hence the end of the Sun's plasma influence. Measurements taken by the two Voyager spacecraft have recorded the extent of the heliosphere. In December 2004, the Voyager 1 spacecraft measured a sudden reduction in the solar wind velocities as the space craft passed the termination shock of the heliosphere at 94 AU and finally entering the

outer limits of the heliosphere, the heliosheath (Cowen, 2012). The Voyager 1 spacecraft in 2010 reached, at a distance of 118 AU, what has been dubbed the stagnation region, where the solar wind particle's outward speed reduces to zero. In July/August 2012 the Voyager 1 space craft measured the solar wind particles to have finally come completely to rest (Cowen, 2012). In May 2012 Voyager 1 arrived at the heliopause measured at 120 AU (Witze, 2013). In August 2013, Voyager 1 detected locally generated electron plasma oscillations leading to the agreement that the Voyager 1 spacecraft had finally entered interstellar space at 121 AU (Gurnett *et al.*, 2013).

### **1.3 Solar Activity**

The Sun is not the quiet, consistent structure as might be believed from visible light observations of the disk. It is constantly changing with many different forms of events from the serene, in the form of Sunspots, coronal holes, prominences and filaments, to the very extreme events, in the form of flares and Coronal Mass Ejections (CME). Often these events can have a dramatic effect on the Earth and its magnetosphere, such as the *Aurora Borealis* (and *Aurora Australis*): displays often observed towards the Earth's polar regions known often as the northern (and southern) lights. These may have potentially harmful effects on human society as technology infrastructures can be damaged by space weather.

#### **1.3.1 Sunspots and the 11- (22-) Year Solar Cycle**

One of the most long-studied features of the Sun are dark circular regions on the solar disk, known as Sunspots. A continuum image of a sunspot is shown in figure 1.11. Sunspots are cooler regions on the solar surface, thus appearing as dark spots, with sizes up to and above 20Mm. Sunspots are usually found in pairs with a Sunspot in each of the Sun's hemispheres and will usually form on a region of the Sun which has a very strong localised magnetic field, known as an active region. Sunspots are regularly counted and measured to provide important information regarding solar activity. These long-running sunspot studies give data over several centuries, and show that the Sun has periods where many sunspots may occur (solar maximum) and periods where very few may occur (solar minimum). This fluctuation in the number of sunspots was found to have a regular pattern, with the number of sunspots increasing from solar minimum to maximum and then back to solar minimum approximately every 11 years (*e.g.* Kutner 1987, Kivelson and Russell 1995).

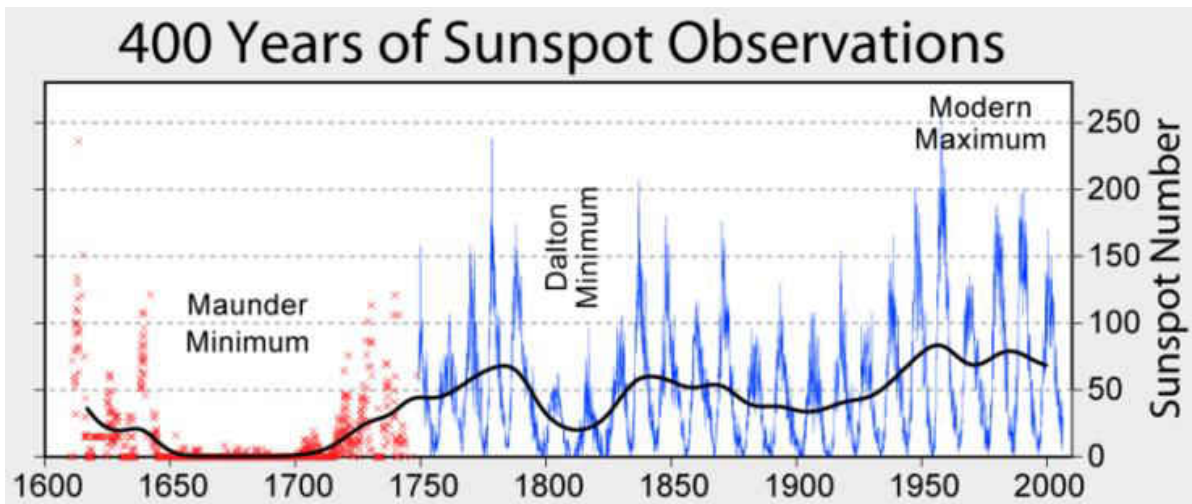


**Figure 1.9** Sunspot numbers for a 400 year period between the years 1600 and 2000. Sunspot events in red are taken through observation using the naked eye and events in blue are taken from observations using telescopes. The black line denotes the line of best fit for the annual sunspot number averages (image created by Robert A. Rohde for Global Warming Art: <http://www.globalwarmingart.com>).

During the solar minimum period very few sunspots may be observed with sunspot numbers very close to zero at the minimum trough. During a solar maximum the sunspot number can vary greatly. The sunspot numbers for a 400 year period between the years 1600 and 2000 are shown in figure 1.9. Figure 1.9 also displays two periods of reduced sunspot numbers, known as the Maunder Minimum and the Dalton Minimum. There is also a period displayed with enhanced sunspot numbers, known as the Modern Maximum (or a Grand Maximum). Along with the variation in the number of sunspots over periods of time, it has also been observed that the average latitude at which sunspots form also changed with the solar cycle. During the start of a new solar cycle sunspots will be observed at higher latitudes, but as the cycle progresses, the sunspots approach the solar equator, an effect known as Spörer's law (Roshchina and Sarychev, 2011). Spörer's law is shown in the butterfly diagram of figure 1.10.

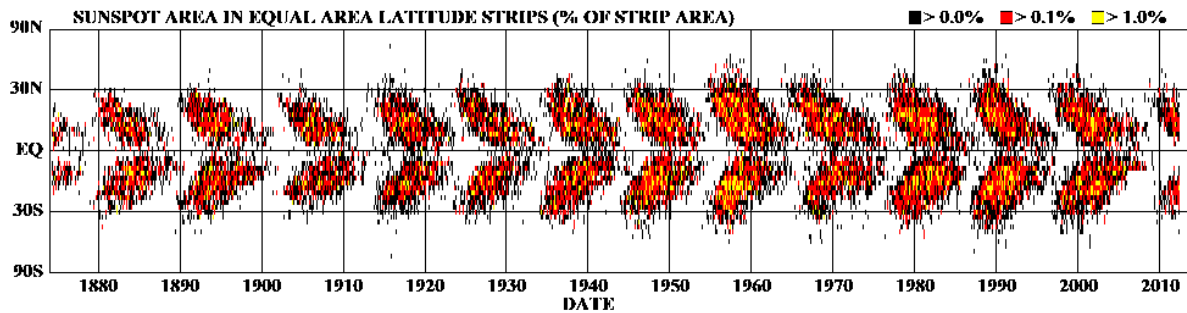


**Figure 1.10** NASA daily sunspot numbers between during the period between 1885 and 2012 (completed solar cycles 12 to 23), also showing the latitude of the sunspots observed (from Hathaway, 2010).

It is often proposed that the sunspot numbers, or more accurately the solar activity, may have a profound effect of the Earth's environment with a particular example being the Maunder Minimum. Between 1645 and 1715 very few sunspots were observed on the solar surface and at the same time lower-than average temperatures in North-Western Europe were recorded (Eddy, 1976) with strong correlations between these two events. More recent studies by Lockwood (2011a; 2011b; 2012) have proposed that some regions may be more susceptible to seasonal temperature influences from solar activity such as Eurasia offering lower winter temperatures during times of low solar activity. A recent extended solar minimum has also been observed as with the solar minimum at the end of sunspot cycle 23 and entering solar cycle 24 (Lockwood *et al.*, 2012).

### 1.3.2 Filaments (and Prominences)

Above an active region it may be possible to observe dark lines of cooler plasma on the solar disc, or a bright loop of extending material from the photospheric limb. These features are named filaments or prominences respectively. It should be noted that prominences and filaments are the same feature, although given different names depending on their position. Prominences and filaments are loops of plasma which extend from the photosphere into the chromosphere with temperatures around 70000 K which are held up by the local magnetic field (Kivelson and Russell 1995). On occasions it may be possible for the filament to destabilise which causes the material to twist and erupt into space as a CME (discussed in the section following). Such an event is observed in chapter 6. When a prominence is observed in the hydrogen and helium wavelengths, on the limb of the Sun it appears as a bright feature against the background space as the electrons in the prominence

scatter solar radiation towards the observer. When viewed as a filament it will appear as a dark feature which is absorbing the solar radiation. The immediate surroundings above a filament show a hot shroud reduced of emission in white-light known as a cavity (Habbal *et al.*, 2010). Filaments are always located above polarity inversion lines (PILs), where the radial magnetic field component changes in polarity, and is formed by the sheared arcades which bridge these PILs (van Ballegoijen, Priest and Mackay, 2000; Mackay, *et al.*, 2010). Filaments may appear over PILs of an active region, to produce an active region filament, or over the more quiescent Sun, to produce a quiescent filament.

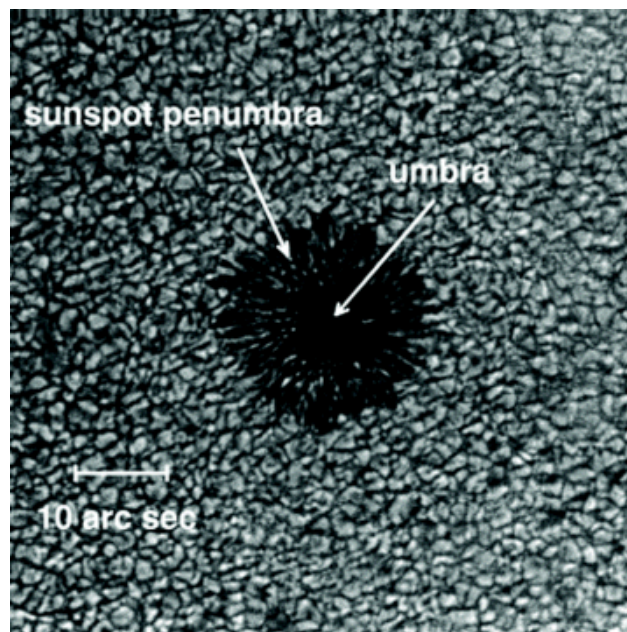


**Figure 1.11** The left image shows a continuum image of a sunspot and its structure surrounded by the granulation effect in the photosphere. The umbra and penumbra regions of the sunspot are labeled (from Shine and Title, 2001).

Assuming a filament as a flux rope, means that a filament that experience perturbations will displace causing a kink in the tube, while foot points remain anchored in their fixed position. This kink will induce further perturbations with an increased magnetic pressure forming on the inner-side of the kink. The stabilising force of the filament will deliver an responsive force to the kink causing the flux rope to become unstable and force a magnetic reconnection, ejecting coronal material in space (see section 1.3.3) (Lui, 2008). The two primary kink instabilities are of a Torus Instability with a lateral

instability (Kliem and Török, 2006), and helical kink instability with a twisting of the flux rope (Fan and Gibson, 2003).

### 1.3.3 Coronal Mass Ejections (CMEs)

One of the largest and most-powerful forms of solar activity is that of Coronal Mass Ejections (CMEs). CMEs are large energetic events which release large amounts ( $10^{12}$  -  $10^{13}$  kg) of solar material into the heliosphere at typical velocities of  $400 \text{ km s}^{-1}$  with a large variation in mass and velocity. Velocities between  $50$  and well over  $2,000 \text{ km s}^{-1}$  have been observed (*e.g.* Harrison 2003; Bewsher, Harrison and Brown 2008). CMEs are a key factor of space weather as they are often denser than the surrounding solar wind and often cause the formation of magnetic-field shocks which may have a noticeable interaction with the Earth's magnetic field and possibly induce magnetic reconnection and increasing precipitation of highly energetic particles (*e.g.* Brekke, 1996).

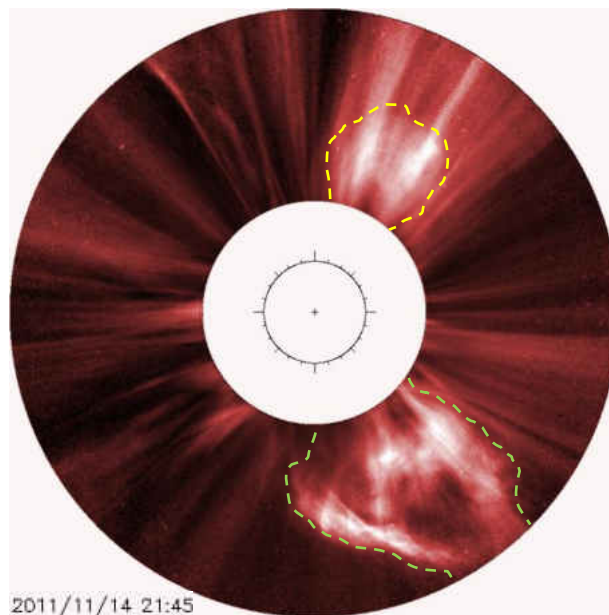


**Figure 1.12** SOHO|LASCO coronagraph image of two CME events on 14 November 2011 at 21:45 UT. The first event is the large cloud of material on the south western solar limb (enclosed with the green dashed lines) and the second smaller event is on the north western limb (yellow dashed lines). It should be noted that east and west are mirrored as directions are given relative to the Sun. The south western event is detailed in chapter 6.

CMEs are much denser than the surrounding solar wind thus they are able to Thomson scatter the white light radiation the Sun (see chapter 2). This is useful for observations as the events appear as bright clouds of material travelling outward from the Sun when the heliosphere and corona are observing in white light. Figure 1.12 shows the appearance of 2 CME events as observed by a coronagraph telescope.

There are multiple probable sources for CME events. CMEs can often be traced back to an unstable structure on the solar surface such as an erupting quiescent filament (gradual CMEs) and active region filaments (impulsive CMEs) due to the kink instabilities previously discussed. CME have been best described as flux rope structures based on LASCO observation which showed a three-part structure of; a bright front edge; a depleted cavity; and a bright core of firmament material gave the appearance of a helical flux rope structure (Cremandes and Bothmer, 2004; Thernisien, Howard and Vourlidas, 2006)

CMEs have been associated with coronal hole dimming events may allow the CMEs to be predicted as dimming events may be observed sooner than a CME becomes visible in coronagraphs (Bewsher, Harrison and Brown, 2008).

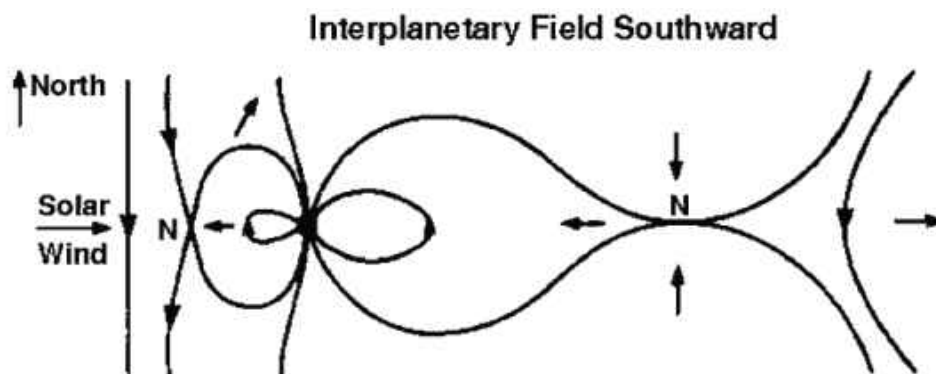


**Figure 1.13** The response of the geomagnetic field due to the impact of a southward IMF (Howard, 2011).

When a CME encounters Earth's magnetic field, the CME's magnetic field (IMF) may have a northward or southward directed field. In the event of a southward IMF a geomagnetic sub-storm may result. The driving force behind this geomagnetic activity is magnetic reconnection. Magnetic

reconnection is an MHD phenomena that may occur between two converging, anti-parallel magnetic fields each frozen into their respective plasmas (Priest, 2011). As the magnetic fields converge, a thin localised region of enhanced magnetic diffusivity develops due to the magnetic gradient of the converging fields. Within the diffusive region an X-type null point will form where the magnetic field no longer exists and weakening the magnetic configuration. This null point may then become unstable and result in the formation of a current sheet at this location (Syrovatskii, 1971). To regain magnetic stability the current sheet can diffuse and allow reconnection of the magnetic fields to occur (Priest, 2011).

During a sub-storm magnetic reconnection will occur between a southward IMF and the geomagnetic field. This will allow the closed field of the magnetosphere to open and expose the magnetosphere to an injection of the CME's energetic particles into the Earth's magnetosphere. The CME also produces an increase in the pressure which impacts the Earth's magnetosphere which causes the magnetosphere to become compressed and result in an expansion of the auroral ovals. An example of such a sub-storm is shown in figure 1.13. From the magnetospheric interaction with large and extended solar events a series of strong sub-storms will result in prolonged period of geomagnetic activity, known as a geomagnetic storm.

A northward IMF approaching the geomagnetic field (figure 1.14) does not result in reconnection on the dayside magnetosphere, however, reconnection may occur in the magnetotail without the formation of a magnetic storm. The two forms of solar wind and magnetospheric interaction make up the mechanisms for the storage and release of energy in the Earth and other planetary magnetospheres and form the Dungey cycle (Dungey, 1961).

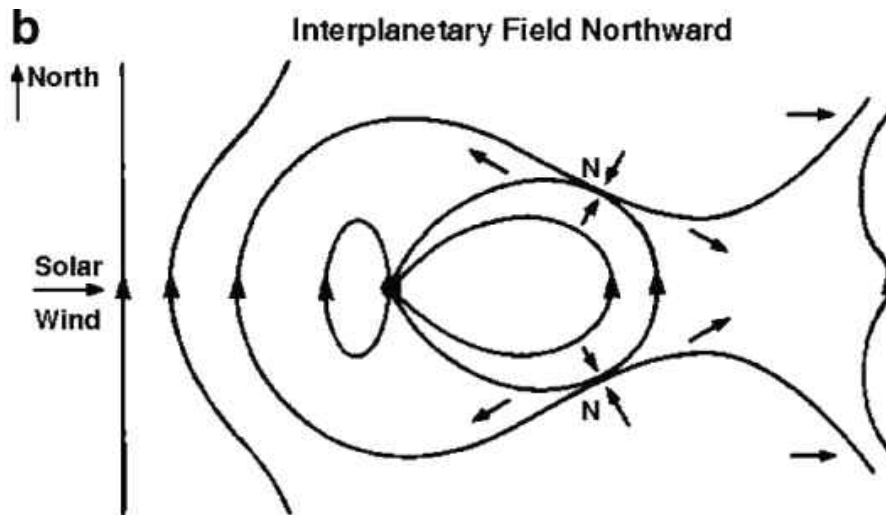


**Figure 1.14** The response of the geomagnetic field due to the impact of a northward IMF (Howard, 2011).

Since CMEs usually have an enhanced density, they are detectable, and distinguishable, from the background solar wind and the dust-scattered F-corona in white-light coronagraph and heliospheric imaging observations. Methods which apply this are detailed in chapter 2.

Regularly transient structures of all sizes may be ejected from the however, for the purpose of this thesis; CMEs will be defined as macro-scale structures extending beyond an elongation of 10 degrees with a latitudinal position angle greater than 20 degrees.

# Chapter 2

## Observations and Methods

Throughout this thesis, a number of different instruments and associated methods have been used to analyse the solar disk, inner corona and heliosphere. The remote-sensing observations are performed either by ground-based radio telescopes, Interplanetary Scintillation (IPS), or by imaging systems aboard spacecraft in white light and extreme ultraviolet (EUV). Within this chapter the IPS and various imaging methods will be introduced and their relevant theory described in detail.

### 2.1 Radio Observations of the Sun

Satellites are sparsely distributed throughout the heliosphere and provide only single-point *in-situ* measurements of particular heliospheric phenomena. Thus, it is also important to complement these observations with remote-sensing methods. These include the imaging of direct or scattered electromagnetic radiation from the Sun. Remote sensing techniques that are based on observations at radio frequencies include of interplanetary scintillation (IPS), which is the detection of the scintillation (or “twinkling”) caused by the solar wind on radio waves travelling from a distant point-like astronomical radio source such as a quasar. Although IPS can also be carried out with spacecraft beacons (*e.g.* Tokumaru *et al.*, 2012), in this thesis, only natural astronomical radio sources are observed.

#### 2.1.1 Interplanetary Scintillation (IPS)

When recording the signal from a distant, compact, astronomical radio source, it may be observed that the received radio signal has been modulated on its passage between the source and antenna. This is due to the presence of density irregularities in that region of the solar wind between the radio

source and antenna (*e.g.* Hewish, Scott and Wills, 1964; Bourgois *et al.*, 1985). This effect is known as interplanetary scintillation (IPS). The exploitation of IPS has developed greatly since the initial use of the effect for studying the interplanetary medium in the 1960s. There are a variety of IPS analysis techniques currently being used such as; the estimation of a scintillation index derived using observations from a single radio antenna site; single-site velocity model fitting (*e.g.* Manoharan and Ananthakrishnan, 1990; Mejía-Ambríz *et al.*, 2012); and two-site cross-correlation solar wind velocity estimations (*e.g.* Breen *et al.*, 1996a; 1996b; Fallows *et al.*, 2006; Tokumaru *et al.*, 2012). The latter is the technique of IPS used throughout this thesis; the cross-correlation analysis methods used are those by Fallows *et al.* (2006; 2013).

### **2.1.1.1 The Beginnings of IPS**

The technique of observing IPS to study the inner heliosphere was developed by Hewish in the early 1960s (Hewish, Scott and Wills, 1964) as an extension of earlier work in which it was used to study the corona (*e.g.* Machin and Smith, 1951; 1952). Machin and Smith (1951; 1952) had suggested using scintillation from distant astronomical radio sources for the study of the outer corona. They proposed that, when passing through the corona, the radiation of an astronomical radio source would deviate. They suggested that the amount of deviation detected at a receiver at Earth would be highly dependent on the angular distance of the source from the Sun, and that beyond a critical angular distance, the radio source's radiation may no longer reach the receiver. This critical angular distance was described as 'the effective radius of the corona for occultation', which was proposed to be dependent on the effective wavelength being observed (Machin and Smith 1951). Thus, it was suggested that it could be possible to estimate the electron density of the corona by measuring the occultation radius over a range of different wavelengths.

Hewish 1955 presented the first IPS-style observations of the type advocated by Machin and Smith (1951) observing the scintillation in the solar corona. Using the Crab nebula as the distant radio source, early attempts to measure the electron density in the corona using the technique suggested by Machin and Smith (1951), were performed in 1950 and 1951 using interferometry at Cambridge. However, the experiments were unsuccessful, which was believed to be due to the presence of intense radiation produced by sunspots. Successful attempts were performed in 1952 and 1953, the results of which suggested the presence of scattering of the radio waves due to the occurrence of irregularities/variations in electron density in the interplanetary medium (Hewish 1955). From 1962, Hewish began to "develop" the IPS technique, using a single dedicated antenna to observe small-

diameter radio sources passing near to the Sun on the sky which could detect scintillation in the interplanetary medium (Hewish, 1962; Hewish, Scott and Wills, 1964). This technique is discussed in the sub-section following (2.1.1.2).

### **2.1.1.2 Scintillation Theory**

The solar wind, which is material ejected from the Sun, has a very variable plasma density structure. This means that a radio wave, from a distant radio source, crossing the solar wind will pass through many different plasma density regimes each having their own refractive index that will alter the speed of light in the medium. This will in turn, cause phase modulation on the passing radio wave. As waves are refracted at the interface between different plasma regimes, a radio receiver will detect waves arriving at the antenna from many different directions from a single source. The received combination of waves may be in phase or out of phase that, due to the constructive or deconstructive interference, will result in maxima or minima in amplitude, respectively. These phase changes are what produce the IPS amplitude scintillation (Stokes I – the intensity) that this thesis is concerned with.

The scintillation level is highly dependent on a number of key factors, possibly the most important of which is the astronomical radio source that is selected to be observed. The location of this source will determine the region of the solar wind that will be observed (the region along the line of sight from the receiving antenna to the source). An ideal radio source would be a point-like source, so that it can be assumed that all of its power emanates from in a single point. As a source increases in cross-section, scintillation will begin to diminish due to destructive interference between different parts of the radio source; this can be particularly problematic for structured radio sources.

While observing a distant radio source, it is inevitable that the radio waves will be scattered by the solar wind medium passing across the antenna's line of sight. For IPS, the scattering medium may be represented by a thin screen (or ideal phase screen) for which the diffraction will impose phase fluctuations on the radio wave. This is known as a thin screen approximation. Over a distance determined by the size of the density variations in the screen, a series of thin screens will build up producing the amplitude variations (Stokes I). Scintillation will occur along the entire length of the line of sight between the radio receiver and the source. Note that the point along the line of sight that is nearest to the Sun is known as the P-Point and is often assumed to be the primary source region of the scintillation for a single stream of solar wind passing over the entire line of sight. Under weak scattering conditions (which will be discussed shortly) the final diffraction pattern, as received

by the antenna, may be considered as a combination of the range density variation scales (Fallows, 2001; Bisi, 2006).

By calculating the relative electron permittivity, it is possible to determine the variation in the refractive index between multiple plasma regimes. Assuming no particle collisions and independence from the magnetic field, the electron permittivity of the solar wind,  $\epsilon$ , is given as:

$$\epsilon = n^2 = 1 - \frac{f_p^2}{f^2} \quad (2.1)$$

For which:

$$f_p^2 = \frac{N_e e^2}{4 \pi^2 \epsilon_0 m_e} \quad (2.2)$$

Where:

$f_p$  = Plasma frequency;

$n$  = Refractive index;

$N_e$  = Electron density;

$\epsilon_0$  = Permittivity of free space;

$e$  = Electron charge;

$m_e$  = Electron mass;

and  $f$  = Observing frequency.

Equation 2.1 may then be expanded using a Binomial Expansion in which terms higher than the first order approximate to zero, since, for IPS, the plasma frequency of the solar wind is much smaller than the observation frequency. Thus the refractive index is given by:

$$n = 1 - \frac{f_p^2}{2 f^2} \quad (2.3)$$

From Uscinski 1977:

$$n = n_0 - \delta n \quad (2.4)$$

Where:

$n_0$  = Mean refractive index;

and  $\delta n$  = Variation in refractive index from the mean which can hence be represented thus.

$$\delta n = \left( 1 - \frac{N_e e^2}{8 \pi^2 \epsilon_0 m_e f^2} \right) - \left( 1 - \frac{\langle N_e \rangle e^2}{8 \pi^2 \epsilon_0 m_e f^2} \right) \quad (2.5)$$

Where:

$\langle N_e \rangle$  = Mean electron density at the P-Point.

Simplified by assuming that  $\delta N_e = \langle N_e \rangle - N_e$  equation 2.5 then becomes:

$$\delta n = \frac{\delta N_e e^2}{8 \pi^2 \epsilon_0 m_e f^2} \quad (2.6)$$

There are a number of implications for IPS associated with equation 2.6 that are important, such as the dependencies of the refractive index variation on electron density and observing frequency. As the radio source on the sky (*i.e.* the P-point location) approaches the Sun as viewed from the receiver, the electron density ( $N_e$ ) will tend to increase and thus the variation in refractive index ( $\delta n$ ), and in turn the amount of scintillation (*i.e.* the scintillation level) will also increase. Conversely, as the radio source on the sky moves further away from the Sun, the opposite is true. With increasing distance from the Sun, the density of the same regime of solar wind will tend to decrease, thus reducing the scintillation level. Observations of the level of scintillation were made by Hewish, Scott, and Wills (1964), where they showed the level of scintillation to increase nearer for a given observing frequency. Later observations by others such as Little and Hewish (1966) and Bourgois (1969) however, demonstrated that although the level of scintillation peaks at a given radial distance from the Sun for a given frequency, it subsequently decreases inward from that point, despite the fact that density tends to increase towards the Sun. This is an indication of the existence of two

different scattering regimes weak scattering (far from the Sun) and strong scattering (close to the Sun).

As the electron density, and hence the scattering level, tend to decrease with distance from the Sun, the maximum scattering will tend to occur at the P-Point. Equation 2.6 shows that the refractive index variation is inversely proportional to the square of the observing frequency. Thus to counteract changes in the solar wind density, it is possible to adjust the observing frequency, *i.e.* using a lower frequency will improve the signal further from the Sun by increasing the scintillation level.

### 2.1.1.3 Single-site Observations

Although its extended theory and development are not an aspect of this thesis, for completeness, the IPS power spectrum is given by equation 2.7 (using the notation of Salpeter, 1967):

$$P(f) = 2 \pi r_e^2 \lambda^2 \int_0^\infty \frac{2 \pi}{v_p(z)} \int_{-\infty}^\infty 4 \sin^2 \left( \frac{q^2 \lambda z}{4 \pi} \right) |V(q, z, \theta_0)|^2 q^{-\alpha} \exp - \left( \frac{q}{q_i} \right)^2 R^{-4} dq_y dz \quad (2.7)$$

Where:

$r_e$  = Classical electron radius;

$v_p$  = Perpendicular component of the solar wind velocity;

$z$  = Distance between radio receiver and 'scattering screen';

$\lambda$  = Observing wavelength;

$q$  = 2-dimensional spatial wave number;

$\theta_0$  = Angular diameter of radio source;

$\alpha$  = Power law exponent;

$V(q, z, \theta_0)$  = Visibility function of the radio source;

$R$  = Radial distance from the Sun;

and  $q_i$  = Scale of turbulence dissipation.

(Scott *et al.*, 1983; Klinglesmith, 1997; Moran, 1998; Fallows *et al.*, 2006; Bisi, 2006).

IPS signal can be characterised in its most simple form as the scintillation index. The scintillation index can be described as the “proportion of the total flux density contained in the small-diameter component of the source” (Breen, *et al.*, 1996a) and it is obtained by calculating the root mean square (rms) of the total power received at the antenna (*e.g.* Canals *et al.*, 2002). As previously mentioned, the amount of scintillation is highly dependent on the regime that is being observed. Each scattering event within the weak scattering region may be considered as unique and independent, and the Born approximation (Born and Wolf, 1964) may be applied (see Fallows, 2001). The Born approximation requires that the phase fluctuations across a diffracted radio wave front within the weak scattering region may be considered small, such that the phase change across the wave front ( $\delta\varphi$ ) is much smaller than 1 radian (Moran, 1998):

$$\delta\varphi = k \cdot \mu \cdot r_0 \ll 1 \text{ radian} \quad (2.8)$$

Where:

$\delta\varphi$  = Wave front phase change;

$k = \frac{2\pi}{\lambda}$  = Wave number;

$\mu$  = The standard deviation of the variation of the refractive index from the mean;

and  $r_0$  = Scale size of plasma irregularity.

As these phase changes are small, In the weak scattering regime, the scattered waves will add constructively producing large fluctuations in the total received power (Little and Hewish, 1966; Fallows, Williams and Breen, 2002).

In the strong scattering regime, the phase fluctuations across the diffracted wave front become large, such that:

$$\delta\varphi = k \cdot \mu \cdot r_0 \gg 1 \text{ radian} \quad (2.9)$$

and the Born approximation is no longer valid. Conversely to the weak scattering situation, the large phase variations that occur in the strong scattering regime do not add constructively and thus the total received power will only contain small amplitude fluctuations.

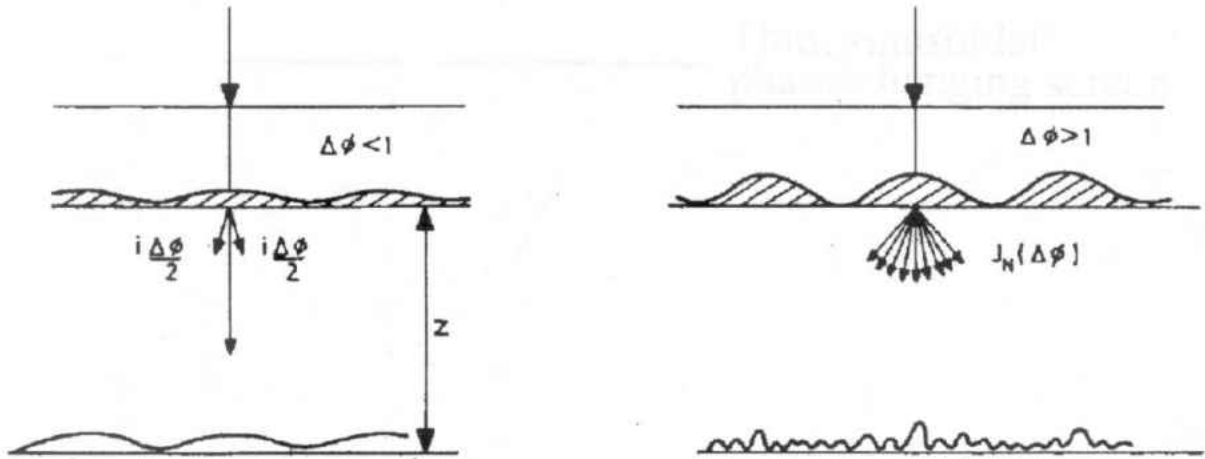


**Figure 2.1** Scintillation by a sinusoidal phase-changing screen for weak (left) and strong (right) scattering regimes. For weak scattering the phase variations are small ( $\delta\phi \ll 1$ ) and for strong scattering the phase variations are large ( $\delta\phi \gg 1$ ) (from Daly, 2000).

This thesis is only concerned with IPS along lines of sight that pass, solely, through the weak scattering regime. The point at which each scattering method becomes dominant is dependent on the source frequency being observed and the solar wind medium. Equation 2.6 demonstrates the importance of electron density and frequency on the scintillation level ( $\delta n$ ). When the electron density of the solar wind increases, the region at which strong scattering will be encountered is confined to a region closer to the Sun. To reduce the distance from the Sun at which the weak scattering becomes dominant it is possible to observe using a higher observational frequency, *i.e.* the greater the density of the regime observed the higher the observing frequency needed to remain within the weak scattering regime. An example of the frequency dependence of the scintillation index is displayed in Figure 2.2.

The scintillation index can be used as a measure of solar wind density and turbulence. In the weak scattering regime, the observed scintillation index is directly proportional to the variation of solar wind plasma density through which the signal passes, *i.e.* line of sight integration, although an approximation to the P-Point can be made. The scintillation index ( $m$ ) may also be given as:

$$m = \sqrt{\frac{\langle (J - \bar{J})^2 \rangle}{\bar{J}^2}} \quad (2.10)$$

Where:

$\mathcal{I}$  = Intensity of the incident radiation from the radio source at a given instant;

and  $\bar{\mathcal{I}}$  = The mean intensity at a given point.

(Fallows, 2001)

The solar wind electron density ( $N_e$ ) can easily be derived from measurements of scintillation index shown in equation 2.10. The electron density in the solar wind has been found to be proportional to the variation of the solar wind density ( $\delta N_e$ ). However, the exact proportion of this relationship has yet to be fully determined. Suggested values are;  $\delta N_e \propto N_e$  (Houminer and Hewish, 1972),  $\delta N_e \propto N_e^{0.5}$  (Tappin, 1986), and  $\delta N_e \propto N_e^{0.3}$  (Jackson *et al.*, 1998). Tokumaru, Kojima and Fujiki (2009) observed that  $\delta N_e$  is inversely correlated with the solar wind velocity ( $v$ ) such that  $\delta N_e \propto v^{-0.36}$  under the assumptions that  $\delta N_e \propto N_e$  and  $v > 350 \text{ km s}^{-1}$ . From this, Tokumaru *et al.* (2009) were able to suggest that  $\delta N_e/N_e$  increases with solar wind velocity so that the density variations are greater in the fast solar wind than the slow solar wind.

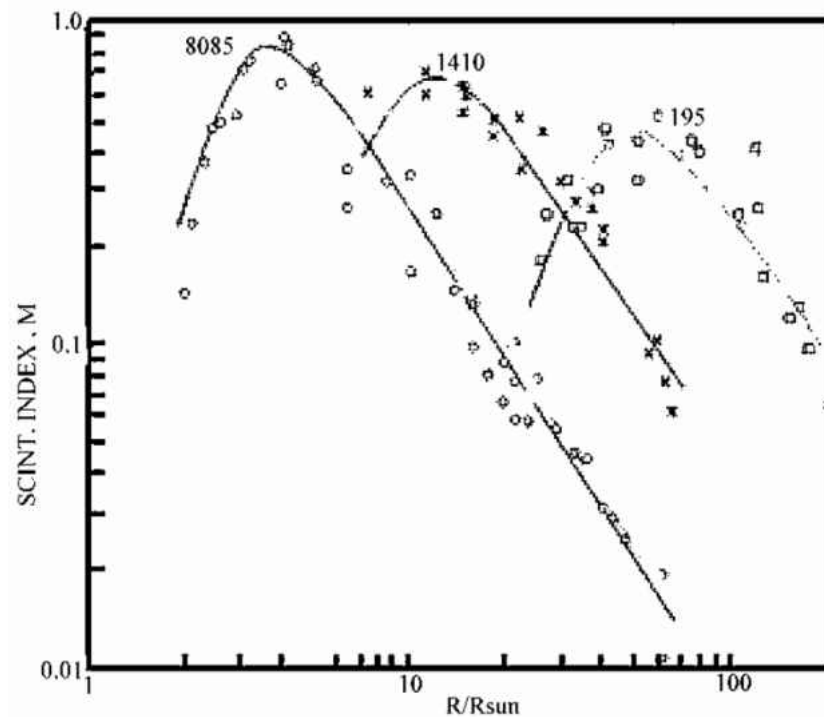


**Figure 2.2** Observation of scintillation index versus the distance from the Sun (in solar radii) for the observing frequencies of 8085 MHz, 1410 MHz, and 195 MHz. The higher frequency observations encounter the strong scattering region (the point at which the scintillation begins to decrease) at distances closer to the Sun (From Coles and Harmon, 1978).

Observations of scintillation index can be used as a method of mapping the sky. Over a period of time it is possible to observe a large number of astronomical radio source distributed across the sky. By measuring the scintillation of the different regimes in the sky it is possible for a density map to be produced covering a large area of the sky or over a short period of time with a network of antenna systems. This mapping is often performed by radar systems which can very quickly switch between radio sources so that many sources may be observed during the time period (Watanabe and Schwenn, 1989; and references therein).

#### **2.1.1.4 Multi-site Observations**

The technique of IPS has been developed so that if a pair of radio antennas are available for observing a single radio source, provided that the projected orientation onto the plane of the sky of their baseline is close to parallel to the solar wind outflow direction, it is possible to calculate the outflow velocity of the traversing solar wind stream (or streams) (*e.g.* Breen, *et al.*, 1996a; Bisi, 2006; Bisi *et al.*, 2010a; Dorrian, *et al.*, 2010; Fallows *et al.*, 2013). A ‘parcel’ of solar wind will, first, pass across the line of sight of the near-side antenna (the antenna that has its line of sight closest to the Sun); the radio telescope will observe the scintillation pattern that the density structure in the parcel will produce. After a short delay, the far-side antenna will observe the same parcel of solar wind, producing a scintillation pattern very similar to that seen by the near-side radio telescope. By performing a cross correlation between the signals received at the two observing sites, any “similar scintillation” between two sites will be detected. If a correlation between the signals is found, a peak in the cross-correlation function (CCF) will form at the time lag of the signal delay between the radio telescopes. As the distance between the radio telescope lines of sight on the sky is known (the ground separation baseline), it is simple to estimate the solar wind outflow speed from the time lag of the point of maximum correlation (Breen *et al.*, 1996a; Fallows *et al.*, 2006; Dorrian, *et al.*, 2010).

Since IPS is caused by variations in the electron density of passing solar wind, it is effective in detecting structures with high densities such as CMEs and stream interaction regions (SIRs). Enhanced density regions provide a very clear scintillation, compared to that due to the background solar wind, and thus they produce a much higher scintillation received at the two receiver sites than that would have been observed in quiescent solar wind (*e.g.* Bisi 2006; Jones *et al.*, 2007; Bisi *et al.*, 2010b; Dorrian *et al.*, 2010).

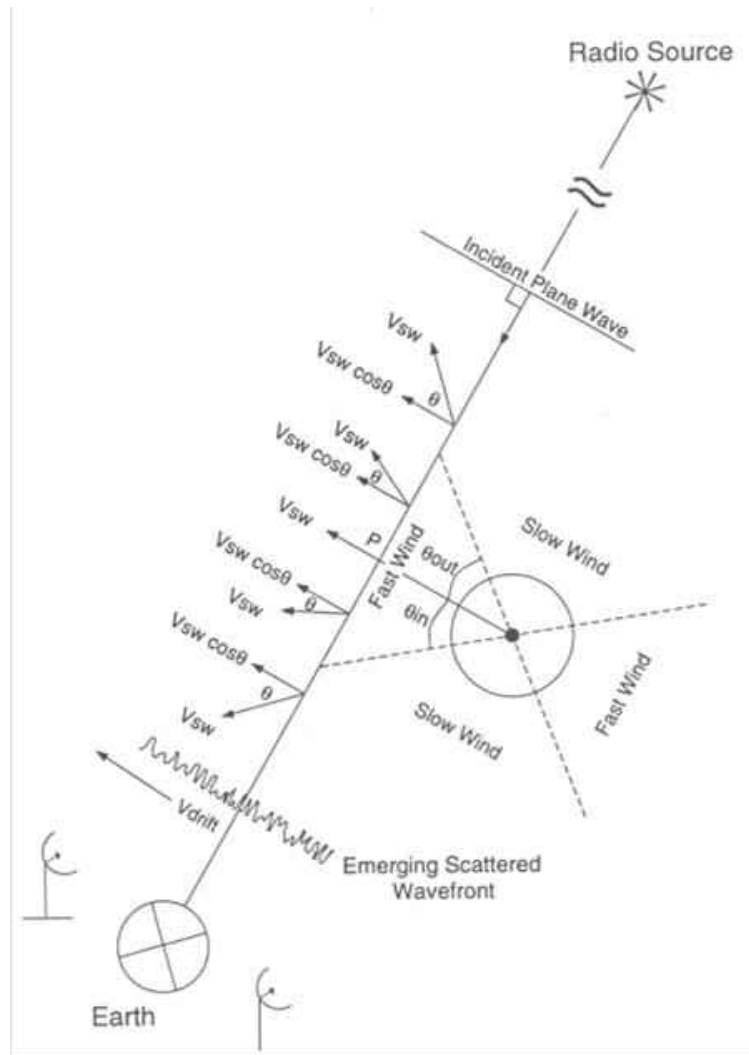


**Figure 2.3** Schematic of the IPS geometry for the solar wind flow across the line of sight of the radio antennas and the solar wind velocity components that occur due to the perpendicular flow sensitivity of the IPS technique. (Taken from Massey, 1998)

The first dual-site IPS observations performed by Hewish used two UK based radio telescopes, one in Cambridge and the other in Alvedon, with a geographic baseline of just 53 km between the two telescopes; the results (Little, Hewish and Dennison, 1966) gave solar wind velocities between  $200 \text{ km s}^{-1}$  and  $400 \text{ km s}^{-1}$  which is consistent with slow solar wind speeds. In 1966, Dennison and Hewish included an additional radio telescope to their experiment, which extended the geographic baseline to a maximum of 85 km and formed a triangular system for which correlations could be produced for each pair of telescopes (Hewish and Dennison, 1967). Thus, they could determine longitudinal and latitudinal components of solar wind velocities from the different orientations of baselines. The observations they performed were out of the ecliptic plane, and allowed them to

observe at any (astronomical radio sources providing) heliographic latitude. This advance resulted in the initial discovery of solar wind speeds of  $\sim 200 \text{ km s}^{-1}$  to  $700 \text{ km s}^{-1}$ , with higher speeds at higher heliographic latitudes, and resulted in them suggesting two discrete modes of solar wind outflow during solar minimum conditions (Dennison and Hewish, 1967). A repeat experiment was performed the following year by Hewish and Symonds; however, this time, the results were inconclusive (Hewish and Symonds, 1969). The multi-site technique was then picked up by Coles and Rickett (amongst others at University of California, San Diego) in 1970 (*e.g.* Coles, 1972; Coles and Maagoe, 1972; Armstrong and Coles, 1972). Their observations provided strong evidence for faster wind speeds when tending towards the polar regions of the Sun, similar to that what Dennison and Hewish had observed. These findings were only later confirmed by the *Ulysses* fly-by of the Solar poles in 1994 and 1995 (*e.g.* Philips *et al.*, 1995).

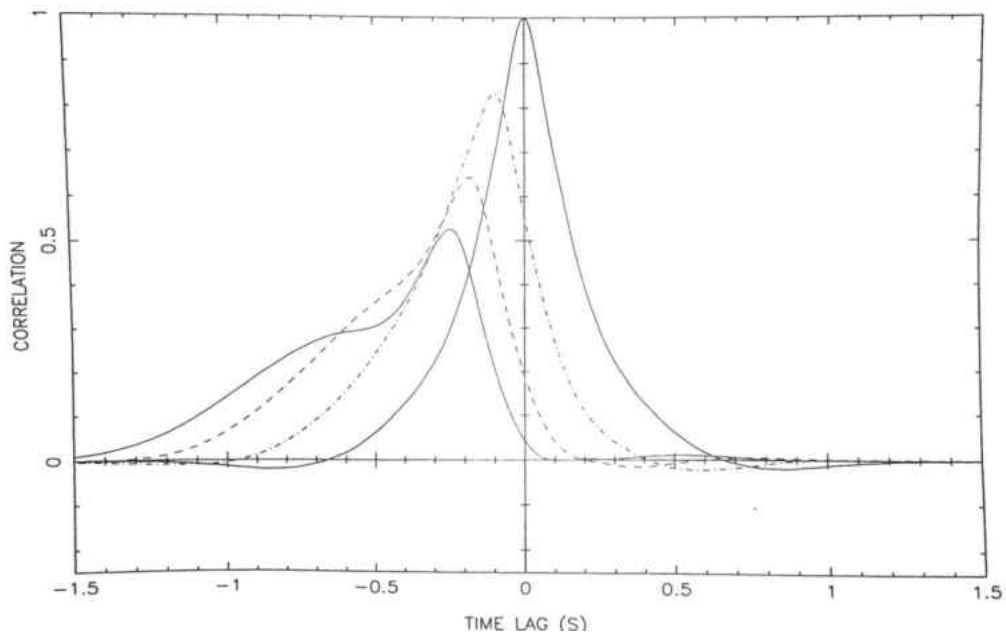


**Figure 2.4** Cross-correlation functions of different-baseline length experiments used for observations of IPS. Baselines used are 210 km (solid line), 150 km (dashed line), and 75 km (dash-dot line) (taken from Klinglesmith, 1997). The solid line peaked at 0 seconds time lag is the auto-correlation function of the radars used to check that there are no inherent errors within the radar system (the auto-correlation expected to be Gaussian).

More recently, longer baselines (extending beyond 300 km) have been used for multi-site IPS (Breen, *et al.*, 1996a; 1996b). Longer baselines allow higher temporal resolution between the radar baseline

observations, and provides the possibility of distinguishing multiple streams of solar wind with different outflow speeds that lie along the line of sight (shown in figure 2.3), and which would have previously been inseparable (Breen *et al.*, 1996b; Fallows, Breen, and Dorrian, 2008). Figure 2.4 shows the effect of changing the baseline length of an IPS experiment.

Baselines of over 1,000 km (extremely long baseline) have also been used for IPS. Bisi *et al.* (2005), Breen *et al.* (2006), and Bisi (2006) performed observations of IPS by combining the *Multi-Element Radio-Linked Interferometer Network* (MERLIN) and *European Incoherent SCATter* (EISCAT) radar networks. This provided baselines approaching 2,000 km and enabled observing correlation time lags of up to 8 seconds (corresponding to a minimum speed of 250 km s<sup>-1</sup>). The observations were able to resolve subtle variations in the outflow speed of the solar wind, with the evolution of solar wind structures resolved to around 100 km scale size.

### 2.1.1.5 Dual-frequency IPS

Often, while using two separate antenna systems, it may not be possible to observe the astronomical radio source using the exact same frequencies. Thus, it is necessary to account for this by performing modifications to the IPS power spectrum given by equation 2.7 so that a cross-correlation may be obtained. Dual frequency requires adjusting equation 2.7 such that the  $\lambda$  terms are now split into two unique terms,  $\lambda_1$  and  $\lambda_2$ , corresponding to the observing wavelengths of antenna 1 and antenna 2, respectively. The resulting equation is equation 2.11 (as formulated by Fallows *et al.*, 2006):

$$P(f) = 8\pi^2 r_e^2 \lambda_1 \lambda_2 \int_0^\infty \frac{2\pi}{v_p(z)} \int_{-\infty}^\infty \sin\left(\frac{q^2 \lambda_1 z}{4\pi}\right) \sin\left(\frac{q^2 \lambda_2 z}{4\pi}\right) |V(q, z, \theta_0)|^2 q^{-\alpha} \exp\left[-\left(\frac{q}{q_i}\right)^2 R^{-4}\right] dq_y dz \quad (2.11)$$

Using equation 2.11 it is possible to obtain correlations between signals provided that there exists an overlap in the density scales sizes observed by the different antenna. Common density scale sizes of the medium being observed means that the systems are capable of observing the same density patterns in a region of interplanetary space. Thus, successful cross-correlations have been observed using frequency difference of up to 1,000 MHz. Fallows *et al.* (2006) performed dual-frequency IPS successfully, using receiver frequencies of 500 MHz and 1,420MHz. At greater frequency differences there will be little to no overlap in the density scales sizes observed by the two frequencies.

## 2.2 White Light

The Sun emits radiation over a wide range of the electromagnetic spectrum; however, due to the Earth's atmosphere, only select regions of the electromagnetic spectrum can pass to ground level without undergoing significant filtering. White light (or visible light) is well known to undergo very little filtering by our atmosphere and is thus commonly used for solar-type observations from the ground as well as by spacecraft. The white-light wavelength band allows us to observe the photosphere and, due to scattering effects discussed in section 2.2.1.1, we can also observe the Sun's corona.

White-light observations are performed using a variety of ground- and space-based optical instruments such as coronagraphs and heliospheric imagers (see section 2.2.1.1). These instruments will often use mirrors or lenses to depict an image to be collected by a charge-coupled device (CCD) which determines the angular resolution of the image produced. The angular resolution for the mirror or lens is given by:

$$\theta = \frac{\lambda}{2r} \quad (2.12)$$

Where:

$\theta$  = Angular resolution;

$\lambda$  = Wavelength observed;

and  $r$  = Radius of the lens or mirror.

### 2.2.1 Thomson Scattering

The solar corona and heliosphere is an abundant source of free electrons such that a small portion of the incident solar electromagnetic radiation will become scattered by the electrons. The incident radiation hosts an electric field which exerts a Lorentz force that accelerates the target electron in the direction of the field (in the plane perpendicular to the incident wave). This results in the re-emission of the photon symmetrically perpendicular to the direction of the incident wave. At different scattering angles ( $\chi$ ), observers will detect different polarisations of the scattered light. An observer in the same plane as the incident light radiation (a scattering angle of  $0^\circ$  or  $180^\circ$ ) will see light scattered in all directions (*i.e.* unpolarised). Conversely, an observer positioned perpendicular to the incident wave ( $\chi = 90^\circ$ ) will see linearly polarised scattered light. Away from these planes the

observer will see partially polarised light (Howard and Tappin, 2009). These scattering effects are shown in Figure 2.5.

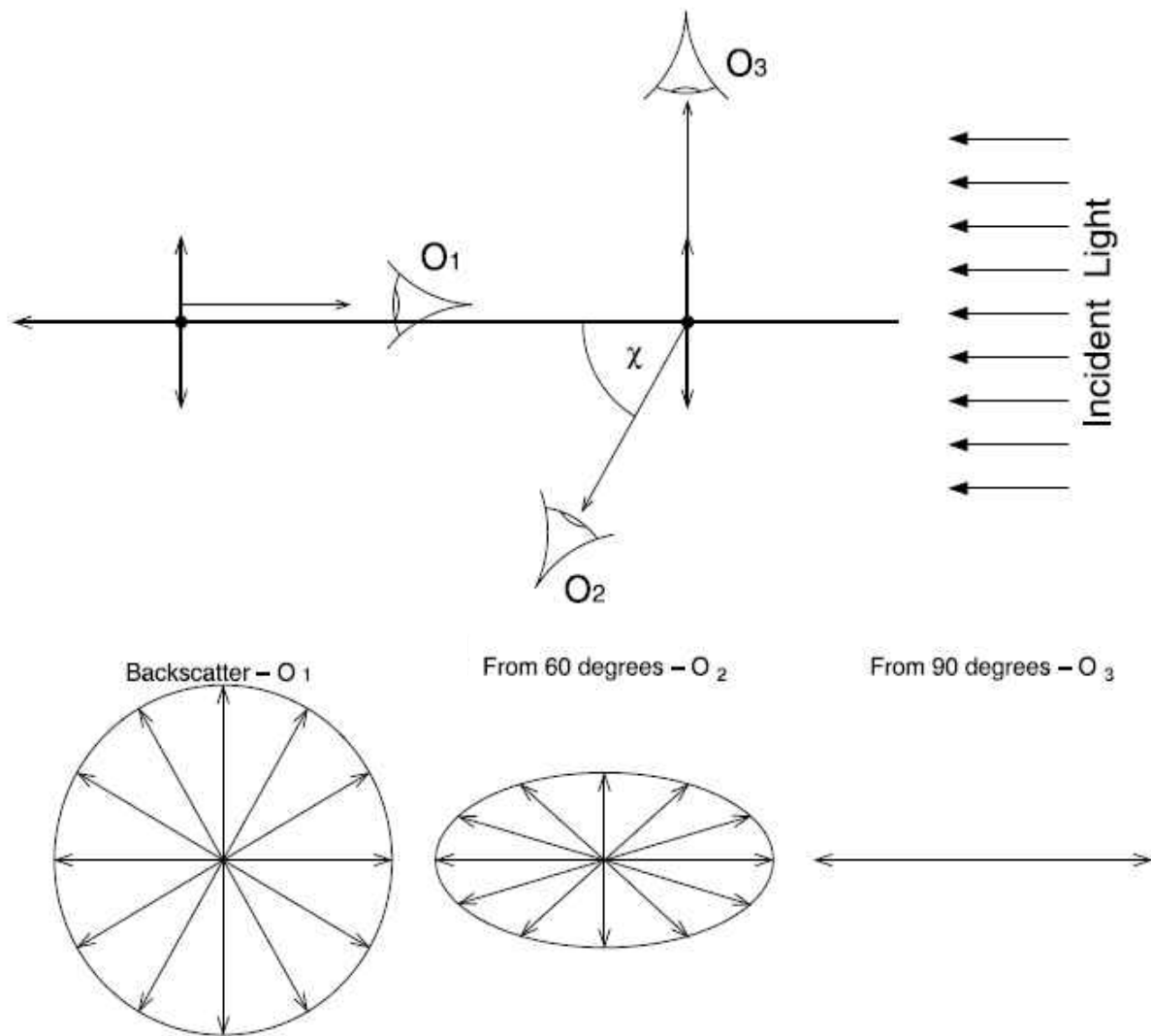


**Figure 2.5** Schematic of Thomson scattering of an unpolarised monochromatic plane wave incident on an electron (top panel), demonstrating the scattering effect (as described in the text) that would be seen by different observers (lower panels) viewing backscatter and scatter from angles ( $\chi$ ) of 60° and 90° (from Howard and Tappin, 2009). The electric field is perpendicular to the direction of propagation of the incident wave.

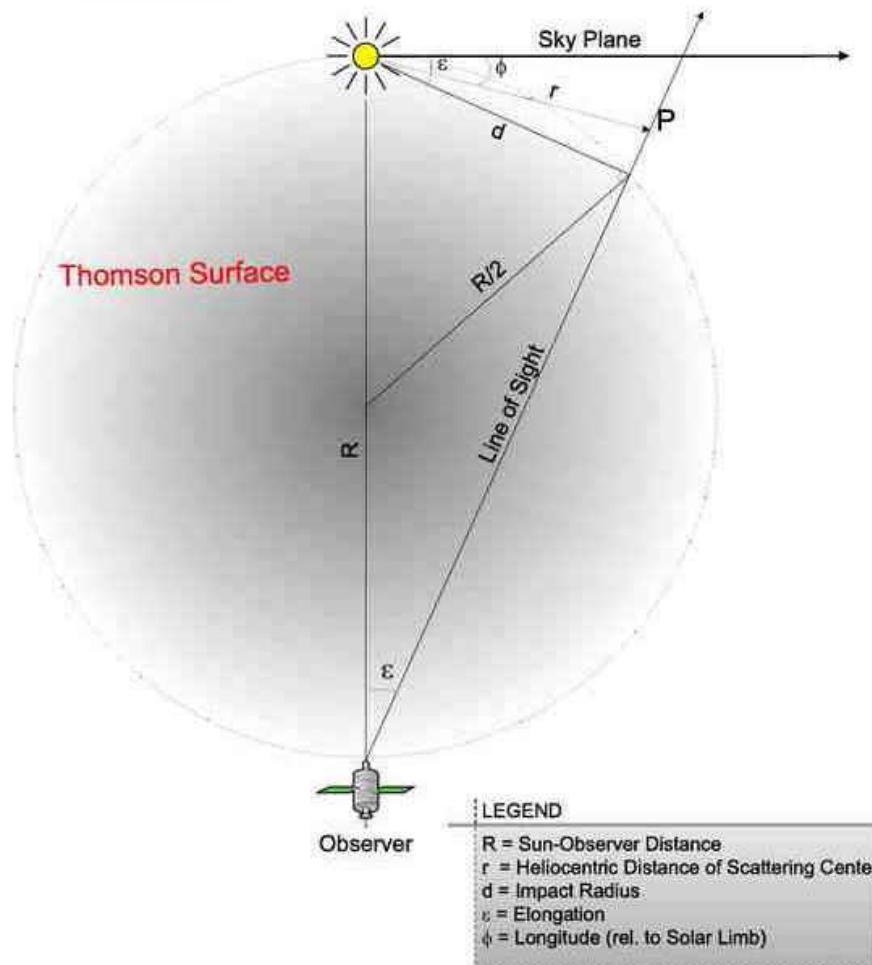


**Figure 2.6** Geometry of generalized Thomson scattering (from Vourlidis and Howard, 2005).

For visible light and the coronal free electrons, the wavelength of the incident photon is smaller than the size of the scattering particle itself and the rest mass of the scattering particles are much greater than the energy of the incident wave, such that the incident wave energy is negligible. These two conditions means that Thomson scattering will occur, and by applying electromagnetic theory, Billings (1966), and later Howard and Tappin (2009), derive the Thomson cross section for an electron as:

$$\sigma_T = \frac{8\pi}{3} \cdot \left( \frac{e^2}{4\pi\epsilon_0 m_e c^2} \right)^2 = \frac{8\pi}{3} \cdot r_o^2 \approx 6.6524 \times 10^{-29} m^2 \quad (2.13)$$

Where:

$\sigma_T$  = Thomson cross-section for electrons;

$c$  = Speed of light;

and  $r_0$  = Classical electron radius.

In the case of a spherically-symmetric density distribution, the Thomson scattered radiation is at a maximum at the *impact radius* or the *P-point*, where the line of sight from the observer is normal to the radius from the Sun through the scattering electron, *i.e.* when the line of sight is at its closest approach to the Sun (Vourlidas and Howard, 2005). From this it is found that the location of maximum scattering becomes a surface of a sphere, shown in figure 2.6. This sphere is known as the Thomson sphere and similarly the surface of the sphere is known as the Thomson surface. The Thomson sphere has a radius equal to the distance between the Sun and its observer. The Thomson sphere/surface are useful geometrical constructs which help the interpretation of white light heliospheric images.

### 2.2.1.1 Coronagraphs and Heliospheric Imagers

Remote observations of the corona can allow the detection of density structures and their evolution, allowing early interpretations of solar wind phenomena to be made. White-light observations of the solar corona are available using occulted telescopes that block the intense, direct photospheric light thus allowing observations of the faint corona. During a solar eclipse, the Moon acts as an occulting disk to obstruct the Sun's photospheric light so that the corona may be visible from the ground. Solar eclipses are rare and seldom last more than a few minutes, rendering it impractical to observe the corona only during these events. Fortunately, in 1931, the French astronomer Bernard Lyot developed the coronagraph.

The original Lyot Coronagraph, also known as the internally occulted refracting coronagraph, consists of a single lens with an internal circular occulting disc located at the focal plane, at which most of the light from the centre of the field of view (direct light from the photosphere) is absorbed (or rejected). Only a very small amount of light from the original image that would have been observed without occultation reaches the observer, but is just enough to observe the Sun's corona.

Advancing on the Lyot Coronagraph, Gordon Newkirk developed a new design of coronagraph telescope with the Externally Occulted Refracting Coronagraph (Newkirk and Bohlin, 1963).

Newkirk's coronagraph greatly reduced the scattered light taken into the system, which allows much more distant, and thus less bright corona to be observed. The Newkirk telescope suffers from a vignetting effect due to shadowing of the occulter reducing the spatial resolution of the coronagraph close to the occulting disk (Cook, 1994). Although a great improvement for observing more distant and less bright corona, the Newkirk telescope suffered from scattering effects from the Earth's atmosphere. Therefore it became desirable to locate the telescopes outside of the Earth's atmosphere, a relatively simple solution (however expensive) removing this scattering entirely. As such, coronagraph telescopes have been equipped to many solar investigating space missions such as the *Solar Maximum Mission* (SMM) (Macqueen *et al.*, 1980), SPARTAN 201 (Fisher and Guhathakurta, 1994), and much more recently the *SOLar and Heliospheric Observatory* (SOHO) (Brueckner *et al.*, 1995) and the *Solar TERrestrial RELations Observatory* (STEREO) (Howard *et al.*, 2008). Extensive details of SOHO are given in chapter 3. Figure 2.7 shows an example of a ground-based coronal observation during a solar eclipse and an observation performed by coronagraph telescope aboard SOHO.

Similar to coronagraphs, heliospheric imagers are space-based hemispherical telescopes which apply a baffle system which dramatically reduces the direct light from the Sun, so that the outer corona and heliosphere can be observed. These heliospheric imagers are able to observe CMEs and other density transients in the heliosphere. Heliospheric imagers were a development of the zodiacal light photometers that were originally designed for use aboard the *Helios* twin-spacecraft mission to observe the scattered light by "space dust" (Leinert *et al.*, 1978). Richter *et al.* (1982) found these photometers suitable to observe large transient structures out to 90° elongation and beyond (Jackson, 1985; Jackson and Benensohn, 1990). The heliospheric imager was then developed for the next generation of spacecraft, producing the *Solar Mass Ejection Imager* (SMEI) instrument (Jackson *et al.*, 2004; Howard *et al.*, 2013; and references therein). More recently, heliospheric imagers have been developed for use aboard the new twin-spacecraft STEREO mission, which the near-identical spacecraft orbit the Sun with an increasing separation (from Earth) (Howard *et al.*, 2008; Eyles *et al.*, 2009; Harrison *et al.*, 2009). More-specific details of the STEREO Heliospheric Imagers (HIs) are given in chapter 3.

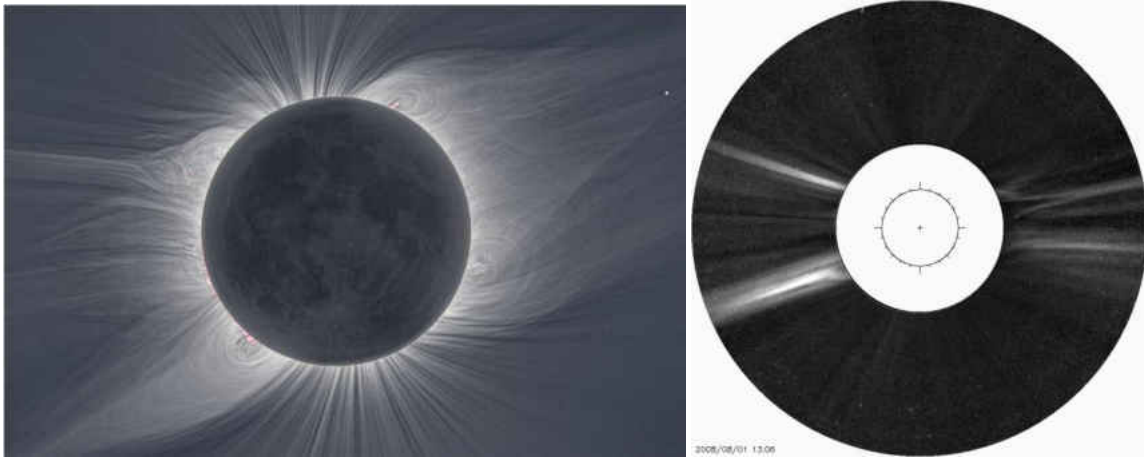


**Figure 2.7** High spatial resolution white-light image of the corona during the 01 August 2008 eclipse (from Habbal *et al.*, 2010), alongside a NRGF LASCO C2 image (details given in chapter 4) on board the SOHO mission taken on the same date.

### 2.3 Extreme Ultra-violet

The extreme ultra-violet (EUV) spans from 100 Å to 1,240 Å. Observations in this waveband are used to make full disc images of the solar transition region and the low corona (*e.g.* Delaboudinière *et al.*, 1995). Narrow bandpasses in the EUV are used to observe emission lines from highly-ionised species, commonly iron (Fe) and helium (He). Different levels of ionisation correspond to plasma at different temperature ranges and often therefore at different heights. The most common wavelengths and their objective features are displayed in Table 2.1. EUV telescopes have been a significant feature of space-based solar observatories and high resolution cameras have allowed constant observations of the Sun in these wavelengths. The Atmospheric Imaging Assembly (AIA) aboard the Solar Dynamic Observatory (SDO) has been providing rapid cadence, full disk EUV solar images with a range of observing channels (94 Å, 131 Å, 171 Å, 193 Å, 211 Å, 304 Å, 355 Å, 1600 Å, 1700 Å and 4500 Å) capable of observing the solar disk and near atmosphere of the up to 1.5  $R_{\odot}$ .

<b>Wavelength</b>	<b>Ion</b>	<b>Peak temperature</b>	<b>Observational Region/ Objective</b>
<b>94</b>	Fe XVIII		Flares
<b>131</b>	Fe VIII, XX, XXIII	$4.0 \times 10^5$ K	Flares, Transition region
<b>171</b>	Fe IX-X	$1.3 \times 10^4$ K	Corona/transition region boundary, Coronal holes
<b>193</b>	Fe IX, XXIV		Corona, hot flare plasma
<b>195</b>	Fe XII	$1.6 \times 10^6$ K	Quiet corona outside coronal holes
<b>211</b>	Fe XIV	$2.0 \times 10^6$ K	Active regions in corona
<b>284</b>	Fe XV	$2.0 \times 10^6$ K	Active regions in corona
<b>304</b>	He II	$8.0 \times 10^6$ K	Chromospheric network, Coronal holes
<b>335</b>	Fe XVI	$2.5 \times 10^{6.8}$ K	Active regions in corona

**Table 2.1** Details of EUV wavelengths commonly used for EUV solar observations. (Adapted from Delaboudinière *et al.*, 1995, with more-recently studied wavelengths from Lemen *et al.*, 2012, included)

# Chapter 3

## Sources of Experimental Data

Within this thesis multiple data sources and techniques have been used. The Interplanetary Scintillation (IPS) technique requires the use of ground based radio telescopes to observe distant radio source to detect small and large scale irregularities as they travel through the heliosphere. To produce a broader view of the heliosphere IPS can be combined with observations of Thomson scattered radiation made by spacecraft. Often the sources of heliospheric irregularities can be seen developing on the solar surface or in the lower solar atmosphere in the extreme ultraviolet (EUV) telescopes also taken by spacecraft. Spacecrafts are also able sample the local solar wind plasma and magnetic fields giving a final observation of velocities and densities before structures arrive at Earth. This chapter discusses the many observatories which have been able to provide data towards this thesis.

### 3.1 Ground-based Radio Telescopes for IPS

Throughout this thesis IPS has been a primary source of data of the velocities of the solar wind and detection of any density irregularities such as coronal mass ejections (CMEs) and smaller transient structures in the heliosphere. To source this data Earth-based radio antennas are required which can be directed to precisely observe astronomical radio source in high frequency (HF) and ultra high frequency (UHF) radio frequencies. Two primary radar networks have been used in this thesis; for results prior to 2011 the European Incoherent SCATter Radar (EISCAT) has been used and for results from 2011 the new Low Frequency ARray (LOFAR) has been used.

#### 3.1.1 European Incoherent Scatter Radar (EISCAT)

The European Incoherent Scatter (EISCAT) network in northern Scandinavia was originally built for the use of performing incoherent scatter experiments in the Earth's ionosphere (Rishbeth, 1976; Rishbeth & Williams, 1985). EISCAT is an international association currently supported by research

organisations in China (CRIRP), Finland (SA), Japan (NIPR and STEL), Norway (NFR), Sweden (VR), and the United Kingdom (NERC). Former supporting members also include France (CNRS), Germany (DFG), and the United Kingdom (STFC).

There are four EISCAT radars that are used for making observations of IPS. These are located in Tromsø (mainland Norway), Kiruna (Sweden), Sodankylä (Finland), and Longyearbyen (Svalbard, Norway). The Tromsø UHF radar is a fully-steerable 32m diameter parabolic dish, with transmitting and receiving capabilities at an operating frequency of  $933.5 \pm 3.5$  MHz (Folkestad, Hagfors, and Westerlund, 1983). The Tromsø UHF radar is part of a tristatic network with corresponding receiver-only antennas located in Kiruna and Sodankylä. In 2002, the Kiruna and Sodankylä EISCAT radars were upgraded for IPS so that they could receive (only) at a frequency around 1,400 MHz (Wannberg *et al.*, 2002). The EISCAT Svalbard Radar's (ESR) fully-steerable 32m dish is located on the island of Spitsbergen in the Svalbard Archipelago, and is capable of transmitting and receiving at a frequency of 500 MHz (Grydeland *et al.*, 2004).

As of autumn 2011, 933.5 MHz observations using the Sodankylä antenna site became impossible due to increasing interference at this frequency by GSM mobile communications. In an effort to maintain the usefulness of the antenna, the remote antennas in Sodankylä and Kiruna were upgraded to have observational capacities in the VHF wave band at 224 MHz (Ulich, 2012). This upgrade inherited a number of advantages that extended the lifespan of the receiver antennas. As well as restoring the tristatic EISCAT network, using the EISCAT VHF antenna in place of the UHF antenna based in Tromsø (Ulich, 2012), the receiver antennas operating at VHF frequencies are now compatible with other VHF systems such as the planned frequencies of EISCAT 3D also at 224 MHz (Wannberg *et al.*, 2010), and also the developing LOFAR network (see following section) which poses strong prospects for IPS between these networks (Bisi and Fallows, private communication).

EISCAT has proved effective for IPS investigations of the solar wind and was first used for observations of IPS in 1982 (Bourgois *et al.*, 1985). These observations were successful in obtaining solar wind velocity estimations, proving that EISCAT could indeed be used for IPS. EISCAT was selected to perform observations of IPS since it provided the opportunity for relatively-long baselines of up to 390 km, (*e.g.* Bourgois *et al.*, 1985; Breen *et al.*, 1996b). With the addition of the ESR site, the observable baselines have been extended to greater than 1,000 km, longer than most other individual radar networks currently available for IPS (*e.g.* Bisi *et al.*, 2005; Fallows *et al.*, 2006). The long baselines allow EISCAT observations of IPS to produce lower statistical errors when compared to shorter baseline IPS systems (*e.g.* Systems only having baselines  $\sim 100$  km or less), and,

as discussed earlier in chapter 2, longer baselines may also reveal the presence of multiple solar wind streams that may be undetectable in short baseline experiments.

### 3.1.2 Low Frequency Array (LOFAR)

The Low Frequency Array (LOFAR) is a network of radio interferometers across Europe with the network based in the Netherlands and lead by the Netherlands Institute for Radio Astronomy (ASTRON). The number of LOFAR stations is currently increasing. However as of 2013, the Netherlands was home to 40 unique stations, and 8 international stations located within other European countries (5 in Germany, 1 in Sweden, 1 in UK and 1 in France). The LOFAR stations based in the Netherlands are divided into two groups; LOFAR core; and LOFAR remote sites. The LOFAR core stations are located within a 2 km wide site approximately 30 km from ASTRON headquarters in Dwingeloo (van Haarlem *et al.*, 2013).

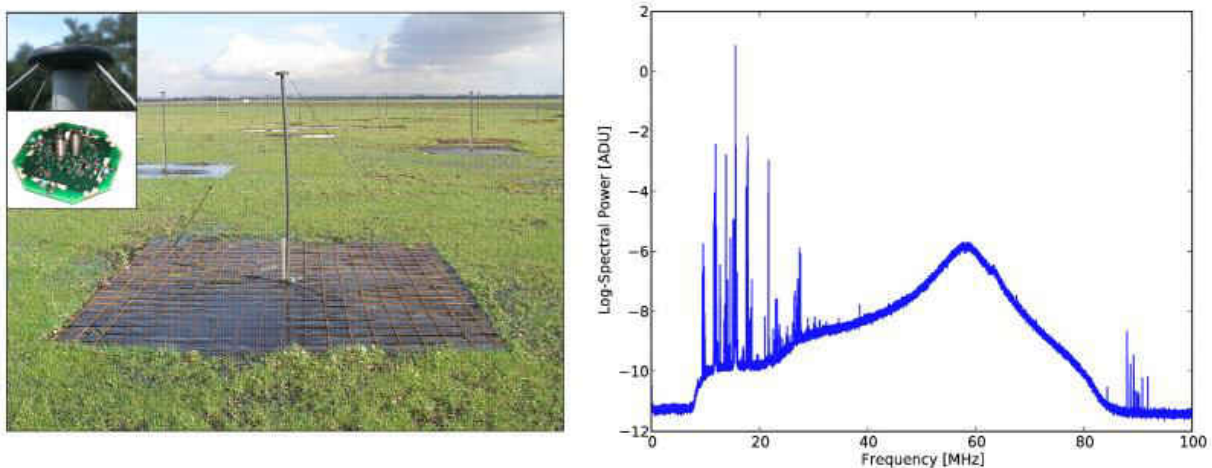


**Figure 3.1** A single LOFAR LBA dipole and ground plate alongside a median averaged spectrum of the LBA dipoles at the CS003 station. Radio frequency interference is strong below 30 MHz due to being near the ionospheric cutoff, and interference near 90 MHz is due to the FM band from (van Haarlem *et al.*, 2013).

The LOFAR sites use interferometric arrays of dipole antennas, advancing on systems such as EISCAT which use large dish radio telescopes. Rather than mechanically moving the antennas to observe regions of the sky, the arrays have an all-sky coverage which can be digitally controlled as a phased

array. Digital manipulation of the arrays may form beams which can rapidly re-point and even perform simultaneous observations of multiple regions of sky (van Haarlem *et al.*, 2013).

Each LOFAR sites is formed of two antenna groups known as the low-band antenna (LBA) and high-band antenna (HBA) systems. The LBAs are designed to operate in the frequency range of 10 MHz to 80 MHz, however is primarily limited to above 30 MHz, which is limited due to the ionospheric cutoff at around 10 MHz and the FM radio band at ~90 MHz. The LBAs elements are dipole antennas which have two copper wires acting as due polarization dipoles connected to a mounted low-noise amplifier. The LBAs are passive and each dipole is omnidirectional which allows the LBA system to monitor the entire visible sky. An example of a LBA dipole is shown in figure 3.1 alongside a typical averaged power spectrum of the LBA array (Falcke *et al.*, 2007; van Haarlem *et al.*, 2013).

The HBAs operate in the frequency range of 110 MHz to 250 MHz but is often limited to a maximum frequency of 240 MHz to reduce noise which from strong radio interference in the upper limits of the HBAs. The HBA arrays use 5 m<sup>2</sup> square tiles for which each tile holds 16 elements forming its own dual polarized phased array. Each tile produces its own 'tile beam' which can be directed into the sky thus must be actively controlled to produce a full array beam. An example of HBA tiles are shown in figure 3.2 alongside a typical averaged power spectrum of the HBA array (Falcke *et al.*, 2007; van Haarlem *et al.*, 2013).

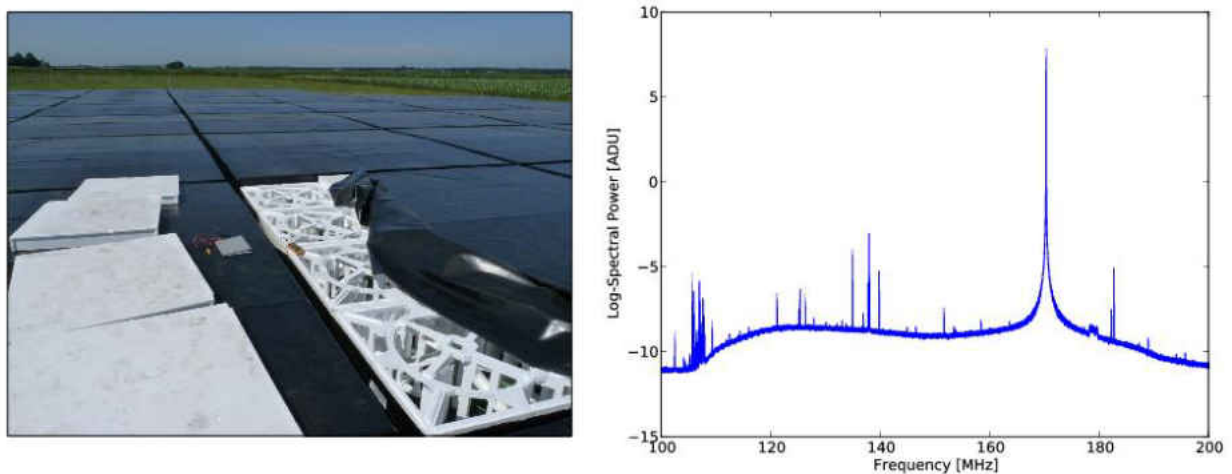


**Figure 3.2** A single LOFAR HBA tiles alongside a median averaged spectrum of the HBA tiles at the CS003 station. A strong peak of radio interference is present near 170 MHz due to this frequency being shared with the local emergency pager signal frequency (van Haarlem *et al.*, 2013).

## 3.2 Spacecraft

Throughout this thesis remote sensing imaging has been used as a source of data to observe heliospheric phenomena as they develop in the lower corona and chromospheres (in EUV) and evolve, influencing the formation of dramatic transient structures that propagating through the heliosphere out to 1 AU and beyond, These-visible as white light structures through coronagraphs and heliospheric imaging telescopes. As the solar wind approaches 1 AU the plasma and magnetic field properties can be accurately observed using *in-situ* methods. For these observations the SOHO, STEREO, SDO, ACE and Wind spacecrafts have been used and will now be discussed.

### 3.2.1 Solar and Heliospheric Observatory (SOHO)

The *Solar and Heliospheric Observatory* (SOHO) launched in August 1995 is a cooperative mission between the European Space Agency (ESA) and the National Aeronautics and Space Administration (NASA). SOHO was entrusted with the mission to observe the Sun with the hopes of investigating; the solar interior by the means of helioseismology; the coronal heating problem with extreme ultraviolet (EUV) and X-ray; and the solar wind by means of *in-situ* and remote sensing. SOHO was placed into a halo orbit in the Sun-Earth L1 (Lagrangian) point, a point of Sun-Earth gravitational equilibrium dayside of the Earth approximately 1.5 million km from the Earth. From here the SOHO spacecraft will have a continuous observation of the Sun and the spacecraft will have a constant pointing, targeting the Sun's center (Domingo, Fleck and Poland, 1995). The 12 scientific instruments onboard SOHO are each lead by principal investigator consortia which involves fifteen countries (Belgium, Denmark, Finland, France, Germany, Ireland, Italy, Japan, Netherlands, Norway, Russia, Spain, Switzerland, United Kingdom and the United States) with a total of 39 involved institutes (Domingo, Fleck and Poland, 1995).

The helioseismology investigation is performed using 3 of the 12 instruments onboard the; Global Oscillations at Low Frequencies (GOLF) (Gabriel *et al.*, 1995); Variability of Solar Irradiance and Gravity Oscillations (VIRGO) (Fröhlich *et al.*, 1995); and the Solar Oscillations Investigation (SOI) (Scherrer *et al.*, 1995). The helioseismology instruments aim to observe pressure and gravity mode oscillations which are capable of penetrating deep into the Sun's core thus revealing new detailed information on the solar interior and the mechanics of the Sun itself. SOI used the Michelson Doppler Imager (MDI) to observe pressure mode oscillations and produce full disk images of the line of sight velocities, line intensity, continuum intensity and longitudinal magnetic field components (Domingo, Fleck and Poland, 1995; Scherrer *et al.*, 1995).

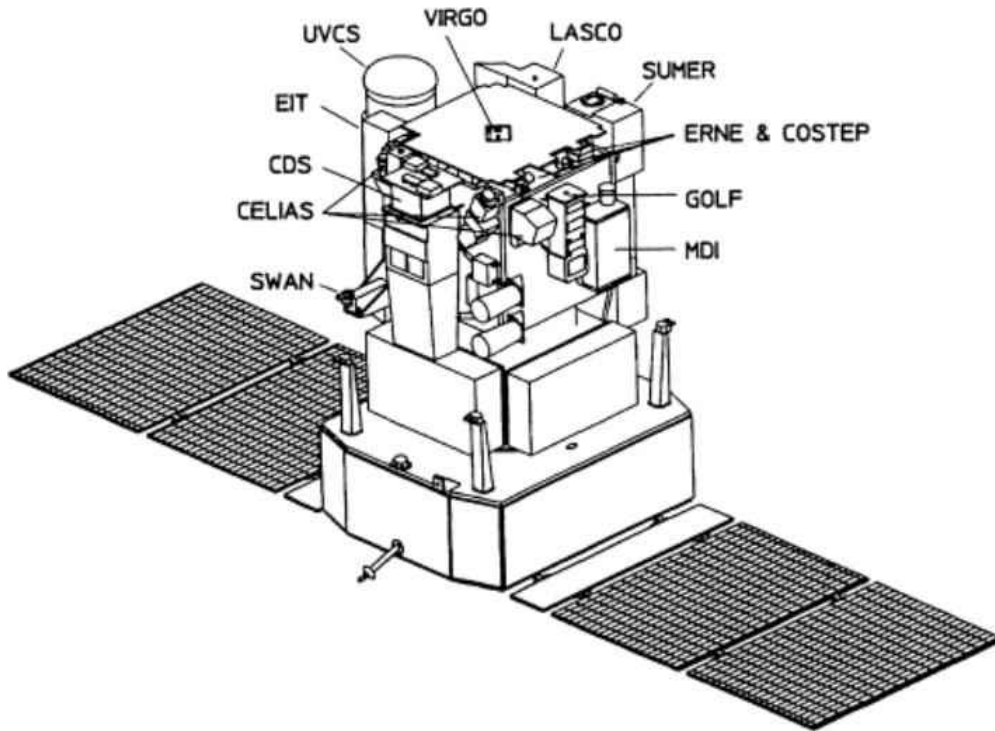


**Figure 3.3** Schematic of the SOHO spacecraft with the locations of the instruments annotated (from Domingo, Fleck and Poland, 1995).

The solar atmosphere remote sensing package onboard SOHO comprises of half of the instruments onboard SOHO and these instruments are telescopes and spectrometers which observe the electromagnetic radiation of the solar atmosphere. This package contains the; Solar Ultraviolet Measurements of Emitted Radiation (SUMER) (Wilhelm *et al.*, 1995); Coronal Diagnostic Spectrometer (CDS) (Harrison *et al.*, 1995); Extreme-Ultraviolet Imaging Telescope (EIT) (Delaboudinière *et al.*, 1995); Ultraviolet Coronagraph Spectrometer (UVCS) (Kohl *et al.*, 1995); Large Angle Spectroscopic Coronagraph (LASCO) (Brueckner *et al.*, 1995); and Solar Wind Anisotropies (SWAN) (Bertaux *et al.*, 1995). The LASCO experiment is discussed in detail in the following section.

Due to SOHO's position at the L1 point it is very beneficial for the spacecraft to perform *in-situ* observations of the solar wind. Any of the solar wind which will pass the SOHO spacecraft will inevitably pass the Earth and possibly interact with the Earth's magnetosphere. The *in-situ* package involves 3 instruments; Charge, Elements and Isotope Analysis System (CELIAS) (Hovestadt *et al.*, 1995); Comprehensive Suprathermal and Energetic Particle Analyser (COSTEP) (Müller-Mellin *et al.*,

1995); and the Energetic particle Experiment (ERNE) (Torsti *et al.*, 1995). A summary of the full scientific payload is provided in table 3.1 and the instrument locations are labeled in figure 3.3.

<b>Investigation</b>		<b>Measurements</b>	<b>Technique</b>
<b>Helioseismology</b>	<b>GOLF</b>	Global Sun Velocity oscillations	Na-vapour resonant scattering cell, Doppler shift and circular polarization
	<b>VIRGO</b>	Low degree irradiance oscillations and solar corona	Global Sun and low resolution imaging, active cavity radiometers
	<b>MDI/SOI</b>	Velocity oscillations, harmonic degree up to 4500	Fourier tachometer
<b>Solar atmosphere remote sensing</b>	<b>SUMER</b>	Plasma flow through the corona (T, $\rho$ , v)	Normal incidence spectrometer 50 - 160 nm
	<b>CDS</b>	Temperature and density	Normal and grazing incidence spectrometers, 15 80 nm
	<b>EIT</b>	Evolution of chromospheric and coronal structures	Full disk imagers in He II, Fe IX, Fe XII and Fe XV
	<b>UVCS</b>	Electron and ion characteristics (T, $\rho$ , v) at 1.1 – 30 $R_{\odot}$	Profiles and/ or intensity of selected EUV lines
	<b>LASCO</b>	Evolution, mass, momentum and energy transport in the corona (1.1 – 30 $R_{\odot}$ )	1 internally and 2 externally occulted coronagraphs. Fabry-Perot spectrometer for 1.1 – 3 $R_{\odot}$
	<b>SWAN</b>	Solar wind mass flux anisotropies and temporal variations	Scanning telescopes with hydrogen absorption cell
<b>Solar wind <i>in-situ</i></b>	<b>CELIAS</b>	Energy distribution and composition (0.1 – 1000 keV/e)	Electrostatic deflection, time-of-flight measurements, solid state detectors
	<b>COSTEP</b>	Energy distribution of ions (0.04 – 53 MeV/n) and electrons (0.4 – 5 MeV)	Solid state and plastic scintillator detectors

<b>ERNE</b>	Energy distribution and isotropic composition of ions (1.4 – 540 MeV/n) and electrons (5 – 60 MeV)	Solid state and plastic scintillator detectors
-------------	--	--

**Table 3.1** Summary of scientific payload onboard the SOHO spacecraft (adapted from Domingo *et al.*, 1995)

### 3.2.1.1 Large Angle and Spectrometric Coronagraph (LASCO)

The LASCO package onboard SOHO is a package of three coronagraph telescopes, known as C1, C2 and C3. LASCO was developed purely for the use onboard the SOHO mission by a consortium of the Naval Research Laboratory (USA), the Laboratoire d’Astronomie Spatiale (France), the Max-Planck-Institut für Aeronomie (Germany), and the University of Birmingham (UK) (Brueckner *et al.*, 1995). The coronagraphs are able to observe the solar corona for a combined field of view of 1.1 to 30  $R_s$  with each of the coronagraph telescopes providing a partial overlapping field of view over another of the coronagraphs to account for any weaknesses in the coronagraph systems used. Each of the coronagraphs is fitted with 1024 x 1024 pixel CCD cameras which receive the occulted image of the solar corona (Cook, 1994; Brueckner *et al.*, 1995). The LASCO coronagraphs are summarized in table 3.2.

The LASCO C1 telescope is based on the original Lyot telescope (as discussed earlier in chapter 2) which uses an internal occulter to greatly reduce the intensity of the Sun’s light such that the very faint scattered light from the corona can be observed. As the C1 telescope is internally occulted the telescope is not limited by the aperture size limitations and does not suffer shadowing at the inner edge of the field of view (vignetting) due to an external occulter thus this preserves the full spatial resolution over the entire field of view (Cook, 1994; Brueckner *et al.*, 1995). The Lyot style coronagraph of LASCO required modifications to become suitable for use in space. The modifications originally suggested by Newkirk and Bohlin (1963) involved replacing the objective element with a mirror which would allow the telescope system to avoid inherent problems with stray light that may occur while using refractive elements. As such the LASCO C1 telescope is capable of observing the solar corona with a field of view of 1.1 to 3.0  $R_s$  (Brueckner *et al.*, 1995). The C1 telescope is also equipped with a Fabry-Perot interferometer which can produce monochromatic images with a spectral resolution of 0.07 nm over the entire C1 field of view. The Fabry-Perot interferometer may perform high resolution imaging spectroscopy, determining line profiles and Doppler shifts over a

narrow bandpass (Brueckner *et al.*, 1995). On 25 June 1998 technical issues hit the SOHO spacecraft and it went into an uncontrollable spin and was not recovered until 16 September 1998. During this time the LASCO C1 telescope became inoperational (Howard, 2011).

	<b>Field of View (R<sub>s</sub>)</b>	<b>Occulter</b>	<b>Spectral bandpass</b>	<b>Objective element</b>	<b>Pixel Size</b>	<b>Brightness Range (B<sub>s</sub>)</b>
<b>C1</b>	1.1 – 3.0	Internal	Fabry-Perot	Mirror	5.6"	$2 \times 10^{-5} - 2 \times 10^{-8}$
<b>C2</b>	1.5 – 6.0	External	Broadband	Lens	11.4"	$2 \times 10^{-7} - 5 \times 10^{-10}$
<b>C3</b>	3.7 – 30.0	External	Broadband	Lens	56.0"	$3 \times 10^{-9} - 1 \times 10^{-11}$

**Table 3.2** LASCO telescope parameters (adapted from Brueckner *et al.*, 1995).

The LASCO C2 and C3 telescopes (shown in figure 3.4) are based on Newkirk's externally occulted coronagraph telescope which was previously discussed in chapter 2 (Newkirk and Bohlin, 1963; Brueckner *et al.*, 1995). The external occultation dramatically reduces the amount of stray scattered photospheric light entering the telescope by completely shadowing out the primary source of the photospheric light, the Sun, from the objective element (Newkirk and Bohlin, 1963). This allows the telescope to observe much fainter scattered light and thus the externally occulted coronagraphs can observe a distances greater than the C1 coronagraph telescope. Using a threaded conical cylinder as an occulter, the C2 telescope has an effective field of view of 1.5 R<sub>s</sub> to 6.0 R<sub>s</sub> with the outer field limit defined by an internal field stop which again reduces stray scattered photospheric light allowing the coronagraph to focus with optimum resolution in its field of view. The final image that is received by the CCD camera has a resolution of 11.4 arc seconds (") to each 0.021 nm CCD pixel (Cook, 1994; Brueckner *et al.*, 1995).

The occulter of the C3 is a triad of disks which are equally spaced on a common spindle. Each of these disks is sized such that the following disks will intercept diffracted light from the edge of the disk that preceded it. This greatly reduces the amount of scattered light which enters the telescope allowing the telescope to observe the corona much up to 32 R<sub>s</sub>. The square CCD camera however limits the circular image size to 30 R<sub>s</sub> at the circular extremities (top, bottom, left and right edges) resolving the coronagraph to a field of view of 3.7 R<sub>s</sub> to 30.0 R<sub>s</sub> with a resolution of 56" per pixel (Cook, 1994; Brueckner *et al.*, 1995).

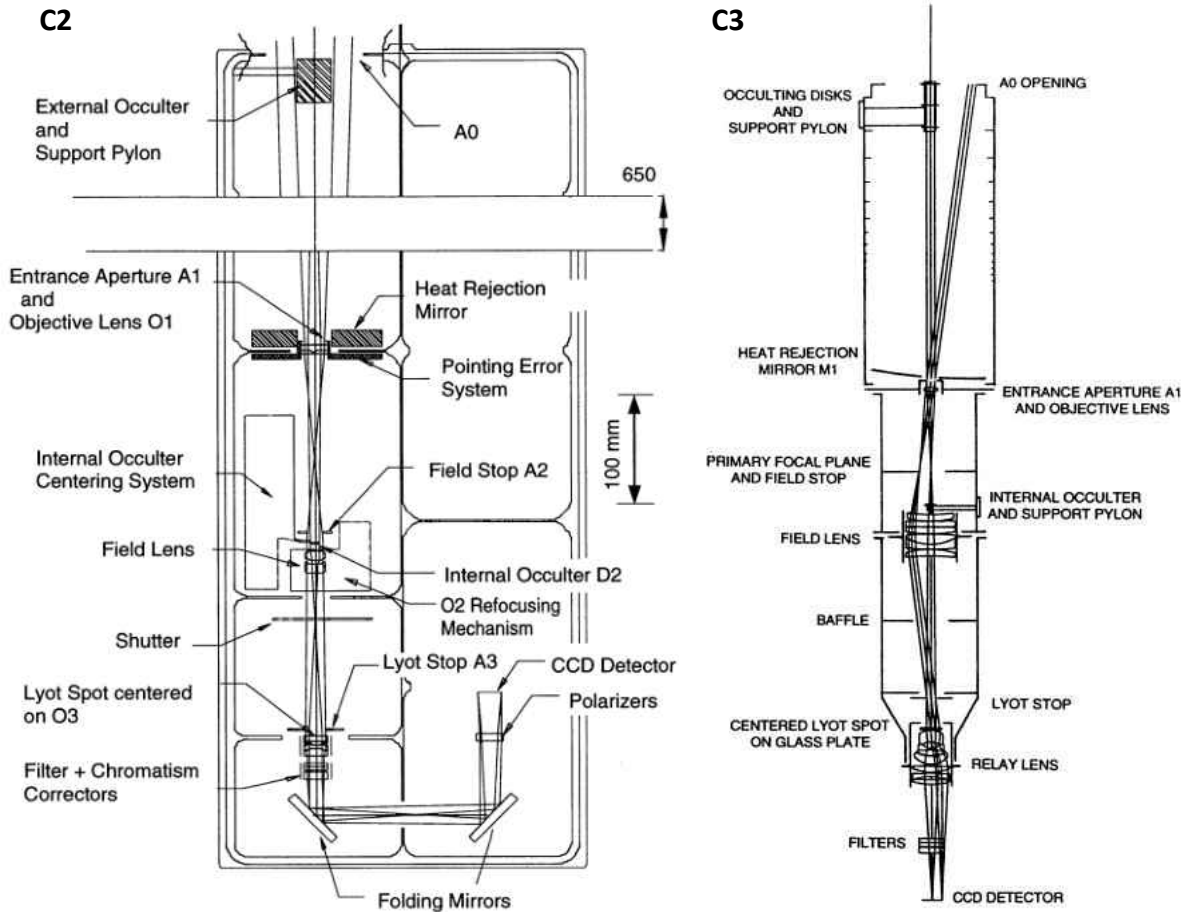


Figure 3.4 Optical layouts of LASCO C2 and C3 coronagraphs (from Brueckner *et al.*, 1995).

### 3.2.2 Solar Terrestrial Relations Observatory (STEREO)

The *Solar Terrestrial Relations Observatory* (STEREO) was launched in October 2006 and consists of nearly-identical satellites, *STEREO-Ahead* (STEREO-A) and *STEREO-Behind* (STEREO-B). The mission is managed by Goddard Space Flight Center and developed by John's Hopkins University Applied Physics Laboratory (JHU/APL). The STEREO mission is unique with regards to its orbital characteristics (shown in figure 3.5) as each of the STEREO spacecrafts orbit the Sun near 1 AU with STEREO-A orbiting slightly faster than the Earth whereas STEREO-B orbits slower. This orbital characteristic is such that each spacecraft drifts away from the Earth at a rate of 22.5° per year (Driesman *et al.*, 2008). The orbital configuration of STEREO allows a stereoscopic view of the Sun and making it possible for three-dimensional (3-D) properties of heliospheric ejecta to be investigated.

Each of the STEREO observatories holds an extensive and varied payload of scientific instruments with optical, particle and electromagnetic wave instruments represented. The instruments can be

divided into four instrument packages and these are; Sun Earth Connection Coronal and Heliospheric Investigation (SECCHI) (Howard *et al.*, 2008); STEREO/Waves (SWAVES) (Bougeret *et al.*, 2008); In-situ Measurements of Particles and CME Transients (IMPACT) (Luhmann *et al.*, 2008); and Plasma and Suprathermal Ion Composition (PLASTIC) (Galvin *et al.*, 2008). The locations of the scientific instruments on the spacecraft are given in figure 3.6.

SWAVES uses a 6 m radio antenna to measure fluctuating electric fields in the three frequency receiver channels; low frequency receiver (2.5 kHz to 160 kHz); high frequency receiver (125 kHz to 16 MHz); and the fixed frequency receiver (30.025 MHz to 32.025 MHz). The instrument is capable of performing 3D localization and tracking of radio emissions often associated with CMEs and solar flares (Bougeret *et al.*, 2008). The IMPACT package of STEREO is capable of sampling the local solar wind to determine 3-D characteristics of the solar wind plasma, solar energetic particles and local interplanetary magnetic fields (Luhmann *et al.*, 2008). The PLASTIC instruments are time of flight/energy mass spectrometers. These spectrometers are responsible for determining the characteristics of protons, alpha particles, heavy ions and suprathermal ions (Galvin *et al.*, 2008).

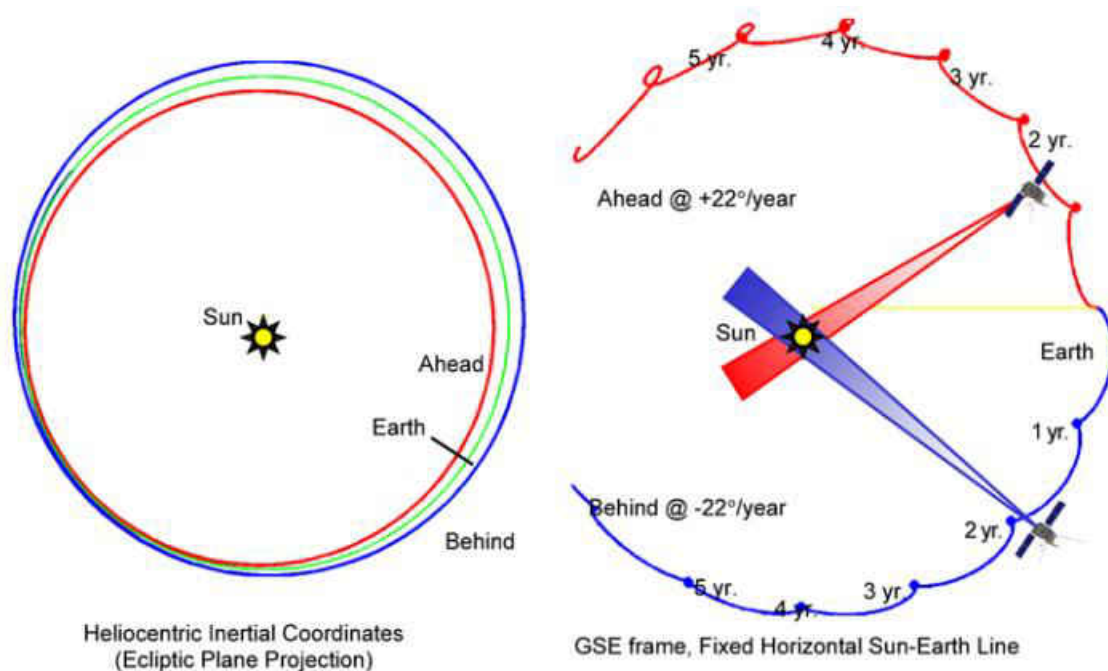


**Figure 3.5** STEREO spacecraft orbit projections in the ecliptic plane for the heliocentric inertial coordinates and the geocentric solar ecliptic (GSE) frame (from Driesman *et al.*, 2008).

The STEREO SECCHI instrument package is a package of 5 optical experiments designed to provide an extensive view of the solar atmosphere ranging from the solar corona encompassing the solar disk out to the inner heliosphere beyond 1 AU. The inner most telescope is an extreme ultraviolet imager (EUVI). The EUVI telescope uses four wavelength filters (He II: 30.4 nm, Fe IX: 17.1, Fe XII: 19.5 nm, Fe XV: 28.4 nm) to observe extreme ultraviolet radiation from the chromosphere corona with a range of  $1 R_s$  to  $1.7 R_s$  (Howard *et al.*, 2008). Observing off the solar disk are two coronagraphs (COR1 and COR2) and two heliospheric imagers (HI-1 and HI-2), and these are discussed in the sections following.

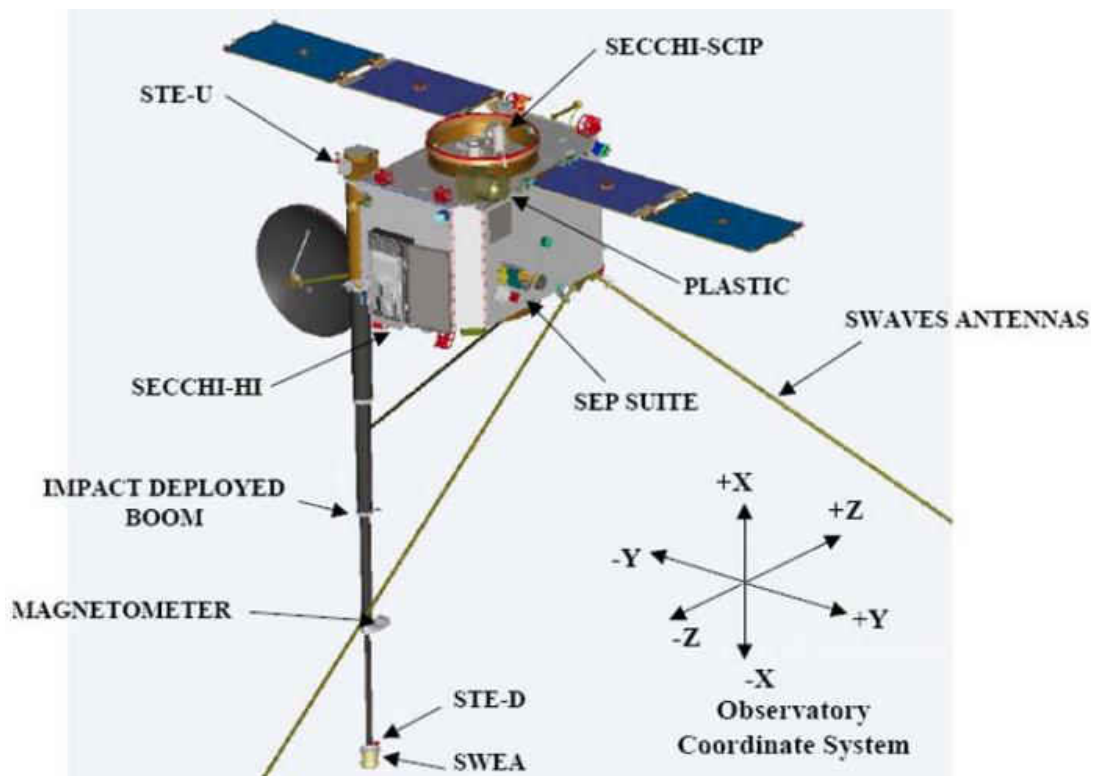


**Figure 3.6** STEREO-B spacecraft illustration with annotated locations of scientific instruments (from Driesman *et al.*, 2008).

### 3.2.2.1 The Coronagraphs of STEREO

Observing the corona between  $1.5 R_s$  and  $15 R_s$  are two coronagraphs. The COR1 coronagraph is a traditional internally occulted (Lyot) telescope, using a lens as the objective element, rather than a mirror as used in the LASCO C1 design. As with LASCO C1, an internally occulted coronagraph was

preferred for the inner most coronagraph reducing the vignetting due to an external occulter and thus preserving the full spatial resolution close to the solar limb.

As the COR1 uses the concept of a traditional Lyot coronagraph it is susceptible to large amounts of stray photospheric light thus small modification are made to the design (shown in figure 3.7) to suppress this stray light. The COR1 coronagraph is designed using two groups of doublet lenses which limit the bandpass of the system to focus only H $\alpha$  line radiation at 656 nm ( $\pm$  11.25 nm), this reduces any systemic chromatic aberration. Before light can even enter the optical system, the occulter in the COR1 design uses a cone shaped tip to help redirect stray photospheric light into a light trap. This is then followed by a circular focal plane mask which blocks diffracted light from the edge of the occulter. The combination of the occulter and the focal plane mask allows the system to completely occult light from the Sun out to 1.4 R<sub>S</sub>, however partial vignetting occurs up to 1.9 R<sub>S</sub>. COR1 has a maximum brightness of  $1 \times 10^{-6}$  B<sub>S</sub> at the inner edge of the occulter (1.4 R<sub>S</sub>) and has a minimum brightness of  $2 \times 10^{-7}$  B<sub>S</sub> giving a limited observational distance of up to 4 R<sub>S</sub> (Thompson *et al.*, 2003; Howard *et al.*, 2008).

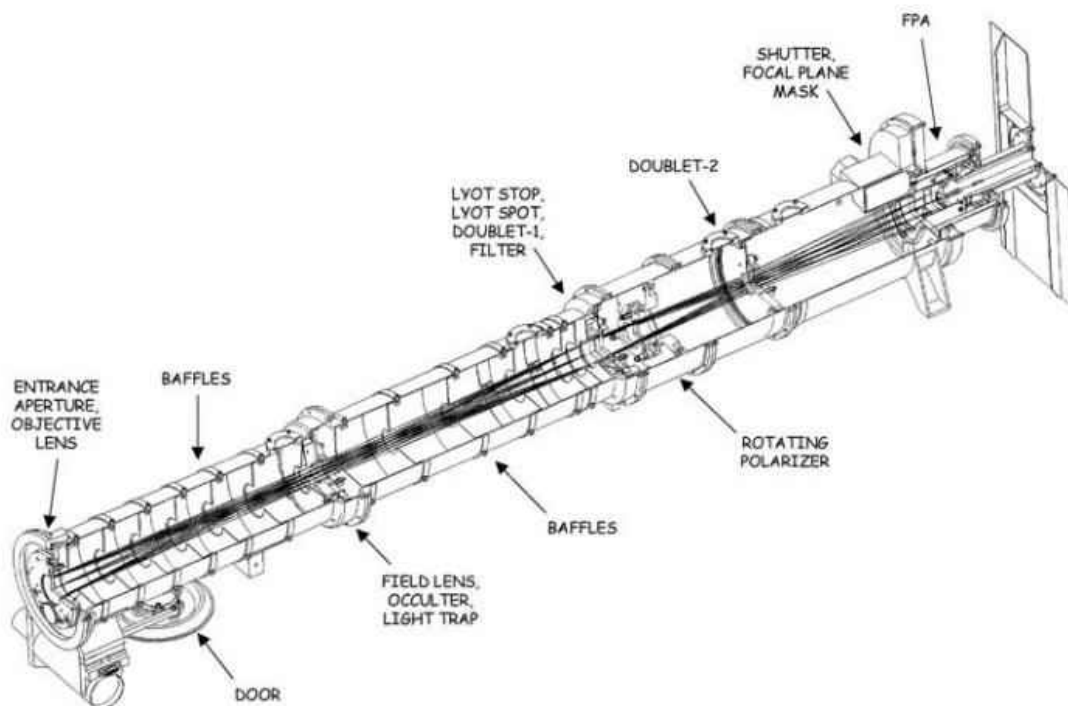


**Figure 3.7** Optical layout of COR1 (from Thompson *et al.*, 2003).

The COR2 coronagraph is an externally occulted telescope and is based on the LASCO C2 and C3 coronagraphs aboard SOHO. The external occulter greatly reduces the amount of stray scattered photospheric light entering the system by completely shadowing out the photospheric light of the solar disk from the objective element. This allows the COR2 telescope to observe more the Sun's more distant corona which is too faint for the COR1 to detect. The optical schematic of COR2 is shown in figure 3.8. COR2 improved upon the LASCO coronagraphs by slightly increasing the aperture size to improve the light gathering power of the system so that COR2 can extend upon the LASCO C2 field of view. An upgraded CCD allows COR2 to have a shorter exposure time, with an image cadence of 15 minutes. The new CCD is a 2k x 2k pixel CCD which allows the COR2 to extend to 15  $R_S$  while maintaining a similar spatial resolution to LASCO C2 (Howard *et al.*, 2008).

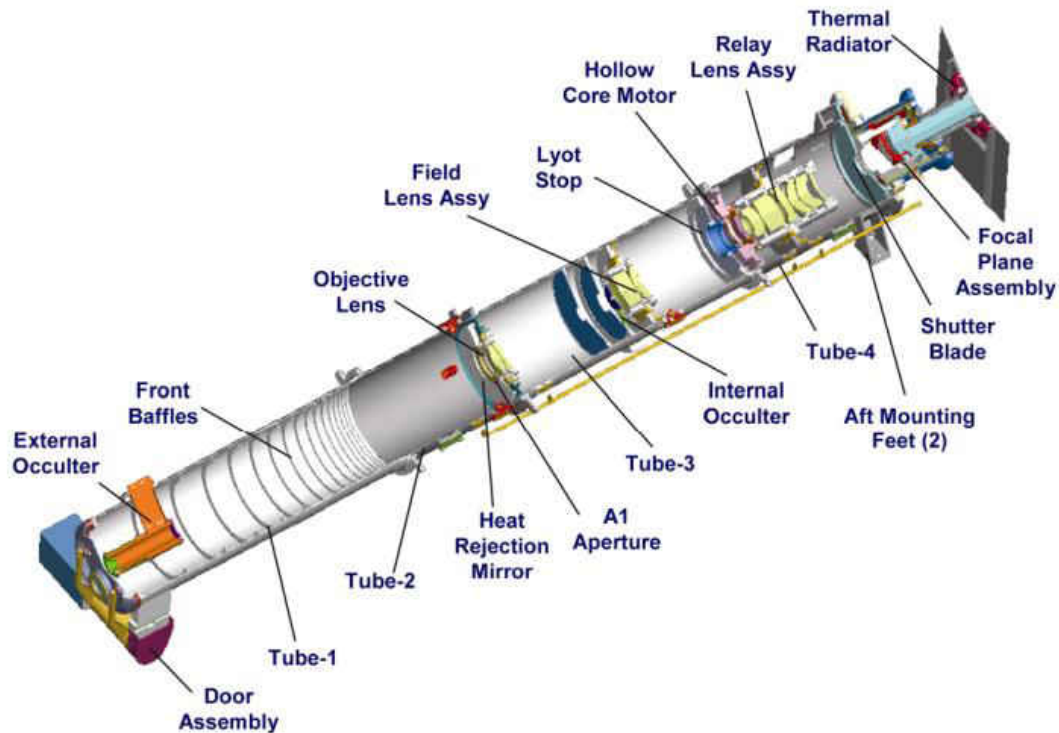


**Figure 3.8** Optical layout of COR2 (from Howard *et al.*, 2008).

### 3.2.2.2 Heliospheric Imagers (HIs)

The STEREO|HI instruments comprise the final part of the SECCHI package (Howard *et al.*, 2008). The HI instrument on each STEREO spacecraft consists of two wide-angle, white-light telescopes: HI-1

and HI-2. By using Thomson scattering of sunlight, the HI telescopes observe solar wind density structures, similarly to coronagraph telescopes. HI observes the heliosphere along the Sun-Earth line with a very wide field of view which during certain phases of the STEREO orbits can observe the Earth and beyond. A detailed schematic and image of the HI instrument is given in figure 3.9.

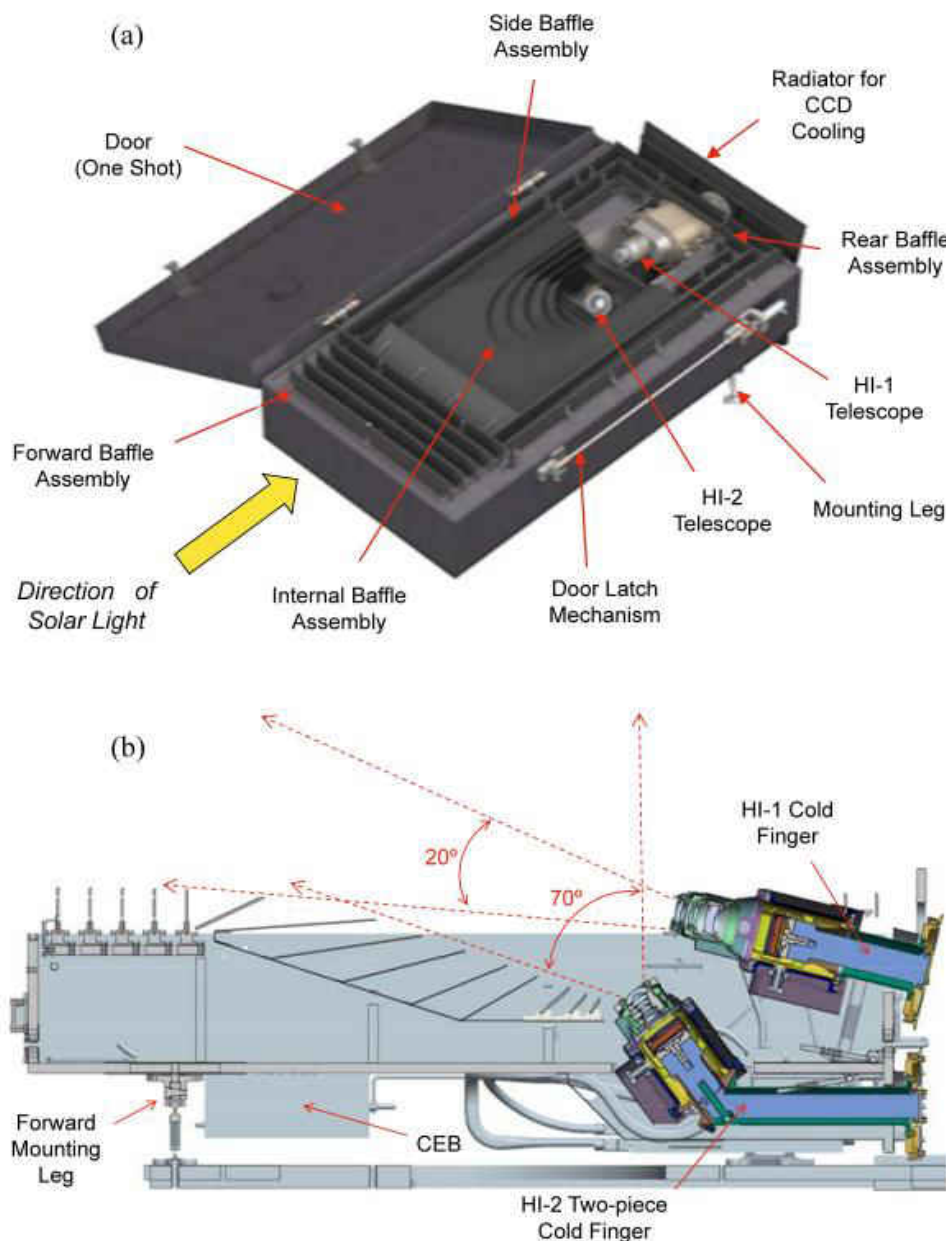


**Figure 3.9** a) Heliospheric imager design with labeled features. b) cross-sectional view of the HI telescopes with telescope fields of view in red (taken from Eyles *et al.*, 2009).

The 20 x 20° field of view (FOV) of HI-1 covers an elongation range of approximately 4° to 24° along the ecliptic in nominal operations. The 70° wide HI-2 FOV extends from around 18.7° out to 88.7°

along the ecliptic. HI-1 and HI-2 operate at a nominal cadence of 40 and 120 minutes, respectively, providing continuous high-resolution 1024 x 1024 pixel images of heliospheric transients (Eyles *et al.*, 2009; Harrison *et al.*, 2008; and references therein). The HIs use a baffle design to reduce stray light from the solar disc so that the instruments are sensitive to  $3 \times 10^{-15} B_s$  and  $3 \times 10^{-16} B_s$  for HI-1 and HI-2, respectively. The HI's principal axis is tilted  $0.33^\circ$  upwards so that the horizon of the baffle is raised above the Sun (Howard *et al.*, 2008; Eyles *et al.*, 2009; Harrison *et al.*, 2009).

The HI-1 cameras are effective in observing features at a scale-size larger than around  $1.6 \times 10^5$  km (corresponding to a feature approximately 20 pixels wide at 0.5 AU from the spacecraft), with a cadence of 40 minutes. A summary of the performance specifications of the HI telescopes are given in table 3.3.

	HI-1	HI-2
<b>Centre of FOV (<math>^\circ</math>)</b>	13.98	53.68
<b>Angular FOV (<math>^\circ</math>)</b>	20	70
<b>Angular range (<math>^\circ</math>)</b>	3.98 – 23.98	18.68 – 88.68
<b>Image CCD (pixels)</b>	1024 x 1024	1024 x 1024
<b>Pixel size</b>	70''	4'
<b>Spectral bandpass (nm)</b>	630 – 730	400 – 1000
<b>Nominal exposure time (s)</b>	12 - 20	60 – 90
<b>Exposures per image</b>	150	100
<b>Nominal image cadence (minutes)</b>	60	120
<b>Brightness sensitivity (<math>B_s</math>)</b>	$3 \times 10^{-15}$	$3 \times 10^{-16}$
<b>Straylight rejection (<math>B_s</math>)</b>	$3 \times 10^{-13}$	$1 \times 10^{-14}$

**Table 3.3** Summary of the performance specifications on HI telescopes (from Howard *et al.*, 2008).

### 3.2.3 Solar Dynamics Observatory (SDO)

The *Solar Dynamic Observatory* (SDO) is part of NASA's Living with a Star (LWS) program with the mission of investigating the causes of solar variability and its impacts on Earth, by observing the generation and structure of the Sun's magnetic field and how this magnetic field enters the heliosphere and transported towards the Earth by means of the solar wind, SEPs, and solar

irradiance variation. SDO was launched in February 2010 into a circular geosynchronous orbit inclined by  $28^\circ$  about the ground station receive at  $102^\circ$  West longitude at an altitude of 36000 km (Pesnell, Thompson and Chamberlin, 2012).

The SDO instrument package consists of 3 experiments, these are; Heliospheric and Magnetic Imager (HMI) (Schou et al., 2012); Atmospheric Imaging Assembly (AIA) (Lemen et al., 2012); Extreme Ultraviolet Variability Experiment (EVE) (Woods et al., 2012). The locations of these instruments on the SDO spacecraft are shown in figure 3.10. EVE measures the EUV irradiance of Sun between 0.1 nm and 105 nm, using spectrographs, photometers and a pinhole camera. EVE has a very high spectral resolution on 0.1 nm with a temporal cadence of 10 seconds (Woods *et al.*, 2012). HMI maps magnetic and velocity fields on the surface of the Sun, similar to SOHO|MDI, by measuring the Doppler shifts in the 617.3 nm (Fe I) absorption line, and is capable of producing full disks images every 45 seconds. Line of sight magnetic field measurements and vector magnetic field maps of the photosphere are also produced by the HMI experiment using the Zeeman Effect of the 617.3 nm spectral line (Schou *et al.*, 2012).

The AIA instrument package is an array of four filtered telescopes observing the solar disk and near atmosphere of the Sun to produce full disk images of the solar atmosphere up to  $1.5 R_\odot$ . Each of the telescopes has approximately  $41'$  field of view and uses  $4096 \times 4096$  pixel CCD detectors allowing the telescopes to produce images with  $1.4''$  resolution. The AIA telescopes may observe the Sun using 7 wavelength channels. The channels are 94 Å, 131 Å, 171 Å, 193 Å, 211 Å, 304 Å, 355 Å, 1600 Å, 1700 Å and 4500 Å. The primary ions and atmospheric regions these channels relate to are given in table 2.1. Figure 3.11 shows SDO|AIA images of an active region observed on 15 February 2011 01:45 UT in all of the AIA wavelength channels (Lemen, *et al.*, 2012; Pesnell, Thompson and Chamberlin, 2012).

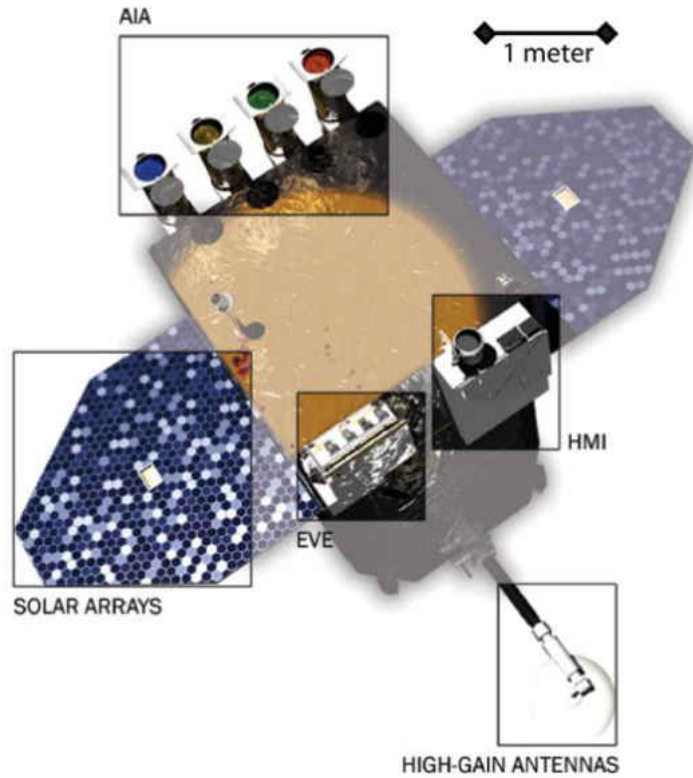


**Figure 3.10** Annotated image of the SDO spacecraft with the scientific instruments highlighted (from Pesnell, Thompson and Chamberlin, 2012).

Investigation		Returned Data
Heliospheric and Magnetic Imager	<b>HMI</b>	Full disk Dopplergrams Full disk LOS magnetograms Full disk vector magnetograms
Atmospheric Imaging Assembly	<b>AIA</b>	Rapid cadence, full disk EUV solar images
Extreme Ultraviolet Experiment	<b>EVE</b>	Rapid cadence EUV spectral irradiance

**Table 3.4** Summary of SDO scientific instruments (from Lemen, *et al.*, 2011).

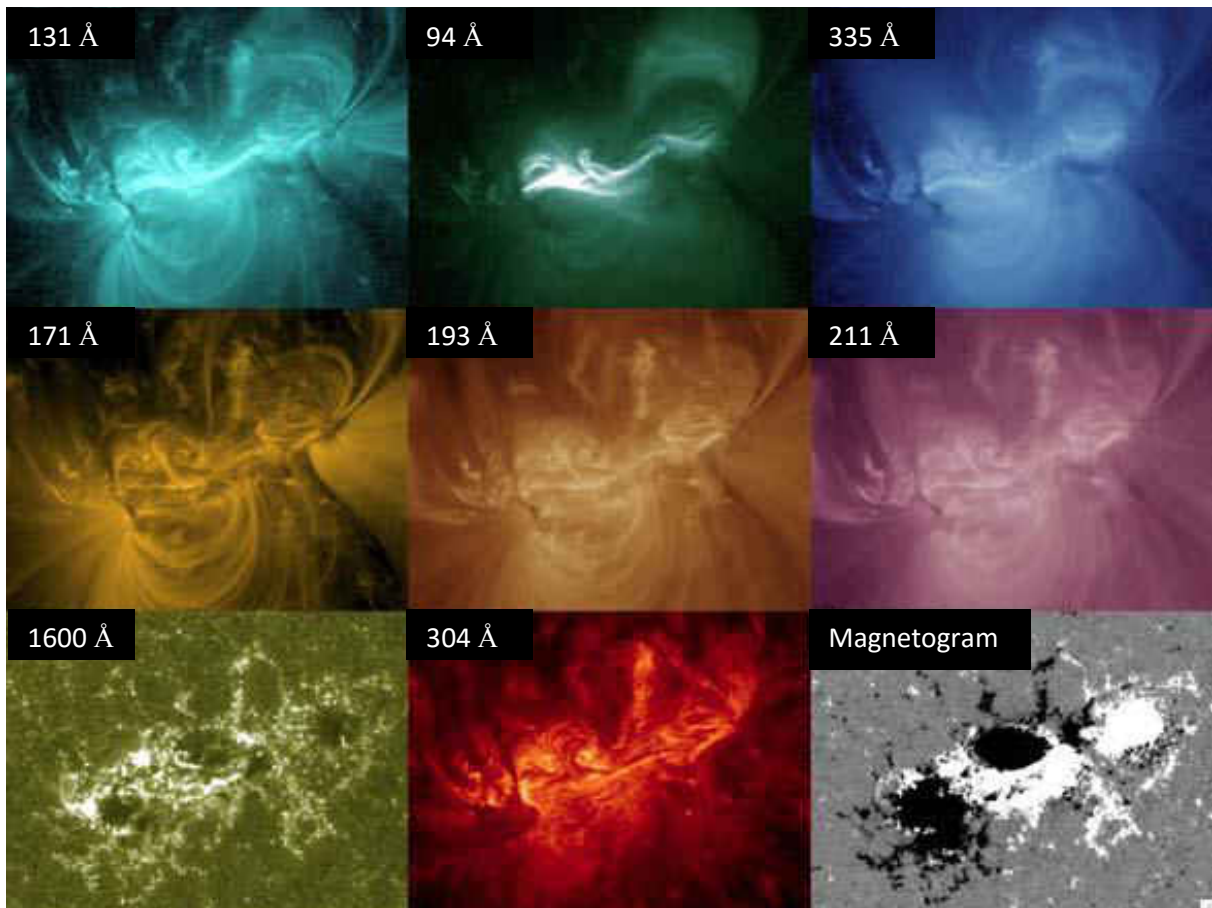


**Figure 3.11** SDO|AIA images of an active region observed on 15 February 2011 01:45 UT at different wavelengths. Bottom right image is magnetogram image of the same active region taken using SDO|HMI (adapted from Lemen, *et al.*, 2011).

### 3.2.4 Advanced Composition Explorer (ACE)

The *Advanced Composition Explorer* (ACE) launched 25 August 1997 orbits the Sun along with the Earth from the Sun-Earth L1 (Lagrangian) point, approximately 1.5 million km from the Earth. ACE provides near real-time continuous *in-situ* measurements of solar wind parameters and space weather providing an advanced warning (approximately 1 hour) of the solar wind ahead of its arrival at Earth.

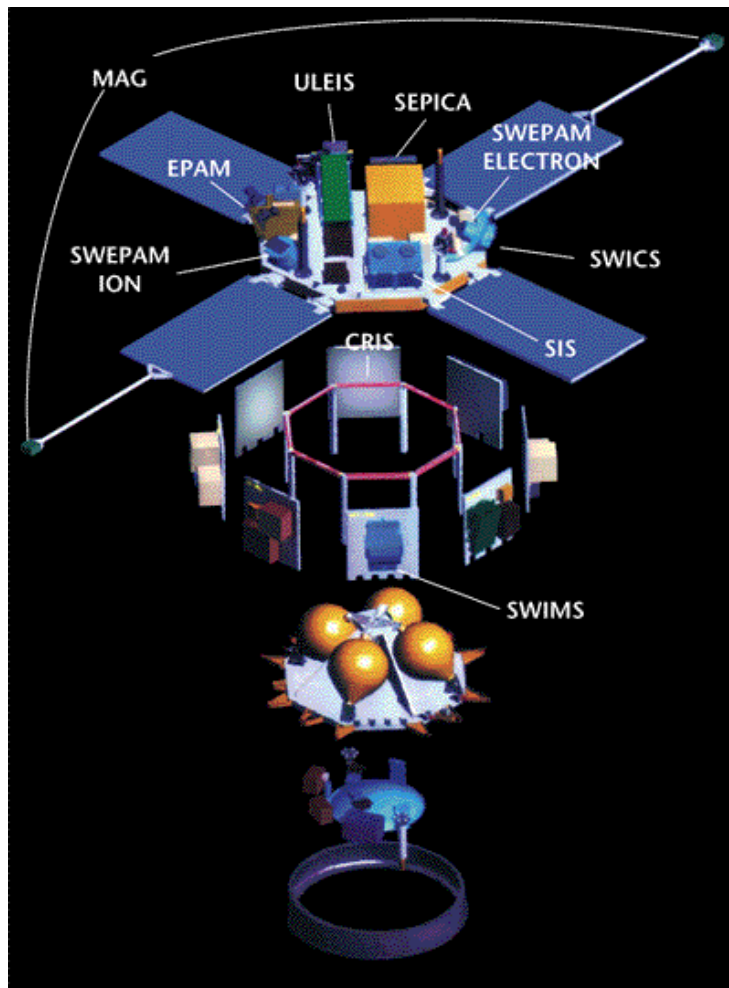


**Figure 3.12** Deconstructed view of the ACE spacecraft displaying the locations of the 9 scientific instruments. The top of the spacecraft (relative to the image) is positioned sunward (from Stone *et al.*, 1998).

Under contract with NASA, the Goddard Space Flight Center (GSFC) developed the ACE mission, in collaboration with the John's Hopkins University Applied Physics Laboratory (JHU/APL) for spacecraft development, and the California Institute of Technology (Caltech) for the development of the spacecraft's instruments (Stone *et al.*, 1998).

The objectives of the ACE spacecraft mission were to investigate the composition of the solar corona, interplanetary medium, local interstellar medium and galactic matter. To perform these objectives the ACE spacecraft holds 9 instruments: Cosmic-ray isotope spectrometer (CRIS), Solar isotope spectrometer (SIS), Ultra low energy isotope spectrometer (ULEIS), Solar energetic particle ionic charge analyzer (SEPICA), Electron, proton and alpha monitor (EPAM), Solar wind ion mass spectrometer (SWIMS), Solar wind ion composition spectrometer (SWICS), Solar wind electron,

proton and alpha monitor (SWEPAM), and Magnetometer (MAG). A summary of these instruments is provided in table 3.5 and their locations on the spacecraft are shown in figure 3.12.

Instrument	Acronym	Measured species	Measured quantities	Typical energy (MeV nucl <sup>-1</sup> )	Technique
Cosmic-ray isotope spectrometer	<b>CRIS</b>	$2 \leq Z \leq 30$	$Z, M, E$	$\sim 200$	$dE/dx - E$
Solar isotope spectrometer	<b>SIS</b>	$2 \leq Z \leq 30$	$Z, M, E$	$\sim 20$	$dE/dx - E$
Ultra low energy isotope spectrometer	<b>ULEIS</b>	$2 \leq Z \leq 28$	$M, E$	$\sim 1$	TOF - E
Solar energetic particle ionic charge analyzer	<b>SEPICA</b>	$2 \leq Z \leq 28$	$Q, Z, E$	$\sim 1$	$E / Q$ $dE/dx - E$
Electron, proton and alpha monitor	<b>EPAM</b>	H, He, $e^-$	$Z, M, E$	$\sim 0.3$	$dE/dx - E$
Solar wind ion mass spectrometer	<b>SWIMS</b>	$2 \leq Z \leq 30$	$M, E/Q$	$\sim 0.001$	$E / Q$ TOF - E
Solar wind ion composition spectrometer	<b>SWICS</b>	$2 \leq Z \leq 30$	$Z, E$	$\sim 0.001$	$E / Q$ TOF - E
Solar wind electron, proton and alpha monitor	<b>SWEPAM</b>	H, He, $e^-$	$E/Q$ dist.	$\sim 0.001$	$E / Q$
Magnetometer	<b>MAG</b>	B	$B_x, B_y, B_z$		Triaxial fluxgate

**Table 3.5** ACE instrumentation and their measurement properties where  $E$  = energy,  $M$  = mass,  $Z$  = nuclear charge,  $Q$  = ionic charge,  $B$  = magnetic field (Adapted from Stone *et al.*, 1998).

As this thesis is primarily concerned with the solar wind velocities and densities the SWEPAM instrument is used as it provides real-time and readily available. The SWEPAM experiment provides the ACE spacecraft with the majority of the solar wind observations providing three dimension

observations of electron and ion distribution functions allowing the determination of the bulk flow and kinetic properties of the solar wind (McComas *et al.*, 1998). The SWEPAM experiment was originally designed and used on the *Ulysses* mission as part of the Solar Wind Over the Poles of the Sun (SWOOPS) (Bame *et al.*, 1992) and due to its success was selected and refurbished for the ACE mission (McComas *et al.*, 1998).

	<b>SWEPAM-I</b>	<b>SWEPAM-E</b>
<b>Particle species</b>	3-D protons and alphas	3-D electrons
<b>Energy range</b>	260 eV/q – 36 keV/q	1.6 eV – 1350 eV
<b>Energy resolution <math>\Delta E/E</math> (FWHM)</b>	5% (2.5% at 128s resolution)	12 %
<b>Polar angle FOV</b>	(-)25° to 65°	21°
<b>Time resolution</b>	64 s	64 s

**Table 3.6** Summary of the SWEPAM instrument capabilities (adapted from McComas *et al.*, 1998).

The SWEPAM experiment is a combination of two instruments, the Solar Wind Ion Instrument (SWEPAM-I) and the Solar Wind Electron Instrument (SWEPAM-E). Ions and electrons are able to enter the instruments through apertures and then enter spherical section electrostatic analyzers (ESA). The particle is able to enter a narrow gap between two ESA plates for which the inside plate is charged to oppose the charge of the particle which bias the analyzers so that only suitable particles are analyzed. For SWEPAM-I these are ions within 5% energy per charge range and for SWEPAM-E these are electrons within 12% range of energies. Immediately following the ESA are channel electron multipliers (McComas *et al.*, 1998). A summary of the two SWEPAM instrument capabilities is given in table 3.6.

### 3.2.5 Wind

The *Wind* spacecraft was launched in November 1994 and entered a halo orbit around the L1 (Lagrangian) point, approximately 1.5 million km ahead of the Earth. Similar to the ACE spacecraft, *Wind* is able to observe the solar wind ahead of its arrival at the Earth giving an advanced warning and measurements of the solar wind which will impact the Earth's magnetosphere. The instruments onboard *Wind* are capable of measuring the plasma and fields around the spacecraft and the energetic particles and radio waves *in-situ* of the solar wind.

The Solar Wind Experiment (SWE) onboard the *Wind* spacecraft capable of performing 3-D *in-situ* measurements of the velocities, densities and temperatures of solar wind ions. SWE consists of two Faraday cup (FC) sensors, vector electron and ion spectrometer (VEIS), a strahl sensor, and onboard calibrator. The instruments are controlled by a data processing unit (DPU) which receives commands and interprets them to control the SWE individual instruments. For this thesis the FC and VEIS subsystems are used to determine ion and electron properties. The range and precision of the SWE instrument is given in table 3.7.

<b>Parameter</b>	<b>Range</b>	<b>Precision</b>
<b>Proton velocity (3-D)</b>	200 – 1250 km s <sup>-1</sup>	± 3%
<b>Proton number density</b>	0.1 – 200/ cc	± 10%
<b>Thermal speed</b>	0 – 200 km s <sup>-1</sup>	± 10%
<b>Alpha/ proton number density ration (x 100)</b>	0 – 100%	± 10%

**Table 3.7** Observable parameters of the SWE instrument (adapted from Ogilvie *et al.*, 1993).

The Faraday cup subsystems determine the ion distribution functions and basic flow parameters. The two FC sensors are formed of a cup a set of planar grids and two semi-circular collector plates. The solar wind enters the cup system and arrives at the collector plates where the corresponding electric current due to the positively charged ion is measured. A time-varying positive potential is applied to a highly-transparent metal grid which limits a portion of the charged particle flux to 200 Hz. This allows the system to identify the incoming charged particles from the photoelectric current produced by sunlight and calculate the energy of the incoming charged ions (Ogilvie *et al.*, 1993).

The vector electron and ion spectrometer (VEIS) is used to determine the ion and electron distribution functions over the energy/ charge range of 7 V to 24.8 kV. The VEIS consists of two identical groups of three electrostatic analyzers which deflects the particles through 127° in a cylindrically-symmetric electric field. The electric field charge alternates to measure ions and electrons sequentially. The analyzers of the VEIS of have a field of view of 7.5° x 6.5° allowing the system to obtain 3-D coverage the particle distributions (Ogilvie *et al.*, 1993).

# Chapter 4

## Analysis Methods

Due to the high number of data sources used within this thesis, a significant amount of data-processing techniques have been applied throughout this work. These techniques include: the handling of raw radio signal data received at the EISCAT and LOFAR antenna systems used to determine IPS; image data handling to improve the visualization of solar events and structures with running difference imaging; NRGF filtering and the separation of CMEs from quiescent corona; and methods to form associations between the different data types with the mapping of IPS onto images observed by the STEREO HIs. This chapter is concerned with the explanation and theory of each of these techniques applied within this thesis.

### 4.1 IPS Analysis Package

The radio signals received by each of the radio antennas of the EISCAT and LOFAR systems must be properly analysed to remove background noise and filter the signals so that they may be time matched with other systems where suitable baselines exist. Upon time matching, the received signals of each receiver antenna are then processed and both the auto- and cross-correlation functions are produced in order to determine any common features in the radio signal. Any time lag between the signals of the receivers may be used to calculate any outflow velocity(ies) since the determined time lag provides the solar wind velocity estimation between the two ray paths. The IPS analysis package was written and developed for use by the Aberystwyth University (originally University of Wales, Aberystwyth) IPS group by R.A. Fallows (Fallows, 2001), advancing on work by Grall (1995), Coles (1996) and KlingleSmith (1997), and later updated again and used by Fallows *et al.* (2008), Dorrian *et al.* (2010), and Fallows *et al.* (2013).

It should be noted that Aberystwyth University, and also this thesis, adopts the J2000 coordinate system for its source naming convention. This coordinate system uses the Equatorial Coordinate System (right ascension and declination) based on the position of the vernal equinox at the time of the J2000.0 Julian epoch i.e. 1 January 2000 at 12:00 Terrestrial Time (TT), thus the coordinates are

given the prefix J. Where available in this thesis, common naming and catalogue identities are also provided.

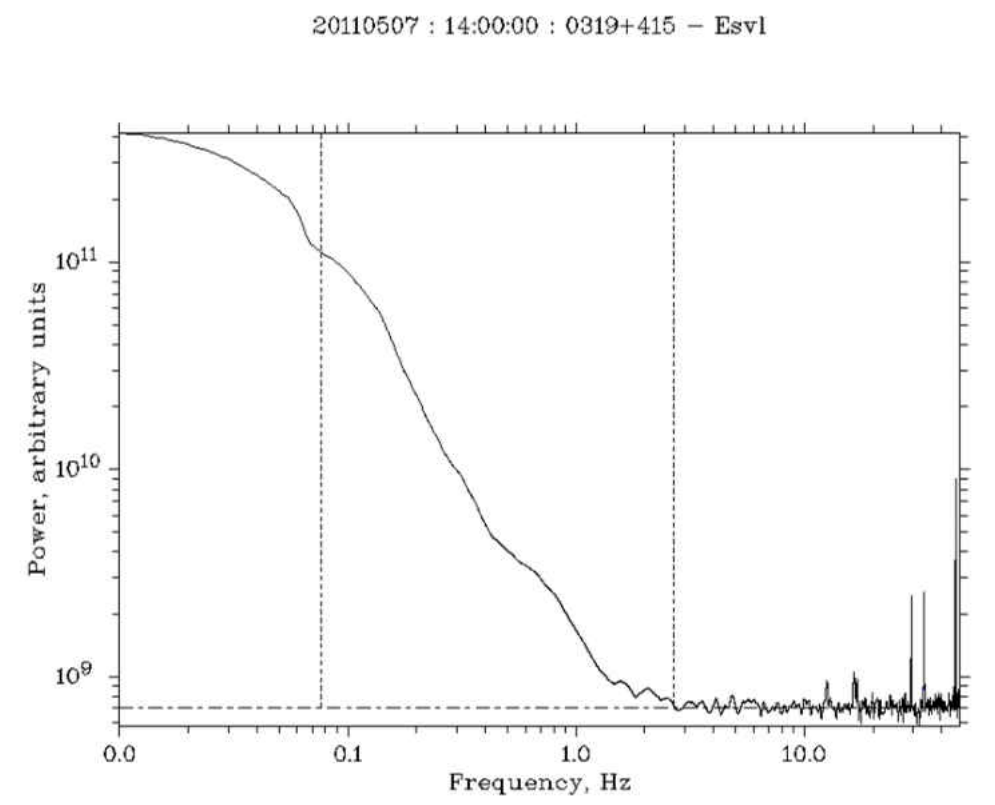


**Figure 4.1** Power spectrum of an IPS observation from the EISCAT Svalbard radar observed at 500 MHz with a 10 MHz bandwidth starting at 14:00:00 UT on 7 May 2011 for a 15-minute observation of radio source J0319+415. The horizontal dashed line indicates the noise floor applied in the system and the dotted lines at  $\sim 0.08$  Hz and  $\sim 1.8$  Hz are the positions of high- and low-pass filters, respectively (from Fallows, 2011).

Before the radio signals are analysed they are separated into intervals, generally 10 or 15 minutes in length, which will undergo integration. A longer integration interval will provide the analysis with a more averaged signal allowing a stronger correlation between antennas signals. This however may also cause small/fast changes in velocity or tracers of multiple streams to become smoothed, reducing the resolution of the cross-correlation. A sliding window technique is then applied to advance the integration by a user define step size until the entire observational period has been covered. For the purpose of this thesis the sliding window step size has commonly been 3 minutes. Cross-correlation is applied to each of the integration intervals and thus velocity estimations are

determined for each interval. Throughout this thesis the start time of the interval has been used to define each integration interval.

The radio signals received at the radio antennas are initially contaminated with some noise from many local sources such as system-temperature variations of the receiver system, internal system interference, atmospheric effects, and man-made radio interference from mobile phones, television, radio, *etc...* The total noise of the system can be described as the sum of the background noise, receiver variation, and the IPS spectra as shown in equation 4.1 (Bisi, 2006).

$$Total\ Noise = Receiver\ Variation \left( \frac{1}{f} \right) + IPS\ (Scintillation\ Spectra) \quad (4.1)$$

The first stage of the analysis is to remove this noise from the received signal. Often the noise will appear in the radio signal as spikes which can be simply trimmed; however, data sections may be filled with large amounts of noise and these may be clipped out of the signal completely. The clipped data sections are filled with an average of data from either side of the clipped region provided the data section does not exceed one second; sections exceeding one second will be rejected (Fallows, 2011).

The second stage of the analysis performs a fast Fourier transform on the signal to determine the power spectrum of the data. A noise floor limits the power spectrum at low power where the power spectrum begins to level off into the region of “white noise”. A sample of white noise taken from 25 Hz to 40 Hz is used to subtract from the band-pass filtered data in order to remove the white noise which is present at all frequencies (Fallows, 2001).

A frequency dependent high-pass filter is applied to remove low frequency  $\frac{1}{f}$  noise. For 928 MHz and 1420 MHz observations this filter will be between 0.05 Hz to 0.25 Hz (Bisi, 2006) The position of this high pass filter this can vary depending on observing frequency since ionospheric contamination of the signal becomes more dominant at higher frequencies the lower you go in observing frequency and so the high-pass filter needs adjusting accordingly to compensate for this so that it is still removed prior to the CCF part of the analyses. Great care must be taken when choosing this filter. If the high-pass filter is set too low, then slow-moving irregularities may be filtered out of the system which may remove important data (Fallows, 2001; Bisi, 2006; Fallows, 2011). A low-pass filter is also applied to the higher frequencies where the signal comes down to approximately two standard deviations ( $\sigma$ ) above the background-noise level so as to maintain an adequate S/N ratio for the entire part of the IPS spectrum used. A typical low-pass filter will be applied between 1.00 Hz and 20.00 Hz (Bisi, 2006) depending on the strength of the scintillation and the observing frequency.

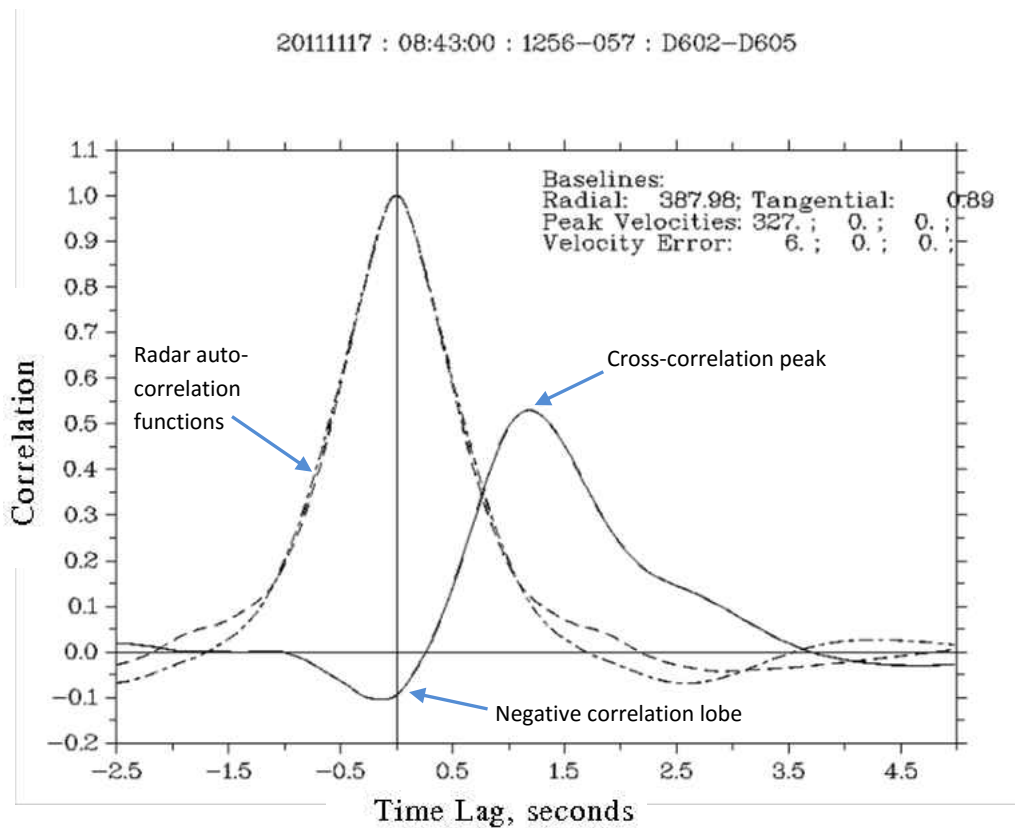


**Figure 4.2** Example cross-correlation function (solid line) of an observation of the J1256-057 radio source by the Garching (D602) and Jülich (D605) LOFAR sites at 08:43 UT on 17 November 2011. The experiment observes a CME (indicated by the negative lobe and very strong correlation strength) crossing the IPS ray path with a radial velocity of  $327 \text{ km s}^{-1}$ . The auto-correlation functions for the radars are also given in this plot as dashed lines (from Bisi *et al.*, 2014).

As the received radio signals have been defined by the filters, suitable baselines which may provide cross-correlation between the two signals must now be determined. These baselines must have a maximum off-radial angle of  $10^\circ$  for cross-correlation to be successful (Fallows, 2011). A successful cross-correlation between the received signals of the selected baseline will result in the plot of the cross-correlation function against time to show any latency between similar signals which have been observed between the two antennas. The cross-correlation function will show a peak or possibly multiple peaks in the correlation strength at the time lags between any correlated signal features which are approximations of the perpendicular component of outflow velocity crossing the line of sight. Provided an extremely long baseline has been used for the observation, up to three peaks may be resolved by the system and each of the peak velocities can be determined from the time lags at which these peaks occur (Grall, 1995; Breen *et al.*, 1996b; Fallows, 2001; Bisi, 2006).

## 4.2 Analysis Techniques of HI Observations

The Heliospheric Imagers (HIs) aboard the twin STEREO spacecraft have come to be extensively used for observing the heliosphere; as such, a large number of analysis and imaging techniques have been developed for use with the HI data. The analysis techniques are primarily used to determine locations and properties of observed transients as they propagate through the heliosphere. Techniques such as running-difference imaging also provide better visualization of dynamic structures in the heliosphere which previously may have been very faint. The techniques applied to these data used in this thesis are thus discussed in this section.

### 4.2.1 Difference Imaging

Heliospheric imager and coronagraph images will often contain very dynamical features such as CMEs. However, these features may be difficult to resolve against the background quiescent streamers or other stable noise such as background star fields. Using running-difference imaging the dynamical features can become distinguishable against any unwanted quiescent background. Difference imaging is performed by subtracting the target image from an image taken prior as showing in equation 4.2 (from Shih, 2010).

$$D = I_C - I_R \quad (4.2)$$

Where:

$D$  = The final differenced image,

$I_C$  = The target (or current) image,

and  $I_R$  = The reference (or previous) image.

Dynamic features being observed will have changed their position in the newer image relative to the previous reference image whereas the quiescent structures will not have changed. Difference imaging subtracts the bright features in the reference image from the frame of the target image which leaves bright features at the locations where there had been no previous feature. Conversely there are darker regions where there had previously been a bright structure but is no longer present in the target image. As CMEs are not point like, the difference-imaging technique may only accurately resolve the CME front as trailing plasma structure also has brightness and will cause

overlapping between the target and reference images (Shih, 2010). An example of a difference image is given in figure 4.3 along with the original images used in its developments.

Running-difference imaging is very susceptible to erroneous data and artefacts in the reference image and these can produce further erroneous features in the difference images produced using this reference image. For running-difference imaging to be feasible the reference and target images must be taken in the same frame, thus the ever moving frame of the STEREO HIs due to the orbit of the spacecraft must first be corrected to share a matching reference frame *i.e.* an image taken from the same position.

#### **4.2.2 IPS P-point mapping**

Without the high-resolution, white-light views of the inner heliosphere produced by the STEREO HI instruments, it would be difficult to determine the global structure of a feature observed using the IPS technique at all scales because of the finite view of the IPS technique (although several tomographic techniques work around this in many ways *e.g.* Bisi *et al.*, 2010(b) and references therein). However, in turn, the HIs cannot observe the much smaller-scale structure contained in the large transient features that are easily seen in the white-light imagery. A combination of the two observational techniques allows a far-more-detailed analysis of solar-wind structures to be performed, covering both the large-scale structure and the small-scale internal structure of transient features.

To perform a combined observation of IPS and STEREO HI, it is possible to determine the location of the point of closest approach of the IPS line of sight to the Sun, the IPS P-point, within the HIs fields of view, which can be projected onto the white light imagery. The first step in this process is to determine a common heliocentric coordinate system, *e.g.* Heliocentric Aries Ecliptic (HAE). The positions of the Sun, observing spacecraft, and the Earth (the location of the radio telescope) can be found easily in this coordinate system. Within this coordinate system the IPS line of sight can also be determined converting its coordinates from Geocentric Equatorial Inertial (GEI) coordinates. Since the IPS line of sight and the location of the Sun are known, it is relatively simple to determine the point of closest approach of the IPS line of sight to the Sun; however, this must then be projected into the HI field of view to determine which pixel in the HI image contains the IPS P-point.

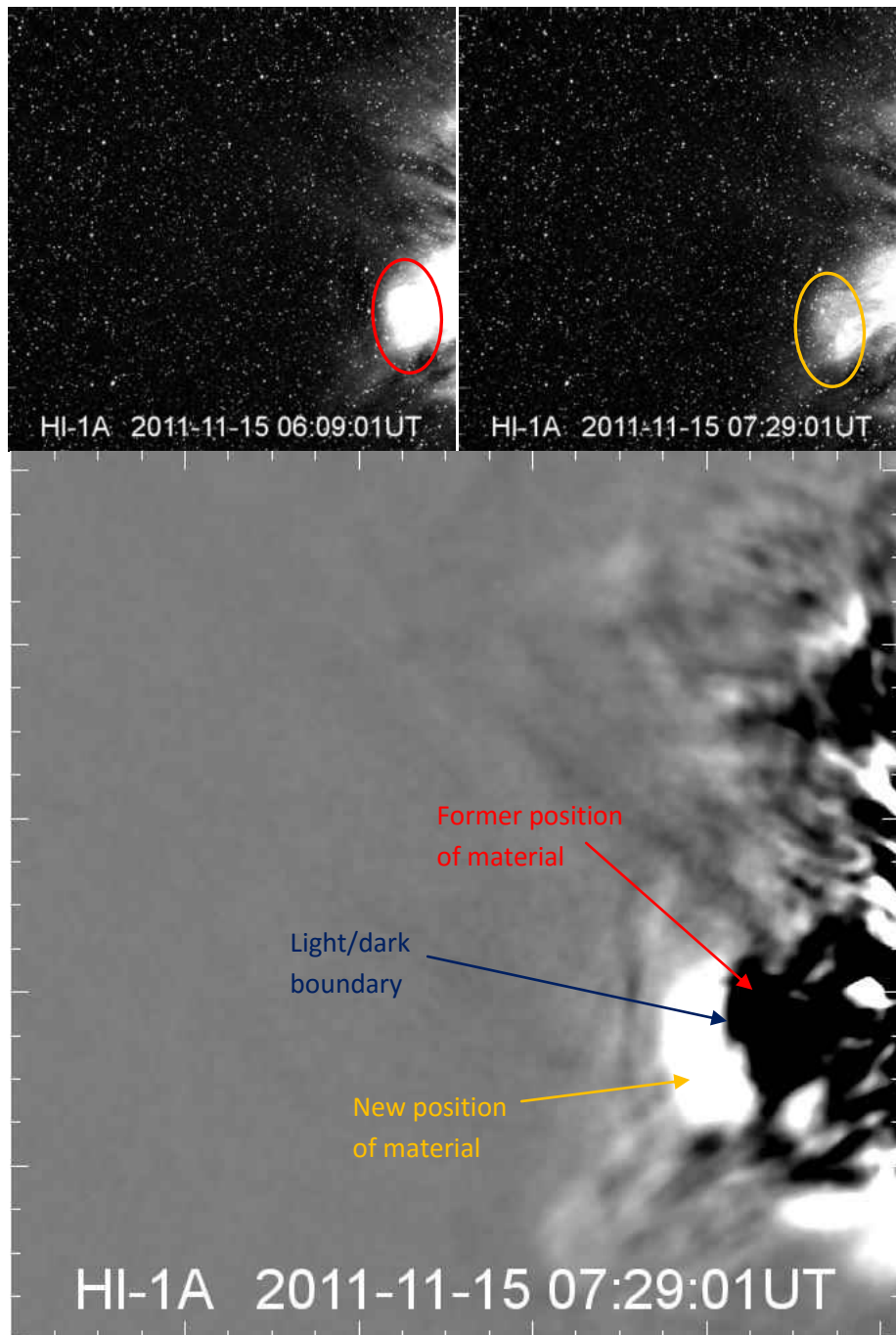


**Figure 4.3** Upper panels: STEREO HI-1A Images of a CME event observed by STEREO on 15 November 2011 taken at 06:09 UT (left) and 07:29 UT. The position of the leading CME material is circled in red for location the earlier image and yellow for the later image. Lower panel: HI-1A difference image between the HI-1A images presented in the upper panels. The material that had been circled in red is no longer present at its former position in the later image and has thus formed a dark region in the difference image. This material has thus moved into the position circled in yellow which formally had a low intensity and thus has formed a bright region in the difference image. This light-dark boundary is often used as a trace line for a CME in images such as J-maps.



By knowing the heliographic latitude of the IPS P-point ( $L_p$ ), the x and y components can be found using equations 4.3 and 4.4.

$$P_x = a \sin(90 - |L_p|) \quad (4.3)$$

$$P_y = |a| \sin L_p \quad (4.4)$$

The above equations are the first estimates of  $P_x$  and  $P_y$  as would be calculated if STEREO were collocated with the Earth. A number of corrections must be considered however to correctly determine the distance of the P' from the Sun,  $a'$ .

Corrections that must be applied introduce rotation of the 2D vector [ $P_x$ ,  $P_y$ ]. These corrections correct for the STEREO spacecraft roll; and the apparent orientation of the Sun's rotation axis as seen from the STEREO spacecraft. A final correction involves the displacement of STEREO from the Earth. This displacement correction changes  $P_x$  and allows equation 4.5 to become valid. For details regarding these corrections Dorrian (2009) should be referenced. After applying these corrections  $P_x$  and  $P_y$  thus become  $P'_x$  and  $P'_y$  respectively. With the corrections applied Pythagoras' Theorem can thus be applied to determine  $a'$  with equation 4.5.

$$a' = \sqrt{(P_x'^2 + P_y'^2)} \quad (4.5)$$

Now that the distance of the P' from Sun centre is known, the angle between P' and the Sun anchored at STEREO can be calculated by equation 4.6.

$$A = \sin^{-1}\left(\frac{a'}{b}\right) \quad (4.6)$$

The final component of the STEREO, Sun, and P' plane can now be derived, and this is the distance of P' from the STEREO spacecraft. Again this is performed simply using Pythagoras' Theorem as equation 4.7.

$$c' = \sqrt{(b^2 - a'^2)} \quad (4.7)$$

The distance to the IPS P-point from the spacecraft can be determined as a final value from the geometry in figure 4.4 and is given by equation 4.8.

$$c = \sqrt{b^2 - a'^2} + \sqrt{a^2 - a'^2} \quad (4.8)$$

All of the geometric components of the STEREO-IPS systems have now been determined, including the precise HAE coordinates of the point at which the IPS P-point appears in the HI frame. The `get_pprime.pro` program written by Brown performs the above calculations to determine HAE coordinate location of  $P'$ . This point can now be projected onto the HI image. The pointing information of each STEREO HI image is imbedded into the data file of the image and is thus easily extracted. Knowing this information the pixel which contains the required coordinates can be determined using prebuilt programs designed for use with STEREO. It should be noted that due to the extensive software package available for STEREO it is relatively simple to convert between heliospheric coordinate systems e.g. HAE, Heliocentric Earth Ecliptic (HEE), Carrington, Helioprojective Cartesian (HPC) etc.

### 4.2.3 Time-elongation Maps

An effective method of tracking CMEs and other bright dynamic features, which may propagate from the Sun out into interplanetary space, involves plotting a latitudinal path of interest of against time. Time-elongation maps provide an automated method for tracking the outflow or inflows of coronal and heliospheric features and also allow the velocities and accelerations of the features to be determined. This technique was originally developed to observe and track streamer flows in SOHO|LASCO imagery, however, CMEs were also highly visible and very distinct features (Sheeley *et al.*, 1999).

Transients that propagate across the field of view of a stationary camera will appear to accelerate and decelerate depending on the direction at which it is travelling and will thus show a deflection in the time-elongation plot which can be tracked while assuming a constant velocity. With the combination of STEREO|SECCHI coronagraphs and heliospheric imagers, a combined field of view extending beyond  $80^\circ$  in elongation from the Sun-spacecraft line is available, allowing transient structures to be tracked from the lower corona at  $1.4 R_\odot$  (COR1 inner field of view) to beyond 1 AU (HI-2 outer field of view). Within a time-elongation plot, transients may be visible for several days, thus a large bright transient (not moving too quickly) may be accurately tracked to high elongations.

Development of this geometric concept has produced three primary methodologies for determining the properties of visible transient structure seen in STEREO|SECCHI: namely, fixed  $\phi$  ( $F\phi$ ) fitting (Sheeley *et al.*, 2008; Rouillard *et al.*, 2008), harmonic mean (HM) fitting (Lugaz, 2010; Möstl *et al.*, 2011), and self-similar expansion (SSE) fitting (Davies *et al.*, 2012; 2013). The concepts of these models are discussed in the sub-sections following.

#### 4.2.3.1 Fixed Phi Model

Assuming that the CME travels at a constant velocity it can be determined from the apparent properties of; acceleration; velocity; and the direction at which the CME is travelling. Figure 4.5 demonstrates how an event propagating (signified by the red arrow) across the field of view of the HIs, while at first reducing its distance from STEREO until passing the centre of the field of view when the distance begins to increase. The result of this effect means that the event will spend different amounts of time in each pixel and will appear to accelerate as it approaches the centre of the field of view followed by a deceleration as it propagates away from this point. The apparent accelerations can be tracked in the time-elongation maps which can then be used to reveal the velocity and direction of propagation (Sheeley *et al.*, 1999).

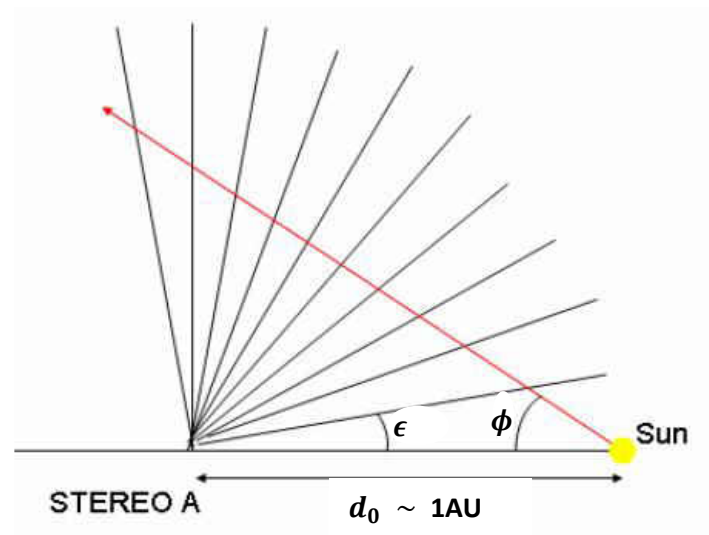


**Figure 4.5** Apparent acceleration of a CME as it propagates, at the angle  $\phi$  relative to STEREO through the HI field of view with apparent elongation  $\epsilon$  (adapted from Davis *et al.*, 2008).

The fixed  $\phi$  (F $\phi$ ) fitting method is the simplest of the three fitting methods and assumes that the transient front is propagating radially through the field of view of the camera with a point-like cross section as demonstrated by the red arrow of figure 4.5. As the CME propagates at an longitude  $\phi$  relative to the observer, the observer will see the CME propagate through the lines of sight (lines emanating from the observer at the STEREO A point in figure 4.5) at the angle  $\epsilon$ . It was thus derived by Sheeley *et al.* (1999), that the radial distance ( $R_{FP}$ ) of a point-like transient propagating with a longitude  $\phi$  relative to the observer, at a distance  $d_0$  from the Sun, observing along an elongation  $\epsilon$  at time  $t$  is given by equation 4.9.

$$R_{FP}(t) = \frac{d_0 \sin \epsilon(t)}{\sin(\epsilon(t) + \phi)} \quad (4.9)$$

Under F $\phi$  conditions of constant velocity  $V_{FP}$  and direction  $\phi$ , the distance  $R_{FP}$  may be replaced with  $V_{FP}t$  (Möstl *et al.*, 2011; Davies *et al.*, 2012). Sheeley *et al.* (2008) and Rouillard *et al.* (2008) thus derived that under the FPF assumptions the transient front will propagate with the elongation variation may be expressed as equation 4.10.

$$\epsilon(t) = \tan^{-1} \left( \frac{V_{FP}t \sin(\phi)}{d_0 - V_{FP}t \cos(\phi)} \right) \quad (4.10)$$

The FPF model has proved that it is efficient to determine the elongations of transients which are very narrow such as very small CME events and small scale plasma blobs such as those observed by Rouillard *et al.* (2008; 2009) and Sheeley *et al.* (2008).

#### 4.2.3.2 Harmonic Mean Model

The harmonic mean (HM) model uses the approximation that the transient cross section is an expanding circle, centred in the direction  $\phi$  to the observer, which is anchored to the centre of the Sun at a point along its circumference. Lugaz *et al.* (2009) develop the HM fitting technique which defines the transient front as the expanding front of the circle circumference. The radial distance  $R_{HM}$  is thus determined at the point of the expanding circle with the greatest distance from the Sun and expressed by Möstl *et al.* (2011) as equation 4.11.

$$R_{HM}(t) = \frac{2 d_0 \sin[\epsilon(t)]}{1 + \sin[\epsilon(t) + \phi]} \quad (4.11)$$

Möstl *et al.* (2011) adapted the original derivation for the elongation variation function, by Lugaz *et al.* (2009), for which the adaption has been employ within this thesis. Similarly to the F $\phi$  technique, the radial distance  $R_{HM}$  can be replace with the term  $V_{HM}t$  and also two new expressions are defined, which are given in equations 4.12 and 4.13.

$$a = \frac{2d_0}{V_{FP}t} - \cos \phi \quad ; \quad \text{and} \quad b = \sin \phi \quad (4.12)$$

Resulting in the elongation function (equation 4.13)

$$\epsilon(t) = \cos^{-1} \left( \frac{-b + a \sqrt{a^2 + b^2 - 1}}{a^2 + b^2} \right) \quad (4.13)$$

Due to its design of using an expanding circle as the CME front, the HM fitting model is effective for determining the transient elongations functions of wide transient features in particular large CMEs. Figure 4.6 shows an example of a radially expanding transient for which the F $\phi$  and HM fitting models have been applied. At an elongation  $\epsilon$  it is apparent that the radial distance measured by each technique varies between them and this has an increasing effect and the transient is more distant from the observer.

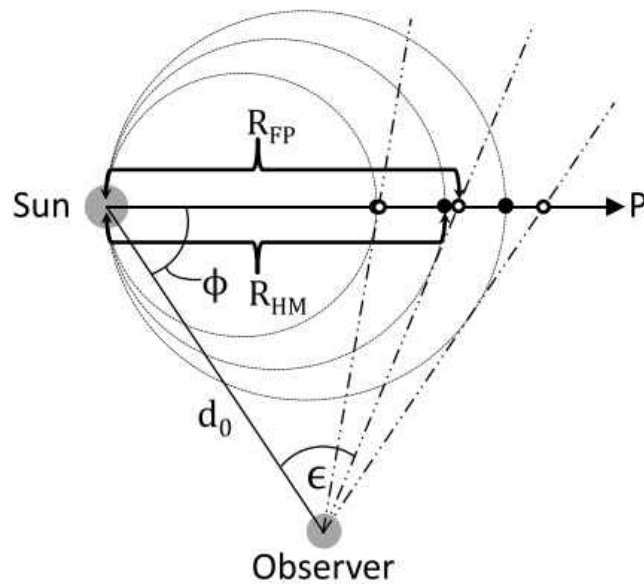


**Figure 4.6** Schematic comparison of the transient front locations for the  $F\phi$  (hollowed dots) and HM (filled dots) models for a radially propagating transient with a direction  $P$  (from Davies *et al.*, 2012).

#### 4.2.3.3 Self-similar Expansion

The Self-similar expansion (SSE) model, first introduced by Lugaz *et al.* (2010) and then developed further by Davies *et al.* (2012), advances on the HM model using an expanding circle to describe the transient cross sections. The SSE model however, no longer anchors the circle to the Sun but allows the circle to propagate away from the Sun while enclosed within a fixed half width of angle  $\lambda$  with respect to the Sun. Davies *et al.* (2012) suggested that realistic values for the half width should be applied, as such the lower limit of  $\lambda = 0$  will be identical to the  $F\phi$  fitting with the transient becoming point like. Similarly the upper limit of  $\lambda = 90$  will anchor the circle at the centre of the Sun producing the solution of the HM fitting model. Thus the SSE model produced an intermediate between the  $F\phi$  and HM fitting model.

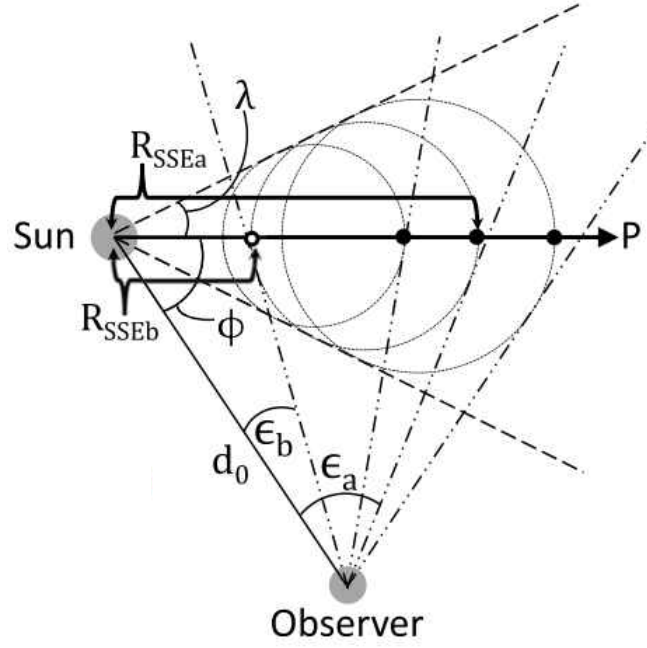


**Figure 4.7** Geometric schematic of the transient front locations for the SSE model for a radially propagating transient with a direction P (from Davies *et al.*, 2012).

For the SSE model the properties of the leading and trailing points of the expanding circle can be measured, as such the radial distances  $R_{SSEa}$  and  $R_{SSEb}$  for the transient front and trailing edge can be determined from their apparent elongations  $\epsilon_a$  and  $\epsilon_b$  using equations 4.14 and 4.15 respectively as derived by Davies *et al.* (2012).

$$R_{SSEa}(t) = \frac{d_0 \sin[\epsilon_a(t)] [1 + \sin(\lambda)]}{\sin[\epsilon_a(t) + \phi] - \sin \lambda} \quad (4.14)$$

$$R_{SSEb}(t) = \frac{d_0 \sin[\epsilon_b(t)] [1 + \sin(\lambda)]}{\sin[\epsilon_b(t) + \phi] - \sin \lambda} \quad (4.15)$$

The elongation variation functions  $\epsilon_a(t)$  and  $\epsilon_b(t)$  can be solved similarly to that of the HM method, as such they can both be described by the solution derived by Möstl *et al.* (2011) which is given in equation 4.16. When solving for the transient front,  $\epsilon_a(t)$ , the positive solution for  $c$  is to be applied and conversely for the trailing edge,  $\epsilon_b(t)$ , the negative solution is applied.

$$\epsilon(t) = \cos^{-1} \left( \frac{-b c + a \sqrt{a^2 + b^2 - c^2}}{a^2 + b^2} \right) \quad (4.16)$$

Here,  $a$ ,  $b$  and  $c$  are defined as:

$$a = \frac{d_0(1+c)}{V_{SSE}t} - \cos \phi ; \quad b = \sin \phi ; \quad \text{and} \quad c = \pm \sin \lambda_{SSE} .$$

### 4.3 The Normalizing Radial Graded Filter (NRGF)

With the SOHO|LASCO and STEREO CORs imagery, it is possible to observe two forms of solar wind structures. These two forms are time-evolving plasma structures such as CMEs and time-stationary phenomena such as streamers and/or stream/co-rotating interaction regions (SIRs/CIRs). It is highly desired to observe each of these forms independently so that the complete structures of these forms may be clearly visible without noise from the other form and also enhance the features observed. The normalizing radial graded filter (NRGF) of Morgan *et al.* (2006; 2010; 2012) enhances the coronal structures which allows the isolates the dynamic and quiescent components of a coronagraph image and produces two new images purely showing only each of these components. An example showing the separated components from a LASCO C2 image is shown in Figure 4.8.

The NRGF technique is based on the radial extent of structures in coronagraphs as such the quiescent coronal structure is radially extended and changes very slowly in time, whereas CMEs change very rapidly in time and are not extended radially. NRGF processes the latitudinal brightness profiles of the image which are normalized against the mean and standard deviation. This process removes any quantitative information from the image however the normalized image is very effective to view the coronal structure over all heights. The NRGF processed image intensity (also known as NRGF brightness) is thus determined by equation 4.17.

$$I'(r, \phi) = \frac{I(r, \phi) - I(r)_{(\phi)}}{\sigma(r)_{(\phi)}} \quad (4.17)$$

Where:

$I(r, \phi)$  = Original intensity at height  $r$  and position angle  $\phi$ ,

$I(r)_{(\phi)}$  = Mean intensity over all position angles at height  $r$ ,

and  $\sigma(r)_{(\phi)}$  = Standard deviation of intensity over all position angles at height  $r$ .

(Morgan, Habbal and Woo, 2006; Morgan, Byrne and Habbal, 2012)

The separation method developed by Morgan, Byrne and Habbal (2012) is highly dependent on the quiescent corona having very slow variation in the radial direction and CMEs having very fast variation in the radial direction. By smoothing the original signals in the time and radial dimensions the resulting image will become similar to the quiescent corona due to its slow variation compared to that of dynamic events. Subtracting this quiescent corona image from the original image reveals a new image in which the dynamic structures, such as CMEs, has been isolated. Morgan, Byrne and Habbal (2012) developed an iterative method of deconvolution, over space and time, to smooth the original image which iterates the deconvolution of the image signal as a function of radius  $r$  and time  $t$  at a position angle as the array  $X(r, t)$  to form a new background signal  $B$  at iteration number  $n$ , such as given by equation 4.18.

$$B^n = X - [(X - [B^{n-1} \otimes k]) > 0] \quad (4.18)$$

Where

$$B^0 = X,$$

and  $k =$  A Gaussian profile kernel in the radial dimension with FWHM of  $0.67 R_S$ .

(Morgan, Byrne and Habbal, 2012)

The iteration is performed until the convergence rate of the average absolute difference between the new and previous background signals passes below a set value, for which Morgan, Byrne and Habbal (2012) had selected to be  $10^{-5}$  of the maximum value of  $B^0$ . After passing this threshold, the deconvolution steps are repeated for a single iteration however, this time smoothing against the time dimension and using a sliding window kernel of three observations in width. The process is repeated over all position angles. The final CME component  $C$  can be determined by simply subtracting the smoothed quiescent structure  $B^n$  from the original signal  $X$  such as in equation 4.19,

$$C = X - B^n \quad (4.19)$$

An example of the separation technique applied to an NRGF LASCO C2 image is shown in figure 4.8. The original image (left) of figure 4.8 shows the combined quiescent and dynamic solar wind with a visible CME erupting from the Eastern solar limb and a fainter CME structure on the Western limb, which is nearly over shadowed by the quiescent solar wind streams at its location. The subsequent images of this figure show each of the separated quiescent and dynamic solar wind. In the dynamic

component (centre) the fainter CME structure of the Western limb can now be revealed as part of a possible haloing of the CME observed on the Eastern limb. The quiescent component also reveals much fainter structure which had previously been overshadowed by the intensity of the light scattered by the denser CME structure. This example thus highlights the effectiveness of the separation process in revealing the true solar wind structure.

Within this thesis this technique has been applied to retrieve both the dynamic and quiescent components. Chapter 6 makes use of the dynamic components to show a very clear image of the CME involved in the observations so that its structure may be observed free from any quiescent structures. The quiescent component of the NRGF coronagraph images are the base of chapter 7. Within chapter 7, quiescent coronal maps are used to produce a tomographic map of the corona at  $5 R_s$  which are then used to model the Parker spiral of the quiescent solar wind.

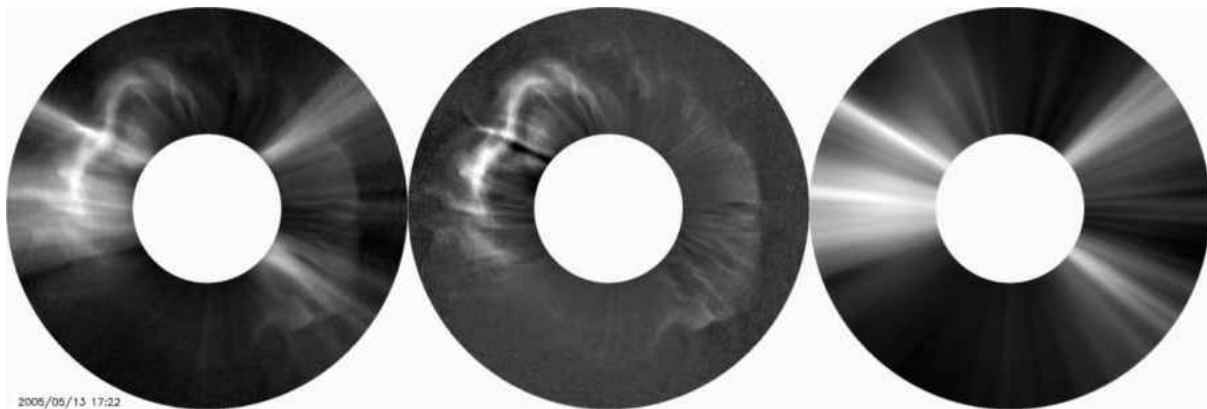


**Figure 4.8** Example images taken by LASCO C2 coronagraph with an original NRGF image (left), the separated dynamic component (centre) and quiescent corona (right) (taken from Morgan, Byrne and Habbal 2012).

# Chapter 5

## Rapid Velocity Variations in the Slow Solar Wind

A survey of a 12 month period, starting in April 2007, of the EISCAT IPS observing campaigns beginning shortly after the commencement of full science operations of the STEREO mission has been performed in a bid to identify common density structures in both EISCAT and STEREO|HI datasets. A detailed investigation and presentation of joint IPS/HI observations from four specific intervals for which the IPS P-Point was located between 60 and 90 solar radii out from the Sun's centre is discussed in detail within this chapter. The four case studies involve the IPS observations for the 23 April 2007 of radio source 0318+164 (case study 1); 19 May 2007 of radio sources 0521+166 (case study 2); and 0431+206 (case study 3); and 20 May 2007 of radio source 0521+166 (case study 4).

During the intervals of case studies 1 and 4 meso-scale (of the order of  $10^5$  km or larger) transient structures are observed by HI-1A to pass over the IPS ray path near the P-Point. The observations of IPS for these cases show rapid velocity variations occurring during the transition of the transients across the ray-path, proposing a micro-scale (of the order  $10^2$  km) structure contained within the meso-scale transients. The two IPS observations of case studies 2 and 3 revealed similar micro-scale velocity changes, however, no related transient structures were detected by the HIs during that period due to limitations of the spatial resolutions of the HIs. Each of these case studies are discussed in detail within this chapter. The works in this chapter extend upon those present by Hardwick *et al.* (2013).

### 5.1 Complementary Nature of IPS and the STEREO HIs

The STEREO HIs observe a large region of interplanetary space which is approximately centred on the ecliptic plane. Fortunately for IPS, this covers a region of the sky where there are numerous

strong astronomical radio sources that can be used for observations of IPS. The Right Ascension/Declination (RA/Dec) coverage of each of the HIs varies through the year with the motion of the two spacecraft around the Sun (as detailed in chapter 3). As such, a fixed point in RA/Dec will move roughly horizontally at a rate of around 1 pixel between consecutive HI-1 or HI-2 images, hence the projection of the IPS P-Point onto the two-dimensional (2-D) sky plane will also move between adjacent HI images.

The HI-1 cameras are effective in observing K-CORONAL features at a scale-size larger than around  $1.6 \times 10^5$  km (corresponding to a feature approximately 20 pixels wide at 0.5 AU from the spacecraft), with a cadence of 40 minutes (the HIs may also be effective to observe bright single pixel features such as stars). In comparison, observations of IPS can provide information on the much more rapid (of the order of seconds) and smaller-scale ( $1 \times 10^4$  km or less) variations in velocity, density, and inferred changes in magnetic-field orientation. The structure of a solar transient drifting across the IPS ray path will be observed in greater resolution (dependent on IPS observing frequency) with its fine structure being revealed when compared to the HIs; the latter may observe the larger bulk flow of the transient as it travels through the inner heliosphere. Thus, the IPS and HI methods provide highly-complementary information on the solar wind over a range of spatial and temporal scales, with the former providing information on the micro-scale physics of solar transients and the latter providing the larger-scale contextual information.

Previous studies of the slow solar wind have revealed that it is possibly made up of blob-like small-scale structures. From observations of the streamer belt, made by Sheeley *et al.* (2009) using the STEREO HIs, small-scale blobs were revealed to exist in the slow solar wind, formed through the disconnection of streamers. These blobs and their relation to the slow solar wind are discussed in chapter 1.

Studies by Dorrian *et al.* (2008; 2010) presented observations of transient structures in the slow solar wind over a range of spatial scales. The transient structures observed by Dorrian *et al.* (2008; 2010) in both HI and IPS were classified into three groups as determined by their scale size and this nomenclature has also been retained in this chapter. Transient structures with a scale size of 100 km were termed as “micro-scale transients”. These micro-scale transients are the density structures that allow scintillation to occur in interplanetary space, existing in the IPS ray path for only a few seconds. Transient structures that exist in the IPS ray path for up to 30 minutes were classified as “small-scale transients”. These small-scale transients have a scale size of less than  $6 \times 10^5$  km and are found within the slow solar wind travelling with velocities typical of the slow wind. The larger “meso-scale

transient” structures are commonly observed by heliospheric imagers, with scale sizes between  $6 \times 10^5$  and  $1.2 \times 10^6$  km.

## **5.2 Observations**

Solar wind radial outflow velocity estimates (methodology described in detail within chapter 2), were performed for all available two-site EISCAT IPS observations taken in 2007 and 2008 by University of Wales, Aberystwyth (UWA) and funded by the Science & Technology Facilities Council (STFC). A sliding window technique is used, using a 15-minute integration period advanced every three minutes to provide velocity estimations by cross-correlation to determine a three-minute resolution solar wind velocity profile for each radio source observation. Table 5.1 summarises all of the IPS slow solar wind observations (wind speeds below  $650 \text{ km s}^{-1}$ ) performed during the one year sample period, showing the velocities calculated by IPS and noting any corresponding white-light features observed by the STEREO HIs. Only observations containing a single velocity stream have been used for the analysis to avoid discrepancies between two or more streams during the analysis procedure.

Due to the increasing separation of the STEREO spacecraft from Earth, the comparison between IPS and HI observations was limited to an interval early in the STEREO mission, during which the STEREO spacecrafts were separated from Earth by no more than  $25^\circ$ . During this period, the IPS ray path from Earth was closely aligned with the HI line of sight. This provides the smallest possible distance between the position of the IPS P-Point and the analogous closest point along the HI line of sight to the Sun. This also means that wherever any enhanced density features are observed by the IPS experiments it is highly likely that it will also be observed in the HIs. The strongest correlation of single-stream slow wind observation of IPS is assumed to occur at the P-Point where solar wind flow is perpendicular to the IPS line of sight. For this investigation it is reasonable to assume an association of any visible structures in STEREO HI which pass over the HI line of sight which intersects the IPS P-point.

### **5.2.1 Survey of Observations**

The observations of IPS performed within the one year time period starting on 20 April 2007 were performed in a late spring campaign in 2007 and an early spring campaign in 2008. From these

campaigns the observations which included fast solar wind streams (velocities greater than  $650 \text{ km s}^{-1}$ ) or multiple wind streams were filtered out such that only single-stream slow solar wind remained. A final filter provided observation which contained evidence of transients passing the IPS ray path i.e. negative correlation lobes – the cause of which is described in chapter 2. For each of the observations the velocity profiles have been analysed to determine the variations that occur between each sequential window to reveal any dynamic velocity structures observed by IPS. Table 5.1 shows the results of each filtered observation with its minimum, maximum and mean velocity; largest velocity change between sequential windows, average velocity variation between sequential windows over the entire observation; and any structures which may have been observed by the STEREO HIs to pass the IPS ray path at the time of the observation. Table 5.2 shows a more detailed table of information summarising the velocities, positions and features observed by the IPS experiment and HI cameras.

From the velocity profiles it was revealed that velocity variations between windows, over the course of an IPS observation, rarely diverge greatly from the observation's mean velocity variation. Within a sample of slow solar wind observations however, there are occasions (18 out of the 34 sample slow wind observations used here) where large variations in the velocity do occur at least once during the observation. We define cases with "large velocity variations" as having a maximum velocity variation (ninth column of table 5.1) more than twice the average velocity variation (shown in the eighth column of table 5.1). For five of this sub-sample of observations there are no visible HI structures which may be associated with these large velocity variations. Note that 10 of the sample IPS observations have a P-point outside the field of view (FOV) of all four of the STEREO HI cameras making analysis of meso-scale structures crossing ray path unreliable and as such are not considered to determine the scale sizes of transient structures as a source of the rapid velocity variations.

Date	Observation Start Time (UT)	Observation Length (Minutes)	Radio Source (J2000)	Baseline Antenna Systems	Largest Velocity (km s <sup>-1</sup> )	Mean Velocity (km s <sup>-1</sup> )	Mean Velocity Change (km s <sup>-1</sup> )	Largest Velocity Change (km s <sup>-1</sup> )	Observing STEREO HI Camera	P-Point Heliographic Longitude in STEREO (°)	Visible HI Event
20070420	0530	15	0204+152	Sdky-Trms	342.9	324.4	4.65	12.3	None		N/A
20070421	1515	15	0318+164	Kirn-Sdky	522.9	514.67	14.8	-14.9	HI-1A	3.541	No Visible Feature
20070422	1515	15	0318+164	Kirn-Sdky	607.5	591.12	19.4	-20.3	HI-1A	3.608	No Visible Feature
20070423	0403	42	0318+164	Kirn-Trms	600.4	492.23	16.08	-82.3	HI-1A	3.644	Transient Structure
20070424	1445	45	0318+164	Kirn-Sdky	449.3	412.2	16.73	33.8	HI-1A	3.743	Transient Structure
20070425	1430	45	0318+164	Kirn-Sdky	424.6	403.58	9.51	10.2	HI-1A	3.811	No Visible Feature
20070426	0412	33	0318+164	Kirn-Esvl	335.8	322.63	3.93	19.8	HI-1A	3.870	No Visible Feature
20070427	1500	15	0318+164	Kirn-Sdky	552.7	543.77	13.73	-18.3	HI-1A	3.953	No Visible Feature
20070429	1030	15	0137+331	Kirn-Trms	576.4	558.9	17.62	20.5	None		N/A
20070429	0345	18	0318+164	Kirn-Trms	586.4	571.09	14.17	-15.9	HI-1A	4.063	No Visible Feature
20070430	0745	15	0137+331	Sdky-Trms	635.5	622.85	14.12	-22	None		N/A
20070430	1415	15	0318+164	Kirn-Sdky	560.2	548.4	16.3	-16.6	HI-1A	4.168	No Visible Feature
20070501	0345	15	0318+164	Trms-Esvl	526.3	516.72	6.69	12.3	HI-1A	4.209	No Visible Feature
20070504	1300	15	0318+164	Kirn-Sdky	508.1	497.8	10.87	-13	HI-1A	4.462	Transient Structure
20070505	1245	15	0318+164	Kirn-Sdky	466.2	448.67	8.8	16.5	HI-1A	4.538	No Visible Feature
20070505	0845	15	0319+415	Kirn-Trms	603.8	587.58	19.53	20	None		N/A
20070505	0815	15	0323+055	Trms-Sdky	669.4	588.38	30.5	78.7	None		N/A
20070506	1215	15	0318+164	Kirn-Sdky	466	452.03	14.12	24.6	HI-1A	4.613	CME
20070507	1530	15	0318+164	Trms-Sdky	475.2	467.7	12.75	-19.3	HI-1A	4.702	Transient Structure
20070509	1403	12	0431+206	Kirn-Sdky	438.2	370.52	12.48	84.7	HI-1A	4.854	No Visible Feature
20070515	1533	12	0521+166	Trms-Sdky	419	407.88	6.82	-20.9	None		N/A
20070516	1330	15	0431+206	Kirn-Sdky	451.6	444.32	8.88	-27.7	HI-1A	5.419	Transient material before CME
20070516	1515	15	0521+166	Trms-Sdky	410	359.82	5.77	-68.2	None		N/A
20070518	0530	21	0318+164	Trms-Kirn	445.5	434.65	7.16	7.4	None		N/A
20070519	1630	18	0431+206	Trms-Sdky	343.7	298.03	6.4	89.7	HI-1A	5.682	No Visible Feature
20070519	1430	48	0521+166	Trms-Sdky	447.4	414.5	5.82	33.1	HI-1A	5.674	No Visible Feature
20070520	1415	45	0521+166	Trms-Sdky	407.2	386.2	6.6	43.1	HI-1A		CME

20080319	1315	54	0059+001	Kirn-Sdky	458	424.23	8.075	67.2	None		CME
20080320	1209	54	0059+001	Kirn-Sdky	468	450.82	8.43	-32.1	HI-1A	23.327	Transient/Stream
20080321	1203	57	2232+117	Kirn-Trms	439.6	434.57	9.7	11.6	None		N/A
20080322	1100	15	2232+117	Kirn-Trms	594.7	577.9	21.63	-61.4	None		N/A
20080323	1200	30	2232+117	Kirn-Trms	454.5	426.88	14.64	-32	None		N/A
20080323	1245	45	2232+117	Kirn-Trms	481.4	440.01	10.76	-44.3	None		N/A
20080403	0636	24	0119+084	Kirn-Esvl	359.3	346.53	4.56	-10.9	None		N/A

**Table 5.1** Results of the IPS velocity profiles for source observations throughout the campaign. The columns contained within this table (in order of left to right) show; the date on which the observation began, the start time of the observation (Universal time); the length of the observation (may have been cropped to remove errors data); the J2000 source; the antenna baseline; the largest velocity estimate over the observation; the mean observation velocity; average velocity variation between sequential windows over the observation; largest velocity variation between sequential windows over the observation; the STEREO HI in which the P-point may be projected into the FOV; heliographic longitude of the projected P-point in the STEREO HI FOV; any features observed by STEREO HI, that may pass the P-Point during the observation. Observations where HI FOV do not contain the IPS P-Point are noted as comparison not available (N/A). The EISCAT telescopes used for the observations of IPS are Tromsø (Trms), Kiruna (Kirn), Sodankylä (Sdky), and Longyearbyen Svalbard (Esvl) radars. This table is adapted from Hardwick *et al.*, 2013.

### 5.2.2 Case Study 1: 23 April 2007

The observation of IPS on 23 April 2007 was performed using the Kiruna and Tromsø EISCAT radio antennas observing the astronomical radio source J0318+164, known in the California Institute of Technology (Caltech) source catalogue (Harris and Roberts, 1960) as CTA21. Observations of IPS were performed for a 42-minute period starting at 04:03 UT (see Table 5.1). The P-Point during the observation period was located between 72.6 and 79.0 solar radii ( $R_s$ ) off the eastern solar limb (as viewed from the Earth), and corresponds to Helioprojective Cartesian (HPC) coordinates of  $-19.68^\circ$  longitude and  $-3.77^\circ$  latitude as viewed from STEREO-A, which corresponds to a location within the HI-1A FOV. At the time of the observation STEREO-A was separated from the Earth by  $3.65^\circ$ .

	Case Study 1	Case Study 2	Case Study 3	Case Study 4
<b>Date</b>	23/04/2007	19/05/2007	19/05/2007	20/05/2007
<b>Source</b>	J0318+164	J0521+166	J0431+206	J0521+166
<b>Baseline</b>	Kirn-Trms	Trms-Sdky	Trms-Sdky	Trms-Sdky
<b>IPS Features</b>	Very strong CCF	Strong CCF Negative lobe	Negative lobe	Weak CCF
<b>HI Camera</b>	HI-1A	HI-1A	HI-1A	HI-1A
<b>STEREO SA</b>	$3.65^\circ$	5.72	5.73	5.81
<b>P-Point (HPC)</b>				
<b>Longitude</b>	$-19.68^\circ$	$-22.96^\circ$	$33.4^\circ$	$32.9^\circ$
<b>Latitude</b>	$-3.77^\circ$	$-9.84^\circ$	$0.63^\circ$	$-0.9^\circ$
<b>Distance (<math>R_s</math>)</b>	72.6 - 79.0	86.2 – 97.0	42.0 – 46.6	83.0 – 93.2
<b>HI Features</b>	Large transient	Preceding CME	Preceding CME	Faint transient
<b>Mean Velocity</b>	$492 \text{ km s}^{-1}$	$415 \text{ km s}^{-1}$	$298 \text{ km s}^{-1}$	$386 \text{ km s}^{-1}$
<b>Maximum Velocity</b>	$600 \text{ km s}^{-1}$	$447 \text{ km s}^{-1}$	$344 \text{ km s}^{-1}$	$407 \text{ km s}^{-1}$
<b>Mean Vel Change</b>	$16.1 \text{ km s}^{-1}$	$5.8 \text{ km s}^{-1}$	$6.4 \text{ km s}^{-1}$	$6.6 \text{ km s}^{-1}$
<b>Max Vel Change</b>	$-82.3 \text{ km s}^{-1}$	$33.1 \text{ km s}^{-1}$	$89.7 \text{ km s}^{-1}$	$43.1 \text{ km s}^{-1}$

**Table 5.2** Summary table of the events used in the four case studies. Tables shows the case study number; date of observation; J2000 source; antenna baseline; features observed in the IPS cross-correlation function (CCF); observing HI camera; separation angle of the STEREO spacecraft from the Earth; P-point position in HPC coordinates and solar radii; features observed by the HI camera; the mean observation velocity; the largest velocity estimate over the observation; average velocity

variation between sequential windows over the observation; and the largest velocity variation between sequential windows over the observation.

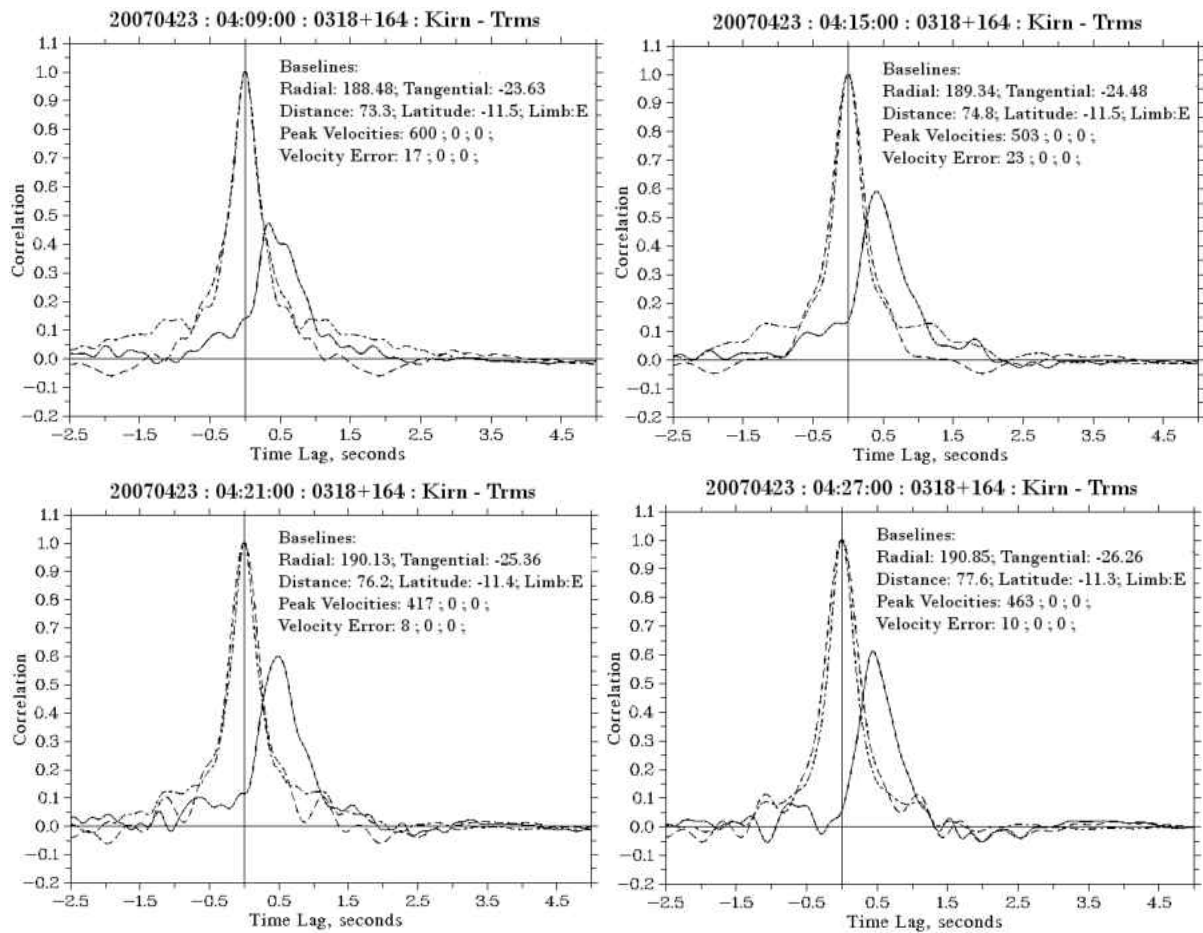


**Figure 5.1** Sample correlation functions for the observation of IPS on 23 April 2007, using the radio source J0318+164 for the times 04:09 UT, 04:15 UT, 04:21 UT, and 04:27 UT. The solid line represents the positively normalised cross-correlation function (CCF) calculated, and the dashed lines represent the auto-correlation functions for each of the radars (see chapter 4). The vertical (y axis) shows the value of the normalised correlation, and the horizontal (x axis) represents the normalised time lag, in seconds, between the correlated radio signals.

Figure 5.1 shows four sample cross- and auto-correlation functions of IPS (solid line) for the 15-minute integration periods starting at 04:09 UT, 04:15 UT, 04:21 UT, and 04:27 UT, for the 23 April 2007 case study. The observation of IPS displays an enhanced value of the cross-correlation function with levels consistently greater than over 40% for all integration periods, with correlation strengths

surpassing 50% for the majority of the observation. Observations of IPS from previous days had maximum correlations of 30% or lower. As described in chapter 2, enhancements in correlation strengths may be an indication that a region of enhanced plasma density (and hence turbulence), such as a streamer blob or larger transients, is passing across the antenna's beams. The plots in figure 5.1 show a high level of correlation, reaching a maximum value of 60% at 04:21 UT. The dashed lines in the figure represent the auto-correlation functions of the IPS signals from the individual radars, which are the inverse Fast Fourier Transform (FFT) of the radar power spectra (see chapter 4), These are used to validate the reliability of the radar showing the level of system noise and, in an ideal system, they will be Gaussian.

A time series of the estimated radial solar wind velocity over the entire interval of observation is shown in figure 5.2. The time series displayed has a resolution that is governed by the time window-increment (three minutes, from the start of each bin). The velocity of the solar wind near the P-point of the IPS line of sight increases from 04:03 UT to a peak at 04:09 UT with a velocity of  $600 \text{ km s}^{-1}$  before it reduces to  $417 \text{ km s}^{-1}$  at 04:21 UT. A slight increase in velocity occurs at 04:24 UT, increasing by  $55 \text{ km s}^{-1}$  to  $472 \text{ km s}^{-1}$ , before stabilising at a more consistent value between  $455 \text{ km s}^{-1}$  and  $463 \text{ km s}^{-1}$  after 04:27 UT. The errors shown in Figure 5.2 represent the error in the position of the peak of the cross-correlation function (Fallows, private communication).

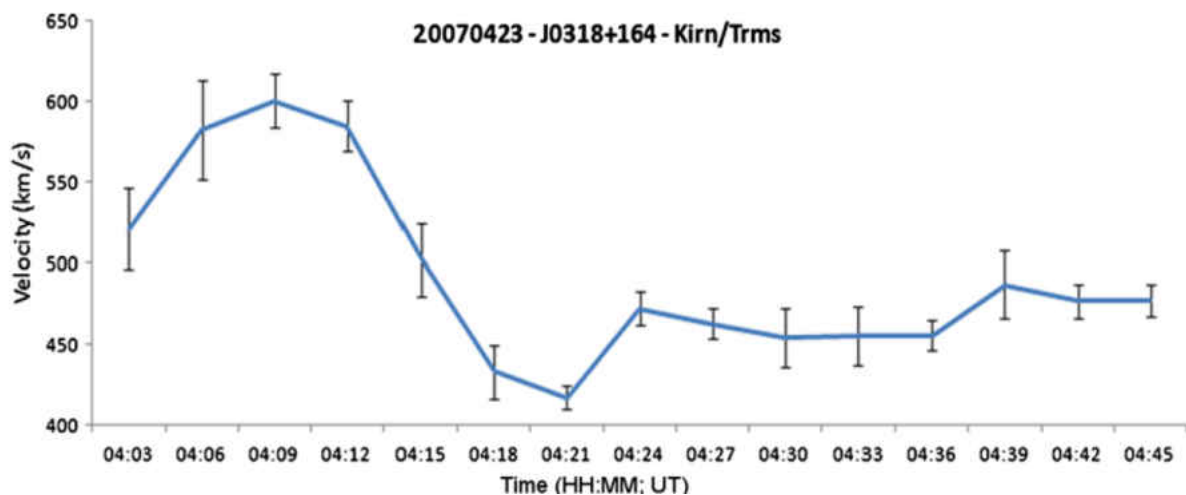


**Figure 5.2** Solar wind stream velocity estimations from the IPS observation of source J0318+164 on 23 April 2007 plotted as a function of time, for each 15-minute integration period. The error bars displayed are the errors produced when calculating the position of the peak cross-correlation function.

Combining STEREO HI imagery with the observations of IPS provides a view of the larger-scale density structures which may be associated with the velocity variations observed by IPS. The IPS P-point to source J0318+164 appears within the FOV) of the HI-1 camera on board the STEREO-A spacecraft (HI-1A), and at the start of this observation (04:03 UT on 23 April 2007) the IPS P-Point was at a heliographic longitude of 3.644°. The HI-1A instrument observed an “initially small” transient that passed over the HI line of sight that intersected the IPS P-Point during the IPS observation period. Figure 5.3 displays HI-1A difference images produced for 06:50 UT (22 April), 16:10 UT (22 April) and 04:10 UT (23 April) (see description in chapter 4). The image pixel that corresponds to the line of sight that crosses the IPS P-point is shown as a yellow cross. The transient structure observed has become faint (less dense) by the time that it approaches the HI line of sight passing through the IPS P-Point; however (assuming near plane of sky propagation), the northern edge of the structure is determined to pass over the IPS P-Point between 02:50 UT and 04:50 UT (note that the IPS observation extends from 04:03 UT until 04:50 UT). This transient is visible in difference imaging of figure 5.3, during this time period, as a slight increase in white-light intensity when compared with the preceding time frames.

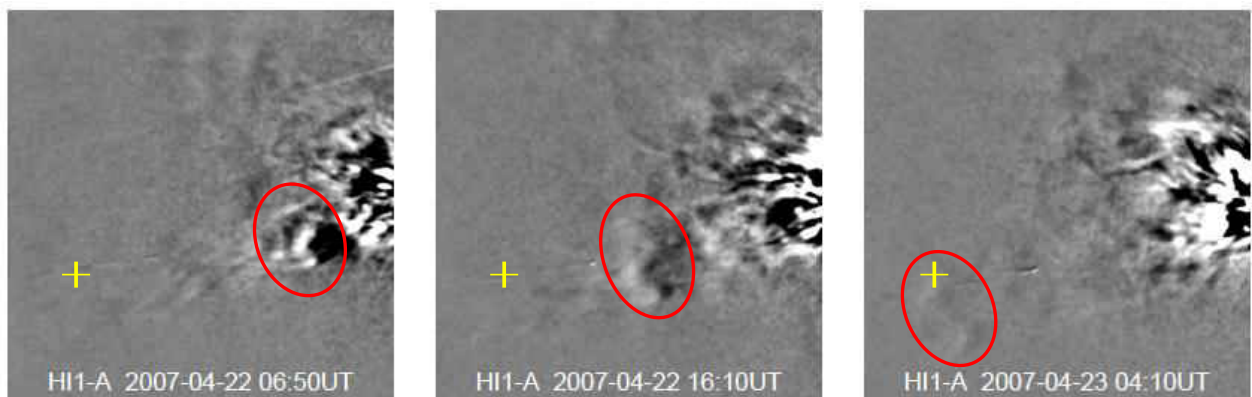


**Figure 5.3** HI-1A difference images of the transient from 22 April 2007 at 06:50 UT (left), 16:10 UT (middle) and its position during the IPS observation on 23 April 2007 at 04:10 UT (right). The observed transient structure is circled and the projected location in the HI FOV of the IPS P-Point is marked by the yellow plus sign (adapted from Hardwick *et al.*, 2013). . The time stamps of the difference images are of the final frame (latest) used in the difference imaging process (see chapter 4).

The time-elongation profile of the observed HI-1A feature was extracted from the difference J-map (see chapter 4) (through the P-point) and analysed using the fixed phi fitting method (Rouillard *et al.*, 2008), giving a propagation direction with a heliocentric Earth ecliptic (HEE) longitude of  $60^\circ$  eastward of the Sun-Earth line, which positions the feature not too far out from the plane of sky from Earth.

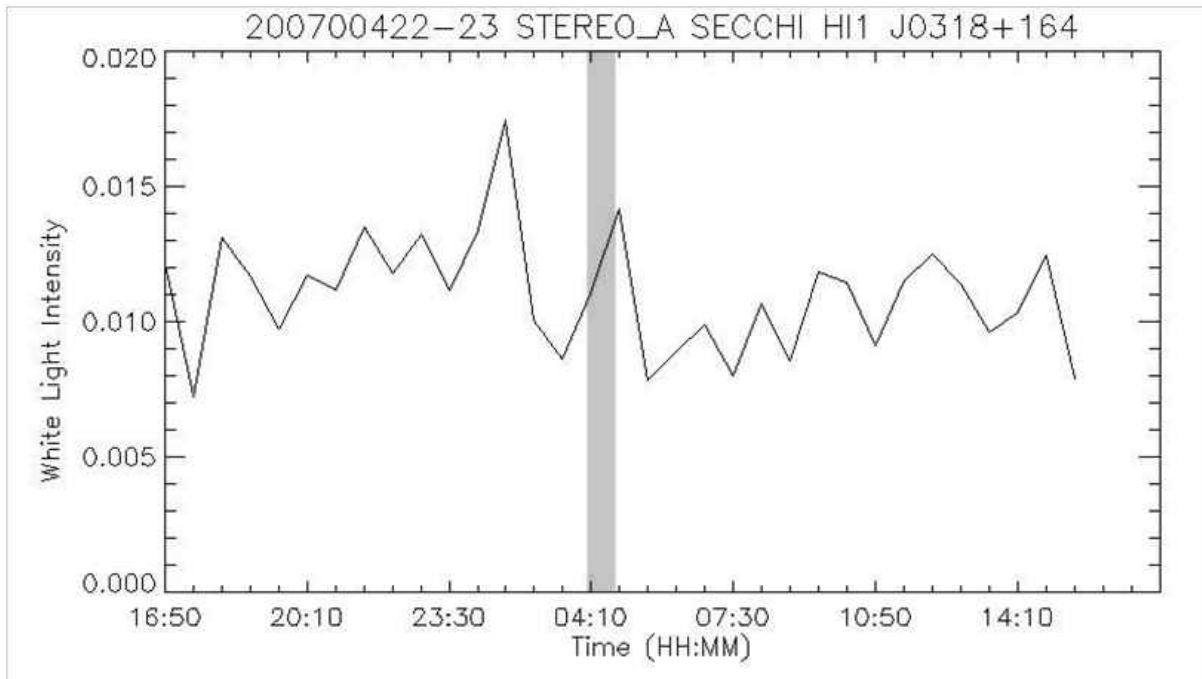


**Figure 5.4** Relative HI-1A white-light intensity observed in the 3x3 pixel neighbourhood of the P-Point, from 16:50 UT on 22 to 15:30 UT on 23 April 2007. The observation of IPS was performed between 04:03 UT and 04:45 UT and is indicated by the shaded region (from Hardwick *et al.*, 2013).

The white-light intensity time series shown in Figure 5.4 is produced from level 2 HI data provided by UK Solar System Data Centre (UKSSDC) which has undertaken steps to; filter corrupted images; orientate images to solar north; remove saturated pixel columns; de-smear images; remove pixels with unknown telemetry; apply a calibration flat field to the image; and remove background F-corona using a 1 day running window (HI processing information provided by UKSSDC). The star field is then removed from the HI images and the location of the P-point in the HI FOV is determined. The white-light intensity at this pixel is smoothed using a resistant mean with a 3x3 pixels neighbourhood and ignoring any data with a standard deviation greater than 2 from the median thus reducing the chance of random spikes and reduce noise. The intensity is displayed relative to the brightest pixel of HI image sample. This transient entered the HI-1A FOV at around 20:10 UT on 21

April 2007. The comet visible within the STEREO HI-1A images is comet Encke (2P/Encke) during its 2007 pass.

At the time of the IPS observation there is strong evidence for an outwardly-propagating structure in the HI frames. However, this feature is relatively small and too unstructured to be classified as a conventional CME but is somewhat larger than the plethora of outwardly-propagating blobs often seen imaged in the inner heliosphere (Sheeley *et al.*, 1997; Sheeley and Rouillard, 2010). The time that the transient takes to cross the IPS line of sight is much greater than the total duration of the IPS observation, therefore, the leading and trailing edge of the transient was not observed using the IPS technique. However, with IPS it is possible to observe the much smaller-scale internal structure contained within the transient itself. The internal structure of the transient is revealed by IPS to contain much variation of velocity with velocities capable of changing by over  $150 \text{ km s}^{-1}$  within a short three-minute period.

### **5.2.3 Case Study 2: 19 May 2007 (J0521+166)**

During an IPS observation on 19 May 2007 beginning at 14:30 UT and lasting for a 48-minute interval, a rapid decrease in the solar wind speed, followed by a steady increase, is observed in the data itself. However, no observable features are present in the HI-A images at this time. For this observation, the radio source J0521+166 was observed using the Tromsø and Sodankylä EISCAT radars and the P-Point was located between 86.2 and 97.0 solar radii from the Sun (centre). The HI-1A line of sight that crossed the P-Point corresponded to the HPC coordinates of  $-22.56^\circ$  longitude and  $-9.84^\circ$  latitude. At the time of the observation STEREO-A was separated from the Earth by  $5.72^\circ$ . The radio source J0521+166 can also be identified in the Third Cambridge Catalogue of Radio Sources – 3CRR (Laing, Riley and Longair, 1983) as source 3C138.

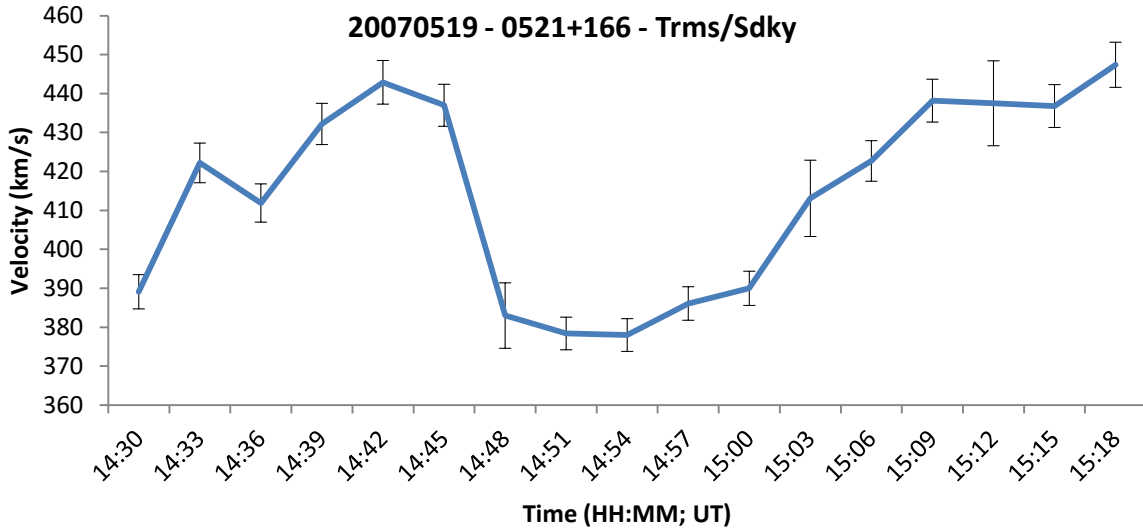


**Figure 5.5** Solar wind stream velocity estimations from the IPS observation of source J0521+166 on 19 May 2007 plotted as a function of time, for each 15-minute integration period. The error bars displayed are the errors produced when calculating the position of the peak cross-correlation function (from Hardwick *et al.*, 2013).

The time series of the velocities, calculated for each sliding window of the IPS observation, is shown in figure 5.5. The initial slow-wind velocities, estimated from the IPS cross correlations, show a steady increase between 14:30 UT and 14:45 UT followed by, between 14:45 UT and 14:48 UT, a sudden fall in the velocity from  $437 \text{ km s}^{-1}$  down to  $383 \text{ km s}^{-1}$ , a very rapid decrease of  $54 \text{ km s}^{-1}$  within a three minute interval. Subsequently there is a slow increase in the velocity, over an interval 12 minutes after which the velocity begins to increase at a faster rate until to a value near to that observed before the decrease. As with figure 5.2, the error bars displayed in figure 5.5 are the errors associated with determining the position of the peak in the cross-correlation function.

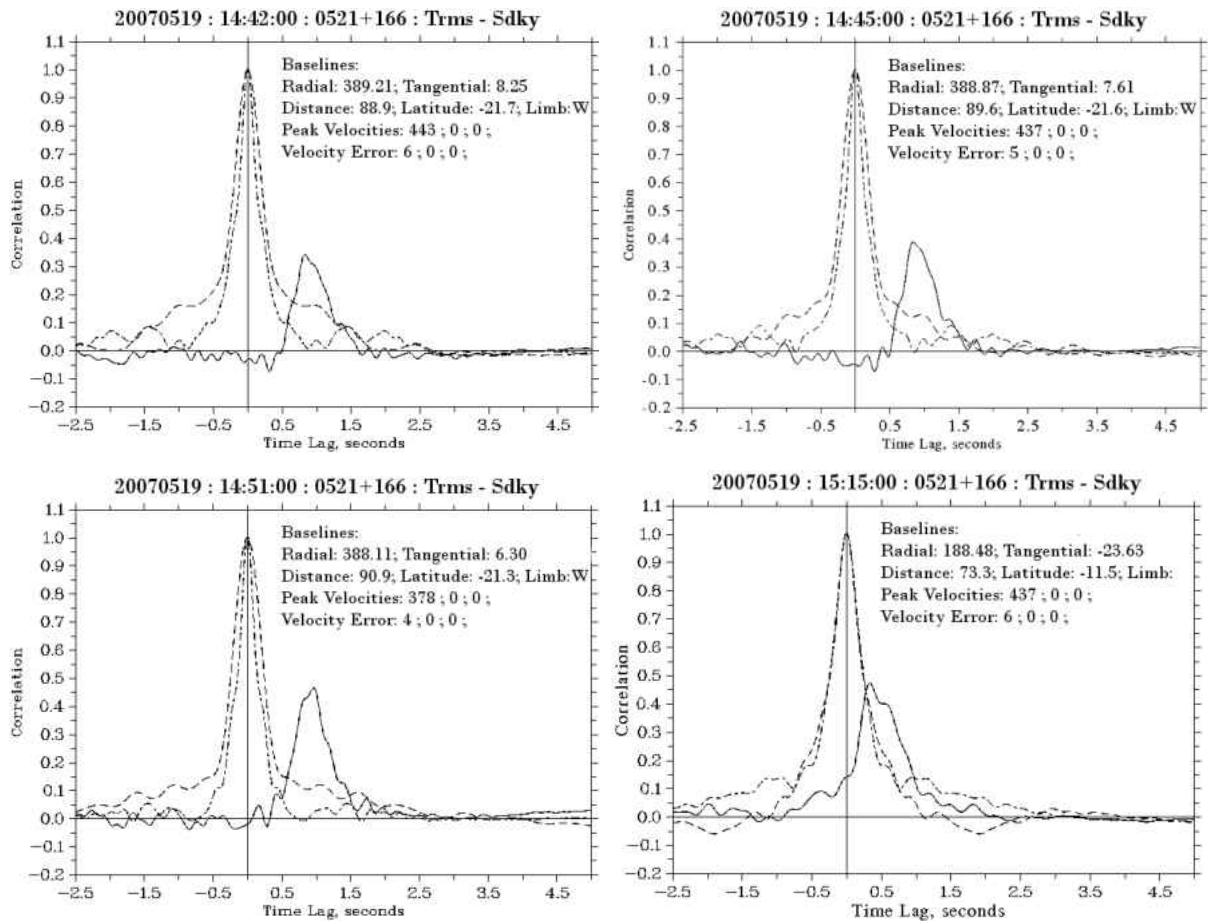


**Figure 5.6** Cross- and auto-correlation functions for the observations of IPS performed on 19 May 2007 at 14:42 UT, 14:45 UT, 14:51 UT, and 15:15 UT of the J0521+166 radio source. The axis and notations are as in figure 5.1.

Cross-correlation (solid line) and auto-correlation (dotted line) plots for the 15 minute bins starting at 14:42 UT, 14:45 UT, 14:51 UT, and 15:15 UT are displayed in Figure 5.6. The cross-correlation is very slightly enhanced between 14:45 UT and 15:09 UT, which covers the period of time at which there is a temporary reduction in the estimated velocity.

With the STEREO-A spacecraft located at a HEE longitude of  $5.674^\circ$ , and latitude of  $-1.43$ , and the J0521+166 source located towards the western solar limb as viewed from Earth, the P-Point for this observation is projected into the HI-1A FOV. Figure 5.7 shows a time series of the intensity of white light observed at this P-Point as a function of time from 00:10 to 23:30 UT on 19 May 2007. The white-light intensity displays a reduction between 12:50 UT and 16:50 UT, a period that includes the observations of IPS. The lower-intensity region implies that the density near the P-Point has decreased in that period, counter to what would be expected with the presence of a slow-wind

transient. The HI features that are responsible for the “high” intensity regions either side of the IPS period are two small unrelated transients. This leads to a proposal of the occurrence of slow, with velocities between  $350 \text{ km s}^{-1}$  and  $450 \text{ km s}^{-1}$ , small-scale ‘blobular’ structures forming in low density solar wind regions.

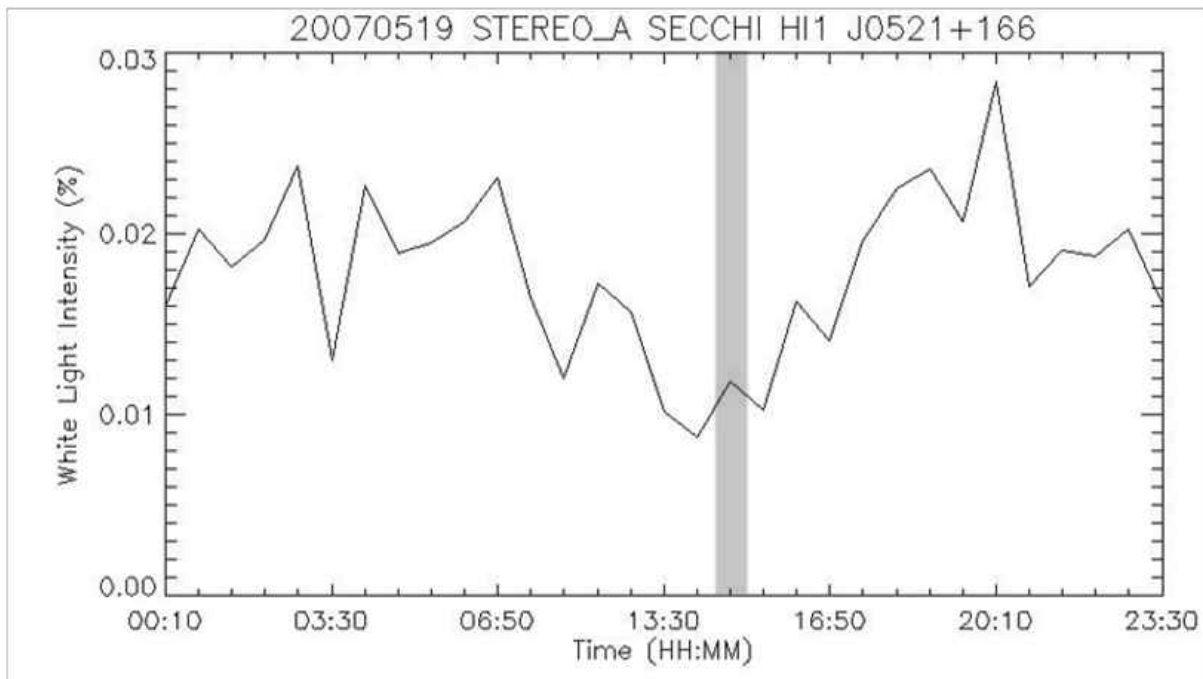


**Figure 5.7** White-light intensity as observed by HI-1A integrated along the line of sight that intersects the P-Point for the 19 May 2007 observation of IPS. The details can be found in the text. The observation of IPS was performed between 14:30 UT and 15:15 UT and is indicated by the shaded region.

Two small CME events traversed the lines of sight of the radio antennas several hours before the IPS experiment, which may have swept up the majority of heliospheric density structures around the P-Point. This could allow the evacuation of a lower-density rarefaction region, possibly disturbed as a result and even containing ‘blobular’ remnants of the CMEs. Additional information regarding the observed CMEs, such as event velocities, propagation directions, and estimated launch times, are taken from the RAL HI Event List (<http://www.stereo.rl.ac.uk/HIEventList.html>).

Event 66 launched: 2007-05-17T21:05:04.020  
 Speed: 418 km/s Angle from Earth: -37 degrees  
 Predicted arrival at 1 AU: 2007-05-22T01:37:54.011  
 Observed with HI-A

Event 65 launched: 2007-05-17T22:13:21.932  
 Speed: 644 km/s Angle from Earth: -99 degrees  
 Predicted arrival at 1 AU: 2007-05-20T15:29:05.186  
 Observed with HI-A

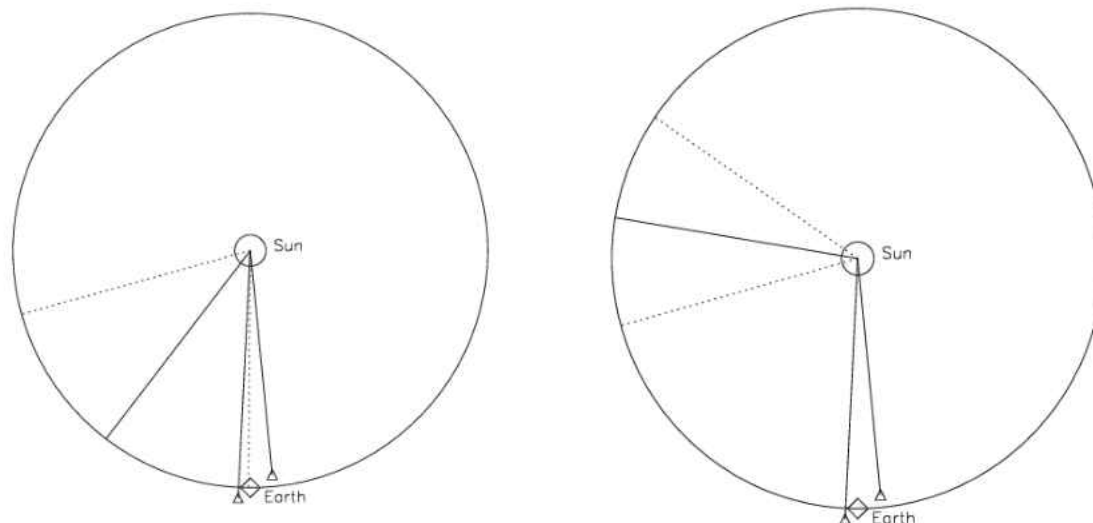


**Figure 5.8** Illustration of CME events launched on 17 May 2007 at 21:05 UT (left) and 22:13 UT (right), showing the trajectories of the CME events in the ecliptic plane. The triangles indicate the locations of the STEREO-A and STEREO-B spacecraft, with the solid lines indicating the Sun-spacecraft line. The dotted lines indicate possible estimates the feature's boundaries. Images produced by RAL for the RAL HI Event List located at <http://www.stereo.rl.ac.uk/HIEventList.html>.

The events were observed by the HI-1A instrument, with the first event (event number 66 of the HI Event List) estimated to have been launched at 21:05 UT on 17 May with a velocity of  $418.0 \pm 85.0 \text{ km s}^{-1}$  at an angle of  $-37.4^\circ \pm 37.0^\circ$  from Earth. The second faster event (event 65) is estimated to have been launched on 17 May at 22:13 UT with a velocity of  $644.0 \pm 226.0 \text{ km s}^{-1}$  at an angle of  $-99.4 \pm 25.0^\circ$  from the Earth. Parameters of the CME propagation were estimated from the analysis of the CME's time-elongation profiles using the fixed-phi fitting technique (Möstl *et al.*, 2011). The time-elongation profiles of events that form part of the RAL HI Event List were extracted manually from ecliptic time-elongation maps (commonly called J-maps) and their production are detailed within chapter 4. The CMEs would have passed through the IPS lines of sight (had the antennas been observing the radio source J0521+166 at this time) between 23:30 UT (18 May 2007) and 06:50 UT (19 May 2007). Figure 5.8 illustrates the trajectories of the CME events observed on the eastern solar limb, viewed in the ecliptic plane.

### 5.2.4 Case Study 3: 19 May 2007 (J0431+206)

An IPS experiment later on the same day as that chosen for case study 2 (19 May 2007), exhibited a smaller variation in the solar wind velocity than was observed in case study 2. An 18-minute observation, between 16:30 UT and 16:48 UT, observed the radio source J0431+206 using the EISCAT radio antennas in Tromsø and Sodankylä. Figure 5.9 displays the velocities obtained from analysis of the IPS cross-correlation functions throughout the observation. The observation begins with a fairly constant velocity until between 16:39 UT and 16:42 UT, where the estimated velocity increased by  $89.7 \text{ km s}^{-1}$ , from  $254.0 \text{ km s}^{-1}$  to  $343.7 \text{ km s}^{-1}$ , within a three-minute period. The velocity remains at the increased level for the remainder of the observation. The P-Point for the observation of the J0431+206 radio source is located at HEE co-ordinates of  $33.4^\circ$  longitude,  $0.63^\circ$  latitude, and at a radial distance of  $42.0 R_S$  to  $46.6 R_S$ .

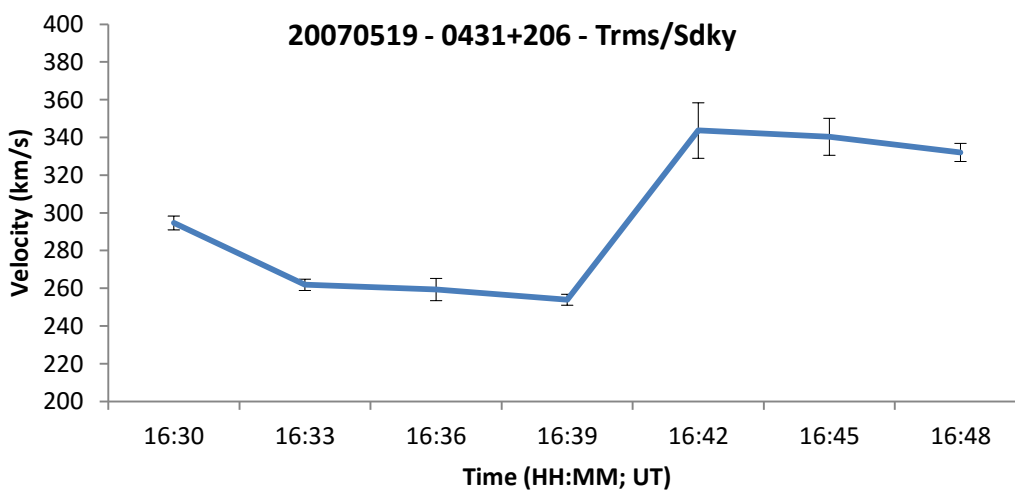


**Figure 5.9** Solar wind stream velocity estimations from the IPS observation of source J0431+206 on 19 May 2007 plotted as a function of time, for each 15-minute integration period. The error bars displayed are the errors produced when calculating the position of the peak cross-correlation function.

Similar to case study 2 there are no apparent features on the western solar limb while observed by STEREO HI and the position of the CME events launched on 17 May at 21:05 UT and 22:13 UT, as displayed in figure 5.7, does not extend out to the P-Point of the observation at any point during the IPS experiment.

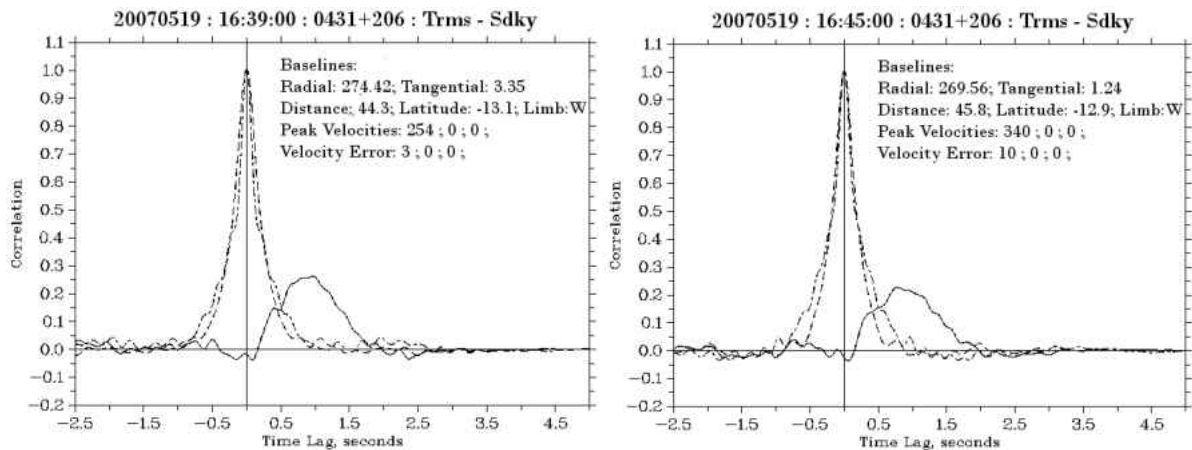


**Figure 5.10** Cross-correlation functions for the observations of IPS performed on 19 May 2007 at 16:39 UT and 16:45 UT of the J0431+206 radio source. The axis and notations are as in figure 5.1.

Sample correlation functions for this observation are given in figure 5.10. The cross-correlation functions for this observation show no enhancement in the correlation strength of the observation relative to observations of IPS on surrounding days; however, there is a very-small negative lobe throughout the IPS observation indicating a small rotation in the magnetic field between the observing radar ray paths, thus there is partial evidence within the IPS observation for a transient structures crossing the line of sight of the radars during the IPS experiment of J0431+206 run on 19 May 2007. The velocity variation observed in figure 5.9 implies that a faster transient feature may enter into the IPS line of sight at 16:42, contrary to the IPS cross-correlation functions which suggest that there may be a permanent transient feature throughout the observation. No apparent white-light feature is observed within the HI-1A telescope along the line of sight that intersects the IPS P-Point at the time of the observation. These observations lead to the proposal that a small-scale transient, which is not visible to the HI telescopes, is traversing the IPS line of sight during the observation period and within this transient is a more complex velocity structure which may cause very rapid velocity variations as with case study 2.

Observations by HI-1A show that the same CME that may have left a disturbed heliosphere in case study 2 also passes across the antenna ray paths for J0431+206 ahead of the IPS experiment. Thus this observation provides further evidence supporting the possibility of small-scale 'blobular' structures forming in slow low density regions, as suggested by the second case. This third case study showing a rapid increase in velocity in a short three-minute time period also suggests that

these structures may have more complex structures contained within them, which can only be observed with the high resolution of IPS.

### 5.2.5 Case Study 4: 20 May 2007

The observations of IPS on 20 May 2007 were performed using the Tromsø and Sodankylä EISCAT radio antennas observing the astronomical radio source J0521+166. Observations of IPS were performed for a 45-minute period starting at 14:15 UT and lasting until 15:00 UT (see Table 5.1). Due to “overly-noisy” auto-correlations towards the end of this observation the analysis has been limited to finish at 14:51 UT. The initial velocity estimations are consistent with very little variation in velocity until 14:36 when there is a rapid increase from  $364.1 \text{ km s}^{-1}$  to  $407.2 \text{ km s}^{-1}$  within the three-minute sliding window. Following this increase, the velocity estimates slowly decrease at a more regular rate and returning to velocities close to that was formally observed before the rapid increase. The P-Point during the observation period was located between  $83.0$  to  $93.2 R_S$  on the western solar limb, with HEE coordinates of  $32.9^\circ$  longitude and  $-0.9^\circ$  latitude.

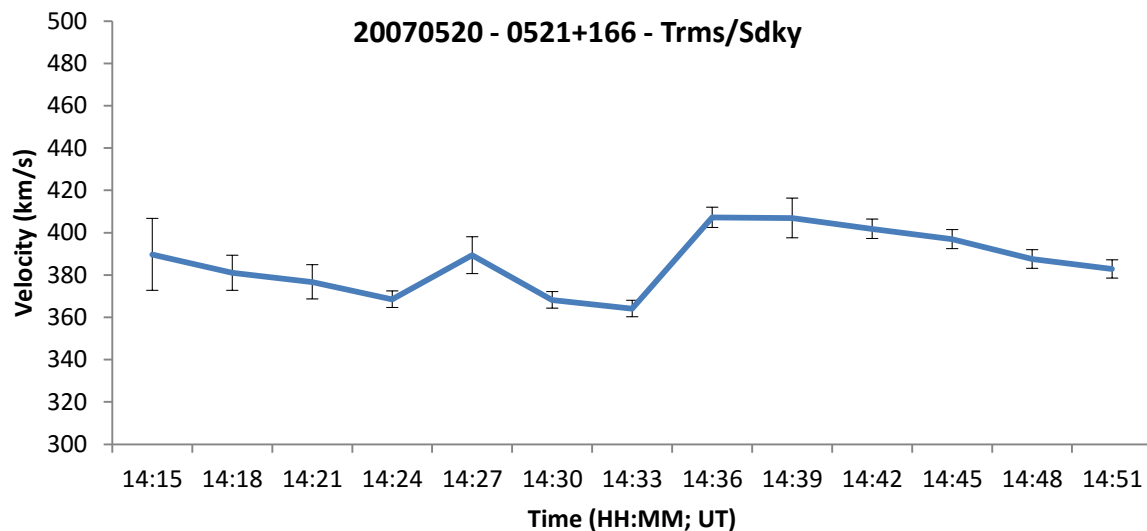


**Figure 5.11** Solar wind stream velocity estimations from the IPS observation of source J0318+164 on 23 April 2007 plotted as a function of time, for each 15-minute integration period. The error bars displayed are the errors produced when calculating the position of the peak cross-correlation function.

From the cross-correlation functions shown in figure 5.12 it is apparent that, at the time of the rapid velocity variation, there is an increase in the maximum relative correlation strength from approximately 0.15 to 0.25. This increased correlation is evidence that there may have been an increase in the density along the IPS line of sight. Following the rapid velocity change, the degree of correlation and the velocity slowly reduce back to their previous values.

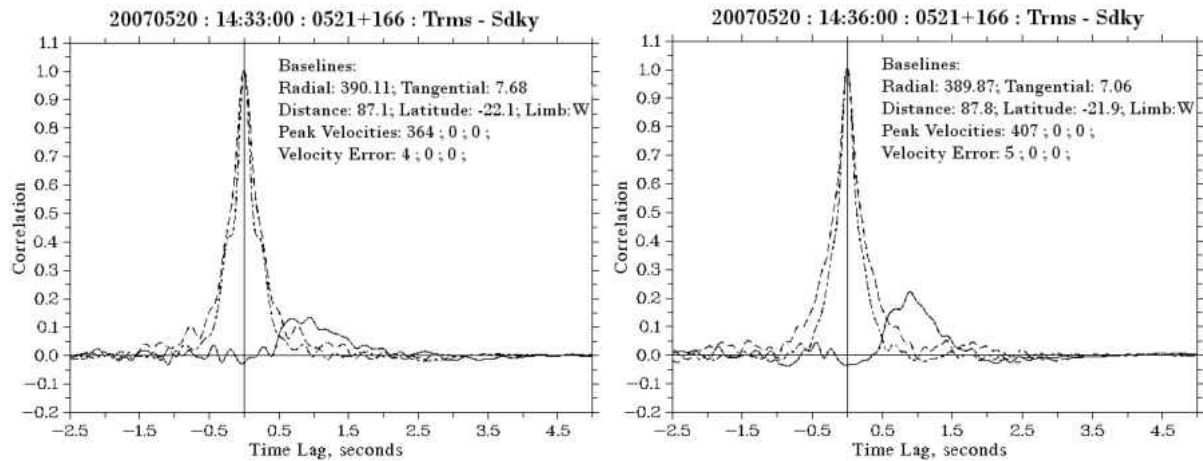


**Figure 5.12** Cross-correlation functions for the observations of IPS performed on 20 May 2007 at 14:33 UT and 14:36 UT of the 0521+166 radio source. The axis and notations are as in figure 5.1.

A transient passed over the P-Point during the entirety of the IPS observation. Figure 5.13 shows the HI difference images of the transient observed on 20 May 2007 at 02:50 UT, and its position “near the start and end” of the IPS observation at 14:10 UT and 14:50 UT (time of current image). This transient that crosses the HI line of sight that intersects the P-point is faint in the HI and requires a high contrast difference image to be clearly visible against the background solar wind. It is likely that the transient is moderately low (however greater than the surrounding solar wind), a plausible reason why the cross-correlation strength is not enhanced and is moderately low density. The IPS observation suggests that a regime change in the velocity and density, with an increase in each of these parameters, occurring at 14:46 UT. The HIs show that the IPS P-Point remains within the same transient structure throughout suggesting that it is unlikely velocity variation is due to the observed transient leaving the IPS ray path. Similarly to the event observed on 23 April 2007, this case suggests that the transient contains a smaller-scale internal structure

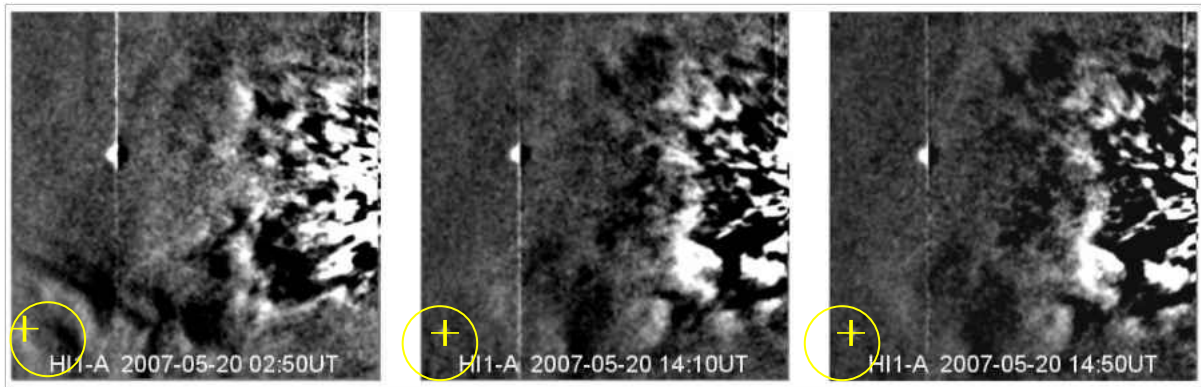


**Figure 5.13** HI-1A difference images of the transient observed on 20 May 2007 at 02:50 UT (left), 14:10 UT (centre) and 14:50 UT (right). The observed transient structure is circled and the projected location in the HI FOV of the IPS P-Point is marked by the yellow cross.

### 5.3 Conclusions

Without the high-resolution, white-light views of the inner heliosphere produced by the STEREO HI instruments, it would be difficult to determine the larger-scale structure of a feature observed using the IPS technique at all scales because of the finite view of the IPS technique (although several tomographic techniques work around this in many ways; see Bisi *et al.*, 2010b and references therein). However, in turn, the HIs cannot observe the much smaller scale structure contained in the large transient features that are easily seen in the white-light imagery. A combination of the two observational techniques allows a far-more-detailed analysis of solar-wind structures to be performed, covering both the large-scale structure and the small-scale internal structure of transient features.

Velocity determinations from observations of IPS using EISCAT performed throughout 2007 and 2008 revealed rapid variations in the slow solar wind. These observations of IPS were compared to white-light observations made using the STEREO HIs to reveal that the rapid velocity variations often correlated with the existence of transient plasma density structures passing over the IPS lines of sight. On twelve occasions, no visible structures were observed by HI to pass the IPS lines of sight (HI observations which do not have an intersecting line of sight to the P-point are excluded). However, the rapid velocity variations associated with the transient-like structures were still observed by the IPS technique.

Four events of rapid velocity variations were selected for detailed analysis to determine the causes of the variations observed. The first case study selected was an IPS experiment performed on 23

April 2007 of the source J0318+164. This experiment observed velocity variations of up to  $82 \text{ km s}^{-1}$  while HI displayed evidence of a high density feature crossing the IPS ray path. The transition of a large transient structure was visible in the HI-1A camera throughout the experiment. The second case study involved the observation of source J0521+166 on 19 May 2007. For this observation the IPS displayed strong evidence that a transient or CME is passing over the ray path during the observation. The observations by the STEREO HIs did not show any evidence of a transient crossing the IPS ray path however. A third observation of the source J0431+206 showed similar features as that of case study 2 however, observing along a different line of sight. The fourth and final case study observed the source J0521+166 on 20 May 2007. For case study 4 there was little evidence of any transient features in the IPS ray path however, the observation still detected a rapid velocity variation in the slow solar wind.

Any density variations associated with rapid velocity variations observed by IPS within the transient were not observed by HI due to the 40-minute cadence of HI-1. HI cannot 'detect' such velocity variations on smaller time scales than this cadence. However, the three-minute time resolution of IPS analysis used here revealed the small scale internal structure of the transient observed on 23 April (case study 1). Separate to the transient's bulk velocity, there is a large amount of variation of velocity within the transient structure itself. The bulk velocity of a transient can be estimated using, for example, the fixed-phi fitting method for the HIs. For the transient within this case study, the velocity of the transient is revealed to be  $350 \text{ km s}^{-1}$ .

An increase in velocity, followed by a rapid decrease, is found in two of the studied events (case 1 and case 2). However, only one of these events (case study 1) is associated with features seen in HI. . For case study 2, a similar pattern is observed but with a smaller velocity decrease over a shorter time scale. In this case, no white-light feature could be observed in the HI imagery. This is believed to be due to the transient structure being too small in spatial scale, given the cadence or pixel size limits of the HIs, to be observed, but it can be observed using IPS due to its greater sensitivity to smaller-scale features and its higher time resolution.

In this chapter, evidence is presented for a blobby slow solar wind, constructed of many small-scale transients. This suggests that the slow solar wind may be produced by multiple sources, such as many small or micro-scale transient events occurring frequently over the Sun, rather than a constant and quiescent stream input. When observing the micro-scale structure contained within the slow solar wind (case studies 2 and 3), we see velocity patterns similar to that observed for the micro-scale internal structure of a transient (case studies 1 and 4). This implies that even if transients aren't visible in the HIs due to its spatial resolution, it is likely that there are still transient structures

present with much smaller scale-sizes. This also raises the question as to what a CME and the slow wind really are, and whether the two are just different scales of the same phenomena?

Blobs in the slow solar wind were first introduced in chapter 1. Studies by Sheeley *et al.* (1997; 2008; 2009), Wang *et al.* (1998), Rouillard *et al.* (2008; 2009) and Kilpau *et al.* (2009) showed observational evidence of small flux rope blobs contained within the slow solar wind and even suggest that these blobs are from what the slow solar wind is formed. From the results presented within this chapter, we propose further evidence to this theory and that these blobs form a micro-scale structure of the slow solar wind. This micro-scale structure gives rise to a turbulent composition that may cause the rapid velocity variations as the differing velocity profiles of the blobs are encountered.

Numerous studies have been performed which have suggested that the slow wind is made up of small transient blobs as suggested within this chapter and Hardwick *et al.* (2013).

To answer this, much more detailed work will need to be accomplished, and some of this may be possible in the coming years with the positioning of the STEREO spacecraft now going to the opposite side of the Sun, mirroring their earlier positions near Earth earlier in the mission and now looking back along the IPS lines of sight from their opposite end.

# Chapter 6

## Multi-technique Remote-sensing

### Observations and Modelling of a CME

#### – The First CME Observed with LOFAR

Coronal Mass ejections (CMEs) occur frequently on the Sun especially at times of high solar activity. These events can be massive and can have a strong influence on the Earth's magnetic field under certain conditions. Modern developments in radio telescopes which may be used for IPS, and the increasing number of spacecraft located in the heliosphere, mean that numerous sources of data are available to observe and track CMEs as they propagate deep into space.

##### 6.1 Preliminary Observation

A CME was first observed by SOHO|LASCO C2 on 14 November 2011 at 20:24:05 UT which appeared to have been ejected in a south-west direction with a plane-of-sky velocity of approximately  $630 \text{ km s}^{-1}$ . Preliminary calculations by the SOHO|LASCO CDAW Catalogue initially estimated the central position angle (PA) of the CME, as measured counter-clockwise from Solar North, to be  $179^\circ$ . The catalogue also had a calculated linear speed for this CME of  $792 \text{ km s}^{-1}$ , with a second-order speed at its final height (last observation before leaving the field of view of LASCO) calculated as  $810 \text{ km s}^{-1}$  and its second-order speed at  $20 R_\odot$  (Solar Radii) to be  $807 \text{ km s}^{-1}$ , with all values calculated at a position angle (PA) of  $179^\circ$ . The coronal image processing (CORIMP) CME catalogue, of the University of Hawaii, also detected the CME. CORIMP first detected the CME at 20:36:05 on 14 November 2011, and determined the central PA at  $200^\circ$ . The maximum velocity of the CME was measured to  $765 \text{ km s}^{-1}$  with a median velocity of  $495 \text{ km s}^{-1}$  and acceleration of  $29 \text{ km s}^{-2}$ . The values by both of the CME catalogues show relatively strong agreement with differences expected due to the differing analysis techniques used by each catalogue.

This CME became of particular interest as it was observed by many different remote sensing systems, such as SOHO|LASCO; STEREO|SECCHI; SDO|AIA/HMI and IPS with LOFAR, throughout its journey out towards Earth, and was first described by Bisi *et al.* 2013.

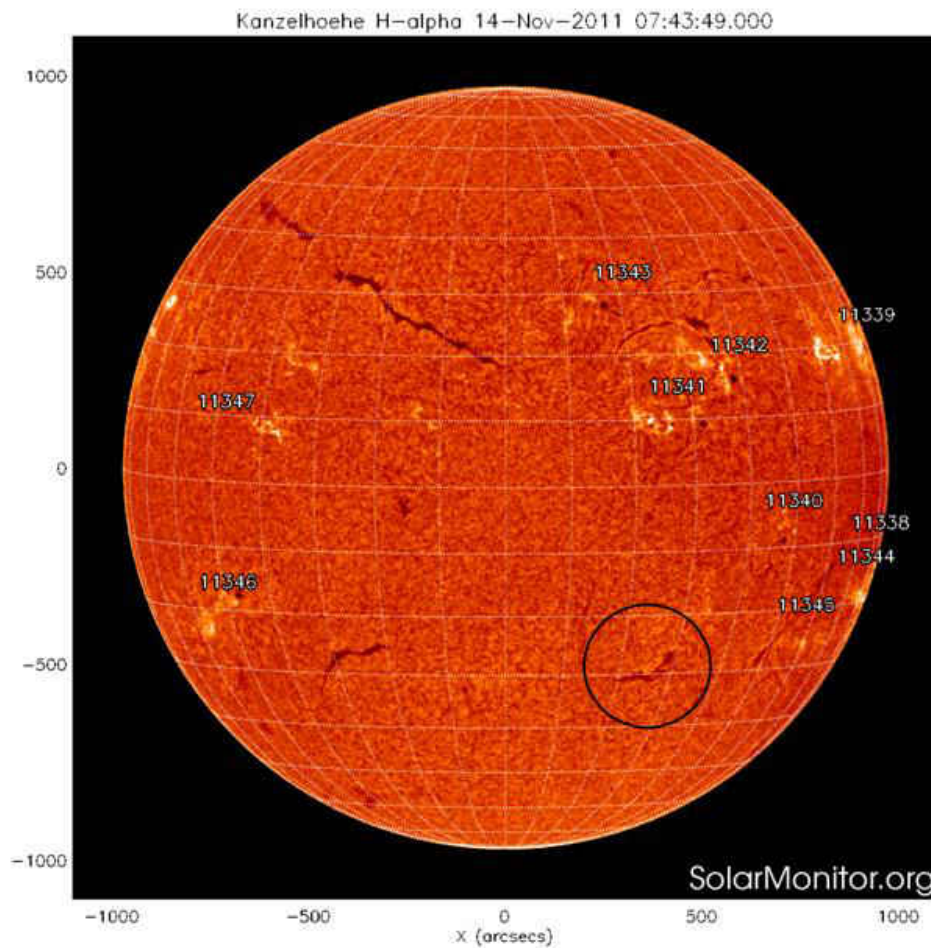
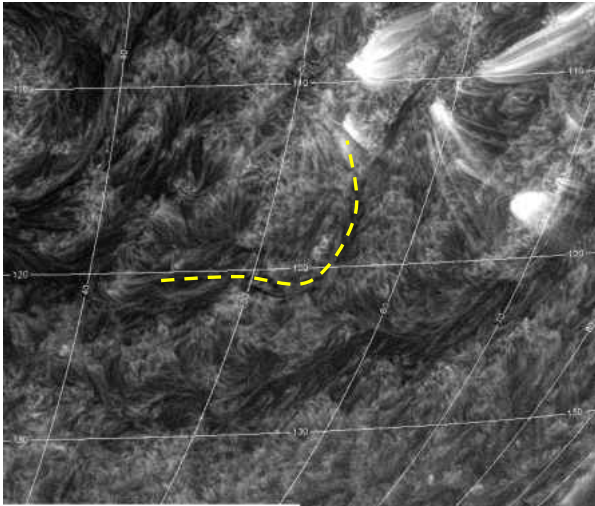


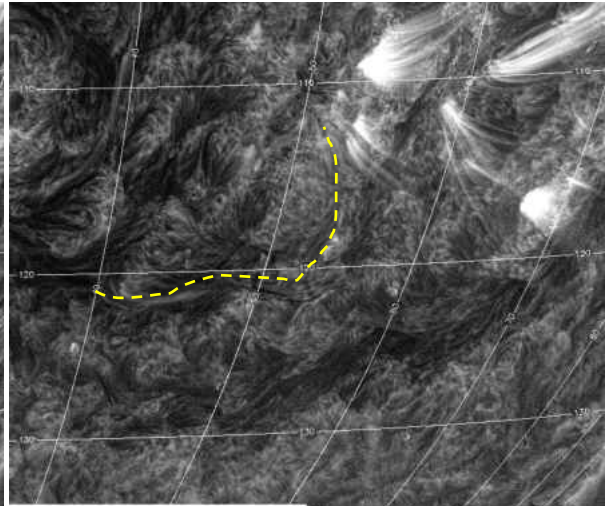
**Figure 6.1** KSO H-alpha (H-alpha) full disk image of the Sun for 14 November 2011 07:43 UT, indicating the active regions on the Sun at this time. The source filament is contained within the black circle.. Courtesy of <http://www.SolarMonitor.org>.

## 6.2 Source Region - Extreme-ultraviolet (EUV)

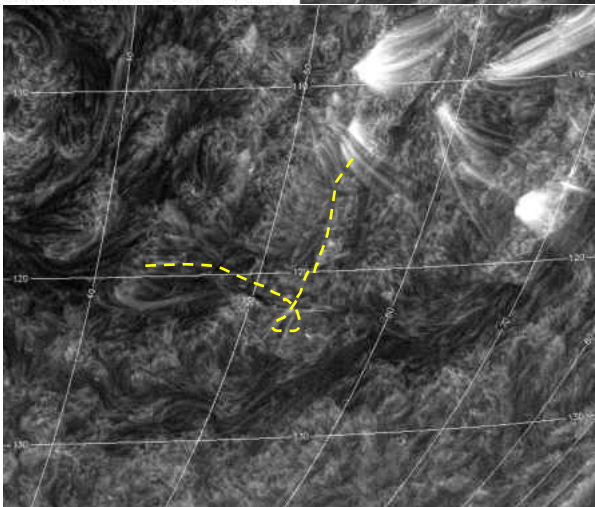
While studying the south-western quarter of the Sun's chromosphere and lower corona using the extreme-ultraviolet (EUV) observations from the AIA telescope onboard SDO and STEREO's EUVI it has been identified that the event originated from an extended filament eruption. The large, initially quiescent filament is situated south-east of the active region 11340 and east of region 11345.



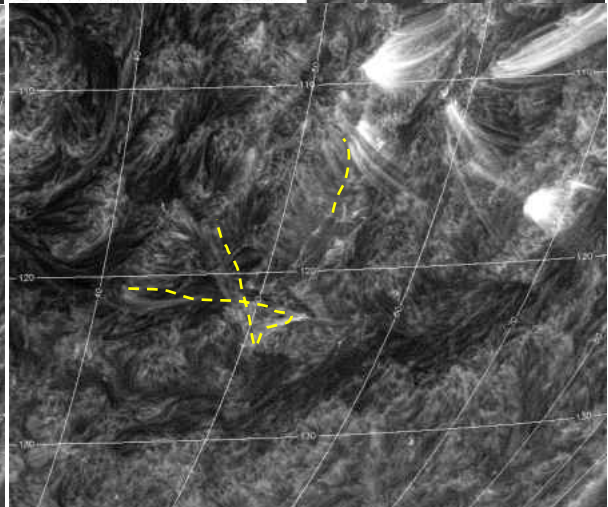
2011-11-14T19:04:12.34 171\_THIN



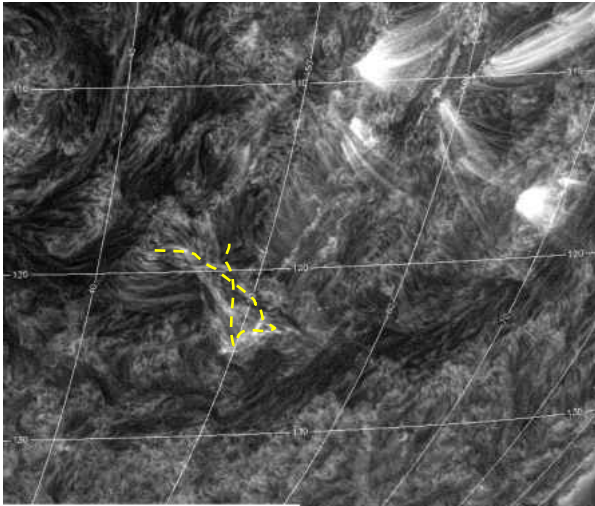
2011-11-14T19:31:12.34 171\_THIN



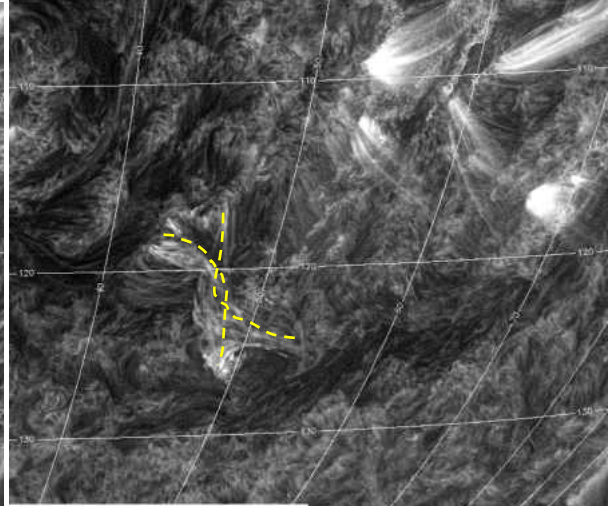
2011-11-14T19:37:12.34 171\_THIN



2011-11-14T19:43:12.34 171\_THIN



2011-11-14T19:49:12.34 171\_THIN



2011-11-14T19:55:12.34 171\_THIN

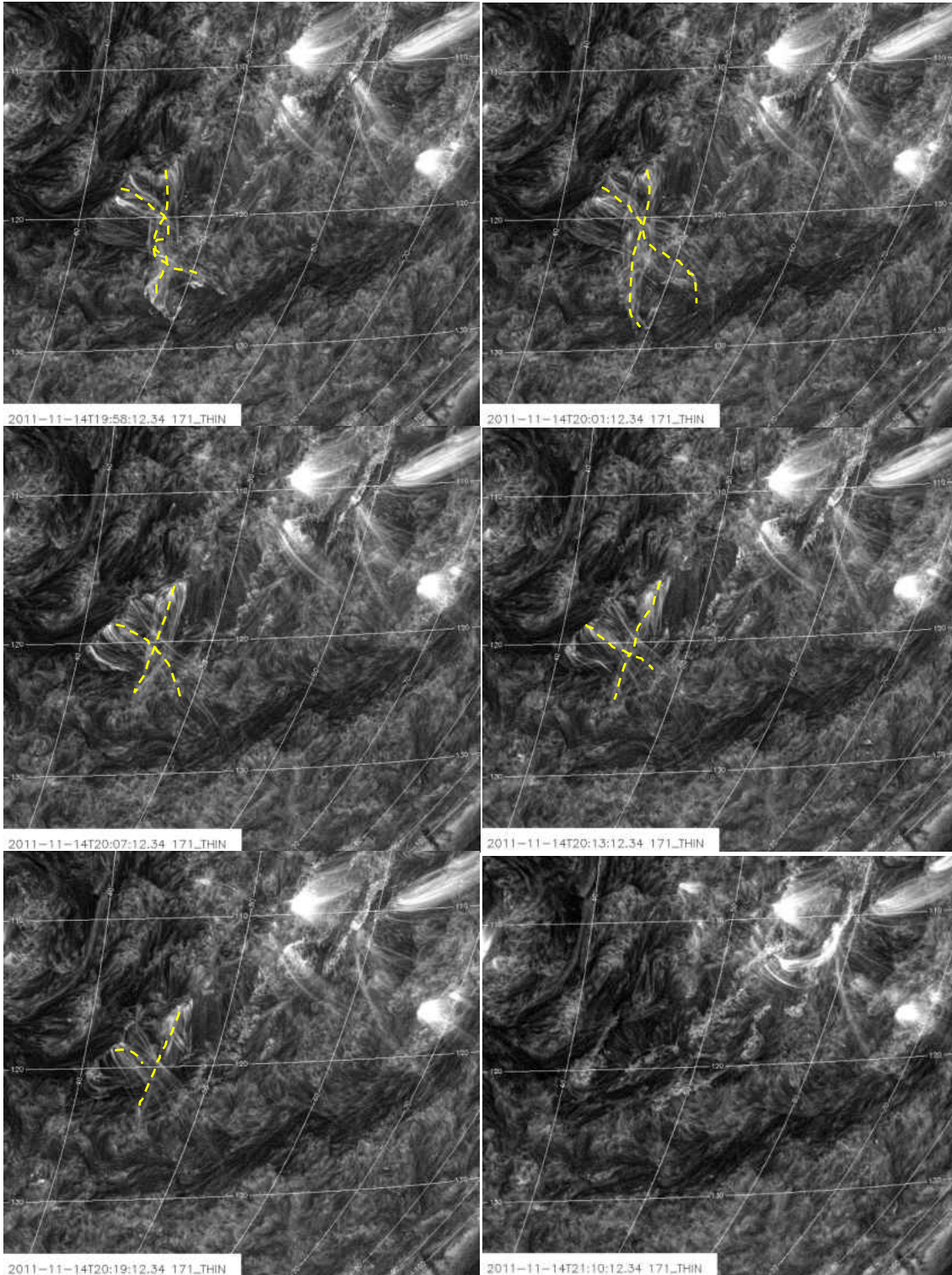
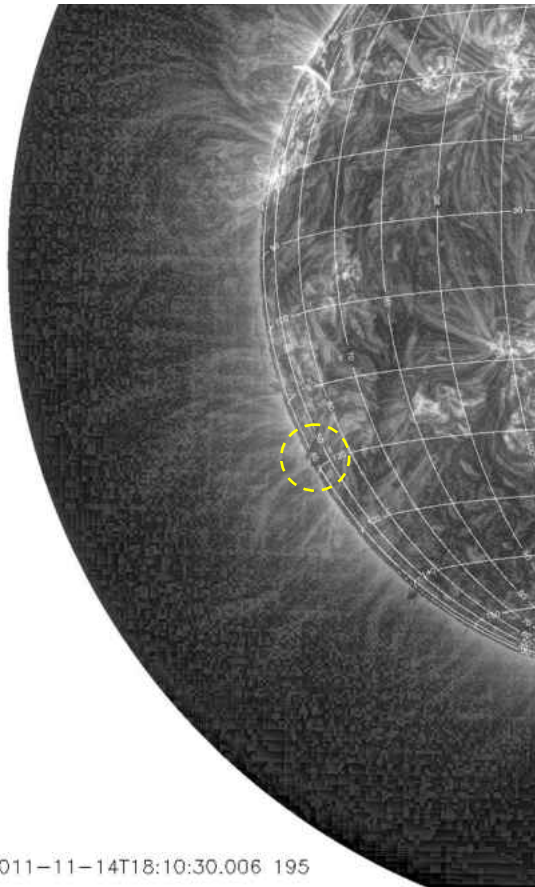
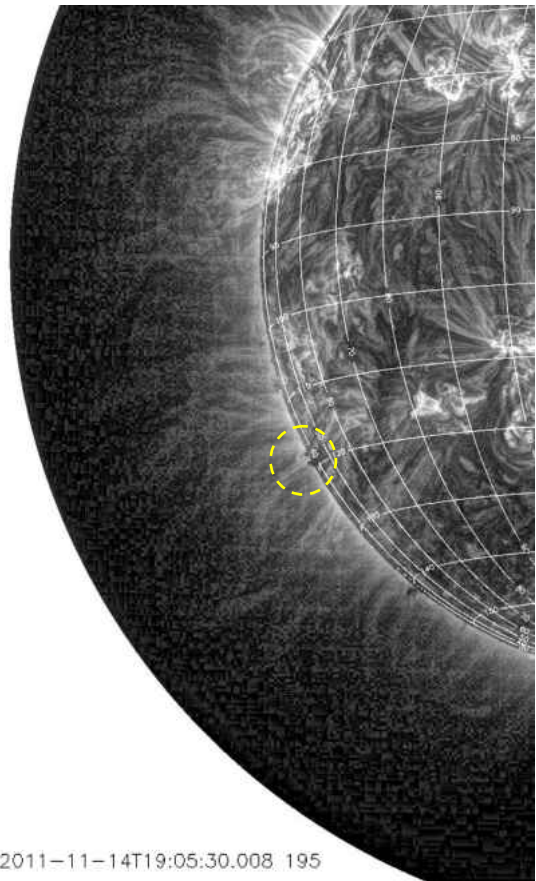


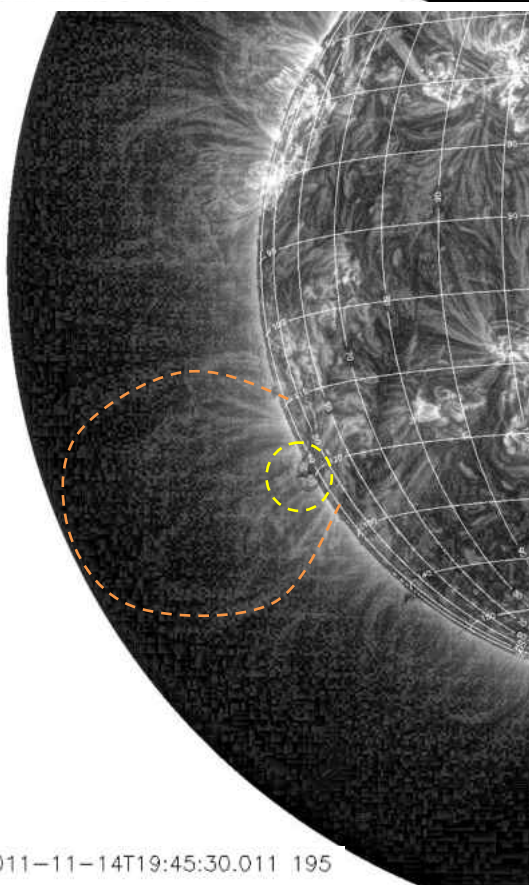
**Figure 6.2** Timeline of the filament eruption attributed to the CME as observed by SDO|AIA in the 171 Å channel. Frames show the evolution of the filament from its quiescent state at 19:04 UT through its eruption, at approximately 19:30 UT, and a return to a quiescent state at 20:37 UT with a residual post-eruptive arcade. The yellow dashed lines in the panels indicates the approximate location of the filament. All images are processed using Multiscale Gaussian Normalization (MGN - Morgan and Druckmüller 2014).



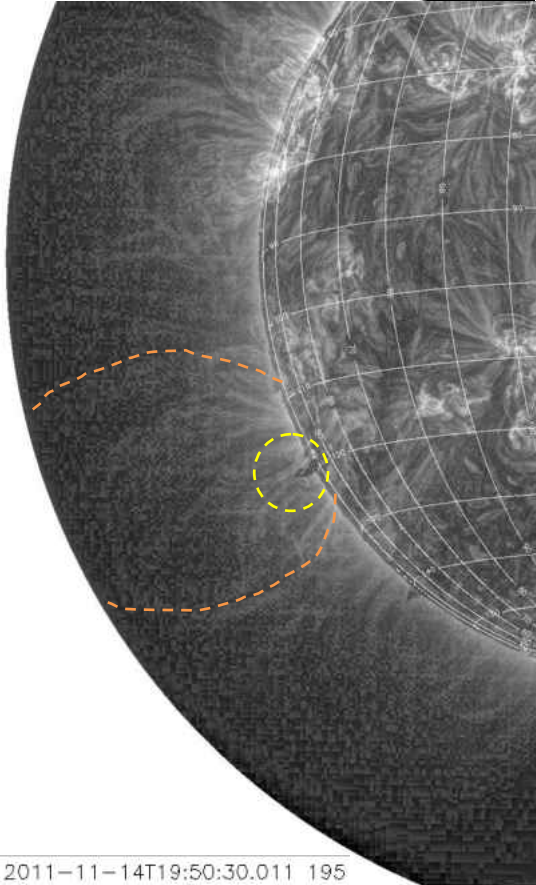
2011-11-14T18:10:30.006 195



2011-11-14T19:05:30.008 195



2011-11-14T19:45:30.011 195



2011-11-14T19:50:30.011 195

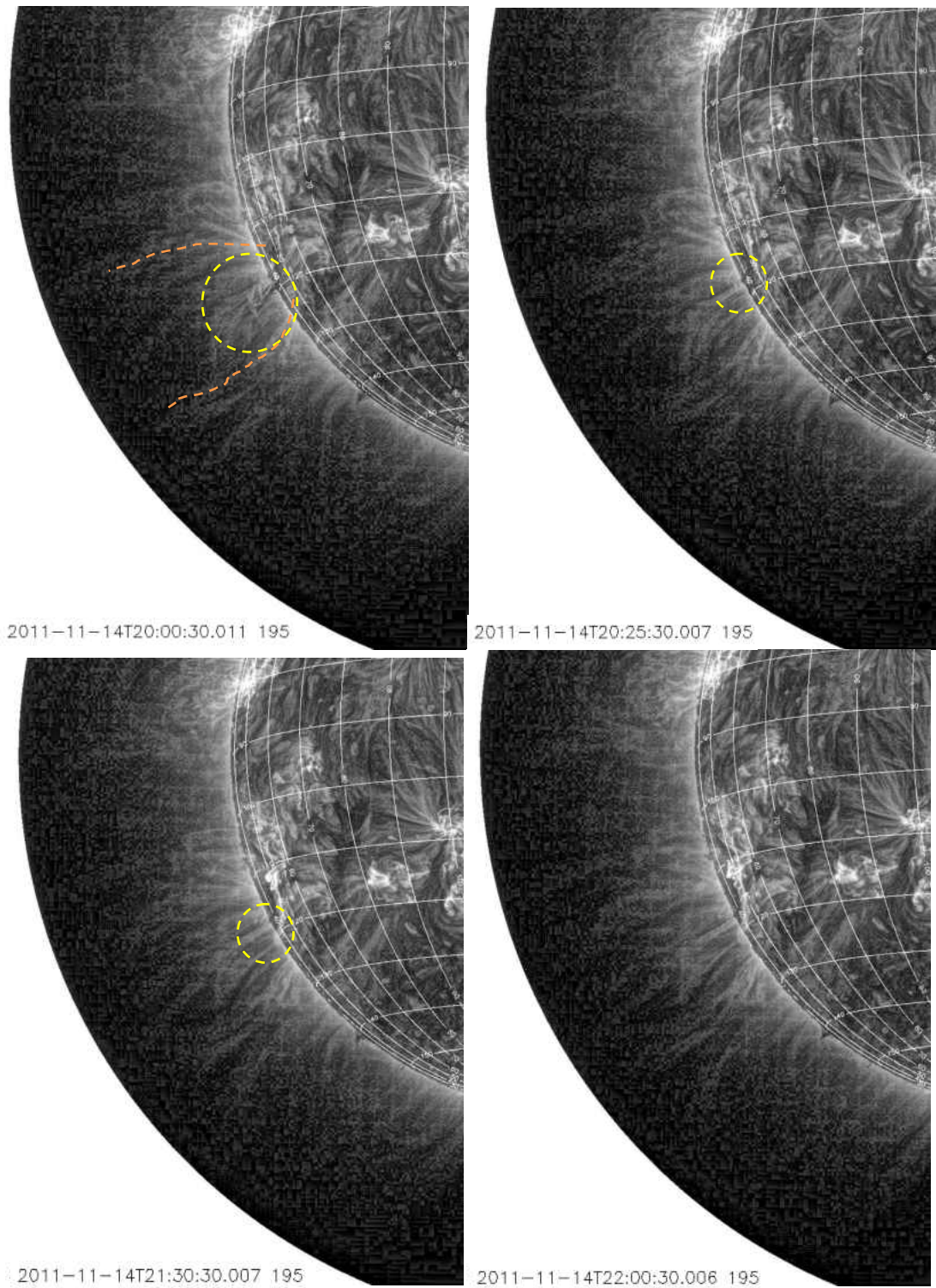


**Figure 6.3** STEREO-A|EUVI 195 observations of the filament eruption. The dashed- yellow circles indicate the location of the filament in each panel. The dashed-orange lines indicate material that is ejected ahead of the core filament from corona. All images are processed using MGN (Morgan and Druckmüller 2014).

Although this event is not directly associated with either active region. This location is circled in figure 6.1, a Kanzelhoehe Solar Observatory (KSO) Hydrogen-alpha (H-alpha) full disk image of the Sun for 14 November 2011 07:43 UT. KSO is a solar observatory located in near Villach, Austria which uses an H-alpha (656.3 nm) telescope to observe the Sun.

The filament began erupting at approximately 19:30 UT on 14 November 2011. After ~70 minutes since the initial instability, at approximately 20:37 UT, the filament returned to a quiescent state. Figure 6.2 displays the detailed evolution of the filament eruption through the 171 Å wavelength.

At 19:04 UT a filament lies from approximately 120° longitude and 45° latitude up to 115° longitude and 55° latitude in heliocentric Earth ecliptic (HEE) coordinates. The filament remains relatively stable although strong flows are visible between frames. Figure 6.2 shows that the filament is apparent in absorption in the 171 Å channel suggesting that the filament is very dense. At 19:31 UT the filament begins to twist showing evidence of classic kink instability (see chapter 1) (earliest frames of figure 6.2). At 19:43 UT the filament breaks away from its north-western anchor point whilst remaining anchored at its south-eastern foot. The north-western filament leg quickly dissipates, whereas the south-eastern leg continues to twist (early to middle panels of figure 6.2). After 20:01 UT the activity reduces and the south-eastern filament leg begins to dissipate until it is no longer visible (middle to end panels of figure 6.2). By 20:34 UT the filament has completely disappeared and a post eruption arcade is present at the location of the north-western foot of the original filament.

A second perspective of the filament eruption was made available by the STEREO-A mission, which at the time of the event was located close to perpendicular to the SDO view of the filament eruption site. Figure 6.3 shows examples of the eruption in the STEREO-A|EUVI 195 Å channel. Large amounts of activity in the corona prior to the eruption can be observed in the middle panels of figure 6.3. When the filament does erupt, a large amount of the corona, indicated by the dashed-orange lines in figure 6.3, is ejected ahead of the filament material at a very high velocity. This ejection is very clearly seen in the 19:45 UT and 19:50 UT frames of figure 6.3. The fast erupting material suggests that there may be two parts of the CME that has erupted; a very fast front followed by a slower and denser core.

### 6.3 Coronagraph Observations with LASCO and COR

As discussed previously the CME entered the LASCO C2 FOV on 14 November 2011 at 20:24:05 UT with an apparent South-West propagation, however when using 2D coronagraph images it is impossible to determine the true 3D direction of the CME without additional information. The source of the CME is the filament eruption, as determined from EUV observations, so we can assume that the primary direction of the CME has a component which is heading in the direction of the SOHO spacecraft and in turn in the direction of Earth with the caveat that eruptions can deflect low down (Byrne *et al.*, 2010). Also eruption has considerable size so is spread out across range of latitudes and longitudes.

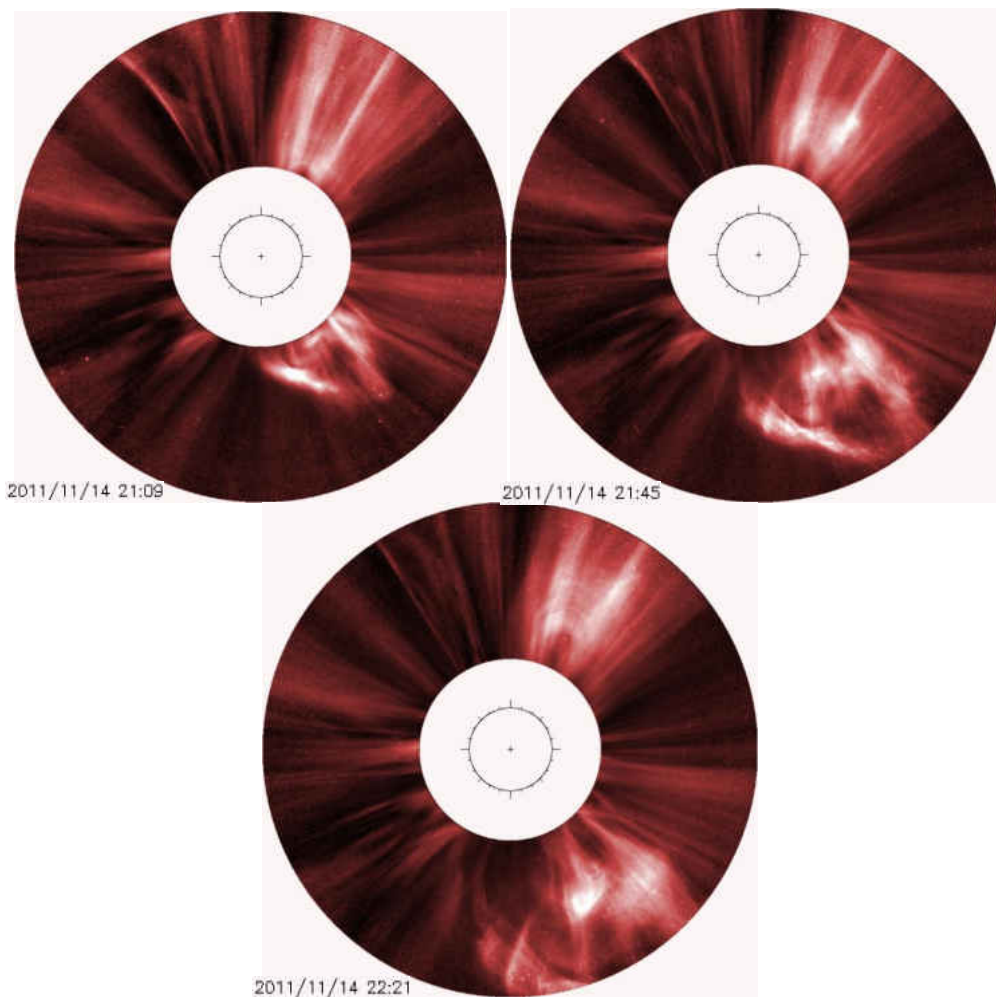


**Figure 6.4** SOHO|LASCO C2 images of the CME for times 21:12 UT (top left), 21:48 UT (top right) and 22:24 UT (bottom) for 14 November 2011. Images have been processed with the NRGF (Morgan *et al.* 2006).

Figure 6.4 shows the propagation of the CME in the SOHO|LASCO C2 telescope. In LASCO, the CME observed to be a large CME of medium angular width with a prominent south-western trajectory. It was clearly visible in the south western quarter and self-similarly with components of the CME later visible directly south of the Sun. As the CME was a partial halo with the bulk of material in a dominant south-west direction, it is possible that the flank of the CME is directed towards Earth and is probably responsible for measured disturbances at Earth.

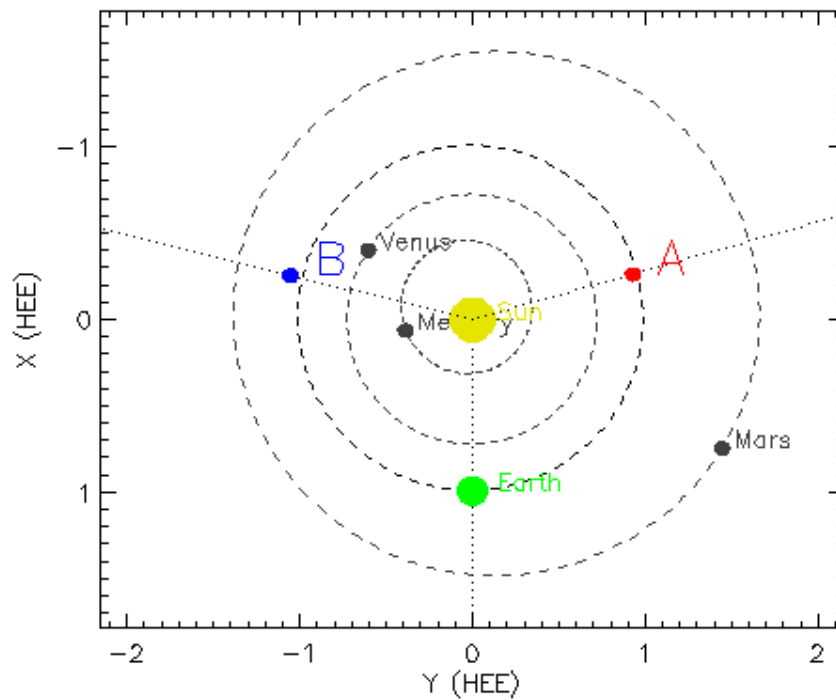


**Figure 6.5** Ecliptic schematic of the positions of the STEREO spacecrafts in their orbit around the Sun (yellow) on 14 November 2011 21:00 UT. The STEREO spacecrafts are depicted as blue (STEREO-B) and red (STEREO-A) points. The Earth (green) and other inner solar system planets (black) are also included within the schematic. The STEREO-A and -B spacecraft were located at  $106.0^\circ$  and  $(-103.7^\circ)$  separation from the Earth respectively. Image generation courtesy of STEREO Science Center (SSC) ([http://stereo-ssc.nascom.nasa.gov/cgi-bin/make\\_where\\_gif.php](http://stereo-ssc.nascom.nasa.gov/cgi-bin/make_where_gif.php)).

Coronagraph observations of the extended inner corona are also available from the COR1 and COR2 coronagraphs onboard the twin STEREO spacecrafts. At the time of the CME, STEREO was in a advantageous configuration for studying the discussed event. At 21:00 UT on 14 November 2011 STEREO-A and STEREO-B were located at HEELongitudes of  $106^\circ$  and  $-104^\circ$  respectively, providing a

geometry which allows an accurate estimate of direction. The position of the STEREO spacecraft relative to the Earth and Sun is shown in figure 6.5.



**Figure 6.6** STEREO-A (right column) and STEREO-B (left column) observations of the CME event on 14 November 2011 at the times 21:25 UT, 22:25 UT and 23:54 UT.

Figure 6.6 displays the CME observations made by the STEREO|COR-2 coronagraphs. The CME becomes visible on the western solar limb (left of the Sun) in COR2-A at 20:24 UT and then slightly later at 21:25 UT it becomes visible on the eastern limb (right of the Sun) in COR2-B. The delay between cameras implies that the CME may have erupted nearer to the STEREO-A spacecraft and on the western limb of the Sun. Further indication of the direction that the CME is propagating is given by the fade speed of the brightness of the CME as it travels away from the Sun. The CME fades quickly in the COR-B cameras when compared to the fade speed in the COR-A cameras, in which the CME fade is very slow. This is strong evidence that the CME is travelling away from the COR-B cameras from the limb of the Sun. As previously mentioned, in COR-A there appears to be little fading of the CME brightness as it propagates away from the Sun thus it can be deduced that the CME is not travelling away from the telescope.

The COR-A telescopes do not observe the CME to have the halo or partial halo effect which is often strong evidence of an observer directed event (or an event directly away from the observer - this has already been disproven for this event). It can thus be assumed the CME does not travel with a plane-of-sky component in the direction of the STEREO-A spacecraft but propagates southward between the two STEREO spacecrafts with a heading more dominant in the direction of STEREO-A.

Combining the STEREO|COR evidence with the evidence from SOHO|LASCO, where a partial halo CME effect was observed, allows us to conclude that the CME is travelling below the Sun-Earth plane-of-sky and in the region between the STEREO-A spacecraft and the Earth with a CME flank of the material extending into the direction of the Earth. This geometrical information is later used to constrain a flux tube model to truly obtain the required positional information of the CME.

### **6.3.1 Determining the CME Geometry Using a Flux Tube Wire Frame Model**

A simple flux tube density model similar to that described by Morgan, Bryne and Habbal, 2012 is used to more accurately determine the CME geometry. The model and fitting procedure is similar to the Croissant model of Thernisien, Howard and Vourlidis (2006), albeit with a more sophisticated control of parameters and a full line-of-sight density integration. The use of the dynamic separation process on the coronagraph observations is also a great advantage. The flux tube's central longitude, latitude, orientation around central axis, width of tube, and breadth from leg to leg are the main parameters which are adjusted to best fit the appearance of the observed CME from the three viewing perspectives of LASCO, COR2-A and COR2-B, thus producing a 3-D model of the CME from the 2-D observations. Figure 6.7 shows Images from LASCO C2 and COR2 A & B (top row) with

corresponding synthetic observations made of the density model of a flux-rope CME in the bottom row. Figure 6.7 shows clearly that the primary direction of the CME is South-Western when viewed from Earth. Combined the images clearly show the CME has propagated further in COR-A, aimed below the equator and between STEREO-A and the Earth.

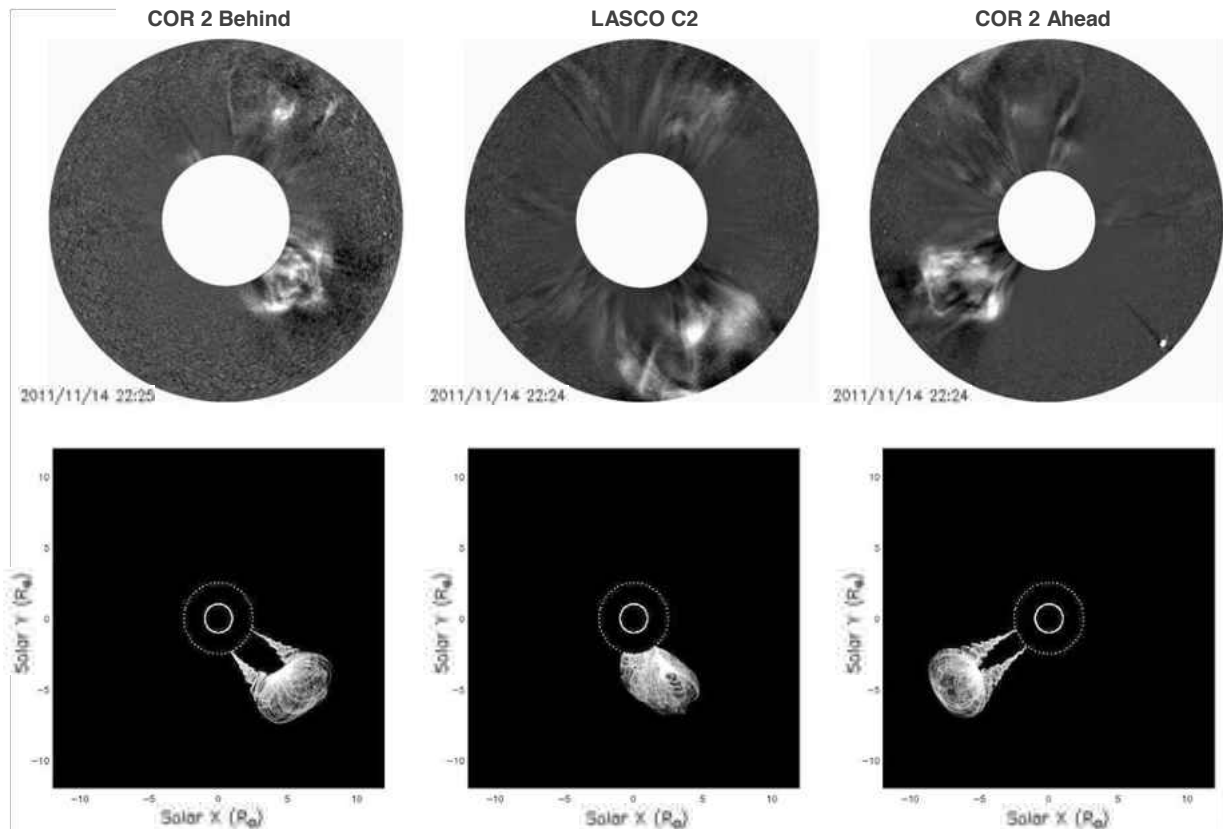


**Figure 6.7** LASCO C2 (top centre) and COR2 from STEREO-A and –B spacecraft (top right and top left respectively) with corresponding synthetic observations gained from a 3D density model of a flux-tube.

From the flux rope wire frame modelling the CME’s propagation properties can be determined. At a distance of  $10 R_s$  the CME covered a longitude range in the HEE coordinate system of  $-11^\circ$  to  $58^\circ$  and a latitude range of  $-22^\circ$  to  $-58^\circ$ . The mean direction of the flow is in the HEE coordinates  $23^\circ$  longitude and  $-40^\circ$  latitude.

## 6.4 Heliospheric Imager (HI) Observations

The event entered the STEREO HI-1A FOV on 14 November 2011 at 22:49 UT and is observed to propagate in a south-western direction covering the majority of the southern PAs of the HI-1A telescope. Due to the orientation of the CME and STEREO satellites, the CME enters the FOV of the HI-1B approximately 180 minutes later at 01:30 UT. The upper panels of figure 6.8 display the background removed HI-1 observations for the event at 13:29 UT on 15 November 2011. In the HI-1A image, the CME appears to have travelled a greater distance than in HI-1B in which the CME appears to only just entering the telescope field of view and moving with a much slower plane of sky velocity than observed by HI-1A, reiterating its trajectory away from the HI-1B camera. HI-1B displays the presence of an ecliptic component of the CME which is not clearly visible in the HI-1A telescope.

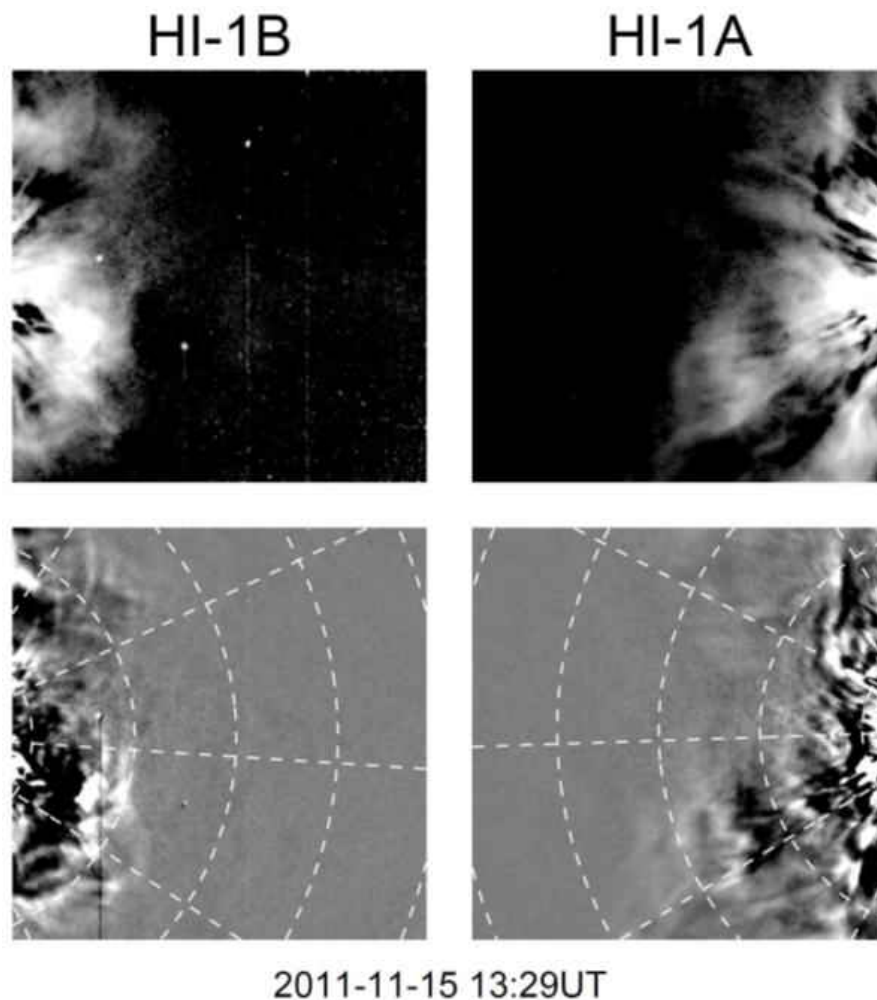


**Figure 6.8** Top panels: 1-day background and star field removed STEREO|HI-1 observations of the CME taken 15 November 2011 13:29 UT. Bottom panels: 60 minute star field aligned difference images for on 15 November 2011 13:29 UT (12:29 UT data subtracted).

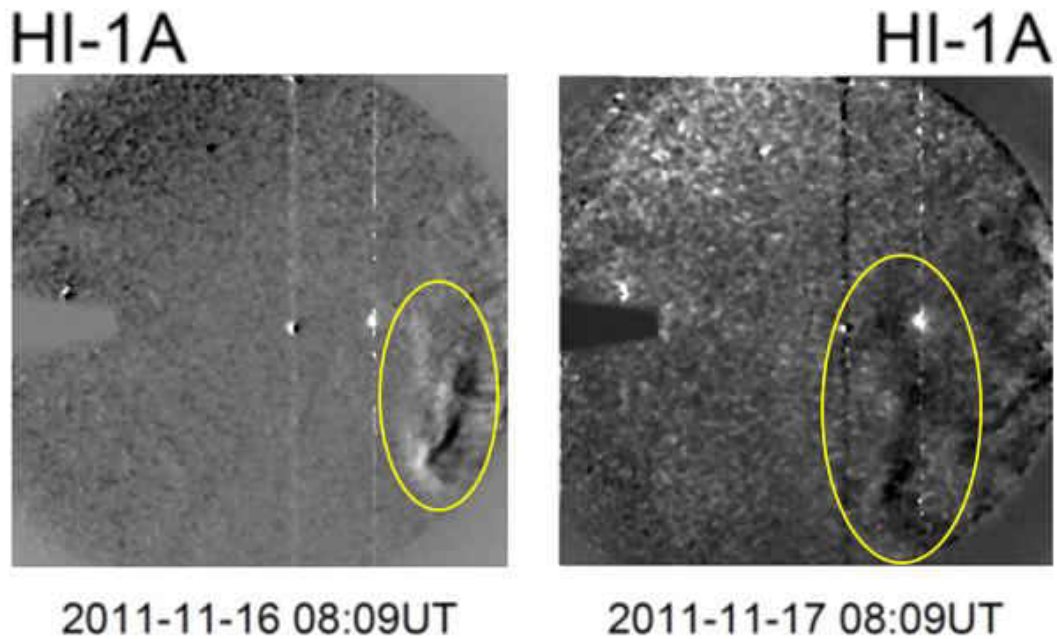


**Figure 6.9** Star-field aligned difference images of the November event. The left image is a 120 minute difference image for 16 November 2011 08:09 UT (06:09 UT data subtracted) and the right image is a 360 minute difference image for 17 November 2011 08:09 UT (02:09 UT data subtracted). For each event the CME has been contained within a yellow oval.

The extent of the CME can be seen clearly in difference imaging, an example of which is given in figure 6.10 and in the lower panels of figure 6.8. Figure 6.10 shows that the CME propagates South-West with a PA centred at approximately  $115^\circ$  and extending up to  $90^\circ$  and down beyond the southern edge of HI-1A. The CME has a very faint component in the ecliptic plane (circled in blue on figure 6.10) which is only made clear in HI-1A, using the difference imaging technique.

The CME appears in the HI-2A FOV at 15 November at 14:09 UT, with a South-West direction consistent with the HI-1A observations. The ecliptic component is visible in HI-2A difference imaging for a short period, until becoming too faint to be observed. The CME is too faint to be visible within the FOV of the HI-2B, which is most likely due to its propagation away from STEREO-B. Figure 6.9 has two difference images showing the propagation of the CME as it approaches the Earth. A greater difference image time is required for later images as the CME very rapidly loses its visibility as it disperses into the HI-2A distance range.

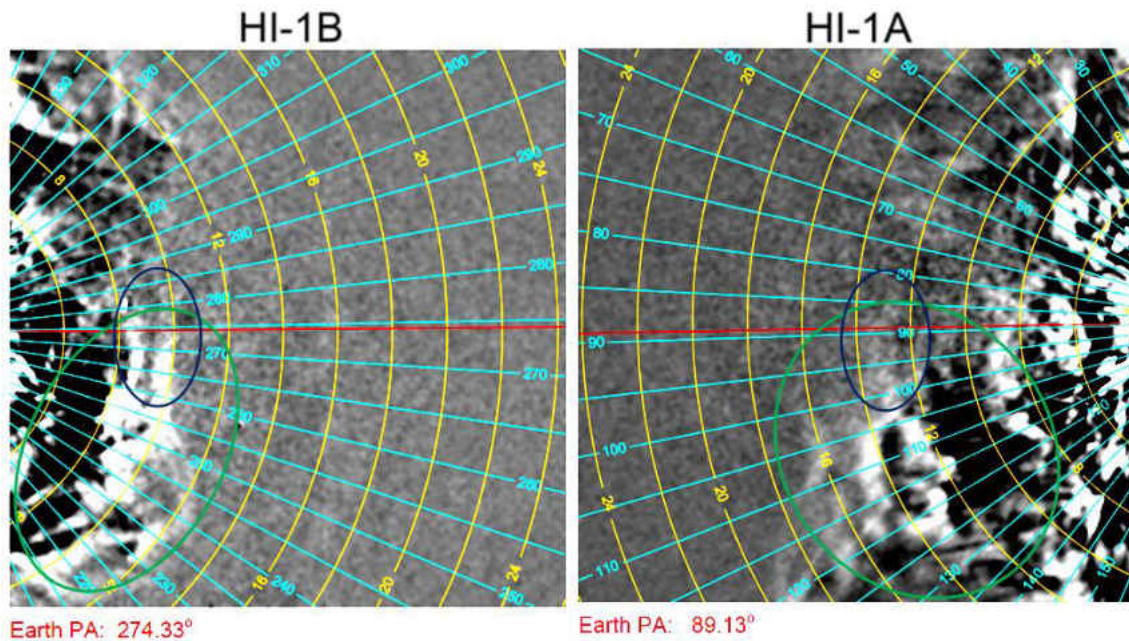


**Figure 6.10** HI-1A 40 minute star field aligned difference image for 15 November 2011 12:09 UT (11:29 UT data subtracted) and HI-1B for 15 November 13:30 UT (12:50 UT removed) showing the propagation of the CME (indicated within the green oval). The blue grid lines indicate the position angle from solar north, with respect to spacecraft view of the Sun, and the yellow lines indicate the elongation from the Sun. The ecliptic component of the CME is visible within the blue oval.

#### 6.4.1 CME Fitting with J-maps

Figure 6.11 shows the J-maps of the STEREO|HI cameras produced at multiple position angles in the field of view of the HI cameras. The J-maps show that the CME is faintly visible in the ecliptic plane and it is much more visible in then camera as it approaches the southern pole. At the position angle of 115° (and near to this position angle) two distinct CME streams appear in the J-maps which can be attributed to a faster CME front. For the fitting performed the first of the streams has been used as it consistent in time with the position angles at which only one stream is clearly visible.

The CME trajectory appears to be at an angle with the northern flank of the CME located primarily located at a longitude over 25° and up to 45°. The southern flank of the CME however appears to be propagating closer towards the Earth with some measurements indicating that CME material may pass below the Earth. These longitudes are slightly different to what was expected as the original filament itself was located between 45° and 55° indicating that there may possibly be deflection causing the CME to rotate as it propagates into the heliosphere.

When the STEREO HI observations are plotted as J-plot it is apparent that the CME can no longer be observed from STEREO-B when it reaches an elongation of  $\sim 30^\circ$ . This is much earlier than where it ceases to be observed by HI on STEREO-A where the CME is easily tracked past the HI-1A camera and well into the HI-2A FOV, This supports the idea that the CME is directed closer the STEREO-A spacecraft, between  $0^\circ$  to  $90^\circ$  Heliocentric Earth Ecliptic (HEE) longitude. It is possible to apply the Fixed Phi, Harmonic Mean, and Self-Similar Expansion (SSE) models (discussed in chapter 4) to tracks of this CME extracted from the J-maps. The results for each fitting model at various PA, using the light/dark boundary region produced from difference imaging are given in table 6.1. Due to the quicker fade of the CME in the HI-2B images the model fits for STEREO-B are less accurate and have much wider ranges.

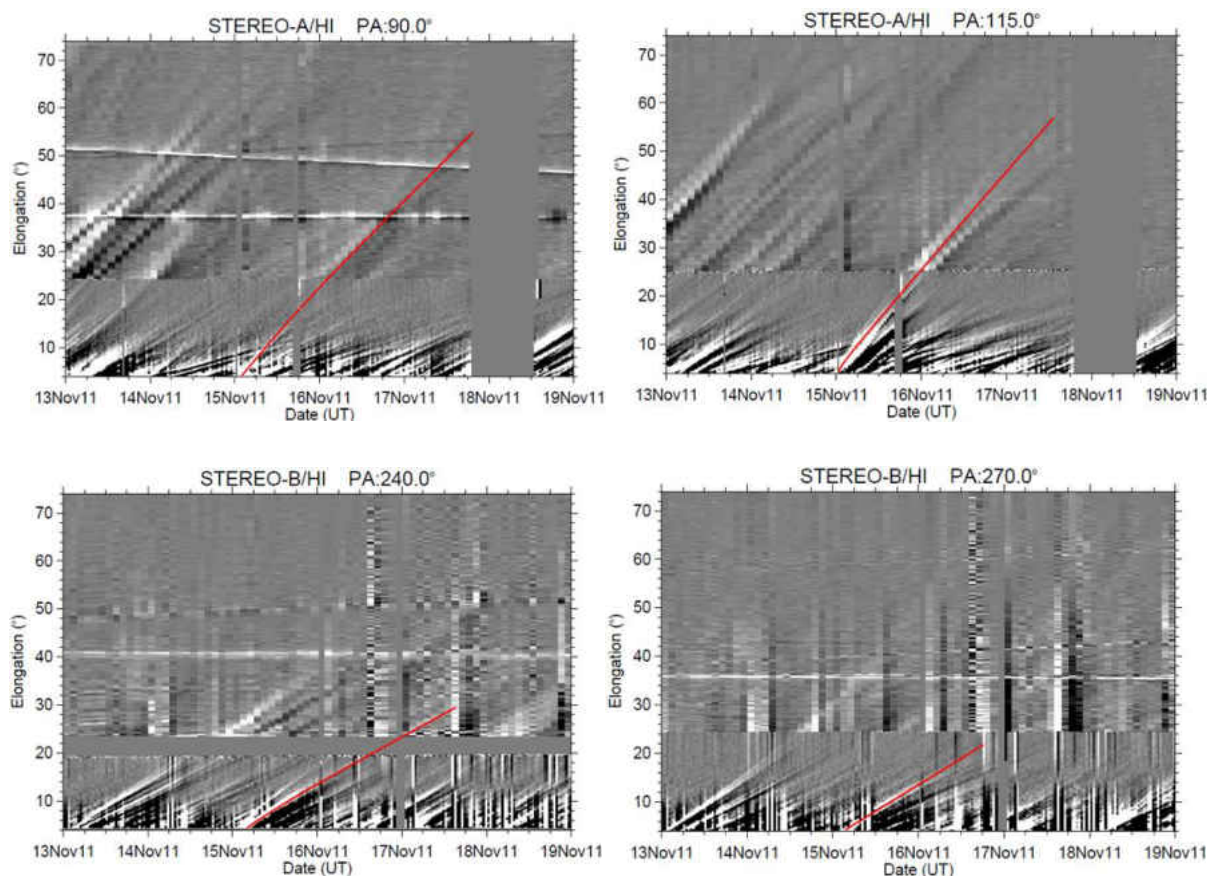


**Figure 6.11** STEREO|HI differenced J-maps for the position angles  $90^\circ$ ,  $115^\circ$  (STEREO-A),  $240^\circ$  and  $270^\circ$  with fitted tracks along the light/dark boundary from difference imaging marked in red.

The CME velocities that have been calculated peak at the maximum PA of the STEREO-A Hi telescopes, indicating that from the fitting the central position angle of the CME is between 115° and out of the field of view of the telescope. Previous observations made from STEREO|COR show that it is highly unlikely that the central PA could be much further beyond 125°. The calculated velocities appear to increase rapidly while the position angle approaches the southern pole, however this is only apparent in STEREO-A. This may be due to a much faster but low density CME front propagating with a stronger southward influence which due to its low density is not visible in STEREO-B. When compared to the predicted direction calculated from the wire frame flux rope earlier, there is a good match between the results calculated from the J-maps with all of the calculated longitudes within the predicted range. The J-map fitting does however predict higher latitudes than the flux rope model; this may be due to the northern flank components of the CME being more visible in the HIs than in the coronagraphs where it had been overshadowed by the brighter core components of the CME.

Position Angle (PA)	Fixed Phi (F $\phi$ )			Self Similar Expansion (SSE)			Harmonic Mean (HM)		
	Vr (km/s)	lon (°)	lat (°)	Vr (km/s)	lon (°)	lat (°)	Vr (km/s)	lon (°)	lat (°)
90°	429.1	43.5	-0.76	441.17	37.51	-0.79	449.35	31.61	-0.8
105°	575.46	24.7	-15.7	616.32	10.98	-15.77	659.27	-3.4	-14.94
115°	555.88	45.8	-22.8	609.81	31.37	-25.01	657.71	16.23	-25.79
125°	601.5	29.2	-35.1	679.62	7.61	-35.48	773.02	-18.4	-15.06
275°	418.69	8.48	0.66	468.25	26.43	0.59	533.11	46.37	0.45
260°	485.77	8.49	-13.2	563.51	28.85	-10.53	677.05	51.93	-5.84
250°	307.87	-5.65	-24.1	323.56	7.33	-22.83	340.61	20.58	-20.39
240°	387.83	-5.99	-34.1	418.33	11.2	-31.68	454.19	28.4	-26.71

**Table 6.1** Result summary of the different CME fitting methods on the 14 November event from the HI telescopes onboard STEREO. The upper half of the table contains the results taken from STEREO-A (PA between 90° and 125°) and the lower half contains the results from STEREO-B (PA between 275° and 240°). All co-ordinates are in given in the heliocentric Earth ecliptic (HEE) frame.

The Earth is visible in the HI J-maps as a bright near-stationary located at  $\sim 40^\circ$  elongation (the precise elongation is dependent on the camera and PA). Although the Earth should only cover the ecliptic PAs ( $89^\circ$  and  $274^\circ$ ), as it is very bright compared to the surrounding heliosphere artefacts will remain at surrounding PAs. This is useful as it allows an estimated arrival time of the western plane-of-sky flank (observed most accurately by STEREO-B) at Earth on 17 November between 18:00 UT and 24:00 UT. The second similar feature which is present in the HI-A equatorial J-maps at an elongation of  $\sim 50^\circ$  is Jupiter.

## 6.5 LOFAR Observations of IPS

This event was also observed by IPS as the ‘first CME observed by LOFAR’ (Fallows *et al.*, 2013; Bisi *et al.*, 2014). The observation of the source J1256-057 (3CRR: 3C279) was performed on 14 November 2011 which began at 08:43 UT and concluded at 08:58 UT, lasting for a total time of 15 minutes.

Observing the astronomical radio source J1256-057 were the German; Garching/Unterweilenbach and Jülich LOFAR antenna systems, resulting in an average radial baseline of around 388 km for the experiment. The radio telescopes observed the radio source using a frequency centred at 150 MHz with a band width of 47 MHz. The radio source J1256-057 was situated in the sky such that the P-Point was located at an average distance of  $133.6 R_s$  and heliographic latitude of  $-3.3^\circ$  from the western solar limb.

The IPS observation was analysed using 7 minute sliding window with a 1 minute step size (the final frames however can only integrate remaining data available). Figure 6.12 shows the cross-correlation functions (solid lines) for the sliding window beginning at 08:48 UT (top left) and 08:53 UT (top right) followed by the total integration of the entire 15 minute observation (bottom). The dashed lines are the auto correlation functions of the radars, which are used to check no inherent errors within the radar system; these are expected to be Gaussian.

Throughout the IPS observation a negative lobe was observed at close to zero time lag in the cross-correlation function. Negative lobes in IPS cross-correlations are typically attributed to rotations in the magnetic field occurring somewhere along the IPS line of site and often this is due to transient structures such as a CME crossing the IPS line of site.

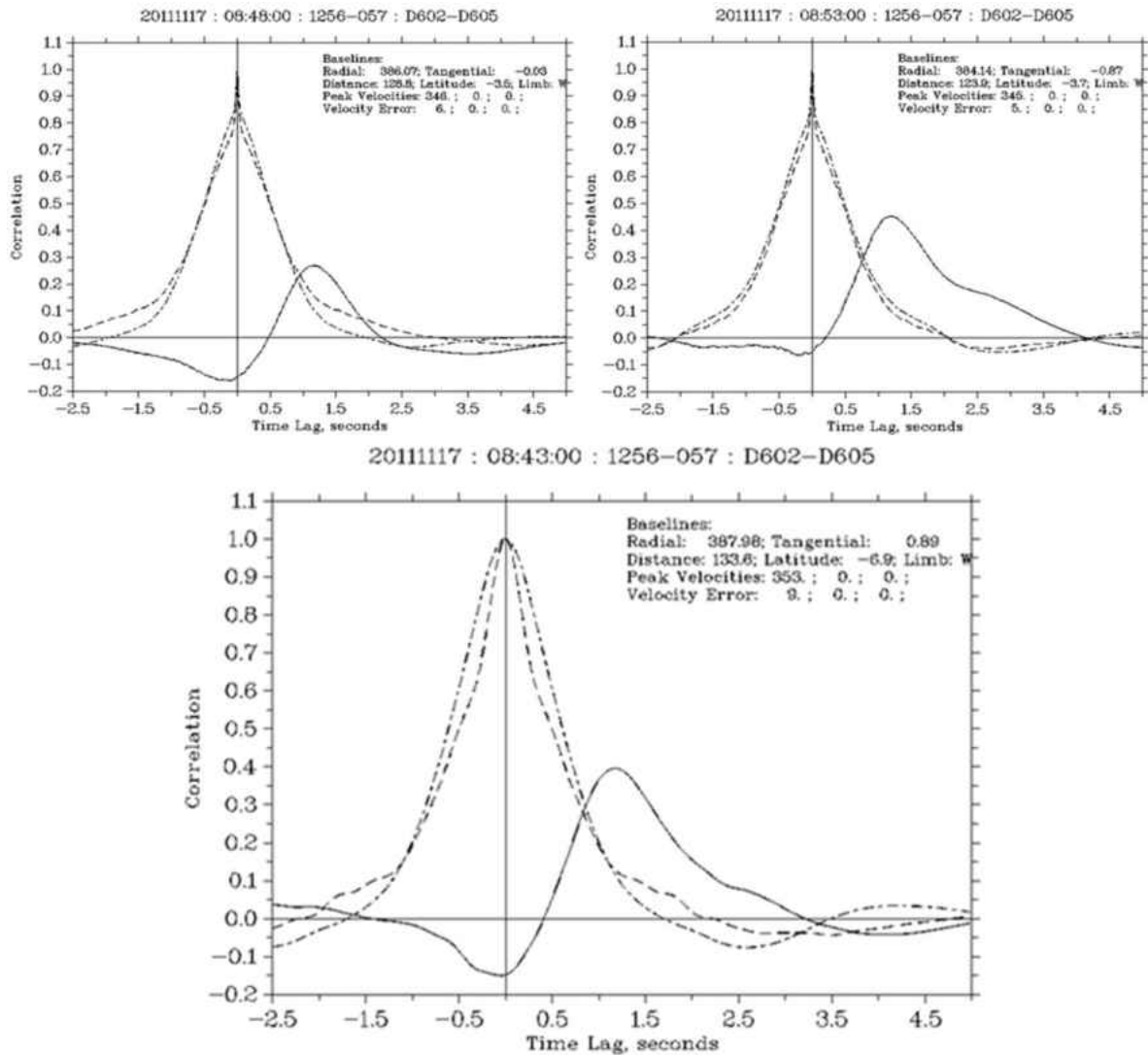


**Figure 6.12** IPS cross-correlation function (solid line) for the observation from Garching/Unterweilenbach (D602) and Jülich (D605) stations of radio source J1256-057 on 17 November 2011. The auto-correlation functions for the radar are also given in this plot as dashed lines.

The cross-correlation function reveals a time lag of the observed scintillation features to be approximately 1.2 seconds which results in an estimated velocity of  $353 \text{ km s}^{-1}$ . The IPS cross-correlation function is displayed in figure 6.12. The IPS velocity estimate is lower than that predicted by the propagation models as expected due to IPS being sensitive only to flow perpendicular to the radar line of sights, however there are additional reasons that the observation speed The IPS observation only observes the most northern flank of the CME (along the ecliptic plane) which is slower than the nose, as can be seen from the STEREO|COR and HI images, and would notionally be

expected since the flanks of a CME have less energy and this Northern-most flank is likely to be ploughing into the densest and slowest ambient slow solar wind compare with the CME nose and the Southern flanks. As IPS observations are sensitive to density structures in the solar wind it is highly likely that the northern flank of a slower and denser core of the CME is what is observed to pass the line of sight of the antennas rather than the very fast front of the CME which has also been identified through STEREO-A|EUVI and propagation modelling performed on STEREO|HI.

### 6.5.1 IPS Projection on to HIs

The projection of the IPS P-Point, for J1256-057 from 14 to 17 November, was in the HI-1B and HI-2A FOVs. The projected P-Point is located at a PA of 274.42 (88.59 HEE)<sup>°</sup> and elongation of 9.19 (40.16 HEE)<sup>°</sup> in the HI-1B (HI-2A) FOV.

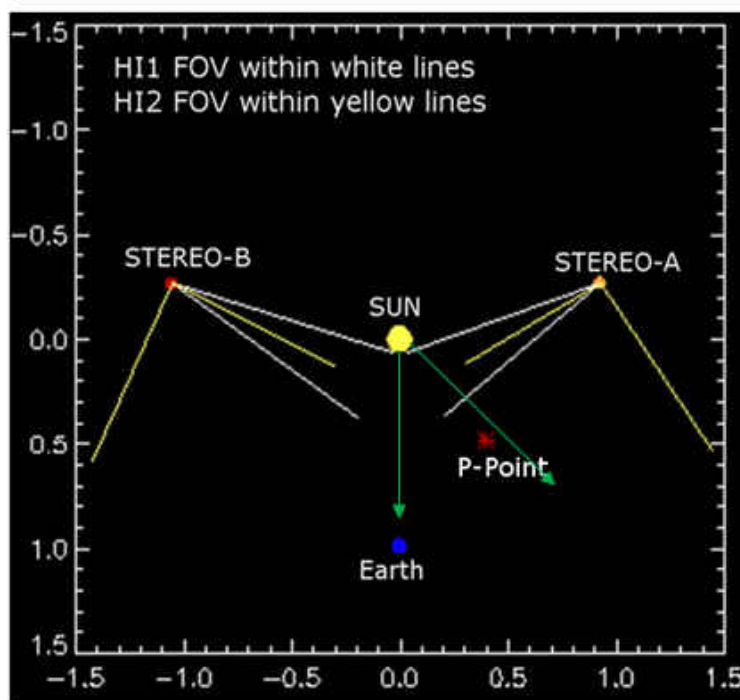


**Figure 6.13** Schematic of the system, showing the positions of the STEREO spacecrafts (and approximate maximum and minimum lines of sight of the HI1 and HI2 cameras), the Sun, the Earth and the IPS P-Point. The green arrows enclose the predicted extremities of trajectory of the event under discussion.

Figure 6.13 shows a schematic of the location of STEREO spacecraft, the view paths of the heliospheric imagers at the time of the LOFAR IPS observation. The IPS P-Point of the J1256-057 astronomical radio source used in the LOFAR observations has also been plotted onto this figure, clearly showing that any structures observed by the LOFAR radio telescope are very likely to be seen by the HI-1A telescope.

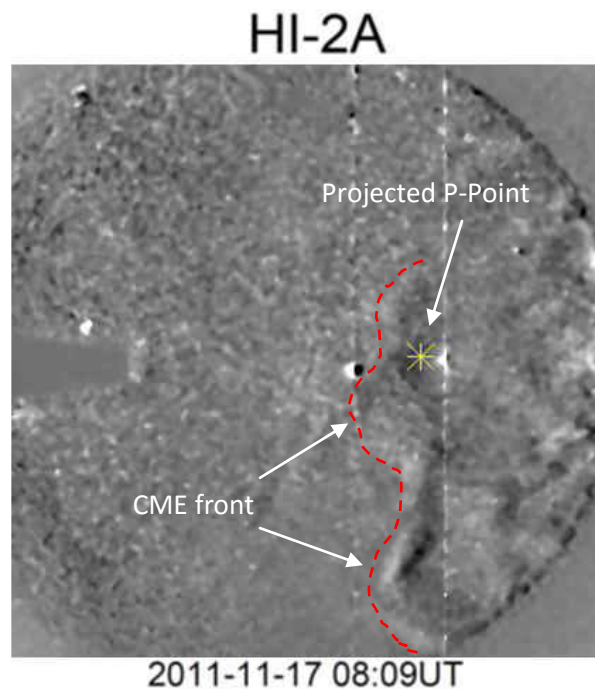


**Figure 6.14** STEREO|HI-2A 240 minute star aligned difference image from 08:09:21 UT on 17 November 2011. The yellow asterisk depicts the IPS P-Point projected onto the HI-2A field of view and the dashed red line indicates the CME front as implied through the difference image. The saturated circular objects and saturation lines protruding from them are the Earth (left) and Mercury (right).

A HI-2A difference image from 08:09:21 UT on 17 November 2011 is shown in figure 6.14, which reveals the Northern flank of the CME crosses the LOFAR ray path, while observing the J1256-057 radio source, with the CME front having only recently passed shortly before the beginning of the experiment. This is consistent with the LOFAR results as the negative cross-correlation lobe is present throughout the experiment and does not appear part-way through the time period. The IPS P-point location is present within the HI-1B field over view however, we suggest that a structure observed by HI-1B to pass over the IPS P-Point at the time of observation was not the CME under

investigation, which faded quickly in the HI-2B FOV, and therefore has been excluded from this investigation.

Previously in chapter 5 it was discussed that in 2007 and 2008 the STEREO mission was in an ideal position of its orbit to relate heliospheric structures observed in the HIs to those detected through IPS. During this early stage of its mission the STEREO spacecrafts were separated by no more than  $25^\circ$  and the HI line of sights were closely aligned with the IPS ray path from Earth, thus providing very small discrepancies between the real position of the IPS P-Point and the analogous closest point along the HI line of sight. The IPS observation of the J1256-057 radio source on 17 November 2011 occurs during a much later phase of the STEREO mission and as shown by figure 6.13 and the STEREO spacecraft were separated beyond  $100^\circ$  from the Earth. At this separation, the HIs no longer have a closely aligned line of sight with the IPS ray path but however provide a near perpendicular view. As such the HIs are now capable of observing the heliospheric material which passes along the IPS ray path. Although the geometry of the system has changed the HIs have proved that they are still capable of effectively observing common heliospheric regions and meso-scale transients propagating through the IPS ray path.

## 6.6 Conclusions

A very detailed description can be made of the 14 November 2011 CME. This is due to the large number of remote sensing data sources available, the configuration of the STEREO spacecraft relative to Earth, and the new observations by LOFAR. In a way, this is a demonstration of current observational capabilities. The CME has been observed and analysed from its source region on the Sun using the extreme ultra-violet (EUV) telescopes SDO|AIA and STEREO|EUVI, and out into the heliosphere in white light with the SOHO|LASCO and STEREO|COR coronagraph experiments as well as STEREO|HI. It was also clearly observed using interplanetary scintillation with LOFAR becoming the first CME to be detected by the new system.

The CME source was observed by SDO|AIA to be an extended filament eruption located within the south-western quarter of the Sun with the initial filament extending from its south-eastern foot point at approximately  $120^\circ$  longitude and  $45^\circ$  latitude to its north-western foot point at approximately  $115^\circ$  longitude and  $55^\circ$  latitude. A near-perpendicular view of the filament from STEREO|EUVI also show large amounts of corona activity prior to the filament eruption with material from the corona also rapidly ejected during, giving the first evidence that the CME is structured with a fast CME front with a slower denser core.

When the CME enters the field of view of the white light coronagraphs, observations from three unique perspectives are available with SOHO|LASCO, and the COR experiments onboard STEREO. SOHO in the Sun-Earth line at the L1 point and the STEREO spacecraft having approximately 100° separation from the Earth provide an excellent view of the CME. This three point perspective allows the approximate trajectory of the CME to be easily determined. The coronagraphs show that the CME is travelling on a path between the STEREO-A spacecraft and the Earth, with a small amount of material possibly directed towards the Earth determined by the partial halo effect observed in the SOHO|LASCO telescope.

Modelling the propagation of the CME in STEREO-HI observations using the fixed phi, harmonic mean and self similar expansion fitting techniques, was consistent with the coronagraphs in determining the trajectory of the CME to be between the Earth and the STEREO-A spacecraft. The fitting methods estimated the primary trajectory of the CME to be at a PA greater than 125° and between 25° and 45° HEE longitude with fitting of STEREO-B suggesting the eastern flank of the CME extended past the Earth. The longitudes modelled from STEREO-HI differed to what was expected from the EUV observations with, the original filament located between 45° and 55°, indicating probable deflection and rotation of the CME while it propagated through the heliosphere. The velocities estimated by the model show that the southern regions of the CME are travelling at a much greater speed than that of the northern flank suggesting the primary material in the southern flank is the fast material observed by STEREO|EUVI and that the northern flank is primarily the slower denser core material.

The interplanetary scintillation experiment observing the astronomical radio source J1256-057 (3C279) performed by LOFAR on 17 November 2011 observed very strong evidence of a CME passing over the ray-path. By using STEREO|HI it is possible to over plot the IPS P-Point into the HI field of views, as such using HI-2A it was possible to confirm that the IPS experiment observed the northern flank of the 14 November 2011 CME pass over the IPS ray path on 17 November 2011. The velocities estimated, through cross-correlation of the received signals, were consistent with velocities of the northern CME flank determined with the HI fitting methods. IPS estimated an average velocity of the observational period of 353 km s<sup>-1</sup> and the fitting models estimated velocities between 300 and 455 km s<sup>-1</sup>.

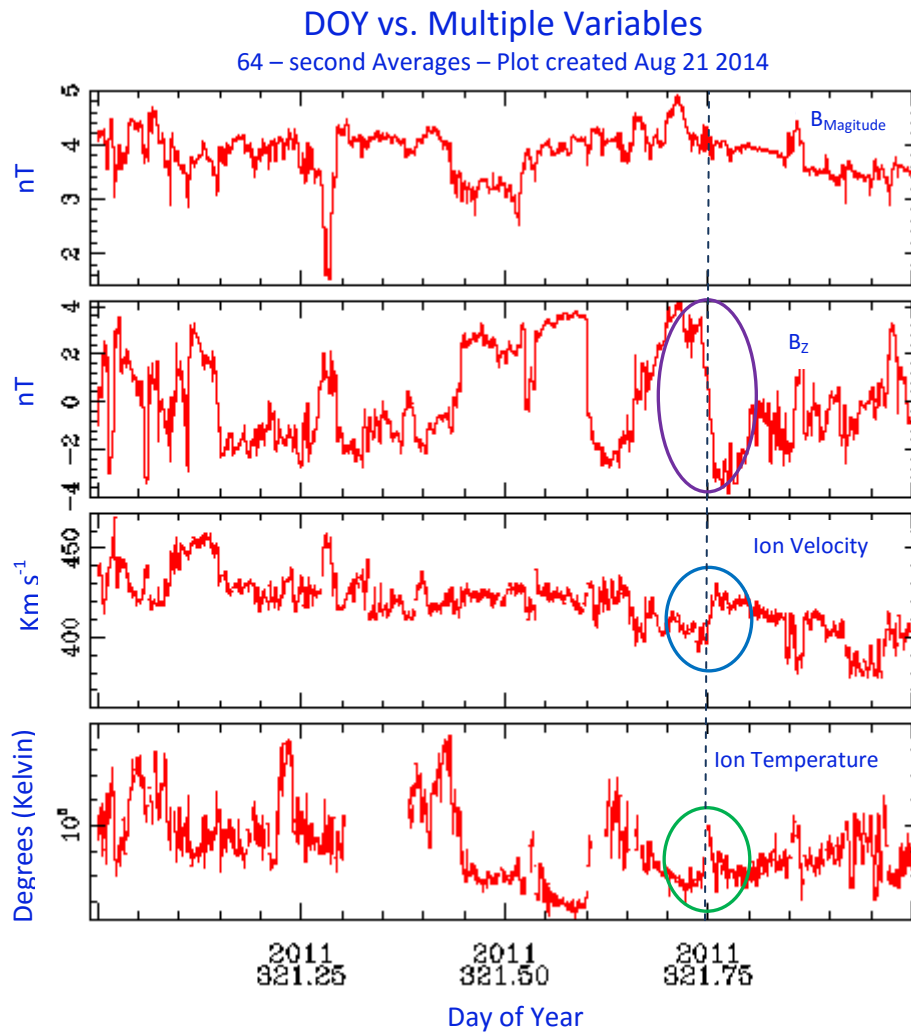


**Figure 6.15** ACE SWEPAM *in-situ* measurements of the magnetic field magnitude and  $B_z$  (nT) component, ion velocity ( $\text{km s}^{-1}$ ); and ion temperature (K). A dashed blue line at 321.75 indicates the time that the CME is believed to have passed the ACE spacecraft causing sudden changes in the components being observed. Data and graph production courtesy of the ACE science center (<http://www.srl.caltech.edu/ACE/ASC/>).

To ultimately conclude the CME observation it desirable to observe the north-eastern flank of the CME interact with the Earth as its predicted trajectory predicted that this would occur. Near Earth *in-situ* data from ACE has been examined to verify if the spacecraft detects any evidence that the CME maintained its trajectory and interacted with the Earth's magnetosphere. Figure 6.15 shows the *in-situ* measurements of the magnetic field (magnitude and  $B_z$  component), ion velocity and ion temperature. The CME was estimated at the Earth at a time between 18:00 UT and 24:00 UT on the 17 November 2011, this corresponds to the day of year (DOY) of 321.75 to 322.00. At 321.75 a sudden increase in the ion temperatures (circled green) and velocities (circled blue) along with a

very strong fall of the IMF  $B_z$  component (circled purple). This is a good indication that an event such as a CME has passed ACE.

As the CME has been detected a small distance ahead of the Earth it was of interest to see if there had been any disturbance in the Earth's magnetosphere. Magnetometer data from the Ny Ålesund, Hopen, Bjørnøya and Tromsø sites hosted by Tromsø Geophysical Observatory (TGO) were used to see any disturbance and the results are given in figure 6.16. At 20:00 UT on 17 November 2011 a sudden change in the magnetosphere was observed to occur. The evidence gathered from ACE and TGO leads to the conclusion that the CME flank has indeed interacted with the Earth and caused a disturbance in the Earth's magnetosphere.

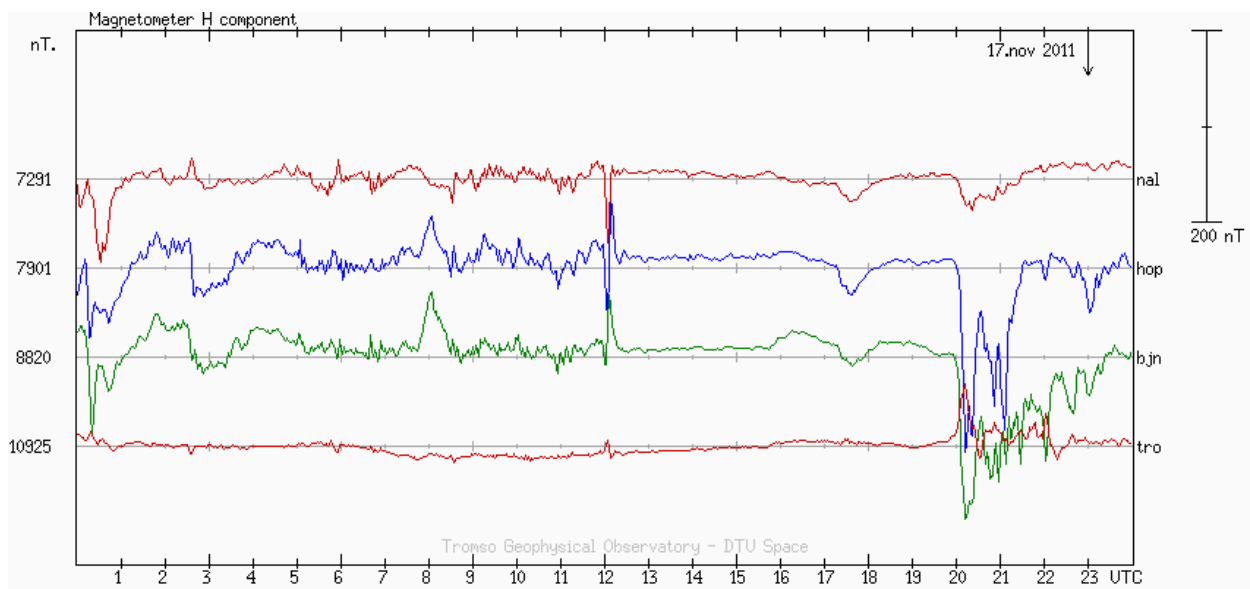


**Figure 6.16** Magnetometer H component data from the Ny Ålesund, Hopen, Bjørnøya and Tromsø sites hosted by Tromsø Geophysical Observatory (TGO) on 17 November 2011. Data and graph production courtesy of TGO (<http://flux.phys.uit.no/stackplot>).

# Chapter 7

## Ballistic Extrapolation Modelling of the Parker Spiral

Mapping of the solar wind from the Sun to Earth orbit is essential to make connections between different solar wind conditions measured in interplanetary space and observed features at the Sun. LASCO C2 observations are used to produce tomographic density maps of the solar corona at  $5 R_{\odot}$  which are used as inputs for a ballistic extrapolation model. This model is used to determine solar wind velocities and densities throughout the heliosphere, with particular focus on a comparison with in situ measurements at 1 AU. The *in-situ* data can be used to verify or improve the model predictions. The technique is therefore a new and novel automated method to map structure throughout the inner heliosphere, without the complexity and computational expense of MHD models, and with a unique empirical boundary condition at  $5R_{\odot}$ .

This method is applied to eight cases covering a time period between 2006 and 2012, with Carrington rotations 2043, 2044, 2046, 2062, 2072, 2081, 2105 and 2128. The investigated time period begins near solar minimum and concludes during the maximum of solar cycle 24, for which the model consistently obtains strong correlations with the *in-situ* data of Wind and ACE.

### 7.1 Parker Spiral Modelling

White light coronagraph observations of the solar corona are routinely made at heights up to  $30 R_{\odot}$  by the LASCO and COR2 instruments aboard SOHO and STEREO. Coronal densities have been estimated using solar rotational tomography for heights below  $\sim 5 R_{\odot}$  (e.g. Morgan, Habbal & Lugaz 2009; Frazin 2000). Further from the Sun white light observations become more difficult to convert to density as the F-corona becomes dominant. In situ measurements of density and other measurable characteristics are limited to single points. To account for this, the solar wind may be modelled from the available data sources using models of solar wind propagation (i.e. the Parker

spiral) combined with models of how the solar wind interacts with itself to produce features such as stream interaction regions (SIRs) and stream rarefactions regions (SRRs). Two methods of solar wind modelling are currently employed; ballistic extrapolation modelling; and magneto-hydrodynamic modelling (Riley and Lionello, 2011).

A ballistic extrapolation model for the mapping of solar wind streams is the simplest form of stream modelling which requires a relatively small amount of data input. For a ballistic model the minimum information required is the velocity at the initial location which can then be used to project the solar wind streams to a new region of the heliosphere, assuming that the plasma parcels travel through the heliosphere while maintaining a constant velocity. The ballistic approach initially may produce large errors while mapping for very large distances. Small uncertainties in velocity grow to large discrepancies with increasing height from the Sun. There is also uncertainty regarding the acceleration of the wind at heights below  $\sim 20R_s$ , and subsequent deceleration in interplanetary space. Stream-interaction regions and rarefaction regions which result in density and velocity irregularities can also lead to error (Riley and Lionello, 2011). To account for these irregularities, and in the absence of high resolution MHD modelling and a full understanding of the interaction, additional approximations are necessary.

Magneto-hydrodynamic (MHD) models such as global heliospheric MHD and time-stationary MHD models have the potential to provide more accurate and physical meaningful results. MHD models however, are very slow and complex (Riley and Lionello, 2011) whereas ballistic modelling is very fast and is still an effective tool for modelling the quiescent solar wind.

## 7.2 The Model

The tomographic ballistic model has been programmed using *Interactive Data Language* (IDL) a data analysis programming language developed by *ITT Visual Information Solutions* (ITT VIS) (<http://www.exelisvis.com>) alongside the specialist solar physics libraries of *SolarSoftWare* (SSW).

The ballistic tomographic parker spiral model uses an initial density input from tomographic Carrington density maps of the quiescent solar wind taken at  $5R_s$  from which, slow and fast solar wind streams are also defined. The model may be applied using two different methods.

- Initial values for outflow velocities of the slow and fast streams are based on sensible estimates gained from measurements by *in-situ* spacecraft (e.g. Wind or ACE), or if available,

IPS velocity estimations. These initial estimates are used to ballistically project the solar wind streams outward to 1.2 AU using the Parker Spiral model described below.

- Velocities may be estimated within the model through computational fitting using in-situ density data from the Wind spacecraft. During the ballistic propagation, the stream densities are corrected to account for the dissipation over distance and also for the changing separation between streams of different wind speeds.

A Carrington map at the new distance is produced using the new positional and density data which can then be compared with its original to show how the solar wind has developed or predict what may be observed at this distance, i.e. the Earth. The model may interpret the solar wind densities, from Carrington maps, and dynamics, from Parker spiral map, at any given distance in the heliosphere (ideally within than 1 AU). This makes the model an effective tool for the interpretation of the solar wind and quiescent structures which may also be observed by other techniques.

The modelled density estimation may be compared with real *in-situ* data from spacecrafts where correlation and covariance is performed on the data to determine its goodness of fit. Due to the fast nature of the model's performance, this step may also be used to improve initial estimates of velocities by determining the highest correlations for the model from multiple velocity profiles, which allows the model to conclude the best velocities for the model through and fully automated empirical method. The steps involved in the model are discussed in detail the following sections.

### **7.2.1 Tomographic Carrington Maps**

Separation of coronagraph images into quiescent and dynamic component (Morgan, Byrne and Habbal, 2012) allows an improved study of coronal large-scale structure without the disruptive signal from large CMEs. The quiescent component allows the application of rotational tomography to estimate the 3D coronal density structure even at times of high solar activity. The tomography density maps are created for a spherical shell of the corona at a height of 5Rs using the following steps (Morgan, private communication):

- Separation of LASCO C2 images into dynamic and quiescent components. Over two weeks of data is needed to create one tomography map.
- Application of new calibration methods, and F-corona removal, to the quiescent component to obtain an estimate of the K-coronal brightness in Mean Solar Brightness (MSB) units.

- Extraction of a thin slice (annulus section) of MSB brightness at a height of 5Rs for each observation, resulting in a Carrington map of K-coronal brightness over two weeks.
- Back-projection of the brightness values over extended lines of sight into a spherical shell reconstruction volume, with a lower height of 5Rs and maximum height  $\sim 10R_s$ . For this purpose, the emission is assumed to have a  $r^{-2.2}$  decrease with height.
- Calculating mean emission in each voxel, and use the reconstruction volume to create a new synthetic Carrington map by line-of-sight integrations.
- Calculate difference between synthetic and observed Carrington map. Backproject differences into reconstruction volume and iterate until convergence is achieved.
- The final step is to convert the volume emissions into densities using standard formulae (see Quemerais & Lamy 2002).

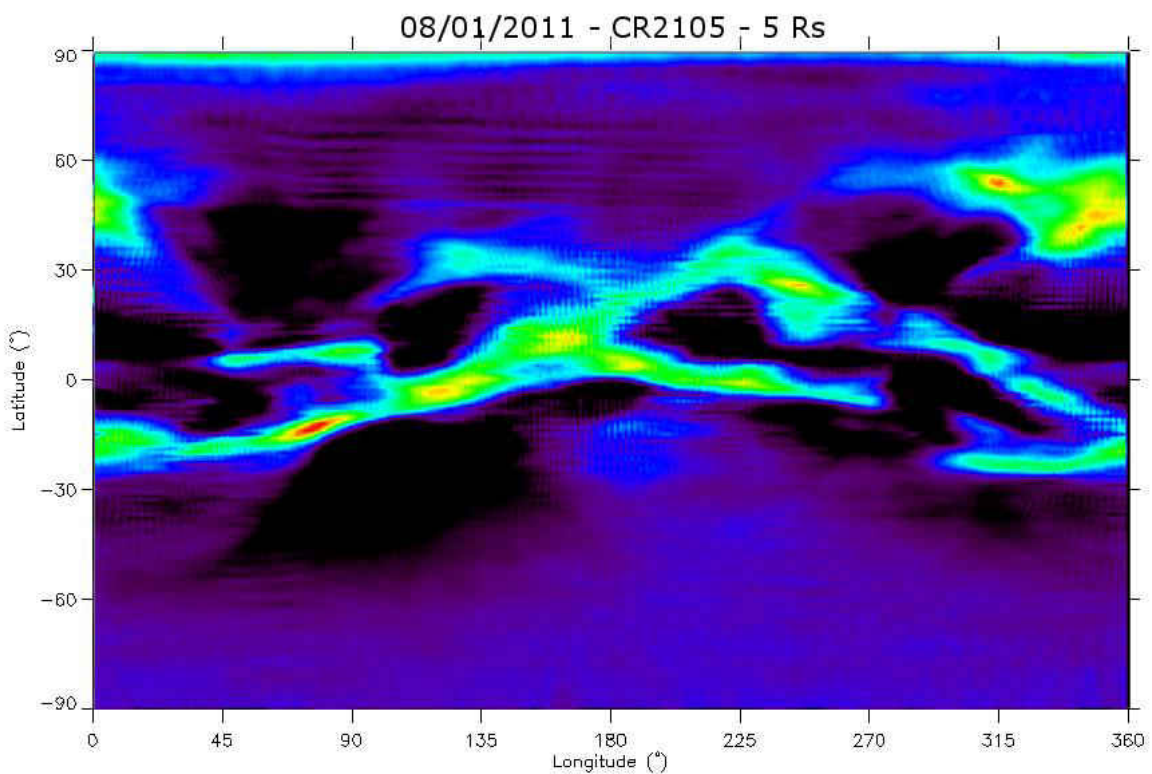


**Figure 7.1** Tomographic map for a Carrington rotation centred on centred on 8 January 2011 (Carrington rotation 2105) which has undergone the NRGF process. The red end of the color spectrum indicates the higher density regions whereas the purple and black end of the spectrum indicates the low and very low density regions

Figure 7.1 shows an example tomographic reconstruction map of the quiescent solar wind centred on 8 January 2011 (Carrington rotation 2105).

We assume that regions of high density are associated with slower streams and inversely the regions with very low density can assumed to be associated with fast solar wind streams. This assumption allows easy distinction between the slow and fast stream regions by a direct conversion of the tomography map densities into radial outflow velocities. The conversion is such that the solar wind is slow where density exceeds a certain threshold, given by:

$$\rho_{\text{norm}} \geq \frac{\rho_F}{10} \quad (7.1)$$

Where:

$\rho_{\text{norm}}$  = The normalised density,

and  $\rho_F$  = Density filter scale.

The density filter scale is thus a thresholding value at which the normalised density is limited to determine the slow (and intermediate) solar wind streams. The solar wind streams are considered fast elsewhere.

Figure 7.2 green component demonstrates the thresholding effect when a filter of  $\rho_F = 2.2$  is applied to the tomographic map centred on 8 January 2011. The majority of the ambient solar wind has been removed leaving only the high density, slow wind streams visible. Increasing the threshold further results in figure 7.2 blue component, for which a threshold of  $\rho_F = 3.0$  has been applied. To increase the complexity of the system two filter values can be applied to the tomographic map, one filter which isolates the very high density structures as slow wind streams and a second filter which can allow less dense material to have an intermediate solar wind velocity. For each unique case study new  $\rho_F$  values are manually determined so that the optimal filter radius may be obtained and applied.

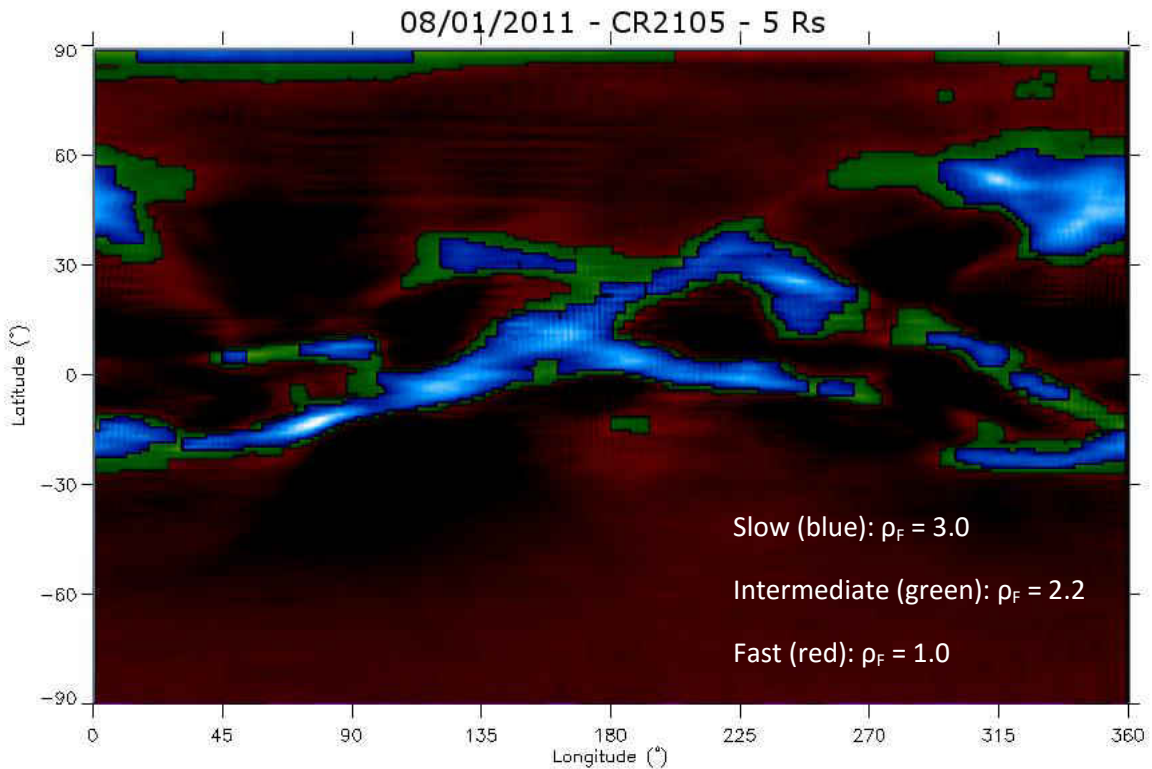


**Figure 7.2** Composite tomographic map for a Carrington rotation centred on 8 January 2011 (Carrington rotation 2105) showing the effects of different filtering values to define the solar wind velocity bands in a tri-modal solar wind system. The slow solar wind ( $\rho_F = 3.0$ ) is indicated in blue, the intermediate solar wind ( $\rho_F = 2.2$ ) in green, and the remaining fast solar wind in red ( $\rho_F = 1.0$ ).

### 7.2.2 Ballistic Propagation of the Parker Spiral

Once the solar wind stream velocities have been determined from the tomographic maps the propagation of these streams through the heliosphere can be mapped through ballistic methods. The solar wind propagates radially from the Sun however the rotation of the Sun produces a spiral-like effect in which the solar wind plasma and magnetic field are entrained within. As assumed by Parker (1958), there are no particle interactions within the solar wind plasma due to the assumption that the magnetic field is frozen into the solar wind plasma. In this model the solar wind acceleration and solar gravitation,  $b$ , are neglected and thus the radial flow velocity,  $v$ , of the solar wind is constant and its rotation is depicted solely by the rotational velocity of the Sun. Each pixel in the tomographic map is assigned as a unique solar wind stream with a velocity estimated from its density in the tomography maps, for which its position in the heliosphere can be propagated from 5  $R_S$  outwards into the heliosphere to a distance,  $r$ , using equation 7.3.

$$\varphi = \left( \frac{\omega}{v \sin \theta} \right) \left( \left( \frac{r}{b} \right) - 1 - \ln \left( \frac{r}{b} \right) \right) + \varphi_0 \quad (7.3)$$

Where:

$\varphi$  = Carrington longitude of stream,

$\varphi_0$  = Initial Carrington longitude of stream,

$\theta$  = Carrington latitude,

$\omega$  = Angular velocity of the Sun,

and  $b$  = Distance at which gravitation and solar wind acceleration can be neglected.

As the solar wind contains numerous streams with different velocities it is inevitable that faster streams will encroach on the slower streams, reducing the separation between the preceding streams and increasing the separation between trailing slower streams. Eventually the faster stream will catch the slower stream and the faster stream will be impeded, affecting the velocities of the streams and the densities of the surrounding region. A detailed description of stream interaction regions (SIR) and co-rotating interaction regions (CIR) are given in chapter 1. As the solar wind streams are not able to cross other streams, due to the plasma being 'frozen-in' to the magnetic field, it is important that restrictions are made in the model preventing fast solar wind streams from overtaking a stream which preceded it. Within this model a simplified approach has been taken to impede the flow velocities of a stream which approaches within  $0.5^\circ$  to a preceding stream, reducing its velocity to that of the preceding stream.

With the changing separations between solar wind streams it is inevitable that the stream densities will vary, decreasing or increasing with greater or smaller stream separation to form compressions and rarefactions. In the model, the stream density is assumed to be evenly divided between its surrounding solar wind streams which at the model base have a regular spacing of  $1^\circ$ . To account for any stream compression or dispersion, the density is calculated between the half distance of the preceding and proceeding solar wind streams, and is scaled against the base separation. The model thus conserves mass flux within any discrete stream. Figure 7.4 shows the final Parker spiral solution as calculated by the method.

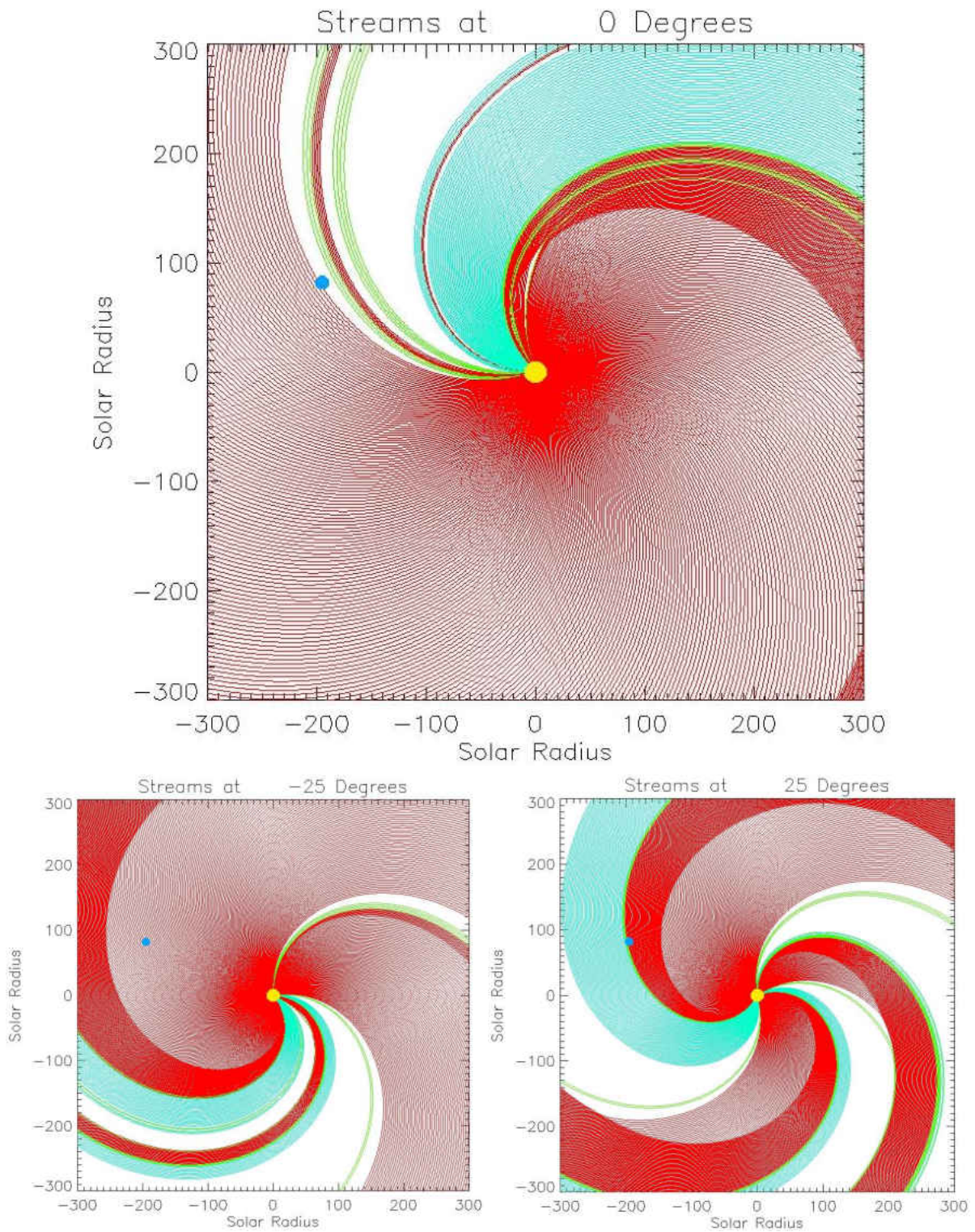


**Figure 7.3** Parker spiral maps for Carrington rotation 2044, centred on the 14 June 2006 showing the solar wind streams as at latitudes of  $0^\circ$ ,  $-25^\circ$  and  $25^\circ$ . Light blue streams represent slow solar wind ( $400 \text{ km s}^{-1}$ ), red streams the fast solar wind ( $600 \text{ km s}^{-1}$ ), and green streams the intermediate solar wind ( $550 \text{ km s}^{-1}$ ). The yellow and blue dots indicate the positions of the Sun and Earth in the ecliptic plane (not to scale). Axis are Cartesian equivalents of the Carrington coordinate system defined by the radial distance from the Sun and Carrington longitude.

### 7.2.3 Propagation of Density

The original tomography Carrington map contains the density information of the solar wind at 5  $R_s$ , which in principle enables an extrapolation of the density information into the solar wind streams by assuming mass flux conservation. In an idealistic model, no acceleration is assumed above 5  $R_s$  and the density will simply reduce naturally to an inverse square law over distance however remnant acceleration is present and must be accounted for within the model (Schwenn, 1990; Riley and Lionello, 2011). For this model a simple scaling factor  $\alpha$  has been introduced to correct the densities. A trial of samples covering both solar maximum and solar minimum periods between 2004 and 2012 was used to determine the optimum value of  $\alpha$  for this model. It was thus concluded that,  $\alpha$  consistently provided comparable densities with those measured by Wind at near-earth distance at a value of 2.3.

As the solar wind streams will not maintain a constant separation the densities must also be corrected. To account for the compression and rarefaction of the area of which the density is contained the half distances of the enclosing streams at the source and present distances have been used. As such the density,  $\rho$ , at distance  $r$ , is calculated using equation 7.4.

$$\rho = \rho_i \frac{D_b}{D} \left( \frac{r_i}{r} \right)^\alpha \quad (7.4)$$

Where:

$r_i$  = Solar radius of initial density observation,

$\rho_i$  = Density (number of protons per  $\text{cm}^3$ ) at distance  $r_i$ ,

$D_b$  = Total distance between target stream and half distance of surrounding streams at  $r_i$ ,

$D$  = Total distance between target stream and half distance of surrounding streams at  $r$ ,

and  $\alpha$  = Scaling factor of density decline through the heliosphere.

### 7.2.4 Projected Density Carrington Maps

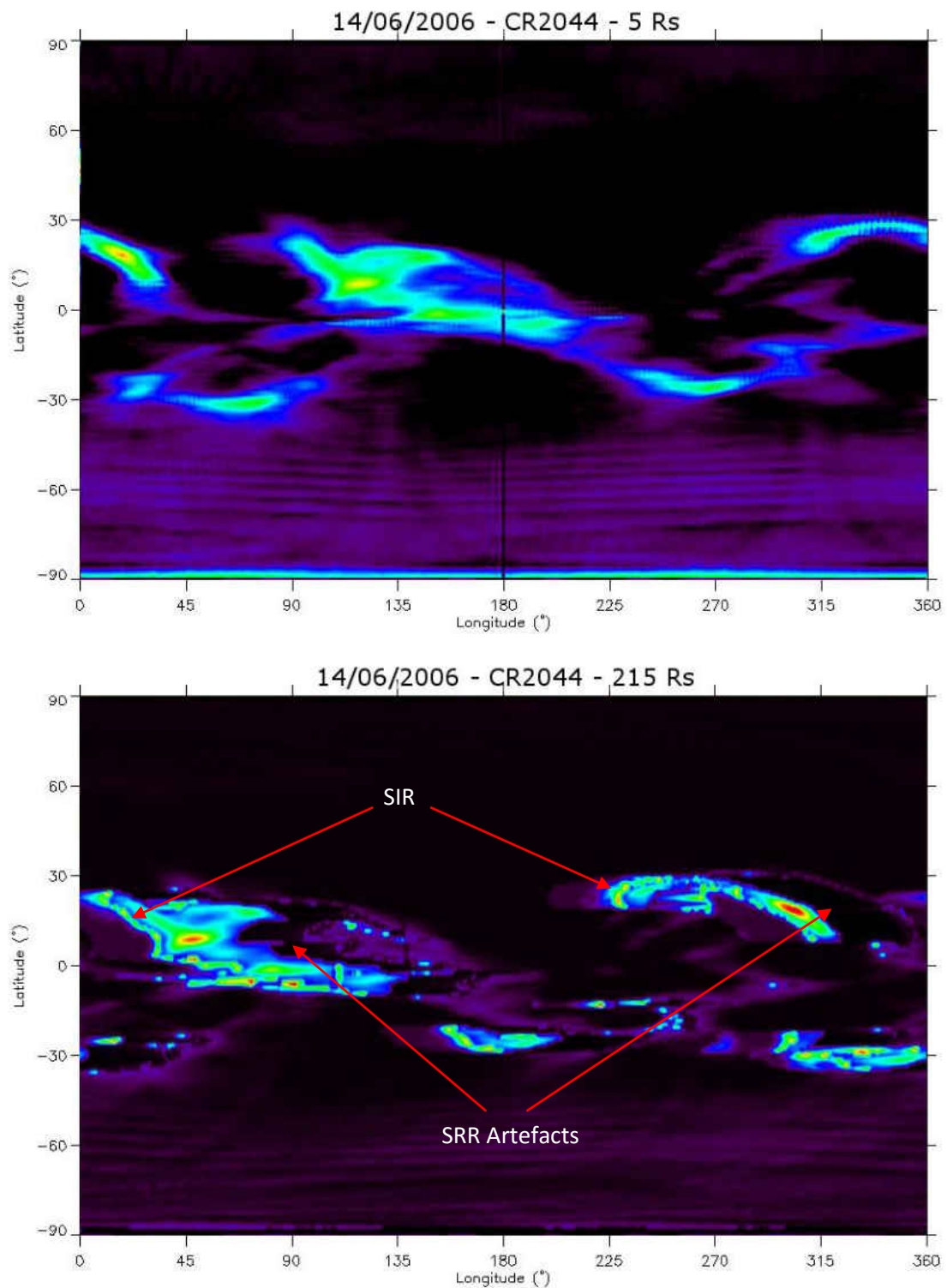
The heliospheric density model is thus incrementally built from the lowest height up to beyond 1AU. The model is time-independent and thus shows an estimated outflow from the quiescent solar wind. This results in the projected density Carrington maps showing the idealised quiescent solar wind

structure along with features which form due to different solar wind velocities (SIRs and SRRs), which may be used as an accurate background data source of the solar wind.

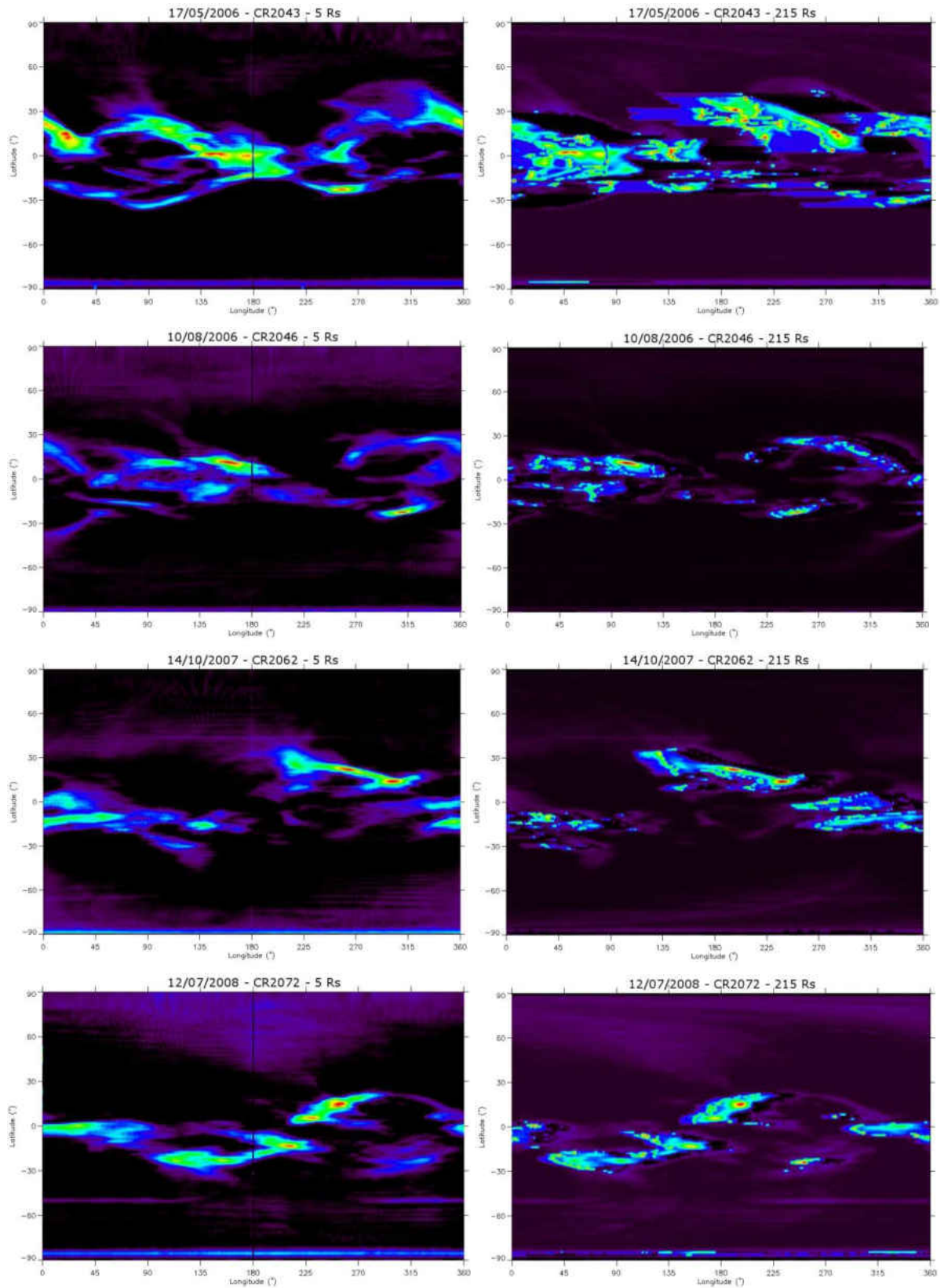
The projected density maps show the estimated density of the solar wind during the same Carrington rotation as the original maps, extrapolated to a greater distance from the Sun. As the quiescent solar wind is very slow to change this assumption is valid. The reconstructed maps accurately show the shift of the density profile which has occurred over the distance  $r$  due to the rotation of the Sun and stream velocities. They also show stream interaction and rarefaction regions which may develop within this distance due to the difference velocities of the solar wind streams. SIRs within the reconstructed maps will appear as thin latitudinal filaments which trail closely behind cells of slow solar wind streams. Conversely following faster streams a cell an artefact region of low density trailing the SIRs and also ahead of slow stream fronts occurs within the maps indicating the presence of a SRR.

The bottom map of figure 7.4 highlights the appearance of the SIRs and SRRs as they appear within the reconstructed density maps. The SRR appear as holes in the maps due to the fast decline of the density as the streams become very sparse in these regions. Figure 7.4 shows intense latitudinal bands of density which have formed behind high density slow solar wind cells. These bands are the SIRs which have formed from the faster solar wind streams which have now began to interact with the slow wind cells. As the SIRs are formed from the low density fast solar wind streams, a large number of these streams are required for a strong SIR to form. For a SIR to be prominent the north-south boundaries must be well defined with large a disparity between the densities of the SIR and the surrounding solar wind.

The reconstruction may be performed at any distance in the solar wind, however by default this is set to  $215 R_{\odot}$  so that the structure of the solar wind may be determined within the radius of the Earth orbit, which also provides an easy comparison with near-Earth based spacecraft data. Figure 7.5 shows the original tomographic maps at  $5 R_{\odot}$  alongside projected maps at  $215 R_{\odot}$ . Reconstructions at distances less than  $215 R_{\odot}$  provide a good interpretation of the densities within the interplanetary space while also mapping the quiescent density structures as they form. The reconstructions combined with the more-global Parker spiral map can provide a powerful tool for the interpretation of the intermediate space between the Sun and Earth absent of the restrictions of spacecraft positions and field of views.



**Figure 7.4** Tomographic maps for Carrington rotation 2044, centred on the 14 June 2006. The upper panel is taken using tomography from LASCO C2, and the lower panel is a projected map at 215  $R_s$  using the ballistic Parker spiral model. Examples of the visual appearance of SIRs and SRRs in the maps are highlighted.



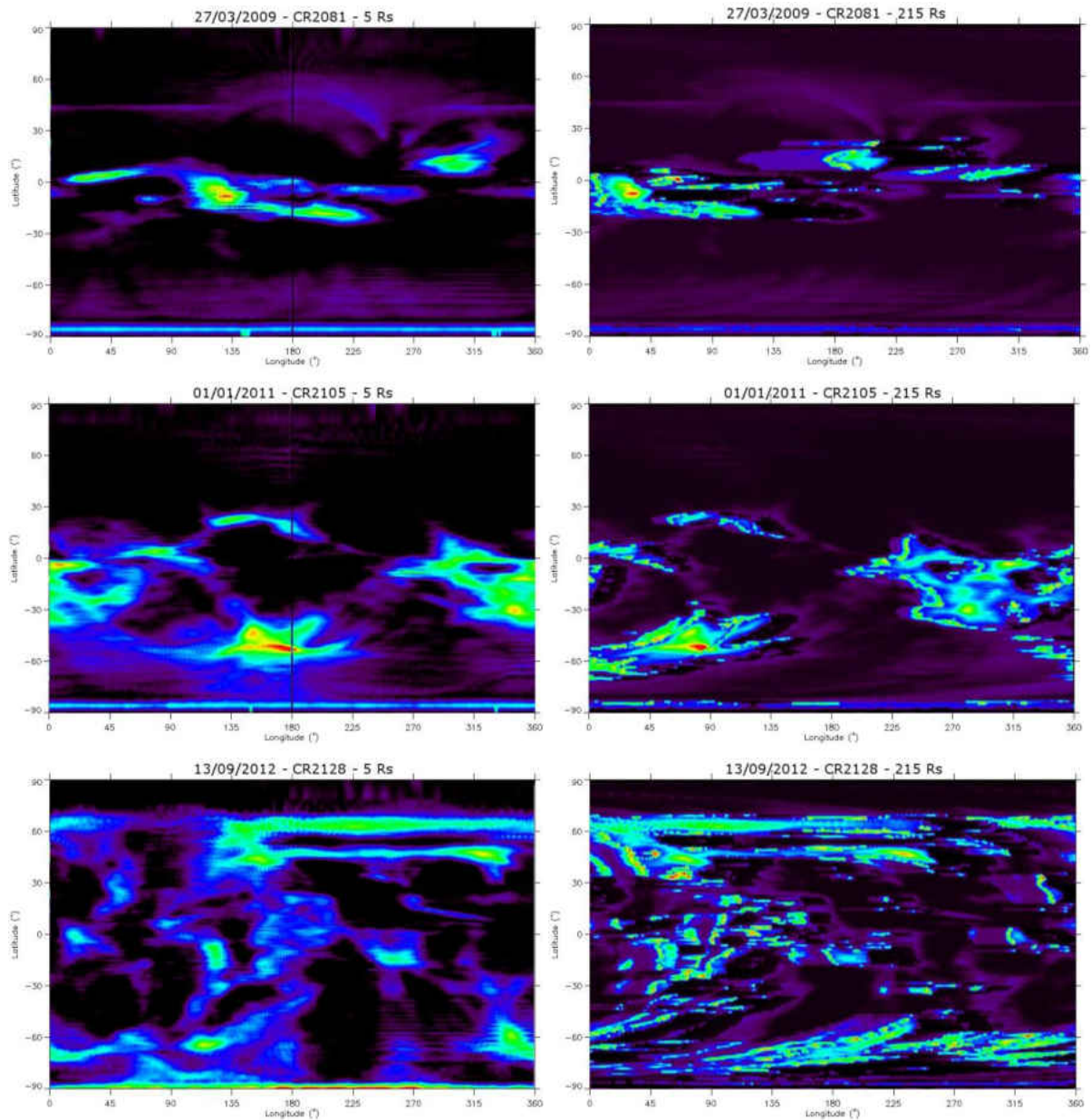


**Figure 7.5** Tomographic maps for a sample of Carrington rotations between 2006 and 2012. The left-hand panels are produced using tomography of LASCO C2, and the right-hand panels are projected maps at 215  $R_s$  using the ballistic Parker spiral model.

### 7.3 Fully Automated Velocity Fitting

The ACE and Wind spacecrafts, in halo orbits around the Sun-Earth L1 (Lagrangian) point, have been used to compare the observed solar wind with model density at a distance of approximately 1 AU. ACE and Wind provide near continuous observations of the solar wind with data available from before 2004 (for which tomography maps are currently produced) until present and each provide

density and velocity data of the solar wind with high accuracy. The position of the spacecraft are converted to Carrington spherical coordinates and mapped onto the 3D model density space. This enables a direct comparison of observed and modelled densities. Provided appropriate velocities are selected for the solar wind model the densities should show reasonable agreement.

To quantify the agreement between observed and modelled densities, linear Pearson correlation is performed. CMEs are of course absent from the tomography maps and ballistic model, but are measured by the *in-situ* data. This is a hindrance to comparing the model and observation, particularly during solar maximum activity. During such periods the number of dynamic events in the solar wind dramatically increases and the complexity of the solar wind structure also increases. This causes an increased number of discrepancies between the modelled data and the observed *in-situ* data thus it is expected that the correlation strength will decrease during solar maximum. During solar minimum the correlation coefficient will commonly encompass 0.4 with rare cases surpassing a coefficient of 0.5 and conversely during solar maximum the correlation coefficient will commonly encompass 0.3 with rare cases surpassing a coefficient of 0.4. Although the correlation strength decreases with high activity the correlation still remains reasonably strong.

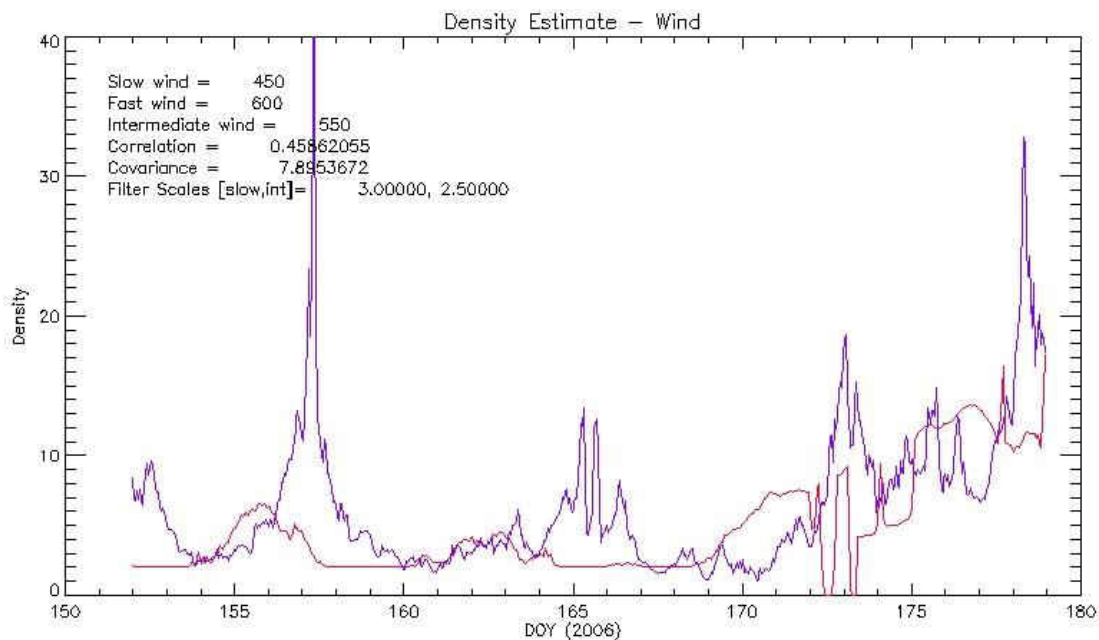


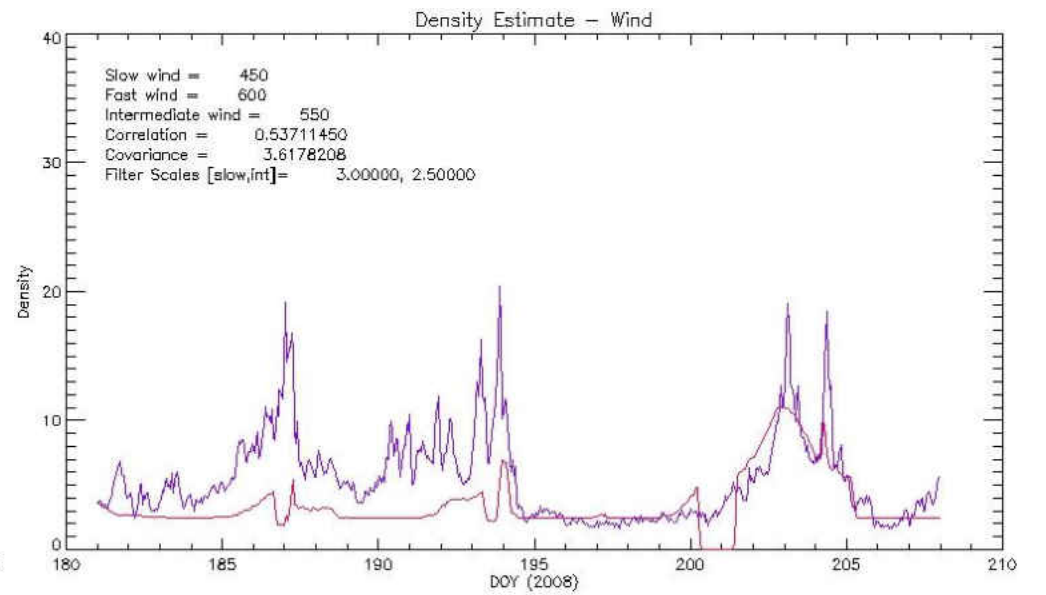
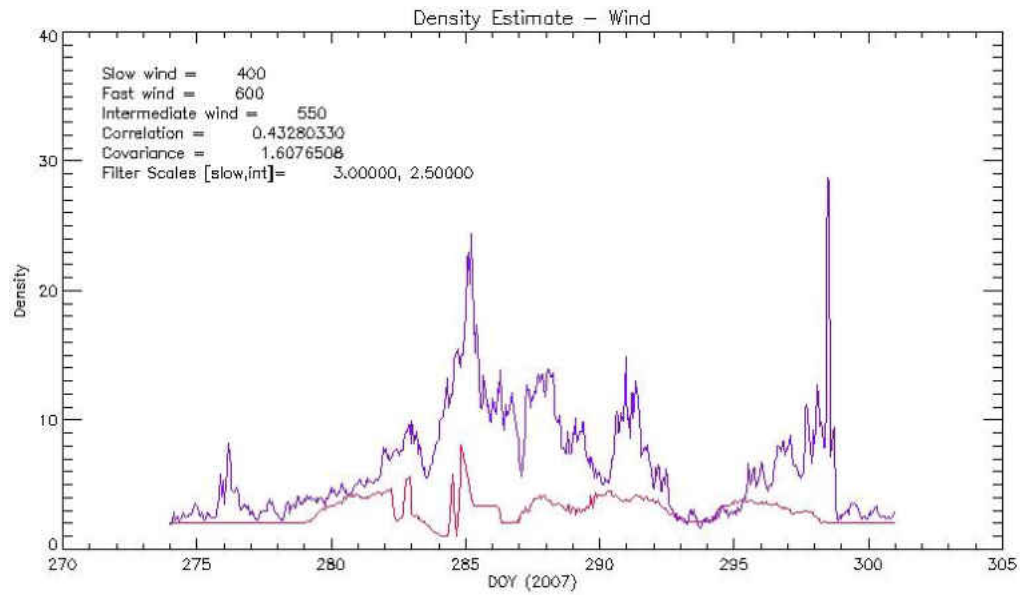
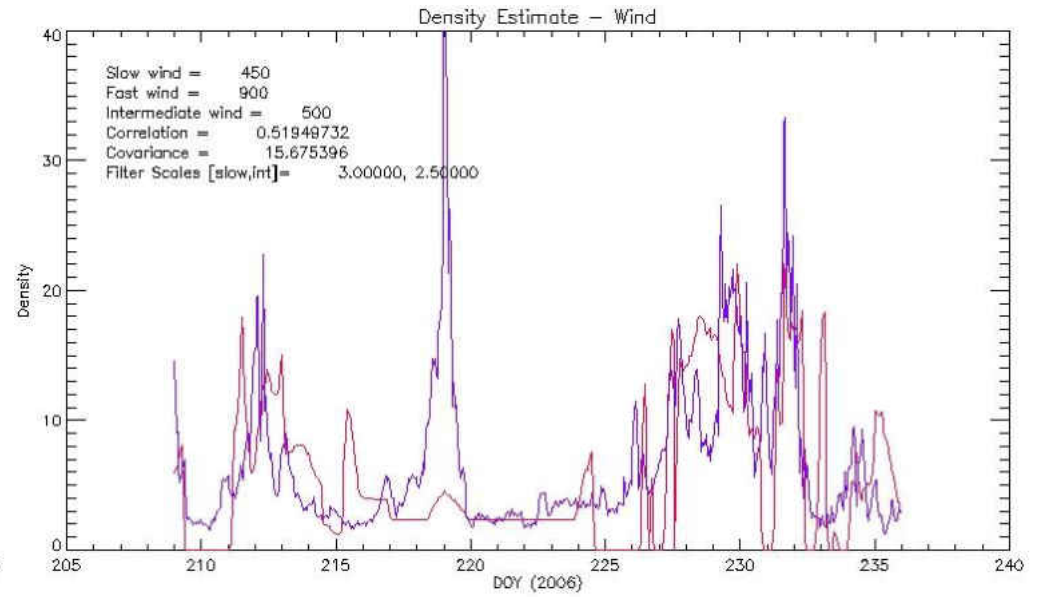
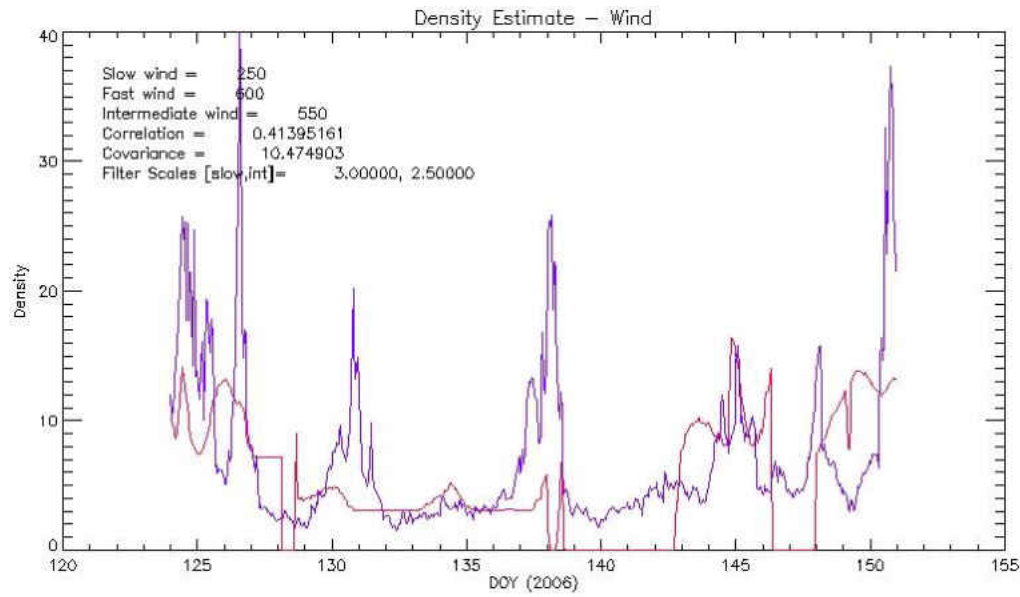
**Figure 7.6** Comparison of density functions for Wind *in-situ* data (purple) and the model densities at the location of Wind (red) for Carrington rotation 2044, centred on the 14 June 2006 (DOY 165).

As the model is a very computationally efficient extrapolation, it is relatively quick to adjust input velocities to produce improved correlation with *in situ* observations. A Monte-Carlo form of analysis

can be performed with variations in all three; slow; intermediate; and fast, solar wind input velocities to explore how the model output varies with each profile. By determining the correlation strengths of the model from a preset range of velocities a peak in the correlation strength will reveal the optimum velocities for the model. This velocity fitting method is thus very fast and its accuracy is dependent on the preset velocities which may be profiled and may be further improved by sacrificing processing speed.

Figure 7.6 displays the density for Wind *in-situ* data and the model densities at the location of Wind for Carrington rotation 2044. The large CMEs observed by Wind on the day of years (DOY) 157, 165 and 175 do not appear in the model predictions. With the slow, intermediate and fast stream velocities of  $450 \text{ km s}^{-1}$ ,  $550 \text{ km s}^{-1}$  and  $600 \text{ km s}^{-1}$  respectively the model density function produced results with a strong correlation coefficient of 0.459 and a covariance of 7.895. The model for this case study has therefore predicted reliable densities projected up to approximately 1 AU and their positions have been mapped accurately. This gives confidence in the mapping of the solar wind structure within the whole model, and the input outflow velocities must be reasonable estimates of the true velocity.

A sample of density comparisons produced using the fully automated method with Wind is displayed in figure 7.7.



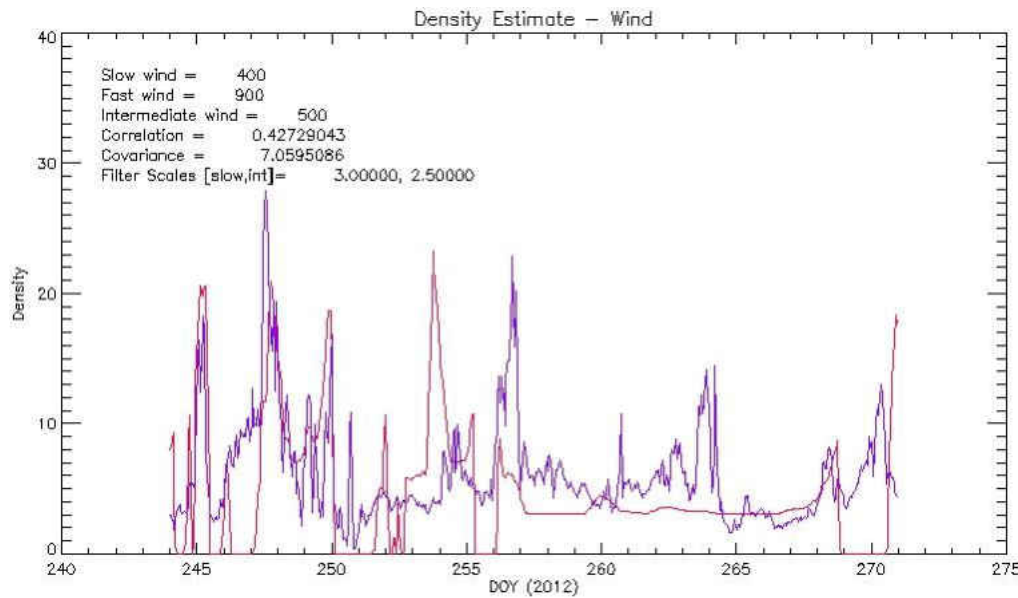
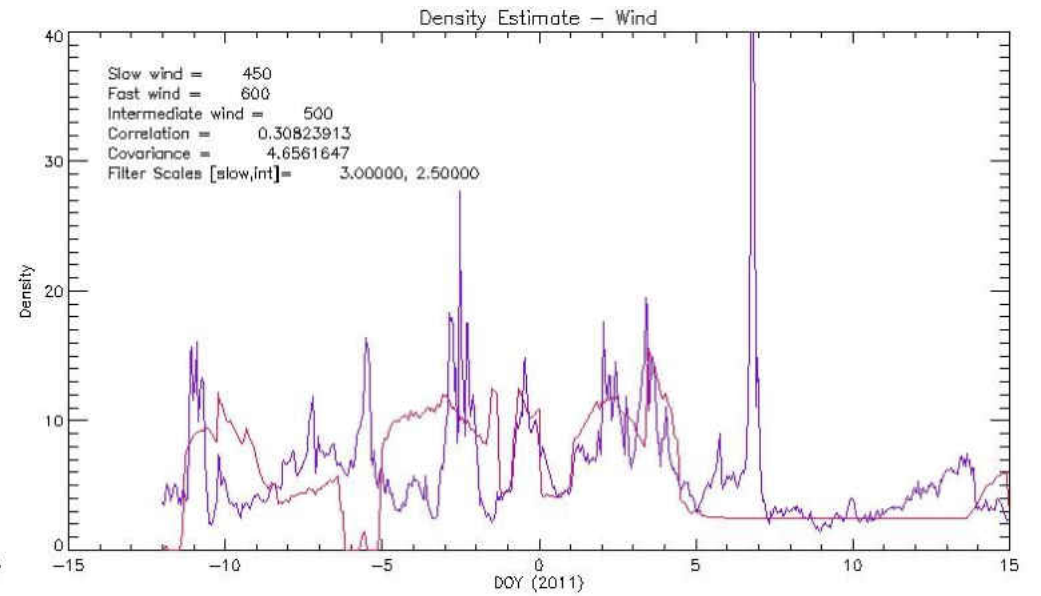
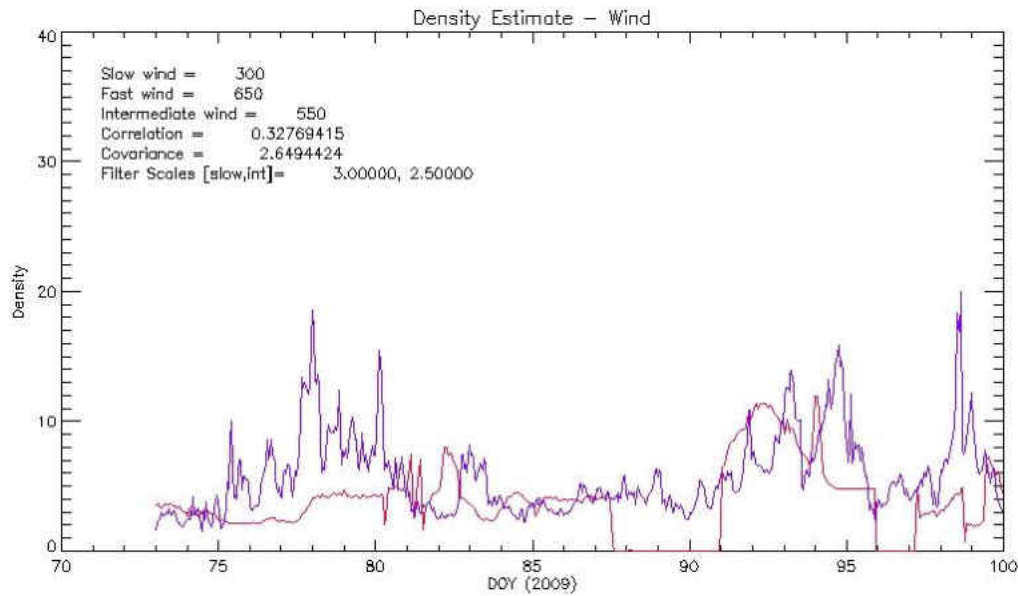
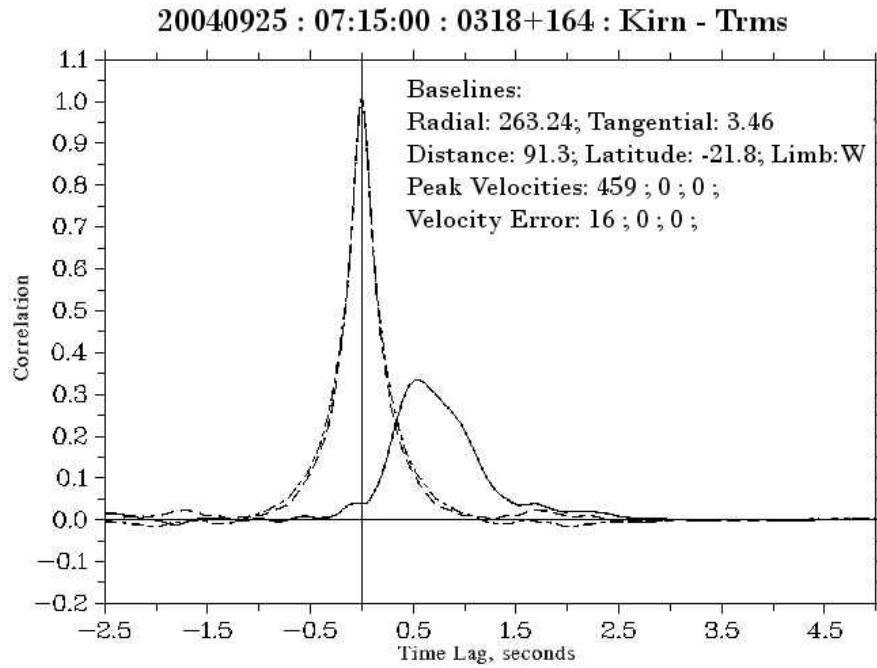


**Figure 7.7** Comparison of density functions for Wind *in-situ* data (purple) and the model densities at the location of Wind (red) for a sample Carrington rotations between 2006 and 2012 cover time periods within solar maximum and solar minimum. The model continues to provide strong correlations within the more complex solar maximum period although the correlation strength tends to fall during highly active periods due to the increased number of dynamic structures present in the Wind data which are not present in the model.

### 7.3.1 Velocity Profile Fitting and Remote-sensing Velocity Input

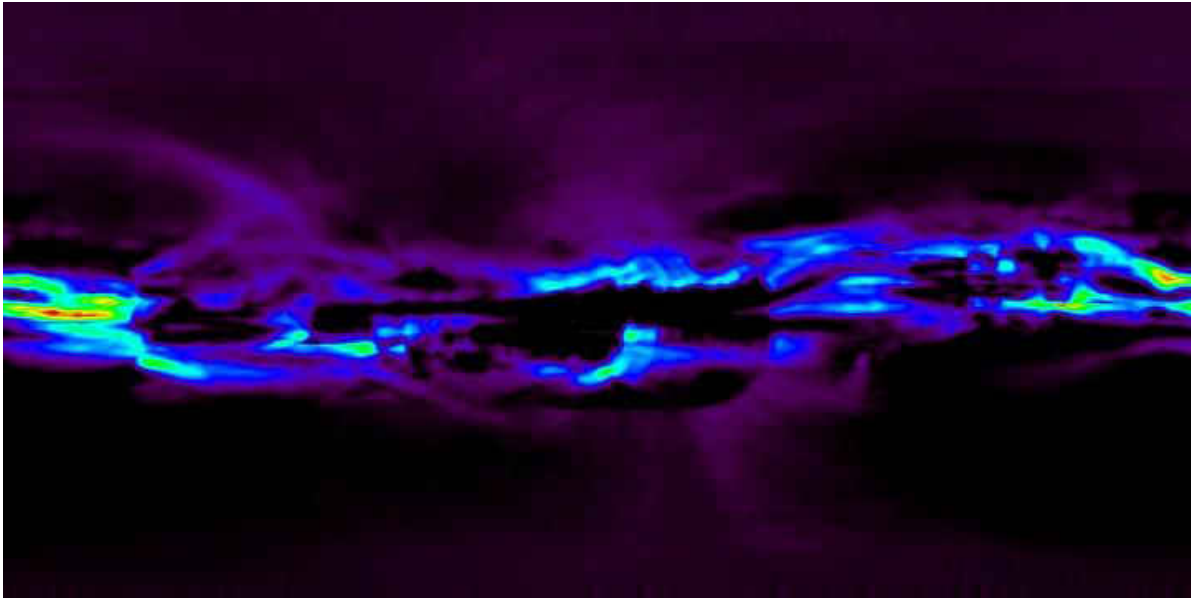
An IPS experiment was performed on 25 September 2004 at 07:15 UT using the source J1042-120. This experiment estimated stable velocities of the solar wind with a velocity of  $459 \text{ km s}^{-1} \pm 16 \text{ km s}^{-1}$ . The experiment observed for 15 minutes and during this period displayed no evidence of any CMEs or transients crossing the ray path during the observation and maintained correlation strength of  $\sim 35\%$ . The cross-correlation function of a sample integration period is shown in figure 7.8. As there are no features of a transient crossing the ray path it can safely be assumed that the IPS experiment is observing the quiescent solar wind at an intermediate flow velocity and is suitable for use as an intermediate velocity input for the ballistic extrapolation model. The P-point of this IPS observation was located at the Carrington coordinates  $287.4^\circ$  longitude and  $8.7^\circ$  latitude at a distance of  $91 R_s$ . On 28 September 2004 at 14:15 UT a second IPS experiment was performed observing the radio source J1150-003. This observation estimated solar wind velocities of  $741 \text{ km s}^{-1} \pm 66 \text{ km s}^{-1}$ . The P-point for this second observation was located at the Carrington coordinates  $259.8^\circ$  longitude and  $-5.4^\circ$  latitude, at a distance of  $30 R_s$ . As no remote sensing velocity estimates are available for the slow solar wind velocities during this Carrington rotation, a sensible estimate of  $350 \text{ km s}^{-1}$ , based on *in-situ* measurements from ACE, was used.

Figure 7.9 shows the tomographic map of Carrington rotation 2021 which has been used in the comparison of methods. Figure 7.10 shows the correlation of the density output by the ballistic projection and the in-situ density as measured by Wind. Using the IPS velocity values for the fast and intermediate wind velocities has given a correlation strength of 0.16. This correlation is weak however, the significant features in the density profile measured by Wind are apparent in the modelled density profile although it is apparent that they suffer from a small time delay. This is delay due to an over estimation of the slow solar wind (for which the default value of  $350 \text{ km s}^{-1}$  was used) which has caused a reduced correlation strength. For an optimum modelling it is thus recommended that the automated fitting technique should be applied to all unknown velocities.



**Figure 7.8** Cross-correlation functions of IPS experiment performed on May 2007 using the source J0318+164. The frames show the cross-correlation functions for two integration periods beginning at 12:18 UT and 12:27 UT. The axis and notations are as in chapter 5.

For comparison, the model was run in its fully automated mode to determine the velocity profile which obtains the strongest correlation between the Wind and modelled density profiles. This analysis method determined the strongest correlation to occur with the solar wind velocity profile of  $330 \text{ km s}^{-1}$  (slow),  $440 \text{ km s}^{-1}$  (intermediate) and  $810 \text{ km s}^{-1}$  (fast) with a correlation strength of 0.29. The density profile comparison for this velocity profile is shown in figure 7.11. The velocity profile determined through the fully automated fitting technique has given velocities comparable to those determined through IPS velocity estimations. The calculated velocities of the slow and intermediate solar wind speeds differed from the observational data by no more than 6% which shows a strong accuracy between them. The fast solar wind speed that had been calculated differed from the IPS velocity observation by 9.3% and the IPS velocity estimation had an error of 8.9%. Although the modelled velocity is outside of the upper limits of the IPS velocity it can still be concluded that the model retains comparative estimations of the velocity profiles of the solar wind with a high degree of accuracy.



**Figure 7.9** Tomographic maps for Carrington rotation 2021 produced from the quiescent component of the NRGF technique.

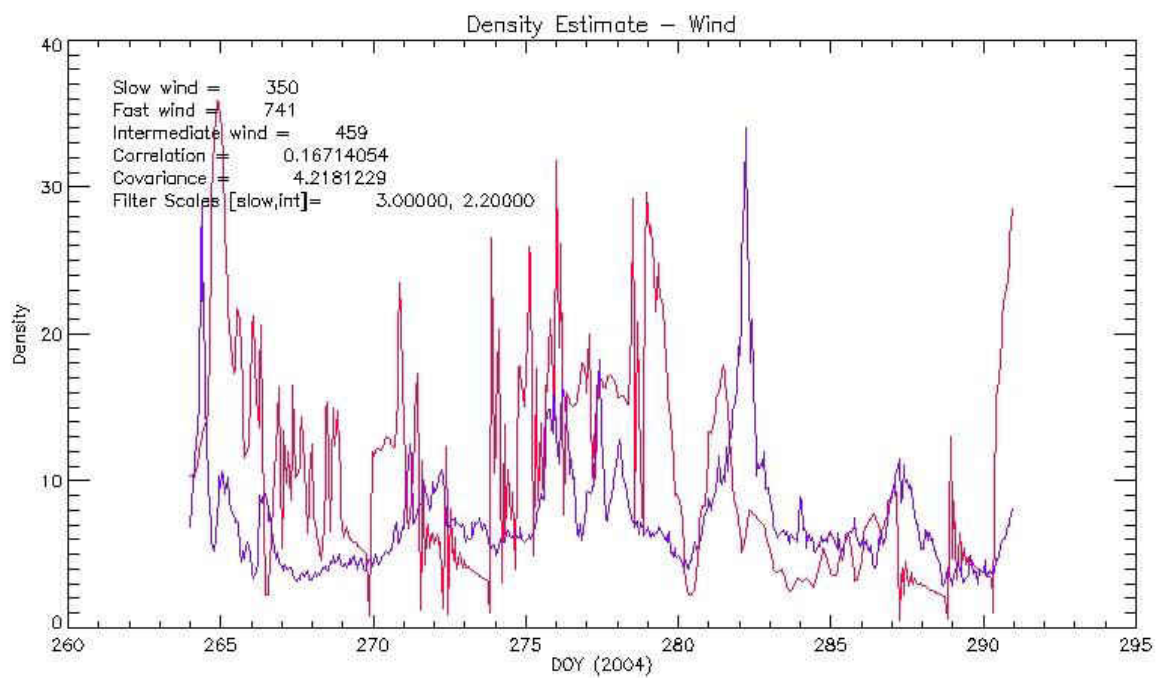


**Figure 7.10** Comparison of density functions for Wind *in-situ* data (purple) and the model densities at the location of Wind (red) using real IPS data for fast and intermediate solar wind velocities.

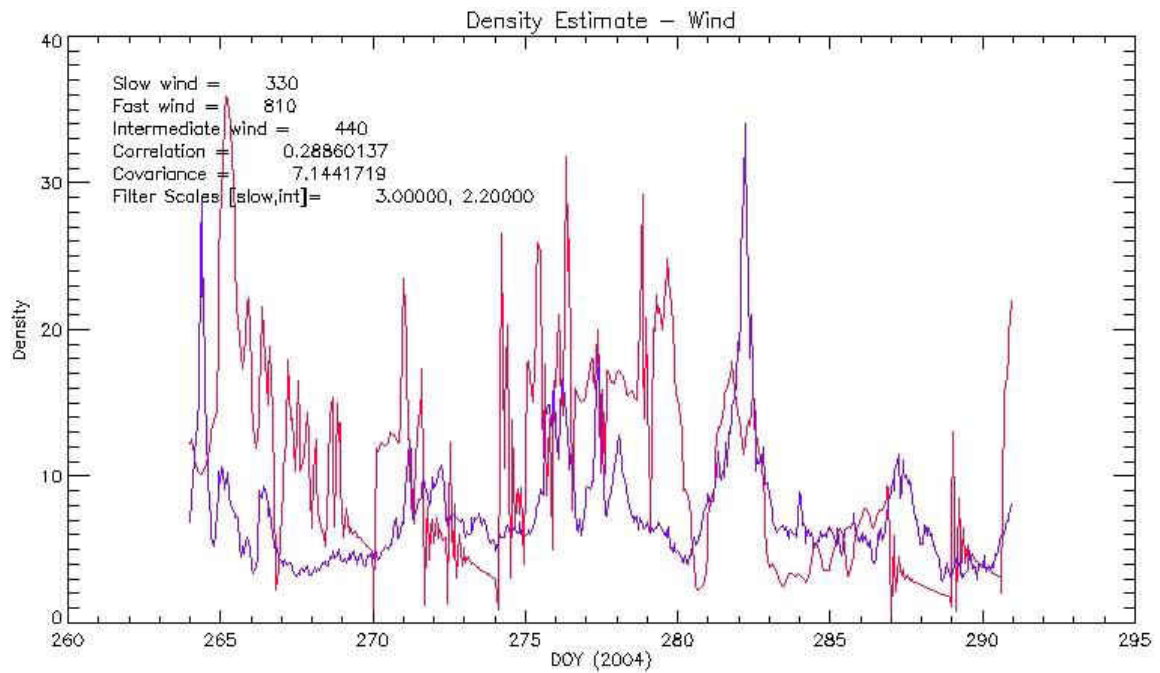


**Figure 7.11** Comparison of density functions for Wind *in-situ* data (purple) and the model densities at the location of Wind (red) using fully automated fitting method to determine the solar wind velocity profile.

## 7.4 Conclusions

Ballistic extrapolation modelling of the solar wind is a fast and effective method for modelling the solar wind propagation in the heliosphere. The ballistic modelling approach for the solar wind requires only one source of data. The white light tomography uses SOHO | LASCOS C2 observations to reveal the coronal density structure at a height of  $5 R_{\odot}$ . The densities are used to differentiate between slow and fast solar wind streams which may then be extrapolated out further into the heliosphere with their associated velocities determined from *in-situ* spacecraft observations and IPS velocity estimations.

Although only the quiescent corona is input into the model, stream interactions will inevitably occur when a faster solar wind stream catches a slower stream. When this occurs the faster stream may not overtake the slower stream but however is impeded, as such further streams will continue to develop into a SIR with an enhanced density profile. Conversely the faster stream regions will also accelerate away from slower regions leaving a void of low density as a SRR. The tomographic ballistic model accounts for these phenomena with an adjustment to densities according to mass flux

conservation. At approximately 1 AU the model density profile can be compared with *in-situ* density profile from spacecrafts such as Wind and ACE. The linear Pearson correlation between the model and *in-situ* density profiles validates the reliability of the model. Furthermore, the correlation can be used to adjust input outflow velocity in the model to maximise the correlation.

The model provides two useful outputs, the first being a map of the individual streams with empirically constrained densities and velocities throughout the heliosphere up to 1AU, thus giving an useful mapping between heliospheric and coronal features and a reasonably accurate mapping of SIRs and SRRs. The second is a map of density and velocity throughout the heliosphere - useful for interpreting other observations and useful for predicting solar wind conditions at Earth. The maps also have potential to provide a background, ambient, empirically-constrained model of the solar wind which can be used as empirical constraints on more sophisticated models.

The ballistic modelling of the parker spiral, which use of coronal tomography as the base data for of the quiescent solar wind is believed to be the first of its kind, using a unique source of data developed by Morgan, Byrne and Habbal (2012). As the separation technique isolates the quiescent solar wind a simple ballistic extrapolation approach is ideal. The ballistic approach requires a relatively small amount of input data to process the model when compared with complex MHD models. Additionally as the tomographic ballistic model does not require any complex models for relatively small-scale dynamic processes such as CMEs, it is very fast and efficient and has proved to provide reasonably accurate results of the quiescent solar wind. We have several ideas for further development. The method and model show great potential as a useful tool for solar wind research.

# Chapter 8

## Conclusions and Further Work

This chapter discusses the overall conclusions of the work within this thesis on solar wind phenomena and the observations and tracking of them. The possibilities of developments and improvements to the work as well as works which follow based on the techniques and results found within this thesis. This chapter will also discuss the importance of space weather research, the primary motivation for the work that has presented in this thesis.

### 8.1 Overall Summary

Within this thesis 3 aspects of the solar wind have been analysed; micro-scale density structures and their possible internal structure; meso-scale structure and propagation of a CME; and the bulk quiescent flow and structure of the solar wind. For each of these aspects modern and developing techniques have been applied to observe and predict the solar wind and its embodied structures in the micro-scale up to the meso-scale as they propagate through the heliosphere out towards 1 AU.

The micro-scale observations of the solar wind were performed with a full analysis of IPS data during the solar minimum period of solar cycle 24. This investigation revealed dynamic velocity fluctuations which were observed within the slow solar wind. White-light imaging from heliospheric imagers provided a near-perpendicular view to that of the IPS observations, thus it was possible to map the IPS observations into the STEREO|HI field of view. This revealed the larger-scale structures of the solar wind during the period of the observations which may have been associated with the dynamic velocity fluctuations observed. As the STEREO spacecrafts move away from the Earth the HI cameras do not remain perpendicular to the IPS observations from Earth introducing geometric complexities when mapping the IPS observation into the HI field of view. To determine whether the mapping method would still be valid a comprehensive case study of a CME observed by LOFAR, later into the STEREO mission, was performed. Propagation models applied to STEREO|HI were used to determine the velocities and positions of the CME which was compared be compared with the position determined from the IPS mapping to reveal a successful mapping.

In the CME study, the NRGF technique applied to the coronagraph observations revealed high clarity images of the dynamic solar wind revealing the detail of the CME absent of the background quiescent solar wind. Contrasting these images the NRGF technique also produces images of purely the quiescent solar wind corona which were used to model the quiescent solar wind, free from the complexities of dynamic features such as CMEs. The modelling used ballistic extrapolation to produce a parker spiral map of the velocity and density of the solar wind which resulted in strong correlations between *in-situ* spacecraft data.

### **8.1.1 Rapid Velocity Variations in the Slow Solar Wind**

The IPS technique has been used to determine the outflow velocities of the slow solar wind during the solar minimum period of solar cycle 24. IPS uses two Earth-based radio antennas which while observing a distant astronomical radio source will observe correlating scintillation from the perpendicular solar wind outflow. A small time lag between the correlating scintillation patterns occurs due to the separation of the antenna, thus a solar wind outflow velocity may be inferred. By applying a short 3 minute sliding window analysis method to 15 minutes integration blocks, high resolution velocity profiles can be observed. In the velocity profiles it was observed that it was not uncommon for large variations in the velocities to occur within very short time periods. A detailed investigation into the solar wind during these occasions revealed two types of situation which lead to the rapid velocity variations.

The first of these situations were during the passing of transient structures across the IPS ray path, large enough to encompass the majority duration of the IPS observation. Two cases were presented for 23 April 2007 and 20 May 2007 which demonstrated an IPS observation that detected rapid velocity variations in the observed solar wind during periods in which a transient structure was present in the IPS ray path. The velocities during these cases were observed to change up to  $15 \text{ km min}^{-1}$  and the changes lasting up to 9 minutes, however more commonly the changes lasted up to 3 minutes. White-light imaging from heliospheric imagers observed the slow transient pass over the location of the IPS P-Point throughout the duration of the IPS observation. As IPS is sensitive to small-scale density structures and their velocities, it was determined that any velocities determined from the IPS sliding window method would be the velocities of the transient's internal plasma. The evidence collected by IPS during these cases strongly suggests that slow wind transients contain an internal structure which is very dynamic with velocities fluctuating over the duration of an IPS observation.

The second of these situations displayed no visible density structures in the solar wind when viewed by heliospheric imagers, however the IPS displayed evidence of contrary to this. Case studies on 19 May 2007 and 20 May 2007 each displayed a negative lobe in the cross-correlation functions at near zero time lag during the time of any rapid velocity variations, a signature of a solar wind transient passing the IPS ray path. The velocities for the case studies on 19 May and 20 May were observed to change by  $18 \text{ km min}^{-1}$  and  $30 \text{ km min}^{-1}$  respectively. It is thus suggested that these variations in the solar wind velocity are due to small-scale transients in the slow solar wind which are not clearly visible by heliospheric imagers, suggesting that the slow solar wind has a 'blobular' structure of many small-scale transients rather than a quiescent stream of plasma.

### **8.1.2 Multi-technique Remote-sensing Observations and Modelling of a CME**

The observations of rapid variations in the slow solar wind had originally been limited to available data up to and including 2008 where the STEREO mission was still young and remained close to the Earth such that the Earth and STEREO imagers shared a near common line of sight. Later into the STEREO mission the STEREO spacecraft have accelerated away from the Earth and as of March 2011 the spacecraft had separated by  $90^\circ$  from the Earth and now including the Earth within its field of view. For the later STEREO mission there are added geometrical complexities when mapping the location of an IPS P-Point onto the field of view of the STEREO HIs thus a case study of large CME was used to test the mapping methods. A CME observed by LOFAR on 17 November 2011 was used for this case study and thus developed into a study of currently available remote sensing observational, tracking and projection modelling methods.

The CME was determined from EUV imaging to originate from an extended filament eruption located within the south-western quartile of the Sun and was independent of any active regions visible at the time. Observations from STEREO-A EUVI saw the eruption occur on the limb of the Sun and also detected a large amount of coronal material ejected ahead of a slower core of material in a southward direction from below the solar equator. The CME front however is visible to extend radially and the northern limb is partially visible to be extending near to the Sun-Earth plane.

At heights between  $2 R_S$  and  $32 R_S$  coronagraph imaging was used to observe the CME's propagation. The coronagraph imaging underwent NRGF processes separating the quiescent and dynamic solar wind features for which the dynamic solar wind extract was used to display a much clearer view of the CME than the unprocessed image

### 8.1.3 Tomographic Ballistic Extrapolation Modelling of the Parker Spiral

The ballistic extrapolation Parker spiral modelling method displayed in chapter 7, applied simple velocity and density ballistic extrapolation methods to tomographic Carrington rotation data source from the quiescent component of NRGF LASCO data. As the model maps only the quiescent solar wind, it is free from MHD complexities produced by the dynamic solar wind as such the model proved to provide a very fast and effective method of mapping the quiescent solar wind outward to distance up to and beyond 1 AU. The model can be utilised in two different ways; the extrapolation using measured via remote sensing methods such as IPS; or the fully automated method of determining the velocity profiles using the correlation of density observed by Wind with that mapped out to 1 AU by the model. The model is also able to detect the formation of SIRs and SRRs and locate their presence in the solar wind. The density enhancements and rarefactions caused by these events have also been accurately mapped outward and combined with the background solar wind have provided strong correlations with densities observed by *in-situ* methods with Wind. As such it may also be feasible to use the ballistic model as a method of locating and predicting the formation of these events.

The Parker spiral ballistic extrapolation method described in chapter 7 will be used in three main ways in the near future. The method is a useful tool for mapping features measured at 1AU back to the inner corona and vice versa. The Aberystwyth group will make considerable use of this tool to explore the sources of different solar wind streams. In particular, the search for the signature of small-scale dynamics in *in-situ* data such as those discovered by Morgan et al (2013) will be greatly aided by the ballistic extrapolation. The Aberystwyth group hopes to use the model to investigate the scale of compression at SIRs. The model can very simply be used to estimate what compression is needed to match the measured density enhancements at 1AU.

The modelling method will form an important part of a global heliospheric model which is being developed in Aberystwyth. The full model uses a large set of 1D 2-fluid solar wind models to build a physical model of the solar wind from the coronal base to 1AU. Many boundary conditions are constrained empirically within the model including magnetic field flux tube geometry close to the Sun, temperatures and densities at the coronal base and densities at 5Rs. The ballistic code will provide the geometry of the flux tube at heights above 5Rs, as well as constrained outflow velocities and possibly densities above 5Rs for the various streams. Such constraints enable the exploration of unobserved solar wind characteristics including coronal heating and acceleration. This is an exciting development in the field of solar wind modelling. The global model has far more stringent empirical constraints than most current global models.

## 8.2 Importance of Space Weather Research

This thesis has revolved around the subject of the solar wind. The observations of IPS presented in chapter 5 questioned the origins and structure of the slow solar wind and suggested that it is not as smoothly varying as we had initially thought but is however more 'blobular' in its structure. Chapter 6 detailed the propagation of a moderately size CME as it travelled outward from the Sun out to 1 AU. The CME was not aimed directly towards the Earth however, a relatively small portion of the north-western flank of the CME was observed to pass over the Earth. Although this flank of the CME was relatively small, the magnetometer data from TGO showed that it was still capable of producing a strong influence on the Earth's magnetosphere. The activity of the Sun can vary greatly over time.

Chapter 7 of this thesis showed the development of a new method for modelling and predicting the quiescent solar wind. Although space weather usually refers to the dynamic solar events which may have influence on the Earth, the quiescent solar wind should not be neglected as the solar particles of the quiescent solar wind are regularly interacting with the Earth's magnetosphere and form the base of the solar atmosphere that surrounds the Earth. The velocities of these particles can be defined into two unique wind types; the fast; and slow solar wind. During a solar minimum the solar wind will be dominated (at equatorial latitudes) by the slow solar wind, which contains a dense flow of low speed ( $\sim 350 \text{ km s}^{-1}$ ) solar particles. At times of solar maximum the slow solar wind will still remain however it will be accompanied by the fast solar wind (typically over  $500 \text{ km s}^{-1}$ ) which is also less dense. The ballistic model presented is able to predict these solar wind flows and how they may interact accurately at any point within the heliosphere and even at position where *in-situ* methods are not available. The model is thus a very powerful tool which can be applied into space weather research.

Chapter 1 introduced the 11-year solar cycle (and also the possibilities of longer) where the Sun will go through periods of high and low activity where CME and flare will be very frequent (high activity) or rare (low activity). Space weather has a constant influence on the Earth's magnetosphere, controlling the magnetic reconnection and allowing the storage and release of energy within the magnetosphere as substorms. During the Sun's peak activity however, it is likely that a very large solar event (superstorm) may occur which will have a dramatic effect on the Earth's magnetosphere producing an even greater influence of magnetic reconnection, and allowing solar energetic particles (SEPs) to enter into the Earth's atmosphere (*i.e.* the ionosphere) more effectively.

Many of the systems on Earth are susceptible to magnetospheric and ionospheric disturbances. During a substorm at Earth the geomagnetic field will fluctuate, this can induce an electrical field on

the Earth's surface which can then induce electric currents in conducting material. If this conducting material is part of the electrical power grid it can cause instabilities in the system causing transformers to fail (JASON, 2011). Ionospheric conditions are particularly important for navigation and communication systems as these systems have been designed around a stable ionosphere and in the case of some communication system wavebands may use the ionosphere to reflect the radio signals. During a substorm the ionosphere may develop small density structures *i.e.* blobs and patches (Brekke, 1996) which can cause ionospheric scintillation of the radio signals.

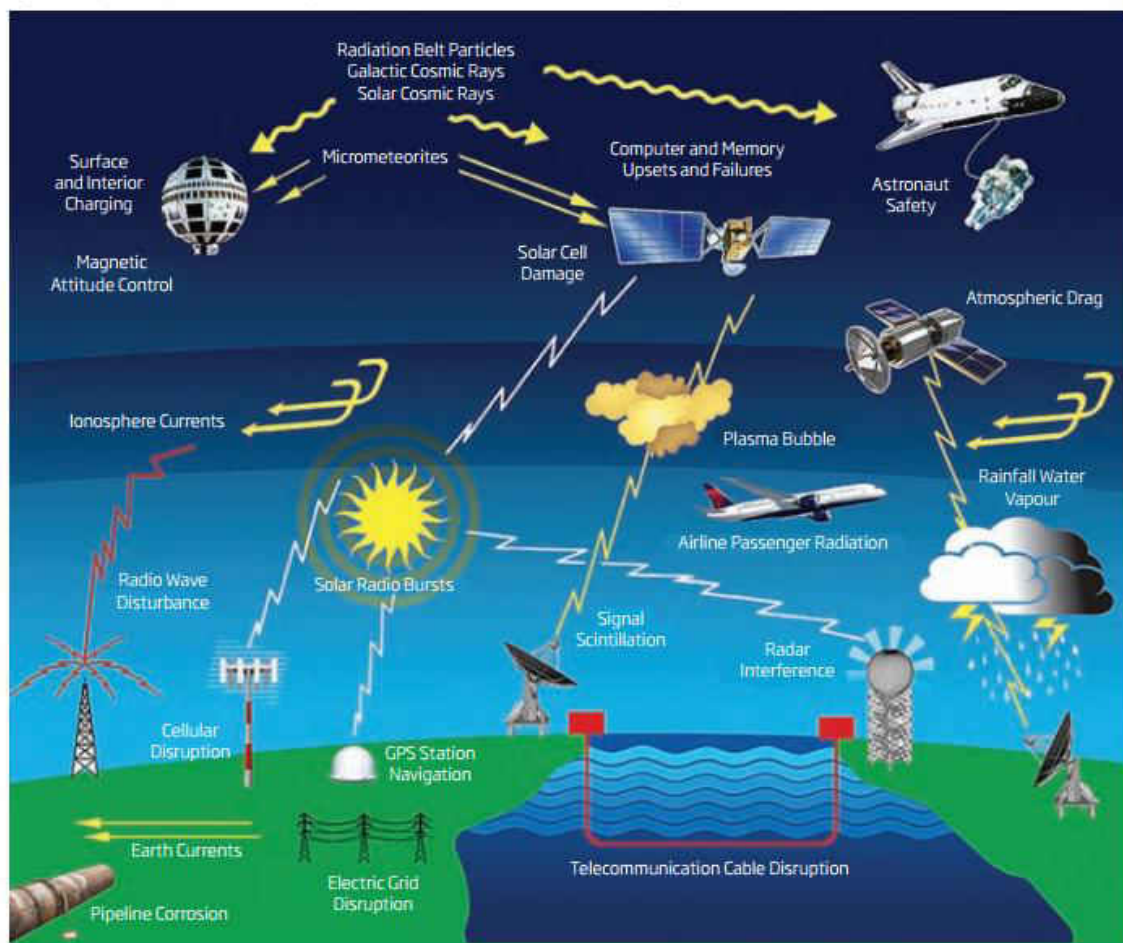


**Figure 8.1** Examples of systems susceptible to the effects of space weather (From Royal Academy of Engineering, 2013)

Aside from the systems on Earth, there are now many satellites and spacecraft positioned in space and outside of the magnetosphere's protection. Satellites, although designed to have a high resilience to space weather and withstand SEPs, may be vulnerable to large solar storms. SEPs will

barrage the satellites causing electrostatic charges on the body and instruments. If these are not fully shielded from the SEPs they may cause interference and even damage the instruments. It is thus imperative that space weather predictions of large events are available so that the systems may be safe during the event. In the modern space age it has been common practice for astronauts to travel into space, usually for satellite repairs and less so for exploration, and it is often required for the astronauts to leave the protection of the spacecraft or satellite. Great care must be taken at these times as dramatic space weather events will have catastrophic effects on the astronaut. In recent years the idea of space travel has become desirable thus if we wish to send more people into space our predictions of space weather must be very accurate so that they may be protected so that travel to more distant regions of space *i.e.* Mars, can be performed safely. Figure 8.1 shows further examples of some of the systems affected by solar particles.

# Bibliography

**Armstrong, J. W. & Coles, W. A.**, Analysis of three-station interplanetary scintillation, *Journal of Geophysical Research*, 77, 25, page 4602, 1972.

**Bame, S. J., McComas, D. J., Barraclough, B. L., Phillips, J. L., Sofaly, K. J., Chavez, J. C., Goldstein, B. E. & Sakurai, R. K.**, The ULYSSES solar wind plasma experiment, *Astronomy and Astrophysics Supplement Series*, 92, 2, 1992.

**Bertaux, J. L., Kyrölä, E., Quémerais, E., Pellinen, R., Lallement, R., Schmidt, W., Berthé, M., Dimarellis, E., Goutail, J. P., Taulemesse, C., Bernard, C., Leppelmeier, G., Summanen, T., Hannula, H., Huomo, H., Kehlä, V., Korpela, S., Leppälä, K., Strömmer, E., Torsti, J., Viherkanto, K., Hochedez, J. F., Chretiennot, G., Peyroux, R. & Holzer, T.**, SWAN: A Study of Solar Wind Anisotropies on SOHO with Lyman Alpha Sky Mapping, *Solar Physics*, 162, pages 403-439, 1995.

**Bewsher, D., Harrison, R. A., Brown, D. S.**, The relationship between EUV dimming and coronal mass ejections, *Astronomy and Astrophysics*, 478, pages 897-906, 2008.

**Billings, D. E.**, *A Guide to the solar corona*, Academic Press, ISBN 978-1-4832-3100-6, 1966.

**Bisi, M. M., Breen A. R., Jackson, B. V., Fallows, R. A., Walsh, A. P., Mikić, Z., Riley, P., Owen, C. J., Gonzalez-Esparza, A., Aguilar-Rodriguez, E., Morgan, H., Jensen, E. A., Wood, A. G., Owens, M. J., Tokumaru, M., Manoharan, P. K., Chashei, I. V., Giunta, A. S., Linker, J. A., Shishov, V. I., Tyul'Bashev, S. A., Agalya, G., Glubokova, S. K., Hamilton, M. S., Fujiki, K., Hick, P.P., Clover, J. M. & Pintér, B.**, From the Sun to the Earth: The 13 May 2005 Coronal Mass Ejection, *Solar Physics*, 265, pages 49-127, 2010b.

**Bisi, M. M., Breen, A. R., Fallows, R. A., Thomasson, P., Jones, R. A. & Wannberg, G.**, Combined EISCAT/ESR/MERLIN Interplanetary Scintillation Observations of the Solar Wind, *Proceedings of the Solar Wind 11 / SOHO 16, "Connecting Sun and Heliosphere" (ESA SP-592)*, page 593, 2005.

**Bisi, M. M., Fallows, R. A., Breen, A. R. & O'Neill, I. J.**, Interplanetary Scintillation Observations of Stream interaction Regions in the Solar Wind, *Solar Physics*, 261, pages 149-172, 2010a.

**Bisi, M. M., Fallows, R. A., Breen, A. R., Habbal, S. R. & Jones, R. A.**, Large-scale structure of the fast solar wind, *Journal of Geophysical Research*, 112, 2007.

**Bisi, M. M., Hardwick, S. A., Fallows, R. A., Davies, J. A., Harrison, R. A., Jensen, E. A., Morgan, H., Wu, C.-C., Asgekar, A., Xiong, M., Carley, E., Mann, G., Gallagher, P. T., Kerdraon, A., Konovalenko, A. A., MacKinnon, A., Magdalenic, Rucker, H. O., Thide, B., Vocks, C. & LOFAR Builders List**, The First Coronal Mass Ejection Observed With The Low Frequency Array (LOFAR), *The Astrophysical Journal Supplementary Series*, In press, 2014.

**Bisi, M. M.**, *Interplanetary Scintillation Studies of the Large-Scale Structure of the Solar Wind*, Ph.D. Thesis, The University of Wales, Aberystwyth, 2006.

**Bisi, M. M., Jackson, B. V., Breen, A. R., Dorrian, G. D., Fallows, R. A., Clover, J. M. & Hick, P. P.,** Three-Dimensional (3-D) Reconstruction of EISCAT IPS Velocity Data in the Declining Phase of Solar Cycle 23, *Solar Physics*, 265, pages 233-244, 2010a

**Born, M., & Wolf, E.,** *Principals of Optics*, Cambridge University Press, ISBN 0-521-64221, 1964.

**Bougeret, J. L., Goetz, K., Kaiser, M. L., Bale, S. D., Kellogg, P. J., Maksimovic, M., Monge, N., Monson, S. J., Astier, P. L., Davy, S., Dekkali, M., Hinze, J. J., Manning, R. E., Aguilar-Rodriguez, E., Bonnin, X., Briand, C., Cairns, I. H., Cattell, C. A., Cecconi, B., Eastwood, J., Ergun, R. E., Fainberg, J., Hoang, S., Huttunen, K. E. J., Krucker, S., Lecacheux, A., MacDowall, R. J., Macher, W., Mangeney, A., Meetre, C. A., Moussas, X., Nguyen, Q. N., Oswald, T. H., Pulupa, M., Reiner, M. J., Robinson, P. A., Rucker, H., Salem, C., Santolik, O., Silvis, J. M., Ullrich, R., Zarka, P. & Zouganelis, I.,** S/WAVES: The Radio and Plasma Wave Investigation on the STEREO Mission, *Space Science Reviews*, 136, pages 487-528, 2008.

**Bourgois, G., Coles, W. A., Daigne, G., Silen, J., Turunen, T. & Williams, P. J.,** Measurements of the solar wind velocity with EISCAT, *Astronomy and Astrophysics*, 144, pages 452-462, 1985

**Bourgois, G.,** Scintillations interplanétaires des radiosources à 2695mhz, *Astronomy and Astrophysics*, 2, pages 209-217, 1969.

**Breen, A. R., Coles, W. A., Grall, R. R., Klinglesmith, M. T., Markkanen, J., Moran, P. J. & Williams, P. J. S.,** EISCAT measurements of interplanetary scintillation, *Journal of Atmospheric and Terrestrial Physics*, 58, pages, 507-519, 1996a.

**Breen, A. R., Coles, W. A., Grall, R. R., Klinglesmith, M. T., Markkanen, J., Moran, P. J. Tegid, B.. & Williams, P. J. S.,** EISCAT measurements of the solar wind, *Annales Geophysicae*, 14, 12, pages 1235-1245, 1996b.

**Breen, A. R., Fallows, R. A., Bisi, M. M., Thomasson, P., Jordan, C. A., Wannberg, G. & Jones, R. A.,** Extremely long baseline interplanetary scintillation measurements of solar wind velocity, *Journal of Geophysical Research*, 111, 2006.

**Breen, A. R., Moran, P. J., Varley, C. A., Wilkinson, W. P., Williams, P, J, S., Coles, W. A., Lechinski, A. & Markkanen, J.,** Interplanetary scintillation observations of interaction regions in the solar wind, *Annales Geophysicae*, 16, pages 1265-1282, 1998.

**Brekke, A.,** *Physics of the Upper Polar Atmosphere*, Springer, 1996.

**Brueckner, G. E., Howard, R. A., Koomen, M. J., Korendyke, C. M., Michels, D. J., Moses, J. D., Socker, D. G. & Linker, J.,** The Large Angle Spectroscopic Coronagraph (LASCO), *Solar Physics*, 162, pages 357-402, 1995.

**Byrne J. P., Maloney, S. A., McAteer, R. T. J., Refojo, J. M., Gallagher, P.T.,** Propagation of an Earth-directed coronal mass ejection in three dimensions, *Nature Communications*, 1, 6, 2010.

**Canals, A., Breen, A. R., Ofman, L., Moran, P. J. & Fallows, R. A.,** Estimating random transverse velocities in the fast solar wind from EISCAT Interplanetary Scintillation measurements, *Annales Geophysicae*, 20, pages 1265-1277, 2002.

**Coles, W. A. & Harmon, J. K.**, Interplanetary scintillation measurements of the electron density power spectrum in the solar wind, *Journal of Geophysical Research*, 83, pages 1413-1420, 1978.

**Coles, W. A. & Maagoe, S.**, Solar-wind velocity from IPS observations, *Journal of Geophysical Research*, 77, 28, page 5622, 1972.

**Coles, W. A.**, Observations of the Solar Plasma Using Radio Scattering and Scintillation Methods – Comments, *Solar Wind*, 1972.

**Coles, W. A.**, A bimodal model of the solar wind speed, *Astrophysics and Space Science*, 243, pages 87–96, 1996.

**Cook, J. W.**, *LASCO Handbook for Scientific Investigators*, <http://lasco-www.nrl.navy.mil/handbook/hndbk.html>, 1994.

**Cowen, R.**, Voyager's long good bye, *Nature*, 489, 7414, pages 20-21, 2012.

**Cranmer, S. R.**, Coronal Holes, *Living Reviews in Solar Physics*, 6, 3, 2009.

**Cremandes, H. & Bothmer, V.**, On the three-dimensional configuration of coronal mass ejections, *Astronomy and Astrophysics*, 422, pages 307-322, 2004.

**Daly, N. M.**, *Scintillation analysis of solar wind dynamics*, Ph.D. Thesis, University of Glasgow, 2000.

**Davies, J. A., Harrison, R. A., Perry, C. H., Möstl, C., Lugaz, N., Rollett, T., Davis, C. J., Crothers, S. R., Temmer, M., Eyles, C. J. & Savani, N. P.**, A Self-similar Expansion Model for Use in Solar Wind Transient Propagation Studies, *The Astrophysical Journal*, 750, 2012.

**Davies, J. A., Perry, C. H., Trines, R. M. G. M., Harrison, R. A., Lugaz, N., Möstl, C., Liu, Y. D. & Steed, K.**, Establishing a Stereoscopic Technique for Determining the Kinematic Properties of Solar Wind Transients based on a Generalized Self-similarly Expanding Circular Geometry, *The Astrophysical Journal*, 777, 2, 2013.

**Davis, C., Bewsher, D., Davies, J. & Crothers, S.**, *Working with data from the NASA STEREO Heliospheric Imager: An essential guide*, [http://www.stereo.rl.ac.uk/Documents/HI\\_user\\_guidejuly.pdf](http://www.stereo.rl.ac.uk/Documents/HI_user_guidejuly.pdf), 2008.

**De Pontieu, B., Hansteen, V. H., Rouppe van der Voort, L., van Noort, M. & Carlsson, M.**, High-Resolution Observations and Modeling of Dynamic Fibrils, *Astrophysical Journal*, 655, pages 624-641, 2007.

**Delaboudinière, J.-P., Artzner, G. E., Brunaud, J., Gabriel, A. H., Hochedez, J. F., Millier, F., Song, X. Y., Au, B., Dere, K. P., Howard, R. A., Kreplin, R., Michels, D. J., Moses, J. D., Defise, J. M., Jamar, C., Rochus, P., Chauvineau, J. P., Marioge, J. P., Catura, R. C., Lemen, J. R., Shing, L., Stern, R. A., Gurman, J. B., Neupert, W. M., Maucherat, A., Clette, F., Cugnon, P. & van Dessel, E. L.**, EIT: Extreme-Ultimate Imaging Telescope for the SOHO Mission, *Solar Physics*, 162, pages 291-312, 1995.

**Dennison, P. A. & Hewish, A.**, The Solar Wind outside the Plane of the Ecliptic, *Nature*, 213, 5074, pages 343-346, 1967.

**Domingo, V., Fleck, B. & Poland, A. I.**, The SOHO Mission: An Overview, *Solar Physics*, 162, pages 1-37, 1995.

**Dorrian, G. D., Breen, A. R., Davies, J. A., Rouillard, A. P., Fallows, R. A., Whittaker, I. C., Brown, D. S., Harrison, R. A., Davis, C. J. & Grande, M.**, Transient Structures and Stream Interaction Regions in the Solar Wind: Results from EISCAT Interplanetary Scintillation, STEREO HI and Venus Express ASPERA-4 Measurements, *Solar Physics*, 265, pages 207-231, 2010.

**Dorrian, G. D., Breen, A. R., Brown, D. S., Davies, J. A., Fallows, R. A. & Rouillard, A. P.**, Simultaneous interplanetary scintillation and Heliospheric Imager observations of a coronal mass ejection, *Geophysical Research Letters*, 35, 24, 2008.

**Dorrian, G.**, *Large Scale 3-Dimensional Structure of the Solar Wind*, Ph.D. Thesis, Aberystwyth University, 2009.

**Driesman, A., Hynes, S. & Crancro, G.**, The STEREO Observatory, *Space Science Reviews*, 136, pages 17-44, 2008.

**Dungey, J. W.**, Interplanetary Magnetic Field and the Auroral Zones, *Physics Review Letters*, 6, 47, 1961.

**Eyles, C. J., Harrison, R. A., Davis, C. J., Waltham, N. R., Shaughnessy, B. M., Mapson-Menard, H. C. A., Bewsher, D., Crothers, S. R., Davies, J. A., Simnett, G. M., Howard, R. A., Moses, J. D., Newmark, J. S., Socker, D. G., Halain, J.-P., Defise, J.-M., Mazy, E. & Rochus, P.**, The Heliospheric Imagers Onboard the STEREO Mission, *Solar Physics*, 254, 2, pages 387-445, 2009.

**Falcke, H. D., van Haarlem, M. P., de Bruyn, A. Ger, Braun, R., Röttgering, H. J. A., Stappers, B., Boland, W. H. W. M., Butcher, H. R., de Geus, E. J., Koopmans, L. V., Fender, R. P., Kuijpers, H. J. M. E., Miley, G. K., Schilizzi, R. T., Vogt, C., Wijers, R. A. M. J., Wise, M. W., Brouw, W. N., Hamaker, J. P., Noordam, J. E., Oosterloo, T., Bähren, L., Brentjens, M. A., Wijnholds, S. J., Bregman, J. D., van Cappellen, W. A., Gunst, A. W., Kant, G. W., Reitsma, J., van der Schaaf, K. & de Vos, C. M.**, A very brief description of LOFAR the Low Frequency Array, *Highlights of Astronomy*, 14, pages 386-387, 2007.

**Fallows, R. A., Asgekar, A., Bisi, M. M., Breen, A. R. & ter-Veen, S.**, The Dynamic Spectrum of Interplanetary Scintillation: First Solar Wind Observations on LOFAR, *Solar Physics*, 285, pages 127-139, 2013.

**Fallows, R. A., Breen, A. R. & Dorrian, G. D.**, Developments in the use of EISCAT for interplanetary scintillation, *Annales Geophysicae*, 26, 8, pages 2229-2236, 2008.

**Fallows, R. A., Breen, A. R., Bisi, M. M., Jones, R. A. & Wannberg, G.**, Dual-frequency interplanetary scintillation observations of the solar wind, *Geophysical Research Letters*, 33, 2006.

**Fallows, R. A.**, *Create-corr Cookbook*, User documents created for Aberystwyth University, 2011.

**Fallows, R. A.**, *Studies of the Solar Wind Throughout a Solar Cycle*, Ph.D. Thesis, The University of Wales, Aberystwyth, 2001.

**Fallows, R. A., Williams, P. J. S. & Breen, A. R.**, EISCAT measurements of solar wind velocity and the associated level of interplanetary scintillation, *Annales Geophysicae*, 20, pages 1279-1289, 2002.

**Fisher, R. R. & Guhathakurta, M.**, SPARTAN 201 White light coronagraph experiment, *Space Science Reviews*, 70, pages 267-272, 1994.

**Folkestad, K., Hagfors, T. & Westerlund, S.**, EISCAT: An updated description of technical characteristics and operational capabilities, *Radio Science*, 18, 6, pages 867-879, 1983.

**Frazin, R. A.**, Tomography of the Solar Corona. I. A Robust, Regularized, Positive Estimation Method, *The Astrophysical Journal*, 530, 2, pages 1026-1035, 2000.

**Fröhlich, C., Romero, J., Roth, H., Wehrli, C., Andersen, B. N., Appourchaux, T., Domingo, V., Telljohann, U., Berthomieu, G., Delache, P., Provost, J., Toutain, T., Crommelynck, D. A., Chevalier, A., Fichot, A., Däppen, W., Gough, D., Hoeksema, T., Jiménez, A., Gómez, M. F., Herreros, J. M., Cortés, T. R., Jones, A. R., Pap, J. M. & Willson, R. C.**, VIRGO: Experiment for Helioseismology and Solar Irradiance Monitoring, *Solar Physics*, 162, pages 101-128, 1995.

**Gabriel, A. H., Grec, G., Charra, J., Robillot, J.-M., Roca Cortés, T., Turck-Chièze, S., Bocchia, R., Boumier, P., Cantin, M., Cespédes, E., Cougrand, B., Crétole, J., Damé, L., Decaudin, M., Delache, P., Denis, N., Duc, R., Dzitko, H., Fossat, E., Fourmond, J.-J., García, R. A., Gough, D., Grivel, C., Herreros, J. M., Lagardère, H., Moalic, J.-P., Pallé, P. L., Pétrou, N., Sanchez, M., Ulrich, R. & van der Raay, H. B.**, Global Oscillations at Low Frequency from the SOHO Mission (GOLF), *Solar Physics*, 162, pages 61-99, 1995.

**Galvin, A. B., Kistler, L. M., Popecki, M. A., Farrugia, C. J., Simunac, K. D. C., Ellis, L., Möbius, E., Lee, M. A., Boehm, M., Carroll, J., Crawshaw, A., Conti, M., Demaine, P., Ellis, S., Gaidos, J. A., Googins, J., Granoff, M., Gustafson, A., Heirtzler, D., King, B., Knauss, U., Levasseur, J., Longworth, S., Singer, K., Turco, S., Vachon, P., Vosbury, M., Widholm, M., Blush, L. M., Karrer, R., Bochsler, P., Daoudi, H., Etter, A., Fischer, J., Jost, J., Opitz, A., Sigrist, M., Wurzel, P., Klecker, B., Ertl, M., Seidenschwang, E., Wimmer-Schweingruber, R. F., Koeten, M., Thompson, B. & Steinfeld, D.**, The Plasma and Suprathermal Ion Composition (PLASTIC) Investigation on the STEREO Observatories, *Space Science Reviews*, 136, pages 437-486, 2008.

**Gosling, J. T. & Pizzo, V. J.**, *Formation and evolution of corotating interaction regions and their three dimensional structure*, *Corotating Interaction Regions*, Kluwer Academic Publishers, ISBN 0-7923-6080-X, pages 22-52, 1999.

**Gosling, J. T.**, Physical nature of the low-speed solar wind, *AIP Conference Proceedings*, 385, pages 17-24, 1997.

**Grall, R. R.**, *Remote Sensing Observations of the Solar Wind Near the Sun*, Ph.D. Thesis, University of California, San Diego, 1995.

**Grydeland, T., Blixt, E. M., Løvhaug, U. P., Hagfors, T., La Hoz, C. & Trondsen, T. S.**, Inferometric radar observations of filamented structures due to plasma instabilities and their relation to dynamic auroral rays, *Annales Geophysicae*, 22, pages 1115-1132, 2004.

**Gurnett, D. A., Kurth, W. S., Burlaga, L. F. & Ness, N. F.**, In Situ Observations of Interstellar Plasma with Voyager 1, *Science*, 341, pages 1489-1492, 2013.

**Habbal, S. R. & Woo, R.**, Connecting the Sun and the Solar Wind: Comparison of the Latitudinal Profiles of Coronal and Ulysses Measurements of the Fast Wind, *The Astrophysical Journal*, 549, pages 253-256, 2001.

**Habbal, S. R., Druckmüller, M., Morgan, H., Scholl, I., Rušin, V., Daw, A., Johnson, J. & Arndt, M.**, Total Solar Eclipse Observations of Hot Prominence Shrouds, *The Astrophysical Journal*, 719, pages 1362-1369, 2010.

**Habbal, S. R., Druckmüller, M., Morgan, H., Scholl, I., Rušin, V., Daw, A., Johnson, J. & Arndt, M.**, Total Solar Eclipse Observations of Hot Prominence Shrouds, *The Astrophysical Journal*, 719, 2, pages 1362-1369, 2010.

**Hardwick, S. A., Bisi, M. M., Davies, J. A., Breen, A. R., Fallows, R. A., Harrison, R. A. & Davis, C. J.**, Observations of Rapid Velocity Variations in the Slow Solar Wind, *Solar Physics*, 285, pages 111-126, 2013.

**Harris, D. E., & Roberts, J. A.**, Radio Source Measurements at 960 Mc/s, *Publications of the Astronomical Society of the Pacific*, 72, 427, pages 237-255, 1960.

**Harrison, R. A., Davies, J. A., Rouillard, A. P., Davis, C. J., Eyles, C. J., Bewsher, D., Crothers, S. R., Howard, R. A., Sheeley, N. R., Vourlidas, A., Webb, D. F., Brown, D. S. & Dorrian, G. D.**, Two Tears of the STEREO Heliospheric Imagers, Invited Review, *Solar Physics*, 256, pages 219-237, 2009.

**Harrison, R. A., Sawyer, E. C., Carter, M. K., Cruise, A. M., Cutler, R. M., Fludra, A., Hayes, R. W., Kent, B. J., Lang, J., Parker, D. J., Payne, J., Pike, C. D., Peskett, S. C., Richards, A. G., Gulhane, J. L., Norman, K., Breeveld, A. A., Breeveld, E. R., Al Janabi, K. F., McCalden, A. J., Parkinson, J. H., Self, D. G., Thomas, P. D., Poland, A. I., Thomas, R. J., Thompson, W. T., Kjeldseth-Moe, O., Brekke, P., Karud, J., Maltby, P., Aschenbach, B., Bräuninger, H., Kühne, M., Hollandt, J., Siegmund, O. H. W., Huber, M. C. E., Gabriel, A. H., Mason, H. E. & Bromage, B. J. I.**, The Coronal Diagnostic Spectrometer for the Solar and Heliospheric Observatory, *Solar Physics*, 162, pages 233-290, 1995.

**Hathaway, D. H.**, The Solar Cycle, *Living Reviews of Solar Physics*, 7, 2010.

**Hewish, A. & Dennison, P. A.**, Measurements of the Solar Wind and the Small-Scale Structure of the Interplanetary Medium, *Journal of Geophysical Research*, 72, page 1977, 1967.

**Hewish, A. & Symonds, M. D.**, Radio investigation of the solar plasma, *Planetary and Space Science*, 17, 3, pages 313-320, 1969.

**Hewish, A., Scott, P. F. & Wills, D.**, Interplanetary scintillation of small diameter radio sources, *Nature*, 203, pages 1214-1217, 1964.

**Hewish, A.**, The irregular structure of the outer regions of the solar corona, *Proceedings of the Royal Society*, A 238, pages 238-251, 1955.

**Hewish, A.**, The Sun's Magnetic Field from Radio Observations, *Transactions of the International Astronomical Union*, 11B, page 431, 1962.

**Hood, A. W., Browning, P. K., & van der Linden, R. A. M.**, Coronal heating by magnetic reconnection in loops with zero net current, *Astronomy and Astrophysics*, 506, pages 913-925, 2009.

**Houminer, Z. & Hewish, A.**, Correlation of interplanetary scintillation and spacecraft plasma density measurements, *Planetary and Space Science*, 22, pages 1041-1042, 1974.

**Hovestadt, D., Hilchenbach, M., Bürgi, A., Klecker, B., Laeverenz, P., Scholer, M., Grünwaldt, H., Axford, W. I., Livi, S., Marsch, E., Wilken, B., Winterhoff, H. P., Ipavich, F. M., Bedini, P., Coplan, M. A., Galvin, A. B., Gloeckler, G., Bochsler, P., Balsiger, H., Fischer, J., Geiss, J., Kallenbach, R., Wurz, P., Reiche, K.-U., Gliem, F., Judge, D. L., Ogawa, H. S., Hsieh, K. C., Möbius, E., Lee, M. A., Managadze, G. G., Verigin, M. I. & Neugebauer, M.**, CELIAS – Charge, Element and Isotope Analysis System for SOHO, *Solar Physics*, 162, pages 441-481, 1995.

**Howard, R. A., Moses, J. D., Vourlidas, A., Newmark, J. S., Socker, D. G., Plunkett, S. P., Korendyke, C. M., Cook, J. W., Hurley, A., Davila, J. M., Thompson, W. T., St Cyr, O. C., Mentzell, E., Mehalick, K., Lemen, J. R., Wuelser, J. P., Duncan, D. W., Tarbell, T. D., Wolfson, C. J., Moore, A., Harrison, R. A., Waltham, N. R., Lang, J., Davis, C. J., Eyles, C. J., Mapson-Menard, H., Simnett, G. M., Halain, J. P., Defise, J. M., Mazy, E., Rochus, P., Mercier, R., Ravet, M. F., Delmotte, F., Auchere, F., Delaboudiniere, J. P., Bothmer, V., Deutsch, W., Wang, D., Rich, N., Cooper, S., Stephens, V., Maahs, G., Baugh, R., McMullin, D. & Carter, T.**, Sun Earth Connection and Heliospheric Investigation (SECCHI), *Space Science Reviews*, 136, pages 67-115, 2008.

**Howard, T. A. & Tappin, S. J.**, Statistical survey of earthbound interplanetary shocks, associated coronal mass ejections and their space weather consequences, *Astronomy and Astrophysics*, 440, 1, pages 373-383, 2005.

**Howard, T. A., Bisi, M. M., Buffington, A., Clover, J. M., Cooke, M. P., Eyles, C. J., Hick, P. P., Holladay, P. E., Jackson, B. V., Johnston, J. C., Kahler, S. W., Kuchar, T. A., Mizuno, D. R., Penny, A. J., Price, S. D., Radick, R. R., Simnett, G. M., Tappin, S. J., Waltham, N. R. & Webb, D. F.**, The Solar Mass Ejection Imager and Its Heliospheric Imaging Legacy, *Space Science Reviews*, 180, pages 1-38, 2013.

**Howard, T.**, *Coronal Mass Ejections: An Introduction*, Springer, ISBN 978-1-4419-8788-4, 2011.

**Jackson, B. V. & Benensohn, R. M.**, The HELIOS spacecraft zodiacal light photometers used for comet observations and views of the Comet West bow shock, *Earth, Moon, and Planets*, 46, pages 139-163, 1990.

**Jackson, B. V., Buffington, A., Hick, P. P., Altrock, R. C., Figueroa, S., Holladay, P. E., Johnston, J. C., Kahler, S. W., Mozer, J. B., Price, S., Radick, R. R., Sagalyn, R., Sinclair, D., Simnett, G. M., Eyles, C. J., Cooke, M. P., Tappin, S. J., Kuchar, T., Mizuno, D., Webb, D. F., Anderson, P. A., Keil, S. L., Gold, R. E. & Waltham, N. R.**, The Solar Mass-Ejection Image (SMEI) Mission, *Solar Physics*, 225, 1, pages 117-207, 2004.

**Jackson, B. V., Hick, P. L., Kojima, M. & Yokobe, A.,** Heliospheric tomography using interplanetary scintillation observations 1. Combined Nagoya and Cambridge data, *Journal of Geophysical Research*, 103, pages 12049-12068, 1998.

**Jackson, B. V.,** Imaging of coronal mass ejections by the HELIOS spacecraft, *Solar Physics*, 100, pages 564-574, 1985.

**JASON,** *Impacts of Severe Space Weather on the Electrical Grid*, The MITRE Corporation, 2011.

**Jain, R., Browning, P. & Kusano, K.,** Solar coronal heating by forced magnetic reconnection: Multiple reconnection events, *Physics of Plasmas*, 12, 2005.

**Jones, R. A., Breen, A. R., Fallows, R. A., Canals, A., Bisi, M. M. & Lawrence, G.,** Interaction between coronal mass ejections and the solar wind, *Journal of Geophysical Research*, 112, 2007.

**Kilpau, E. K.J, Luhmann, J. G., Gosling, J., Li, Y., Elliot, H., Russell, C. T., Jian, L., Galvin, A. B., Larson, D., Schroeder, P., Simunac, K. & Petrie, G.,** Small Solar Wind Transients and Their Connection to the Large-Scale Coronal Structure, *Solar Physics*, 256, pages 327-344, 2009.

**Kivelson, M. G. & Russell, C. T.,** *Introduction To Space Physics*, Cambridge University Press, ISBN 0-521-45714-9, 1995,

**Kliem, B. & Török, T.,** Torus instability, *Physical Review Letters*, 96, 2006.

**Klinglesmith, M.,** The Polar Solar Wind from 2.5 to 40 Solar radii: Results of Intensity Scintillation Measurements, Ph.D. Thesis, University of California, San Diego (UCSD), 1997.

**Kohl, J. L., Esser, R., Gardner, L. D., Habbal, S., Daigneau, P. S., Dennis, E. F., Nystrom, G. U., Panasyuk, A., Raymond, J. C., Smith, P. L., Strachan, L., van Ballegooijen, A. A., Noci, G., Fineschi, S., Romoli, M., Ciaravella, A., Modigliani, A., Huber, M. C. E., Antonucci, E., Benna, C., Giordano, S., Tondello, G., Nicolosi, P., Naletto, G., Pernechele, C., Spadaro, D., Poletto, G., Livi, S., von der Lühe, O., Geiss, J., Timothy, J. G., Gloeckler, G., Allegra, A., Basile, G., Brusa, R., Wood, B., Siegmund, O. H. W., Fowler, W., Fisher, R. & Jhabvala, M.,** The Ultraviolet Coronagraph Spectrometer for the Solar and Heliospheric Observatory, *Solar Physics*, 162, pages 313-356, 1995.

**Kojima, M., Asai, K., Hakamada, K., Ohmi, T., Tokumaru, M. & Yokobe, A.,** Solar wind measured by interplanetary scintillation method, *AIP Conference Proceedings*, 471, pages 29-34, 1999.

**Kudoh, T.,** Nonlinear Alfvén wave model of spicules and coronal heating, *Proceedings of the International Astronomical Union*, 3, pages 195-200, 2007.

**Kutner, M.,** *Astronomy: A Physical Perspective*, Cambridge University Press, ISBN 0-521-52927-1, 1987.

**Laing, R. A., Riley, J. M., & Longair, M. S.,** Bright radio sources at 178 MHz – Flux densities, optical identifications and the cosmological evolution of powerful radio galaxies, *Monthly Notices of the Royal Astronomical Society*, 204, pages 151-187, 1983.

**Lang, K. R.,** *The Cambridge Encyclopedia of the Sun*, Cambridge University Press, ISBN 0-521-78093-4, 2001.

**Leinert, C., Pitz, E., Link, H. & Salm, N.**, The zodiacal light experiment E9 on HELIOS A and B, *Final Report Max-Planck-Inst. Für Astronomie, Heidelberg (Germany, F. R.)*, 1978.

**Lemen, J. R., Title, A. M., Akin, D. J., Boerner, P. F., Chou, C., Drake, J. F., Duncan, D. W., Edwards, C. G., Friedlaender, F. M., Heyman, G. F., Hurlburt, N. E., Katz, N. L., Kushner, G. D., Levay, M., Lindgren, R. W., Mathur, D. P., McFeaters, E. L., Mitchell, S., Rehse, R. A., Schrijver, C. J., Springer, L. A., Stern, R. A., Tarbell, T. D., Wuelser, J.-P., Wolfson, C. J., Yanari, C., Bookbinder, J. A., Cheimets, P. N., Caldwell, D., Deluca, E. E., Gates, R., Golub, L., Park, S., Podgorski, W. A., Bush, R. I., Scherrer, P. H., Gumm, M. A., Smith, P., Auken, G., Jerram, P., Pool, P., Soufli, R., Windt, D. L., Beardsley, S., Clapp, M., Lang, J., Waltham, N.**, The Atmospheric Imaging Assembly (AIA) on the Solar Dynamics Observatory (SDO), *Solar Physics*, 275, pages 17-40, 2012.

**Little, L. T. & Hewish, A.**, Interplanetary scintillation and its relation to the angular structure of radio sources, *Monthly Notices of the Royal Astronomical Society*, 134, pages 221-237, 1966.

**Little, L. T., Hewish, A. & Dennison, P. A.**, Correlation of interplanetary scintillation at different frequencies, *Planetary and Space Science*, 14, 11, pages 1221-1224, 1966.

**Lockwood, M.**, Was UV spectral solar irradiance lower during the recent low sunspot minimum, *Journal of Geophysical Research*, 116, D16, 2011a.

**Lockwood, M.**, Solar physics: shining a light on solar impacts, *Nature Climate Change*, 1, pages 98-99, 2011b.

**Lockwood, M.**, Solar Influence on Global and Regional Climates, *Surveys in Geophysics*, 27, 3, pages 503-534, 2012.

**Lockwood, M., Owens, M., Barnard, I., Davis, C. & Thomas, S.**, Solar cycle 24: What is the Sun up to?, *Astronomy & Geophysics*, 53, pages 3.09-3.15, 2012.

**Lowder, C., Qui, J., Leamon, R. & Liu, Y.**, Measurements of EUV Coronal Holes and Open Magnetic Flux, *The Astrophysical Journal*, 783, pages 142-154, 2014.

**Lugaz, N.**, Accuracy and Limitations of Fitting Stereoscopic Methods to Determine the Direction of Coronal Mass Ejections from Heliospheric Imagers Observations, *Solar Physics*, 267, 2, pages 411-429, 2010.

**Lugaz, N., Vourlidis, A. & Roussev, I. I.**, Deriving the radial distance of wide coronal mass ejections from elongation measurements in the heliosphere – application to CME-CME interaction, *Annales Geophysicae*, 27, pages 3479-3488, 2009.

**Luhmann, J. G., Curtis, D. W., Schroeder, P., McCauley, J., Lin, R. P., Larson, D. E., Bale, S. D., Sauvaud, J.-A., Aoustin, C., Mewaldt, R. A., Cummings, A. C., Stone, E. C., Davis, A. J., Cook, W. R., Kecman, B., Wiedenbeck, M. E., von Roseninge, T., Acuna, M. H., Reichenthal, L. S., Shuman, S., Wortman, K. A., Reames, D. V., Mueller-Mellin, R., Kunow, H., Mason, G. M., Walpole, P., Korth, A., Sanderson, T. R., Russell, C. T. & Gosling, J. T.**, STEREO IMPACT Investigation Goals, Measurements, and Data Products Overview, *Space Science Reviews*, 136, pages 117-184, 2008.

**Lui, R.**, *Dynamics of Solar Eruptive Filaments*, Ph.D. Thesis, Rice University, 2008.

- Machin, K. E. & Smith, F. G.**, A New Radio Method for Measuring the Electron Density in the Solar Corona, *Nature*, 168, pages 599-600, 1951.
- Machin, K. E. & Smith, F. G.**, Occultation of a Radio Star by the Solar Corona, *Nature*, 170, pages 319-320, 1952.
- Mackay, D. H., Karpen, J. T., Ballester, J.L., Schmieder, B. & Aulanier, G.**, Physics of Solar Prominences: II – Magnetic Structure and Dynamics, *Space Science Reviews*, 2010.
- MacQueen, R. M., Burkepile, J. T., Holzer, T. E., Stanger, A. K. & Spence, K. E.**, Solar Coronal Brightness Changes and Mass Ejection during Solar Cycle 22, *The Astrophysical Journal*, 549, pages 1175-1182, 2001.
- Manoharan, P. & Ananthkrishnan, S.**, Determination of solar wind velocities using single-station measurements of interplanetary scintillation, *Monthly Notices of the Royal Astronomical Society*, 244, pages 690-695, 1990
- Massey, W.**, *Measuring Intensity Scintillations at the Very Long Baseline Array (VLBA) to Probe the Solar Wind*, Ph.D. Thesis, The University of California, San Diego, 1998.
- McComas, D. J., Bame, S. J., Barker, P. L., Feldman, Phillips, J. L., W. C., Riley, P. & Griffee, J. W.**, The Solar Wind Electron Proton Alpha Monitor (SWEPAM) for the Advanced Composition Explorer, *Space Science Reviews*, 86, pages 563-612, 1998.
- McComas, D. J., Barraclough, B. L., Funsten, H. O., Gosling, J. T., Santiago- Muñoz, E., Skoug, R. M., Goldstein, B. E., Neugebauer, M., Riley, P. & Balogh, A.**, Solar wind observations over Ulysses' first fill polar orbit, *Journal of Geophysical Research*, 105, 2000.
- McComas, D. J., Ebert, R. W., Elliot, H. A., Goldstein, B. E., Gosling, J. T., Schwadron, N. A. & Skoug, R. M.**, Weaker solar wind from the polar coronal holes and whole Sun, *Geophysical Research Letters*, 35, 2008.
- Mejia-Ambriz, J. C., Gonzalez-Esparza, J. A. & Aguilar-Rodriguez, E.**, Evolution of solar wind irregularities in the inner heliosphere: IPS observations, *Solar Physics*, 2012.
- Moran, P. J.**, *Interplanetary Scintillation Measurements of the Solar Wind using EISCAT*, Ph.D. Thesis, The University of Wales, Aberystwyth, 1998.
- Morgan, H. & Druckmüller, M.**, Multi-Scale Gaussian Normalization for Solar Image Processing, *Solar Physics*, 289, 8, pages 2945-2955, 2014.
- Morgan, H., Byrne J. P. & Habbal, S. R.**, Automatically Detecting and Tracking Coronal Mass Ejections. I. Separation of Dynamic and Quiescent Components in Coronagraph Images, *The Astrophysical Journal*, 752, 2, 2012.
- Morgan, H., Habbal, S. R. & Lugaz, N.**, Mapping the Structure of the Corona Using Fourier Backprojection Tomography, *The Astrophysical Journal*, 690, 2, pages 1119-1129, 2009.
- Morgan, H., Habbal, S. R. & Woo, R.**, The Depiction of Coronal Structure in White Light Images, *Solar Physics*, 236, 2, pages 263-272, 2006.

**Morgan, H., Habbal, S. R.**, A Method for Separating Coronal Mass Ejections from the Quiescent Corona, *The Astrophysical Journal*, 711, 2, pages 631-640, 2010.

**Möstl, C., Rollett, T., Lugaz, N., Farrugia, C. J., Davies, J. A., Temmer, M., Veronig, A. M., Harrison, R. A., Crothers, S., Luhmann, J. G., Galvin, A. B., Zhang, T. L., Baumjohann, W. & Biernat, H. K.**, Arrival Time Calculation for Interplanetary Coronal Mass Ejections with Circular Fronts and Application to STEREO Observations of the 2009 February 13 Eruption, *The Astrophysical Journal*, 741, 2011.

**Müller-Mellin, R., Kunow, H., Fleißner, V., Pehlke, E., Rode, E., Röschmann, N., Scharmberg, C., Sierks, H., Ruzsnyak, P., McKenna-Lawlor, S., Elendt, I., Sequeiros, J., Meziat, D., Sanchez, S., Medina, J., Del Peral, L., Witte, M., Marsden, R. & Henrion, J.**, COSTEP – Comprehensive Suprathermal and Energetic Particle Analyser, *Solar Physics*, 162, pages 483-504, 1995.

**Narita, Y.**, *Plasma Turbulence in the Solar System*, Springer, ISBN: 978-3-642-25666-0, 2012.

**Newkirk, G. Jr. & Bohlin, D.**, Reduction of Scattering Light in the Coronagraph, *Applied Optics*, 2, 2, pages 131-140, 1963.

**Newkirk, G. Jr.**, Meteoric dust in the stratosphere as determined by optical scattering techniques, *Smithsonian Contributions to Astrophysics*, 11, pages 349-358, 1967.

**Ogilvie, K. W., Geiss, J., Gloeckler, G., Berdichevsky, D. & Wilken, B.**, High-velocity tails on the velocity distribution of solar wind ions, *Journal of Geophysical Research*, 98, A3, 1993.

**Parker, E. N.**, Dynamics of the interplanetary gas and magnetic fields, *The Astrophysical Journal*, 128, pages 664-685, 1958.

**Parker, E. N.**, Nanoflares and the solar X-ray corona, *The Astrophysical Journal*, 330, pages 474-479, 1988.

**Pesnell, W. D., Thompson, B. J. & Chamberlin, P. C.**, The Solar Dynamics Observatory (SDO), *Solar Physics*, 275, pages 3-15, 2012.

**Phillips, J. L., Bame, S. J., Barnes, A., Barraclough, L., Feldman, W. C., Goldstein, B. E., Gosling, J. T., Hoogeveen, G. W., McComas, D. J., Neugebauer, M. & Suess, S. T.**, Ulysses solar wind plasma observations from pole to pole, *Geophysical Research Letters*, 22, 23, pages 3301-3304, 1995.

**Pizzo, V.**, A three-dimensional model of corotating stream in the solar wind, *Journal of Geophysical Research*, 83, 1978

**Quémerais, E. & Lamy, P.**, Two-dimensional electron density in the solar corona from inversion of white light images – Application to SOHO/LASCO-C2 observations, *Astronomy and Astrophysics*, 393, pages 295-304, 2002.

**Richter, I., Leinert, C. & Planck, B.**, Search for short term variations of zodiacal light and optical detection of interplanetary plasma clouds, *Astronomy and Astrophysics*, 110, pages 115-120, 1982.

**Riley, P. & Lionello, R.**, Mapping Solar Wind Streams from the Sun to 1 AU: A Comparison of Techniques, *Solar Physics*, 270, 2, pages 575-592, 2011.

- Rishbeth, H. & Williams, P. J. S.**, The EISCAT ionosphere radar: The system and its early results, *Royal Astronomical Society*, 26, pages 478-512, 1985.
- Rishbeth, H.**, EISCAT: A new project for studying the high latitude ionosphere, *Contemporary Physics*, 17, 5, 1976.
- Roshchina, E. M. & Sarychev, A. P.**, Approximation of 11-year solar cycles, *Solar System Research*, 45, pages 539-545, 2011.
- Rouillard, A. P., Davies, J. A., Forsyth, R. J., Rees, A., Davis, C. J., Harrison, R. A., Lockwood, M, Bewsher, D., Crothers, S. R., Eyles, C. J., Hapgood, M., Perry, C. H.**, First imaging of corotating interaction regions using the STEREO spacecraft, *Geophysical Research Letters*, 35, 10, 2008.
- Rouillard, A. P., Savani, N. P., Davies, J. A., Lacraud, B., Forsyth, R. J., Morley, S. K., Opitz, A., Sheeley, N. R., Burlaga, L. F., Sauvaud, J. –A., Simunac, K. D. C., Luhmann, J. G., Galvon, A. B., Crothers, S. R., Davis, C. J., Harrison, R. A., Lockwood, M, Eyles, C. j., Bewsher, D. & Brown D. S.**, A Multispacecraft Analysis of a Small-Scale Transient Entrained by Solar Wind Streams, *Solar Physics*, 256, pages 307-326, 2009.
- Royal Academy of Engineering**, *Extreme space weather: impacts on engineered systems and infrastructure*, [www.raeng.org.uk/spaceweather](http://www.raeng.org.uk/spaceweather), ISBN 1-903496-95-0, 2013.
- Scherrer, P. H., Bogart, R. S., Bush, R. I., Hoeksema, J. T., Kosovichev, A. G., Schou, J., Rosenberg, W., Springer, L., Tarbell, T. D., Title, A., Wolfson, C. J., Zayer, I. & MDI Engineering Team**, The Solar Oscillations Investigation – Michelson Doppler Imager, *Solar Physics*, 162, pages 129-188, 1995.
- Schou, J., Borrero, J. M., Norton, A. A., Tomczyk, S., Elmore, D. & Card, G. L.**, Polarization Calibration of the Helioseismic and Magnetic Imager (HMI) onboard the Solar Dynamics Observatory (SDO), *Solar Physics*, 275, pages 327-355, 2012.
- Schnack, D. D.**, Ideal MHD and the Frozen Flux Theorem, *Lectures in Magnetohydrodynamics*, 780, pages 49-53, 2009
- Schwenn, R.**, *Large-Scale Structure of the Interplanetary Medium, Physics of the Inner Heliosphere I*, Springer, ISBN 978-3-642-75361-9, 1990.
- Schwenn, R.**, Space Weather: The Solar Perspective, *Living Reviews of Solar Physics*, 3, 2006.
- Sel peter, E. E.**, Interplanetary Scintillations. I. Theory, *The Astronomical Journal*, 147, 1967.
- Sheeley, N. R. Jr., Wang, Y.-M., Hawley, S. H., Brueckner, G. E., Dere, K. P., Howard, R. A., Koomen, M. J., Korendyke, C. M., Michels, D. J., Paswaters, S. E., Socker, D. G., St Cyr, O. C., Wang, D., Lamy, P. L., Llebaria, A., Schwenn, R., Simnett, G. M., Plunkett, S. & Biesecker, D. A.**, Measurements of Flow Speeds in the Corona Between 2 and 30  $R_s$ , *The Astrophysical Journal*, 484, pages 472-478, 1997.

**Sheeley, N. R., Herbst, A.D., Palatchi, C. A., Wang, Y. –M, Howard, R. A., Moses, J. D., Vourlidas, A., Newmark, J. S., Socker, D. G., Plunkett, S. P., Korendyke, C. M., Burlaga, L. F., Davila, K. M., Thompson, W.T, St Cyr, O. C., Harrison, R. A., Davis, C. J., Eyles, C. J., Halain, J. P., Wang, D., Rich, N. B., Battams, K., Esfandiari, E. & Stenborg, G.,** Heliospheric Images of the Solar Wind at Earth, *The Astrophysical Journal*, 675, pages 853-862, 2008.

**Sheeley, N. R., Walters, J. H., Wang, Y.-M. & Howard, R. A.,** Continuous tracking of coronal outflows: Two kinds of coronal mass ejections, *Journal of Geophysical Research*, 104, A11, pages 24739-24768, 1999.

**Shih, F. Y.,** *Image Processing and Pattern Recognition: Fundamentals and Techniques*, John Wiley and Sons, ISBN 978-0470404614, 2010.

**Srivastava, A. K. & Dwivedi, B. N.,** Observations from *Hinode*/EIS of intensity oscillations above a bright point: signature of the leakage of acoustic oscillations in the inner corona, *Monthly Notices of the Royal Astronomical Society*, 405, pages 2317-2326, 2010.

**Sterling, A. C.,** Solar Spicules: A Review of Recent Models and Targets for Future Observations, *Solar Physics*, 196, pages 79-111, 2000.

**Stone, E. C., Frandsen, A. M., Mewaldt, R. A., Christian, E. R., Margolies, D., Ormes, J. F. & Snow, F.,** The Advanced Composition Explorer, *Space Science Reviews*, 86, pages 1-22, 1998.

**Tappin, S. J.,** Interplanetary scintillation and plasma density, *Planetary and Space Science*, 34, pages 93-97, 1986.

**Thernisien, A. F. R., Howard, R. A. & Vourlidas, A.,** Modeling of Flux Rope Coronal Mass Ejections, *The Astrophysical Journal*, 652, 1, pages 763-773, 2006.

**Thernisien, A., Vourlidas, A, Howard, R, A.,** Forward Modeling of Coronal Mass Ejections Using STEREO/SECCHI Data, *Solar Physics*, 256, pages 111-130, 2009.

**Thompson, W. T., Davila, J. M., Fisher, R. R., Orwig, L. E., Mentzell, J. E., Hetherington, S. E., Derro, R. J., Federline, R. E., Clark, D. C., Chen, P. T. C., Tveekrem, J. L., Martino, A. J., Novello, J., Wesenberg, R. P., StCyr, O. C., Reginald, N. L., Howard, R. A., Mehalick, K. I., Hersh, M. J., Newman, M. D., Thomas, D. L., Card, G. L. & Elmore, D. F.,** COR1 inner coronagraph for STEREO-SECCHI, *Proceedings of the SPIE*, 4853, pages 1-11, 2003.

**Tokumar, M., Fujimaki, S., Higashiyama, M., Yokobe, A., Ohmi, T., Fujiki, K. & Kojima, M.,** Two-Station Interplanetary Scintillation Measurements of Solar Wind Speed near the Sun Using the X-band Radio Signal of the *Nozomi* Spacecraft, *Solar Physics*, 276, page 315-336, 2012.

**Tokumar, M., Kojima, M., Fujiki, K. & Hayashi, K.,** Non-dipolar solar wind structure observed in the cycle 23/24 minimum, *Geophysical Research Letters*, 36, 2009.

**Török, T. & Kliem, B.,** Confined and Ejective Eruptions of Kink-unstable Flux Ropes, *The Astrophysical Journal*, 630, pages 97-100, 2005.

Torsti, J., Valtonen, E., Lumme, M., Peltonen, P., Eronen, T., Louhola, M., Riihonen, E., Schultz, G., Teittinen, M., Ahola, K., Holmlund, C., Kelh , V., Lepp l , K., Ruuska, P. & Str mmer, E., Energetic Particle Experiment, ERNE, *Solar Physics*, 162, pages 505-531, 1995.

Ulich, T., EISCAT UHF conversion to VHF, *The EISCAT\_3D Blog*, 17 August 2012, <http://blog.eiscat3d.org/2012/08/eiscat-uhf-conversion-to-vhf.html>, 2012.

Uscinski, B. J., *The elements of wave propagation in random media*, McGraw-Hill, ISBN 978-007066504, 1977

van Ballegooijen, A. A., Priest, E. R. & Mackay, D. H., Mean Field Model for the Formation of Filament Channels on the Sun, *The Astrophysical Journal*, 539, pages 983-994, 2000.

van Haarlem, M. P., Wise, M. W., Gunst, A. W., Heald, G., McKean, J. P., Hessels, J. W. T., de Bruyn, A. G., Nijboer, R., Swinbank, J., Fallows, R., Brentjens, M., Nelles, A., Beck, R., Falcke, H., Fender, R., H randel, J., Koopmans, L. V. E., Mann, G., Miley, G., R ttgering, H., Stappers, B. W., Wijers, R. A. M. J., Zaroubi, S., van den Akker, M., Alexov, A., Anderson, J., Anderson, K., van Ardenne, A., Arts, M., Asgekar, A., Avruch, I. M., Batejat, F., B hren, L., Bell, M. E., Bell, M. R., van Bemmelen, I., Bennema, P., Bentum, M. J., Bernardi, G., Best, P., Birzan, L., Bonafede, A., Boonstra, A.-J., Braun, R., Bregman, J., Breitling, F., van de Brink, R. H., Broderick, J., Broekema, P. C., Brouw, W. N., Br ggen, M., Butcher, H. R., van Cappellen, W., Ciardi, B., Coenen, T., Conway, J., Coolen, A., Corstanje, A., Damstra, S., Davies, O., Deller, A. T., Dettmar, R.-J., van Diepen, G., Dijkstra, K., Donker, P., Doorduyn, A., Dromer, J., Drost, M., van Duin, A., Eisl ffel, J., van Enst, J., Ferrari, C., Frieswijk, W., Gankema, H., Garrett, M. A., de Gasperin, F., Gerbers, M., de Geus, E., Grieb meier, J.-M., Grit, T., Gruppen, P., Hamaker, J. P., Hassall, T., Hoeft, M., Holties, H. A., Horneffer, A., van der Horst, A., van Houwelingen, A., Huijgen, A., Iacobelli, M., Intema, H., Jackson, N., Jelic, V., de Jong, A., Juetten, E., Kant, D., Karastergiou, A., Koers, A., Kollen, H., Kondratiev, V. I., Kooistra, E., Koopman, Y., Koster, A., Kuniyoshi, M., Kramer, M., Kuper, G., Lambropoulos, P., Law, C., van Leeuwen, J., Lema tre, J., Loose, M., Maat, P., Macario, G., Markoff, S., Masters, J., McFadden, R. A., McKay-Bukowski, D., Meijering, H., Meulman, H., Mevius, M., Middelberg, E., Millenaar, R., Miller-Jones, J. C. A., Mohan, R. N., Mol, J. D., Morawietz, J., Morganti, R., Mulcahy, D. D., Mulder, E., Munk, H., Nieuwenhuis, L., van Nieuwpoort, R., Noordam, J. E., Norden, M., Noutsos, A., Offringa, A. R., Olofsson, H., Omar, A., Orr , E., Overeem, R., Paas, H., Pandey-Pommier, M., Pandey, V. N., Pizzo, R., Polatidis, A., Rafferty, D., Rawlings, S., Reich, W., de Reijer, J.-P., Reitsma, J., Renting, G. A., Riemers, P., Rol, E., Romein, J. W., Roosjen, J., Ruiter, M., Scaife, A., van der Schaaf, K., Scheers, B., Schellart, P., Schoenmakers, A., Schoonderbeek, G., Serylak, M., Shulevski, A., Sluman, J., Smirnov, O., Sobey, C., Spreeuw, H., Steinmetz, M., Sterks, C. G. M., Stiepel, H.-J., Stuurwold, K., Tagger, M., Tang, Y., Tasse, C., Thomas, I., Thoudam, S., Toribio, M. C., van der Tol, B., Usov, O., van Veelen, M., van der Veen, A.-J., ter Veen, S., Verbiest, J. P. W., Vermeulen, R., Vermaas, N., Vocks, C., Vogt, C., de Vos, M., van der Wal, E., van Weeren, R., Weggemans, H., Weltevrede, P., White, S., Wijnholds, S. J., Wilhelmsson, T., Wucknitz, O., Yatawatta, S., Zarka, P., Zensus, A. & van Zwieten, J., LOFAR: The Low-Frequency ARray, *Astronomy and Astrophysics*, 556, 2013.

Vourlidas, A. & Howard, R. A., The Proper Treatments of Coronal Mass Ejection Brightness: A New Methodology and Implications for Observations, *The Astrophysical Journal*, 642, pages 1216-1221, 2006.

**Waldmeier, M.**, The coronal hole at the 7 March solar eclipse, *Solar Physics*, 40, pages 351-358, 1975.

**Wang, Y. -M., Ko, Y. -K, Grappin, R.**, Slow solar wind from open regions with strong low-coronal heating, *The Astrophysical Journal*, 691, pages 760-769, 2009.

**Wannberg U. G., Andersson H., Behlke R., Belyey V., Bergqvist P., Borg J., Brekke A., Delsing J., Eliasson L., Finch I., Grydeland T., Gustavsson B., Haggstrom I., Harrison R.A., Iinatti T., Johansson G., Johansson J., Johansson J., La Hoz C., Laakso T., Larsen R., Larsmark M., Lindgren T., Lundberg M., Markkanen J., Marttala I., McCreia I., McKay D., Postila M., Puccio W., Renkowitz T., Turunen E., van Eyken A., Vanhainen L.-G., Westman A. & Wolf I.**, EISCAT\_3D – A next-generation European radar system for upper atmosphere and geospace research, *Radio Science Bulletin*, 332, pages 75-88, 2012.

**Wannberg, G., Vanhainen, L.-G., Westman, A., Breen, A. R. & Williams, P.**, The new 1420 mhz dual-polarisation interplanetary scintillation (IPS) facility at EISCAT, *Proceedings of the Union of Radio Scientists (URSI) 2002*, 2002.

**Watanabe, T. & Schwenn, R.**, Large-scale propagation properties of interplanetary disturbances revealed from IPS and spacecraft observations, *Space Science Reviews*, 51, pages 147-173, 1989.

**Wilhelm, K., Curdt, W., Marsch, E., Schühle, U., Lemaire, P., Gabriel, A., Vial, J.-C., Grewing, M., Huber, M. C. E., Jordan, S. D., Poland, A. I., Thomas, R. J., Kühne, M., Timothy, J. G., Hassler, D. M. & Siegmund, O. H. W.**, SUMER – Solar Ultraviolet Measurements of Emitted Radiation, *Solar Physics*, 162, pages 189-231, 1995.

**Witze, A.**, Voyager: Outward bound, *Nature*, 497, 7450, pages 424-427, 2013.

**Woo, R. & Habbal, S. R.**, Extension of coronal structure into interplanetary space, *Geophysical Research Letters*, 24, pages 1159-1162, 1997.

**Woods, T. N., Eparvier, F. G., Hock, R., Jones, A. R., Woodraska, D., Judge, D., Didkovsky, L., Lean, J., Mariska, J., Warren, H., McMullin, D., Chamberlin, P., Berthiaume, G., Bailey, S., Fuller-Rowell, T., Sojka, J., Tobiska, W. K. & Viereck, R.**, Extreme Ultraviolet Variability Experiment (EVE) on the Solar Dynamics Observatory (SDO): Overview of Science Objectives, Instrument Design, Data Products, and Model Developments, *Solar Physics*, 275, pages 115-143, 2012.